THE UNIVERSITY OF CHICAGO

NON-EQUILIBRIUM STEADY STATES AND DYNAMICS OF OPEN QUANTUM MANY-BODY SYSTEMS

A DISSERTATION SUBMITTED TO
THE FACULTY OF THE DIVISION OF THE PHYSICAL SCIENCES
IN CANDIDACY FOR THE DEGREE OF
DOCTOR OF PHILOSOPHY

DEPARTMENT OF PHYSICS

BY
ANDREW POCKLINGTON

CHICAGO, ILLINOIS
AUGUST 2026

ORCID iD: https://orcid.org/0000-0003-4777-4305

To Mom, Dad, Danny and Willy

I like them to talk nonsense. That's man's one privilege over all creation. Through error you come to the truth!

— Fyodor Dostoevsky (Translated by Constance Garnett)

TABLE OF CONTENTS

LIST OF FIGURES

LIST OF ALGORITHMS

ACKNOWLEDGMENTS

This dissertation would not have been possible without the incredible amount of support and guidance that I received along the way, and for that I am extremely grateful.

Firstly, I would like to acknowledge my family. My parents have been so incredibly supportive of me along my journey. Over the last five years as a Ph. D. student, and nine years at the University of Chicago, I have always had an absolute bedrock to lean back on when it didn't seem like anything could possibly work out. I could not have asked for a kinder, more loving environment that has truly allowed me to get to where I am today. My brother, Dan, has been a constant companion and also a best friend for the last 25 years, who has always indulged me talking about my research and also always has something insightful to say. I'll always remember our trip to the Balkans just before I started my final year here; I loved every moment of it and am so glad we got to do that together. Last, but certainly not least, my brother Will has always been an absolute spark of light in my life and a constant source of inspiration (not to mention how much fun we had in Hyde Park on all of our sleepovers over the years). I could not have done this without all of you.

I want to thank my advisor, Aash, with whom I have had the pleasure of working closely with since before I even started graduate school. I have learned so much from him over the last several years, both about physics but also about what it really means to be a researcher. He has provided deep insights into my research, and also has always been exceptionally good at finding the right way to frame questions and present results. From him, I have learned that sometimes (always) having physical intuition for something can be more important than just a brute-force mathematical result. I appreciate his guidance and oversight, especially in the first few years, and likewise I appreciate the fact that he has given me more freedom and independence as I have grown as a researcher. I imagine that I will still continue to learn from him in the years to come, and cannot imagine myself as a physicist without his help.

I would also like to thank my committee members, Andrew, Michael, and Liang, for their

time, patience, and feedback over the years. I would also like to especially thank Liang, who was kind enough to also write letters of recommendation for postdoctoral positions.

In addition, I want to thank all of the members of Aash's group I have had the pleasure to know and work with over the years. I have been so lucky to work with people that not only have always been extremely generous with their time when I have questions, but also have become some of my closest friends. I want to thank David, Peter, Setiawan, Alireza, Tony, Ron, Michael, Anjun, Sihan, Kalpak, Amir, and Federico, who were always there for fun research discussions. I especially want to thank Xander, Andrew, and Yu-Xin, who helped me find my footing as a young student and welcomed me so openly into the group that I never felt the least bit out of place. I want to thank Martin, for the giving me the greatest possible version of the Alhambra game and for all the dinners we shared. Gideon, Jeffrey, Antoine, Adi, David: I think every research group in the world should be jealous of the incredible community we built for ourselves, and the level of friendship and trust we share. I would also like to thank Yu-Xin, Yariv, Jeffrey, Andrew, Mikhail, and Martin, all of whom I was lucky enough to work and collaborate with directly. I also want to thank everyone in the MeMo office (and the old ACC office for those who remember it); I am eternally grateful for the random physics chats, for the spikeball games, for indulging my incessant need for coffee breaks.

I want to thank Hannes who first introduced me to physics research nearly 8 years ago, along with Kevin, Shankar, and Jordan. You were the best mentors I could have hoped for as an undergrad who had no idea what he was doing, and I will always look back fondly at my time in the Bernien lab. It was there that I actually learned what research was.

I want to thank Vaishika: you only saw the last year of my Ph. D., but it was one of the of the most stressful as I went through the grueling post-doc application process and then the writing of this dissertation. I don't think there is any possible way I could have done it without your support. You were always there to lean on when things were hard, and I

wanted nothing more than to celebrate with you when things were going well.

I also certainly couldn't have gotten through the last five years without my friends. Antoine, you have been not only one of my closest friends but also the best roommate I could've asked for; I will dearly miss living with you next year. Gideon and Antoine, our Monday porch beers was always when I could relax and unwind and get everything off my chest, and I think it was there that I thought most deeply about what I really wanted to get out of both PhD and life. (I also hope we still get to finish our Marz memberships together). Kaleb and Nidhaan, you made Hyde Park what it is to me, even after you moved into different parts of the city. Because of you both, this place will always feel like home. Nayana, Mariesa, Debayan, Mahadevan, Alex, Swathi, Jake, thank you for the incredible times we have had over the years. It is incredible to think how many lifelong friends I have been so lucky to make in just five years; I feel like I've known you all my whole life. In addition to all of the new friends I've made here, I am also lucky enough to still be close to the friends I've had forever: Ian, we've been friends since kindergarten and I truly hope we always will be.

Finally, there are a hundred other people who have left an imprint on my life over the last five years that I don't have enough room to thank. To the Thursday morning Salonica crew, I have never before and probably never will again laugh that hard watching the news. To everyone who came out for their Pub passport every Wednesday, rain or shine: thank you, it is the majority of my wardobe. To everyone at the squatch hill, that was probably the best camping trip I've ever taken. To everyone who came to the Halloween and 4th of July parties ... well, I actually don't remember them so well, but I definitely had a good time. To the Jimmy's crew, thank you for being there when I needed friends, and for making Hyde Park such a warm and welcoming place.

ABSTRACT

Understanding the fate of many-body quantum physics in the presence of noise is of both practical and fundamental interest. Practically, all quantum systems (especially near-term experiments) are interacting with their environment, and so understanding the role that noise plays is crucial to making predictions of observations. Fundamentally, one can find novel physical phenomena in open systems that exists only out of equilibrium. This motivates trying to get a basic understanding of mixed state phases of matter.

This dissertation will be in two parts, linked by the common theme of understanding the dynamics and steady states of open, many-body quantum systems. We will first ask about dissipative state preparation, or thinking about how one can use openness in a quantum system to engineer interesting quantum states. We will present a number of exact solutions for spins, free bosons, and free fermions that have unique properties in the steady state, be they highly entangled or topological in nature. Then, we will discuss their dynamics, and present fundamental limits on the time it takes to prepare highly entangled states under local Markovian channels, and also ways that one can use additional ingredients to evade these bounds.

The second part will focus on a novel technique to simulate the dynamics of open spin-1/2 systems whose coupling to the environment will formally make them interacting. This technique relies on encoding the many-body density matrix into a stochastic covariance matrix of the Jordan-Wigner fermions which we show can be sampled from efficiently. We use this technique to uncover rich phenomena outlined in a number of many-body systems, as well as provide certain situations in which the stochastic observables can be analytically re-averaged to get closed form solutions for the entire interacting system.

CHAPTER 1

INTRODUCTION

The theory of open quantum systems attempts to describe the interaction between a quantum system and its environment. This dissertation will generally be interested in answering two questions that involve the theory of open quantum systems in the many-body limit. Firstly, we will attempt to understand how the environment, or bath, that the quantum system sees can be used as a resource. This often goes by the name of dissipative state preparation, or reservoir engineering, in which an experiment attempts to engineer the coupling to the bath to prepare a novel or useful quantum state. The idea of engineering the coupling of a quantum degree of freedom to its environment is not new, and has been used extensively in, e.g., AMO physics. A canonical example is optical pumping: when driving an atomic ground-to-excited transition with circularly polarized light, the steady state is a highly out-of-equilibrium distribution comprised almost entirely of a single magnetic hyperfine level, which has significantly less entropy than the equilibrium ground state would have. We are interested in using similar ideas, where a combination of tailored interactions, drives, and dissipation prepare useful quantum states, but now in the many-body regime.

First, we will present exact steady state solutions for reservoir engineered schemes. In Chapter 2, we explain how a 1D spin model can be dissipatively cooled into a highly structured and volume-law entangled "rainbow state" using only local interactions and a single engineered dissipative environment. Following this, in Chapter 3, we will explain how one can apply a single, localized dissipative environment to prepare topologically ordered states in a lattice of bosonic modes. We will give explicit proscriptions to selectively excite and squeeze topological edge modes in both one and two spatial dimensions.

In Chapter 4, we will interest ourselves not only in the steady state, but also in the *dynamics* of open quantum systems, especially what is called the relaxation or mixing time, which describes the characteristic time scale required to reach the steady state. In Chapter 2,

we observe numerically that the more entanglement that is present in the steady state, the longer this characteristic time-scale is. We will be able to prove that this is not a fluke or a model-dependent fact. In fact, we will prove the stronger statement that it is impossible to prepare a maximally entangled state with a finite mixing time using local, Markovian quantum channels. Moreover, we will prove a sharp trade-off between the steady state entanglement and the time required to reach the steady state: the more entanglement in the steady state, the longer it takes to reach.

This seems to imply that there is no free lunch, and that it is impossible to use dissipation to prepare entanglement in a scalable or useful way. However, in Chapter 5, we will provide a minimal way to circumvent these fundamental trade-offs using a classical memory (breaking the assumption of time-locality or Markovianity) and provide an explicit mechanism to prepare a maximally entanglement state in finite time using only spatially local resources and a single-bit quantum memory.

If the first half of this dissertation is asking the question *What can the bath do for you?*, the second half will instead try to answer *What can you do for the bath?* More specifically, instead of trying to find engineered models of interest, we will be interested in understanding the generic behavior of many-body systems subject to experimentally relevant, more naturally occuring noise models, as opposed to the highly engineered versions considered in the first half. Here, we will be interested in understanding the emergent nonequilibrium many-body physics that arises when noise competes with coherent dynamics. This is relevant in its own right as a study of new, emergent phenomena out of equilibrium. Moreover, because current experiments are pre-fault-tolerant, the environment can never be neglected and so these questions are critical to make predictions of the outcome of current quantum experiments. Our goal will be both analytic insights as well as efficient computational techniques, where efficient in this case implies that the computational complexity scales polynomially in the number of spins.

In Chapter 6, we will present a new, efficient simulation technique that allows one to simulate a particularly relevant class of quantum systems. The technique relies on the observation that there exist a certain class of dynamics that can be described by averaging over noisy Gaussian trajectories, and we prove that computing individual trajectories is computationally easy and sampling is also efficient. We use this technique to study three paradigmatic models, and make new predictions on previously inaccessible system sizes. We also explain how it can be used in more complicated 2D systems. Moreover, the structure we learn about is more than just a numerical tool and also provides deep physical insights into the role of noise in quantum many-body systems. In Chapter 7, we use this structure to show that this method is even more powerful if we restrict our noise model to Pauli channels. Pauli channels are particularly relevant for digital quantum computers and simulators, as they often utilize randomized compiling to map all noise into Pauli channels. We show that the trajectories for Pauli noise can be analytically re-averaged to get closed form, analytic solutions to the time evolution of arbitrary observables. Utilizing this technique, we get results on decohered quantum critical states in the thermodynamic limit. Finally, in Chapter 8, we will be more pedagogical and explain the explicit construction of the simulation techniques we outlined in Chapters 6 and 7. We will give explicit constructions of the relevant algorithms in pseudocode and use these to calculate theoretically the large system computational complexity.

Each chapter is a self-contained body of work, with the exception of Chapter 8, which is based on the results in Chapters 6 and 7.

CHAPTER 2

STABILIZING RAINBOW STATES WITH LOCAL, MARKOVIAN DISSIPATION

This chapter contains previously-published material found in Ref. [1]. Reuse is permitted according to the copyright agreement used by *Physical Review B*.

2.1 Introduction

Quantum reservoir engineering is a powerful tool in quantum information processing. In its simplest form, it involves tailoring dissipative processes to stabilize non-classical quantum states [2, 3]; when generalized to stabilizing a subspace, it can also be used as a route to quantum error correction [4, 5]. Many experiments have implemented dissipation engineering in few-body quantum systems comprised of 1-2 qubits or bosonic modes (see e.g. [6, 7, 8, 9, 10]). Theoretical work has also considered extensions to truly many-body systems [11, 12, 13], though most proposals are experimentally daunting, as they require engineered dissipation on every site of an extended lattice system. More recent work demonstrated that for non-interacting bosons hopping on a 1D lattice, a single, local engineered squeezing dissipator can be sufficient to stabilize the entire extended system in a state with long-range entanglement [14, 15]; a subtle particle-hole symmetry was shown to be the key ingredient, allowing a generalization to higher dimensions [16]. These protocols are, however, limited to stabilizing Gaussian entangled states, whose use in quantum information is highly constrained [17].

Given this prior work, a natural question is whether a single localized dissipative process can prepare and stabilize more complex many-body entangled states. In particular, can this approach work in systems which have (unlike free bosons) a finite-dimensional local Hilbert space, e.g. lattices of fermions, hard-core bosons or qubits. In this Chapter, we show that the answer is, surprisingly, yes. We describe an extremely simple protocol exploiting symmetry

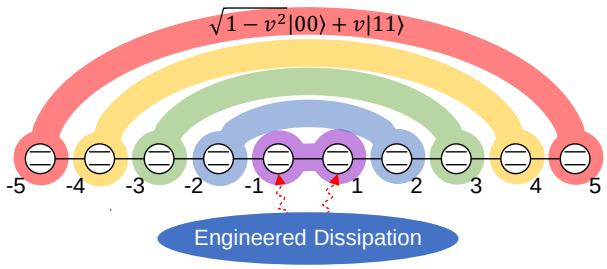

Figure 2.1: Schematic of a 1D qubit array with nearest-neighbour XY interactions, where the two central sites are coupled to a common engineered dissipative reservoir with a pairing parameter v (c.f. Eq. (2.2)). The dissipative dynamics stabilizes an arbitrary initial state of the qubits into a volume-law entangled rainbow state, where each qubit is entangled with its mirror image qubit (as depicted). The model maps to an interacting fermionic model featuring dissipative pairing with phase fluctuations.

and the dissipative analog of Cooper pairing to stabilize highly entangled states in 1D lattices of fermions and qubits, one example being the so-called "rainbow state" (Fig. 2.1). Such rainbow states feature long-range, volume-law entanglement, and are known to be the ground states of highly structured, spatially non-uniform Hamiltonians [18, 19]. Our dissipative approach does not require the realization of such exotic Hamiltonians. Instead, it only uses nearest-neighbour Hamiltonian interactions (which need not be uniform or symmetric) and a *single* localized dissipator; the entangled steady state state is the unique steady state irrespective of the size of the lattice. As we discuss, the resources required to implement our protocol already exist in a number of different quantum information processing architectures.

Our results also have interest in the context of general studies of many-body driven dissipative system. The spin version of our problem *cannot be mapped exactly to free fermions*. Nonetheless, we are able to exactly describe the steady state. We discuss how qualitative features of the dynamics can be connected to a model of dissipative fermionic pairing with phase fluctuations. Note that our work is distinct from a recent proposal for using dissipation to generate entangled states in 1D qubit chains [20, 21]. These protocols also generated rainbow-like entangled states, but only if the system was initially prepared in a non-trivial, highly nonlocal entangled steady state. In contrast, our approach has in general a *unique*

entangled steady state, and hence is completely independent of the initial state: one can start from a trivial product state and still obtain the volume-law entangled rainbow state. Alternate schemes that unconditionally stabilize qubit rainbow states have also been proposed [22, 23]. Our scheme is simpler to implement, and is also far more general: it can stabilize a wide class of entangled pure qubit states (many having a correlation structure considerably more complex than a rainbow).

2.2 Fermions

We begin by considering non-interacting fermions, using this system to build up the key ideas that will enable our qubit protocol. We consider spinless fermions hopping on a $2N$-site lattice with a tight binding Hamiltonian $\hat{H}_F = \sum_{i,j} H_{ij} \hat{c}_i^\dagger \hat{c}_j$, where H_{ij} is a Hermitian matrix, and $\hat{c}_i$ annihilates a fermion at lattice site i. $\hat{H}_F$ is readily diagonalized, with $\hat{d}_\alpha^\dagger = \sum_j \psi_\alpha[j] \hat{c}_j^\dagger$ creating a particle in an energy eigenstate with energy ϵ_α and real-space wavefunction $\psi_\alpha[j]$. Note that we do not assume translational invariance.

Our goal is to now introduce localized dissipation which stabilizes the entire lattice in a finite-density state with long-range entanglement. For non-interacting bosons, this can be accomplished by coupling a single site to a squeezed Markovian reservoir [14, 15, 16]. Such a reservoir attempts to enforce local pairing correlations on the coupled site. For spinless fermions, the Pauli exclusion principle excludes an identical approach. However, one can try the next simplest configuration: introduce a localized Markovian dissipative reservoir that attempts to stabilize fermionic pairing correlations on *two* adjacent sites $j = \overline{0}, \overline{1}$ (i.e. prepare them in the state $(u + ve^{i\phi} \hat{c}_{\overline{0}}^\dagger \hat{c}_{\overline{1}}^\dagger)|00\rangle$). This corresponds to simply cooling a pair of localized fermionic Bogoliubov modes. As we will see, simply cooling one of these modes generally suffices.

The total system dynamics including the localized dissipative pairing is then described

by a Lindblad master equation:

$$\dot{\hat{\rho}} = -i[\hat{H}, \hat{\rho}] + \Gamma \mathcal{D}[\hat{\beta}_L]\hat{\rho}, \tag{2.1}$$

Here $\mathcal{D}[\hat{L}]\hat{\rho} = \hat{L}\hat{\rho}\hat{L}^\dagger - \frac{1}{2}\{\hat{L}^\dagger\hat{L}, \hat{\rho}\}$. For our fermion problem, we have $\hat{H} = \hat{H}_F$ and

$$\hat{\beta}_L = u\hat{c}_{\overline{0}} - ve^{i\phi}\hat{c}^\dagger_{\overline{1}}, \tag{2.2}$$

where $u = \sqrt{1-v^2}$, with the pairing parameter v real and satisfying $0 \leq v \leq 1$, and Γ parametrizes the strength of the dissipation, and corresponds to the cooling rate of the localized Bogoliubov mode $\hat{\beta}_L$. The dissipation in Eq. (2.1) induces an effective non-Hermitian Hamiltonian which includes pairing terms of the form $(iuve^{i\phi}c^\dagger_{\overline{1}}c^\dagger_{\overline{0}} - \text{H. c.})$. Our system thus has the form of an unusual dissipative impurity problem, where the "impurity" corresponds to the local dissipative pairing terms. At a heuristic level, the dissipation injects Cooper pairs on these sites, which can then propagate outward in the lattice. Generically, Eq. (2.1) will lead to an impure steady state, with fluxes of Cooper pairs both into and out of the lattice. We note that quadratic fermionic models with dissipative pairing have been studied previously in the context of cold atoms [24, 13, 25, 26], but unlike our work, these assumed pairing on every lattice site.

We next show that if the lattice Hamiltonian obeys a ubiquitous kind of generalized chiral symmetry, then we can ensure the existence of a unique, pure, entangled steady state (see Appendix A for more details). This includes, but is certainly not limited to, lattices that can be divided into two equal sized sublattices, denoted A and B, such that $\hat{H}_F$ only permits hopping from $A \leftrightarrow B$. This structure is found in many lattice systems, including all nearest neighbor hopping models on square lattices. Observe that this implies that $\hat{H}_F$ has a chiral symmetry, since the symmetry that sends $\hat{c}_i \to -\hat{c}_i$ if $i \in A$ and $\hat{c}_i \to \hat{c}_i$ if $i \in B$ sends $\hat{H}_F \to -\hat{H}_F$. This guarantees we can diagonalize the Hamiltonian such that

$\hat{H}_F = \sum_{\alpha>0} \epsilon_\alpha \left(\hat{d}^\dagger_\alpha \hat{d}_\alpha - \hat{d}^\dagger_{-\alpha} \hat{d}_{-\alpha} \right)$ where $\hat{d}^\dagger_{\pm\alpha}$ creates an eigenmode with energy $\pm\epsilon_\alpha$.

We can use this to rewrite the jump operator as a sum over non-local Bogoliubov modes, which pair positive and negative energy eigenmodes whenever the sites $\overline{0}, \overline{1}$ live on different sublattices (see Appendix A for more details):

$$\hat{\beta}_L = \sum_\alpha N_\alpha (\hat{\beta}_\alpha + \hat{\beta}_{-\alpha}), \tag{2.3}$$

where

$$\hat{\beta}_\alpha = u_\alpha \hat{d}_\alpha - v_\alpha \hat{d}^\dagger_{-\alpha} \qquad \hat{\beta}_{-\alpha} = u_\alpha \hat{d}_{-\alpha} + v_\alpha \hat{d}^\dagger_\alpha. \tag{2.4}$$

These are an independent set of fermionic annihilation operators obeying canonical anticommutation relations. The constants u_α and v_α encode information about the overlap of the eigenmodes with the dissipation sites $\overline{0}, \overline{1}$ (see Appendix A for more details):

$$u_\alpha = \frac{u \psi_\alpha[\overline{0}]}{N_\alpha}, \qquad v_\alpha = \frac{v e^{i\phi} \psi^*_{-\alpha}[\overline{1}]}{N_\alpha}, \tag{2.5}$$

$$N_\alpha = \sqrt{u^2 |\psi_\alpha[\overline{0}]|^2 + v^2 |\psi^*_{-\alpha}[\overline{1}]|^2}, \tag{2.6}$$

where N_α fixes normalization. For certain finely-tuned parameters, it is possible that some $N_\alpha = 0$, in which case those eigenmodes have no overlap with the dissipation sites, and thus are not cooled. However, for a generic Hamiltonian, $N_\alpha \neq 0$, and so the jump operator is a linear combination of all $2N$ of the Bogliubov modes; the steady state is *uniquely* their joint vacuum. This state is pure, and has entanglement that grows linearly with system size. We can express the steady state in terms of the eigenmodes as $|\psi\rangle = \prod_{\alpha>0} \left(u_\alpha - v_\alpha \hat{d}^\dagger_{-\alpha} \hat{d}^\dagger_\alpha \right) |0\rangle$. The correlators in the steady state are:

$$\langle \hat{d}^\dagger_\alpha \hat{d}_\beta \rangle = |v_\alpha|^2 \delta_{\alpha\beta}, \qquad \langle \hat{d}_\alpha \hat{d}_\beta \rangle = -u_\alpha v_\beta \ \mathrm{sgn}(\alpha) \delta_{\alpha,-\beta}. \tag{2.7}$$

In real space, the entanglement structure of our dissipatively stabilized steady state is only between the two sublattices A and B, and the amount of entanglement between the two sublattices grows linearly with N, see Appendix A. However, despite only being between the sublattices, the spatial pattern can be quite complicated. Given a generic Hamiltonian, any given lattice site will be correlated with the entire sublattice it does not reside on. There are many systems that possess the chiral symmetry required for our scheme. A particularly simple example (that, surprisingly, will generalize to the case of spins) is a 1D lattice with $2N$ sites described by a Hamiltonian with nearest neighbour hopping that possesses an inversion symmetry about its midpoint. Since $\hat{H}_F$ is symmetric, if the sites $\overline{0}, \overline{1}$ are mapped to each other by the mirror symmetry, then $u_\alpha = u, v_\alpha = v\ \forall \alpha$. The correlators defined in Eq. (2.7) are then also particularly simple in real space, giving the unique steady state $|\psi\rangle = \prod_{i=1}^{N} \left(u - v(-1)^i \hat{c}^\dagger_{-i} \hat{c}^\dagger_i\right) |0\rangle$. This state exhibits volume-law entanglement (see Fig. 2.1), and is known as a rainbow state [18, 19]. As discussed in Appendix A, many more examples are possible, including the 1D Su-Schriefer-Heeger model [27, 28] and the 2D Hofstadter model [29].

2.3 Qubits

Using the above fermionic setup as inspiration, we now ask whether a similar dissipative preparation scheme is possible for an array of coupled spins or qubits. While any quadratic $A \leftrightarrow B$ hopping Hamiltonian worked for the fermions, it turns out the qubits require the slightly stricter condition of a 1D nearest-neighbor hopping chain. In this case, the sublattices are comprised of every-other lattice sites. Further, while the fermions would take any placement choice of $\overline{0}, \overline{1}$ so long as they were on different sublattices, the qubits require they be neighboring (see Appendix A).

This still leaves all 1D nearest neighbor hopping models, including disordered systems. For simplicity, we will focus below on the case of a lattice with mirror symmetry. It was

in this case that the fermions had simplified spatial correlations, giving rise to the rainbow structure. The master equation is then given by Eq. (2.1) with $\hat{H} = \hat{H}_S$ and

$$\hat{H}_S = -\left[\sum_{i=-N}^{-2} J_i \hat{\sigma}_i^+ \hat{\sigma}_{i+1}^- + \sum_{i=1}^{N-1} J_i \hat{\sigma}_i^+ \hat{\sigma}_{i+1}^- + J_{-1} \hat{\sigma}_{-1}^+ \hat{\sigma}_1^-\right] + \text{H. c.}, \tag{2.8}$$

$$\hat{\beta}_L = u\hat{\sigma}_{\overline{0}}^- + v\hat{\sigma}_{\overline{1}}^+. \tag{2.9}$$

Here $\hat{\sigma}_i^+$ ($\hat{\sigma}_i^-$) is the Pauli raising (lowering) operator on site i. Our lattice has $2N$ sites labeled $(-N, \ldots, -1, 1, \ldots N)$, i.e. there is no 0^{th} lattice site. We will constrain the hoppings to obey $J_i = J_{-i-1}$, so $\hat{H}$ has mirror symmetry. The dissipation-coupled sites $\overline{0}$ and $\overline{1}$ will then be the middle two sites of the lattice, i.e. $\overline{0} = -1, \overline{1} = 1$. While the dissipator here may seem exotic, we show below how they can be realized in a number of platforms using existing experimental tools.

The above spin model can be readily mapped to fermions using the Jordan-Wigner (JW) transformation [30]. However, it necessarily maps to an *interacting* fermionic model (in contrast to the quadratic system considered in Eq. (2.2)). The most convenient mapping to JW fermions $\hat{c}_j$ is given by the transformation

$$\hat{c}_i = \begin{cases} \left(\prod_{j=1}^{i} \hat{\sigma}_j^z\right) \hat{\sigma}_i^- & 1 \le i \le N, \\ \left(\prod_{j=1}^{N} \hat{\sigma}_j^z\right) \left(\prod_{j=-N}^{i} \hat{\sigma}_j^z\right) \hat{\sigma}_i^- & -N \le i \le -1. \end{cases} \tag{2.10}$$

This corresponds to using site 1 as the reference for the string operators. Letting $\hat{N}_{\text{tot}}$ be the total fermion number operator, our model can be expressed in terms of these fermionic

degrees of freedom as:

$$\hat{H}_S = \sum_{i \neq N,-1} J_i \hat{c}_i^\dagger \hat{c}_{i+1} + J_{-1}(-1)^{\hat{N}_{\text{tot}}} \hat{c}_1^\dagger \hat{c}_{-1} + \text{H. c.}, \tag{2.11}$$

$$\hat{\beta}_L = u\hat{c}_{-1}(-1)^{\hat{N}_{\text{tot}}} - v\hat{c}_1^\dagger. \tag{2.12}$$

We see that the presence of the phase operator $(-1)^{\hat{N}_{\text{tot}}}$ in both $\hat{H}_S$ and the dissipative terms ruins a mapping to free fermions. On a heuristic level, we can interpret this as a modification of Eq. (2.2) that now describes fluctuations in the phases of the Cooper pairs injected into the system by the reservoir. For the simple fermionic system described by Eq. (2.2), pairs are always injected with a fixed phase ϕ; in contrast, in Eq. (2.11), they are injected with a phase ± 1 that depends on the system's parity. We stress that even with other gauge conventions for the JW transformation, it is not possible to eliminate these phase fluctuations (i.e. string operators) from the dissipator.

To better understand our system, we can re-write the nonlinear dissipation operators in terms of a fixed basis of local Bogoliubov operators $\hat{\tilde{\beta}}_A = u\hat{c}_{-1} - v\hat{c}_1^\dagger, \hat{\tilde{\beta}}_B = u\hat{c}_1 + v\hat{c}_{-1}^\dagger$. As was noted in the preceding section, we can write $\hat{\tilde{\beta}}_A$ as a sum over the modes defined in Eq. (2.4). Further, in the special case of a mirror symmetric Hamiltonian $\hat{\tilde{\beta}}_B$ will also be a sum over these modes, see Appendix A. Defining $\hat{P}_{\text{ev}} = (1 + (-1)^{\hat{N}_{\text{tot}}})/2$ as the projection operator onto even number-parity states, we have:

$$\hat{\beta}_L = \hat{\tilde{\beta}}_A \hat{P}_{\text{ev}} - \left[(u^2 - v^2)\hat{\tilde{\beta}}_A + 2uv\hat{\tilde{\beta}}_B^\dagger\right](1 - \hat{P}_{\text{ev}}). \tag{2.13}$$

This provides a simple way to understand the phase fluctuation physics: it is as though the dissipation has a parity-dependent temperature. For even-parity states, the dissipation can only remove Bogoliubov exctiations, i.e. it acts like an effective zero temperature bath. In contrast, for odd-parity states and $v \neq 0$, we see that there are amplitudes for the dissipation

to either create or destroy excitations (like an effective bath at a non-zero temperature).

Eq. (2.13) also leads to an important conclusion: despite the additional nonlinearity and phase fluctuations in our spin model, the steady state of our simple free fermion model in Eq. (2.2) is also a steady state of the spin model. This steady state (which here is a rainbow state, given the mirror symmetry of $\hat{H}$) has a definite even number parity, and hence the Liouvillian acting on this state is identical to the free fermion Liouvillian. At a heuristic level, this state has a definite number parity, and hence phase-fluctuations are irrelevant. Returning to our original qubit degrees of freedom, the pure steady state takes the form:

$$|\psi_{\text{ss}}\rangle = \prod_{i=1}^{N} (u + (-1)^i v \hat{\sigma}_i^+ \hat{\sigma}_{-i}^+)|0\rangle. \tag{2.14}$$

Eq. (2.13) also lets us show that as long as $v^2 \neq 1/2$, this steady state is unique. Since the Hamiltonian conserves Bogoliubov excitations, moving between manifolds with different Bogoliubov number can only happen dissipatively. The state with no Bogoliubov excitations has even parity, so it can only be cooled by Eq. (2.13); however, there is no lower number state, and so it is dark to the dissipation. On the other hand, every higher excitation state can be cooled, and so eventually all of the population flows to the Bogoliubov vacuum. Note, this argument also holds for non-rainbow symmetric systems, see Appendix A. We thus have a central result of this Chapter: any initial state of our qubit array (irrespective of its purity or entanglement) will relax into this volume-law entangled pure state. Further, this result holds independently of the magnitude of the hopping parameters J_j/Γ, and even in the presence of additional Hamiltonian terms that preserve the mirror symmetry of $\hat{H}_S$, see Appendix A.

We can now also understand the additional constraints put on the qubits to maintain the purity of the steady state. The fact that the chain must be 1D and nearest neighbor is a result of the non-local nature of the Jordan-Wigner transformation. In the same vein,

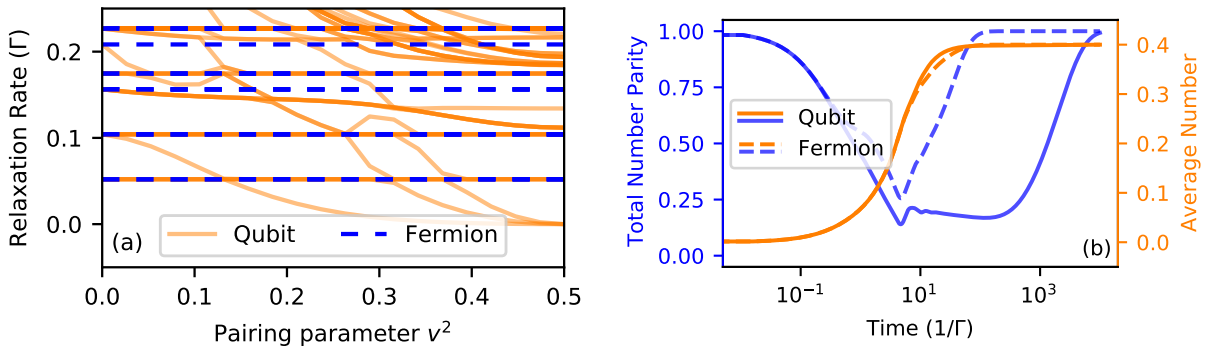

Figure 2.2: (a) Low-lying dissipative spectrum of our master equation in Eq. (2.1) (i.e. real part of Liouvillian eigenvalues) for a 6 site 1D lattice with $\Gamma = J_j$, plotted as a function of v^2. We take the simple case where the Hamiltonians $\hat{H}_F, \hat{H}_S$ have a mirror symmetry. Both the qubit model (orange) and the free-fermion model (blue) are shown. While the spectra coincide for the trivial $v = 0$ case, the fermionic spectrum is independent of v, whereas for qubits, slow modes and complex level structure arise as v is increased. (b) Time evolution of both the average excitation number (orange) and total number parity $(-1)^{\hat{N}}$ (blue) for an 8-site lattice, $v^2 = 0.4$, starting from the vacuum state; other parameters same as (a). The qubit model exhibits an extremely slow relaxation of total number parity, a direct reflection of the pairing phase fluctuations that emerge in its fermionic representation.

requiring the sites coupled to the engineered dissipation to be neighboring tells us the only string operator that appears in the master equation is $(-1)^{\hat{N}_{\text{tot}}}$. Despite these constraints, we can see that our model is still incredibly robust to disorder. The steady state will still be pure, unique and entangled regardless of the different hopping amplitudes between lattice sites. See Appendix A for more details.

2.4 Dynamics and multi-stability

While the qubit and free-fermion dissipative arrays share the same pure steady state, the models have strikingly different dynamics. This is a direct consequence of the form of the dissipator given in Eq. (2.13). The phase fluctuations in the fermionic representation of the qubit model lead to slower overall relaxation, due to the effective non-zero temperature and excitation-creation associated with odd-parity states. As can be seen from Eq. (2.13), this

odd parity heating increases as v is increased from 0, with an amplitude $\propto v\sqrt{1-v^2}$. For free fermions, there is no heating: the dissipative dynamics always corresponds to removing excitations, irrespective of the system state.

Shown in Fig. 2.2a is the numerically-calculated dissipative spectrum of the Liouvillians for the free fermion and qubit versions of our model as a function of the pairing parameter v^2. For free fermions, the relaxation rates are independent of v^2; one can show that for large N, the slowest relaxation rate (dissipative gap) scales as $1/N^3$, see Appendix A. In stark contrast, the relaxation rates in the qubit model depend on v^2, with the emergence of an extremely small dissipative gap as $v^2 \to 1/2$. Fig. 2.2b demonstrates that this emergent slow timescale manifests itself directly in observable quantities. We see that for both the qubit and free-fermion models, the average particle numbers relax on a similar timescale $\sim 1/\Gamma$. The average parity relaxes on the same timescale for fermions, but for the qubit model, exhibits exponentially slower relaxation. This is a direct manifestation of the effective phase fluctuations encoded in Eq. (2.11).

The case $u^2 = v^2 = 1/2$ is also of special interest. Eq. (2.13) indicates that in this case, the dissipation can only remove excitations from even parity states, and can only add excitations to odd parity states. This immediately leads to multi-stability, as if the system starts in a state with $2m$ Bogoliubov excitations, it will forever be stuck in a manifold of states having either $2m$ or $2m-1$ excitations. This immediately leads to at least $N+1$ steady states (see Appendix A for more details). We stress that there is no multi-stability in the free-fermion model. the presence and absence of multi-stability in these models will be explored more in Chapters 4 and 5.

2.5 Experimental Implementation

The basic qubit master equation in Eqs. (2.8) and (2.9) could be realized in a variety of platforms. Linear arrays of tunnel-coupled qubits have been realized in many systems, including

trapped ions [31, 32, 33] and superconducting qubits [34, 35, 36]. The required dissipation on sites $j = -1, 1$ could be achieved by driving these qubits with two-mode squeezed light via transmission lines or waveguides [37]. In this case, Γ would represent the waveguide coupling rates, and $v/u = \tanh r$, with r the squeezing parameter. While such a scheme could be realized by driving superconducting qubits with two-mode squeezed microwave radiation generated by a Josephson parametric amplifier [38, 39], implementation routes that do not require non-classical microwaves or light are also possible. The required dissipator can be realized by coupling qubits $j = -1, 1$ to a common dissipative bosonic mode (e.g. a lossy microwave cavity), and then either modulating the qubit frequencies, or modulating the qubit-resonator couplings (as was recently achieved in Ref. [40]). By interfering, e.g., a red sideband process on one qubit with a blue sideband process on the second qubit, the required dissipator can be achieved (with u, v being determined by the modulation amplitudes). Interfering red and blue sideband processes has been used previously in both trapped ion [9] and superconducting qubit [41] experiments for reservoir engineering bosonic modes, but not to control qubit dissipation in the way we suggest. More details on this modulation approach, and on the resilience of our scheme to disorder and unwanted dissipation (i.e. qubit dephasing and relaxation) are presented in Appendix A.

2.6 Conclusions

We have demonstrated that the combination of spatially-localized pairing dissipation with symmetry contrained Hamiltonian dynamics can be used generically to stabilize entangled states in systems with locally-constrained Hilbert spaces. These states can exhibit long range, volume-law entanglement. In the case of a qubit array, our setup corresponds to a dissipative spin chain that is equivalent to an interacting fermionic model, which can be interpreted in terms of dissipative Cooper pairing with phase fluctuations. Our ideas are compatible with a number of different experimental platforms, and could provide an important resource for

a variety of quantum information processing protocols.

CHAPTER 3

DISSIPATIVE PAIRING INTERACTIONS

This chapter contains previously-published material found in Ref. [42]. Reuse is permitted according to the copyright agreement used by *Physical Review Letters*.

3.1 Introduction

Hamiltonian bosonic pairing interactions (where excitations are coherently created or destroyed in pairs) arise in many settings, and underpin a vast range of phenomena. In the context of quantum optics and information, they are known as parametric amplifier interactions, and are a basic resource for generating squeezing and entanglement [43, 44]; they also form the basis of quantum limited amplifiers [45]. In condensed matter settings, bosonic pairing underlies the theory of antiferromagnetic spin waves, interacting Bose-condensates, and can also be used to realize novel topological band structures [46, 47].

Given the importance of bosonic pairing, it is interesting to explore the basics of purely *dissipative* (or non-Hermitian) bosonic pairing. Non-Hermitian dynamics have garnered attention in a wide range of fields, from condensed matter [48, 49, 50] to optics [51, 52, 53] to classical dynamical systems [54, 55, 56]. In this Chapter, we provide a comprehensive analysis of dissipative bosonic pairing in a fully quantum setting, showing it possesses a number of surprising and potentially useful features. We focus on minimal, experimentally realizable models, where bosons (e.g. photons) hop on a lattice, in the presence of a single dissipative pairing interaction. Remarkably, we find that while the dissipative pairing interaction on its own yields fully stable dynamics, when combined with simple lattice hopping (which is also stable), one can have dynamical instability. Further, close to such an instability, the quantum steady state is perfectly pure, with a selected subset of modes having high densities and strong squeezing and/or entanglement correlations. The complete state purity up until the

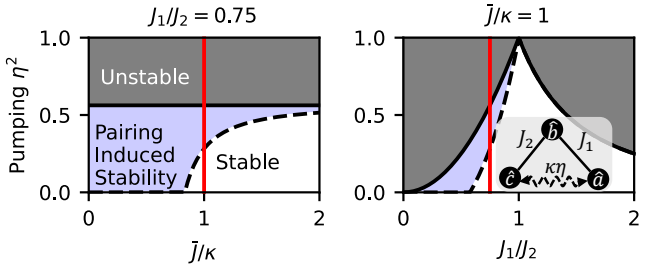

Figure 3.1: Stability diagram for a minimal three-mode bosonic system (see inset) with loss on mode $\hat{a}$ (rate κ), gain on mode $\hat{c}$ (rate $\eta^2\kappa$), and tunnel couplings J_1, J_2 (c.f. Eq. (3.3)). In the absence of dissipative pairing, the system is dynamically unstable above the dashed line. Adding dissipative pairing $i\eta\kappa(\hat{a}\hat{c} + h.c)$ shifts the onset of instability to the solid line, see Eq. (3.4). Remarkably, this boundary is independent of $\overline{J}/\kappa$, where $\overline{J} = \sqrt{J_1^2 + J_2^2}$. The dissipative steady state remains pure (with a high density) as one approaches instability, see main text. Red lines in each plot are the same cut of parameter space, $\overline{J}/\kappa = 1.5$ and $J_1/J_2 = 0.75$. Solid lines show hopping, dashed line shows the dissipative pairing interaction.

instability threshold is a clear distinction from more standard instabilities associated with Hermitian pairing terms. Dissipative pairing is also distinct from the well-studied situation where a system is driven with squeezed noise; in particular, driving a quadratic, particle-conserving system with squeezed noise can never generate instability, whereas this readily occurs with dissipative pairing.

Dissipative pairing becomes even more interesting when combined with topological band-structures. We find that our new pairing instabilities are highly susceptible to wavefunction localization of the underlying lattice Hamiltonian. Hence, if the lattice supports exponentially-localized topological edge modes, we are able to selectivity excite and entangle them. Such topological systems remain a cornerstone of condensed matter physics [57, 58, 59] and photonics [60, 61, 62], and selectively exciting edge modes has been the subject of a flurry of recent proposals [63, 64, 65, 66, 67, 68]. These are motivated by applications including topological lasing [65, 68, 69, 70, 71] and topological amplification and squeezing [66, 72, 73, 74]. However, these proposals often require complicated momentum and/or energy selectivity [66, 67, 68], as well as control over the entire lattice, [66, 67, 68, 72]. Here, we are able to get edge-mode selectivity almost for free, using a single quasi-local dissipative interaction.

3.2 Minimal model

We start with a three-mode system (bosonic annihilation operators $\hat{a}, \hat{b}, \hat{c}$) that exhibits much of the surprising physics of interest. The key ingredient will be a dissipative pairing interaction between $\hat{a}$ and $\hat{c}$, that is an interaction generating dynamics of the form $\partial_t\langle\hat{a}\rangle = -\lambda\langle\hat{c}^\dagger\rangle$ and $\partial_t\langle\hat{c}^\dagger\rangle = \lambda^*\langle\hat{a}\rangle$. Because of the relative sign here, this dynamics *cannot* be obtained from a Hermitian pairing interaction. Instead, it would seem to correspond to a non-Hermitian effective Hamiltonian:

$$\hat{H}_{\text{pairing}} = -i(\lambda\hat{a}^\dagger\hat{c}^\dagger + h.c.). \tag{3.1}$$

To obtain this Markovian dissipative dynamics in a fully quantum setting, this dissipative interaction must necessarily be accompanied by noise as well as local damping and anti-damping [49, 75]. The resulting description has the form of a Lindblad master equation [76, 77]. Using a minimal noise realization of the interaction, and letting $\hat{\rho}$ denote the system density matrix, we obtain

$$\dot{\hat{\rho}} = \hat{L}\hat{\rho}\hat{L}^\dagger - \left\{\frac{\hat{L}^\dagger\hat{L}}{2}, \hat{\rho}\right\} \equiv \mathcal{D}[\hat{L}]\hat{\rho}, \quad \hat{L} = \sqrt{\kappa}\hat{a} + \eta\sqrt{\kappa}\hat{c}^\dagger. \tag{3.2}$$

This purely dissipative evolution generates local damping on $\hat{a}$ with strength κ, local anti-damping on $\hat{c}$ with strength $\eta^2\kappa$, and a dissipative interaction of the form of Eq. (3.1) with $\lambda = \eta\kappa/2$. We take $\eta < 1$ (i.e. more local damping than anti-damping), which ensures dynamical stability (i.e. no tendancy for exponential growth), see Appendix B.

The dissipation in Eq. (3.2) is reminiscent of the dynamics generated by driving modes $\hat{a}$, $\hat{c}$ with broadband two-mode squeezed (TMS) noise [37]. There are however crucial differences. Driving with TMS noise always generates two dissipators; to make Eq. (3.2) equivalent to injected TMS, we would thus have to add the additional dissipator $\mathcal{D}[\sqrt{\kappa}\hat{c} + \eta\sqrt{\kappa}\hat{a}^\dagger]$. This complementary dissipator would completely cancel the effective dissipative interaction

between a and c generated by $\mathcal{D}[\hat{L}]$, leaving only driving with correlated noise. There would thus be no interaction from the dissipation in the equations of motion between $\langle \hat{a}(t) \rangle$ and $\langle \hat{c}^\dagger(t) \rangle$. In contrast, we will show that in Eq. (3.2), the direct dissipative interaction between modes $\hat{a}$ and $\hat{c}$ plays a crucial role.

To see explicitly that dissipative pairing is distinct from input TMS vacuum noise, we will add coherent hopping interactions to our system, and consider the evolution of average values. The hopping is described by $\hat{H} = J_1 \hat{a}^\dagger \hat{b} + J_2 \hat{b}^\dagger \hat{c} + h.c$, with the evolution now given by $\partial_t \hat{\rho} = -i[\hat{H}, \hat{\rho}] + \mathcal{D}[\hat{L}]\hat{\rho}$. Because of linearity, the equations of motion for averages of mode operators are insensitive to noise, and only influenced by interactions (coherent and dissipative). For our system, a symmetry argument lets us reduce the dynamics of these averages to the closed linear dynamics of the quadratures $\vec{v} = (x_a, p_b, x_c)$, where $\langle \hat{a} \rangle = (x_a + i p_a)/\sqrt{2}$, etc; the orthogonal quadratures (p_a, x_b, p_c) have an analogous closed evolution (see Appendix B for details). We find $\partial_t \vec{v} = -iD\vec{v}$, where the dynamical matrix $D = D_J + D_\kappa$ can be interpreted as an effective 3×3 Hamiltonian matrix, and

$$D_J = \begin{pmatrix} 0 & iJ_1 & 0 \\ -iJ_1 & 0 & -iJ_2 \\ 0 & iJ_2 & 0 \end{pmatrix}, \; D_\kappa = \frac{\kappa}{2} \begin{pmatrix} -i & 0 & -i\eta \\ 0 & 0 & 0 \\ i\eta & 0 & i\eta^2 \end{pmatrix}. \tag{3.3}$$

The off-diagonal $\pm i\eta\frac{\kappa}{2}$ terms in D_κ are the dissipative interaction, which surprisingly adds a *Hermitian* contribution at the level of the dynamical matrix. This mirrors the fact that had we started with a non-dissipative Hermitian pairing interaction, we would generate a *non-Hermitian* dynamical matrix [78]. Note that the hopping dynamics on its own generates stable dynamics, as does the dissipative dynamics on its own. More formally, both the matrices D_J and D_κ have no eigenvalues with positive imaginary part and hence are dynamically stable (in the Lyapunov sense [79] that there is no tendency for exponential growth).

We now come to our first surprise: while each part of our dynamics (hopping, dissipation)

is stable individually, combining them can lead to instability. We find that for the full dynamics, whenever $J_1 \neq J_2$, there will be a critical value of η beyond which we have exponential growth. Specifically, one can show (see Appendix B) that the dynamical matrix in Eq. (3.3) will be unstable if

$$\eta > \min\left(\left|J_1/J_2\right|, \left|J_2/J_1\right|\right). \tag{3.4}$$

We stress that this phenomenon is distinct from recently studied "dissipation-induced instabilities" [80], where the purely dissipative dynamics is already unstable on its own. Again, in our case the system is always stable in the dissipation-only limit $J_1 = J_2 = 0$.

The instability threshold Eq. (3.4) can be understood from a simple perturbative argument that is formally valid only when $\kappa \ll J_1, J_2$ (akin to a Fermi's Golden Rule (FGR) calculation). If we define $|\psi_i\rangle (i = 1, 2, 3)$ to be the (non-degenerate) eigenvectors of D_J, and treat D_κ as a small perturbation on top of this, then to first order $|\psi_i\rangle$ has a relaxation rate:

$$\Gamma_i = -\mathrm{Im}\langle\psi_i|D_\kappa|\psi_i\rangle. \tag{3.5}$$

If an eigenmode has more amplitude on $\hat{c}$ than $\hat{a}$, there will be a value of $\eta < 1$ at which Eq. (3.5) is negative. This corresponds exactly to the condition in Eq. (3.4), and is easy to understand intuitively (i.e. the eigenmode sees more anti-damping than damping). Surprisingly, this simple FGR argument turns out to be exact to all orders in κ: Eq. (3.4) is not perturbative, as is shown in Appendix B. We stress that this is a non-obvious phenonmenon. For example, consider a modified model where we eliminate dissipative pairing by replacing $\mathcal{D}[\hat{L}] \to \mathcal{D}[\sqrt{\kappa}\hat{a}] + \mathcal{D}[\sqrt{\kappa}\eta\hat{c}^\dagger]$ in our master equation. We are left with just incoherent gain and loss. In this case, the instability threshold would depend sensitively on the value of κ, with the FGR prediction only valid for $\kappa \to 0$, see Fig. 3.1.

We thus see that even at the semiclassical level, the dissipative pairing interaction yields

surprises: instability from the combination of two individually-stable dynamical processes, with a threshold that is independent of the overall dissipation scale. Note that the above phenomena could alternatively be described (in a squeezed frame) as the interplay of asymmetric loss and Hermitian pairing interacting (see Appendix B for details and application to 2-mode models).

3.3 Extension to quantum lattices

We now explore dissipative pairing in general multi-mode lattice systems, focusing on the possibility of non-trivial dissipative steady states. Consider an N-site bosonic lattice, with annihilation operators $\hat{a}_i$ for each site. The coherent dynamics corresponds to a quadratic, number conserving Hamiltonian $\hat{H} = \sum_{ij} H_{ij} \hat{a}_i^\dagger \hat{a}_j$. The only constraint we impose is that H possesses an involutory chiral sublattice symmetry U, such that $UHU^\dagger = -H$; our simple three-site model also had this symmetry. Chiral symmetry ensures that for every eigenmode of H with non-zero energy, there is a different eigenmode with an opposite energy.

We now add a single dissipative pairing interaction to the lattice, between two arbitrary sites $\overline{0}, \overline{1}$. Motivated by our three-mode example, we take $\overline{0}, \overline{1}$ to be on the same sublattice (as defined by the chiral symmetry). The full dynamics on the lattice is given by [81]

$$\partial_t \hat{\rho} = -i[\hat{H}, \hat{\rho}] + \mathcal{D}[\hat{L}]\hat{\rho}, \quad \hat{L}/\sqrt{\kappa} = \hat{a}_{\overline{0}} + \eta \hat{a}_{\overline{1}}^\dagger. \tag{3.6}$$

Our goal is to understand instabilities and steady states of this setup. Note that previous work studied chiral-symmetric bosonic lattices driven by single-mode squeezing [16]. Such systems are completely distinct from our setup: they do not have any dissipative pairing interaction, never exhibit dynamical instability, and (unlike what we describe below) always yield steady states with a *spatially uniform* average density.

We start by diagonalizing $\hat{H}$. Using chiral symmetry, we can write $\hat{H} = \sum_{\alpha \geq 0} \epsilon_\alpha (\hat{d}_\alpha^\dagger \hat{d}_\alpha -$

$\hat{d}^\dagger_{-\alpha}\hat{d}_{-\alpha}$). Eigenmode annihilation operators are given in terms of real space wavefunctions by $\hat{d}_{\pm\alpha} = \sum_i \psi_{\pm\alpha}[i]\hat{a}_i$. $\hat{H}$ is invariant under two-mode squeezing transformations that mix a pair of $\pm\alpha$ modes (see Appendix B): for arbitrary $r_\alpha, \phi_\alpha \in \mathbb{R}$, if we take

$$\hat{\beta}_{\pm\alpha} \equiv \cosh(r_\alpha)\hat{d}_{\pm\alpha} + e^{i\phi_\alpha}\sinh(r_\alpha)\hat{d}^\dagger_{\mp\alpha}, \tag{3.7}$$

then $\hat{H} = \sum_\alpha \epsilon_\alpha(\hat{\beta}^\dagger_\alpha\hat{\beta}_\alpha - \hat{\beta}^\dagger_{-\alpha}\hat{\beta}_{-\alpha})$.

We would like to find a set of r_α, ϕ_α such that:

$$\hat{L} = \sqrt{\kappa}\sum_\alpha N_\alpha(\hat{\beta}_\alpha + \hat{\beta}_{-\alpha}). \tag{3.8}$$

If this is possible, the system dynamics are stable, and we will have a unique steady state (vacuum of the $\hat{\beta}_{\pm\alpha}$ operators). Achieving Eq. (3.8) requires for each $\alpha > 0$ (see Appendix B):

$$\tanh r_\alpha = \eta\left|\frac{\psi_\alpha[\bar{1}]}{\psi_\alpha[\bar{0}]^*}\right|, \quad \phi_\alpha = \arg\left(\frac{\psi_\alpha[\bar{1}]}{\psi_\alpha[\bar{0}]^*}\right). \tag{3.9}$$

with $|N_\alpha|^2 = |\psi_\alpha[\bar{0}]|^2(1 - |\tanh r_\alpha|^2)$.

We now make a crucial observation: Eq. (3.9) only has a solution if $\eta < (|\psi_\alpha[\bar{0}]^*/\psi_\alpha[\bar{1}]| \equiv \eta_\alpha)$. If this condition is violated for a particular α, then the dynamics is unstable: in this case, we are forced to write $\hat{L}$ in terms of a Bogoliubov raising operator in the $(\alpha, -\alpha)$ sector, implying that the dissipation looks like anti-damping in this sector. At a heuristic level, for $\eta > \eta_\alpha$, the α modes see more gain than loss. Overall stability requires $\eta < \min \eta_\alpha \equiv \eta_c$, a condition that is independent of the dissipation strength κ. We thus have a generalization and rigorous justification of the surprising FGR-like instability condition in Eqs. (3.4) and (3.5) we found for the three-mode model.

Our arguments above imply that as long as $\eta < \eta_c$, we are dynamically stable and have a pure steady state, where each $(\alpha, -\alpha)$ pair is in a two-mode squeezed vacuum with a

squeezing parameter given by Eq. (3.9). This will in general be a highly entangled state. Further, as $\eta \to \eta_c$ from below, the squeezing parameter of the critical modes is diverging, meaning that we will have a pure state where a small subset of modes contribute to a diverging photon number. Note this is very distinct from just incoherent gain and loss, which never has a pure steady state. This behaviour is also completely distinct from standard parametric instabilities, where the steady state becomes extremely impure as one approaches instability [82, 83]. The mode selectivity leads to a highly non-uniform density that can be exploited for applications, as we now discuss.

3.4 Dissipative pairing and topological edge states

The physics discussed above is particularly striking when applied to chiral hopping Hamiltonians $\hat{H}$ that have topological bandstructures. There are many such models, as chiral symmetry is a key part of the standard classification of topological bandstructures [84]. As our dissipative interaction always pairs opposite energy modes, edge modes will only be paired with edge modes, bulk modes only with bulk modes. Moreover, it is easy to ensure that the correlated steady-state photon density is concentrated on the edges. Edge-mode wavefunctions are exponentially damped in the bulk, so Eq. (3.9) tells us for an edge state α

$$\tanh r_\alpha = \eta \left| \frac{\psi_\alpha[\overline{1}]}{\psi_\alpha[\overline{0}]} \right| \propto \eta e^{(d_{\overline{0}} - d_{\overline{1}})/\zeta_L}, \tag{3.10}$$

where $d_{\overline{1},\overline{0}}$ is the distance from $\overline{1}$ and $\overline{0}$ to the edge, respectively, with ζ_L the localization length scale of the edge modes. If $d_{\overline{0}} - d_{\overline{1}} > 0$ (i.e. the gain site closer to the edge than the loss site), we obtain a super-exponential enhancement in the squeezing parameter of the edge modes. This yields large populations and squeezing on the edge (while still having a pure state), see Figs. 3.2 and 3.3.

For large enough systems, the bulk modes will be nearly translationally invariant, imply-

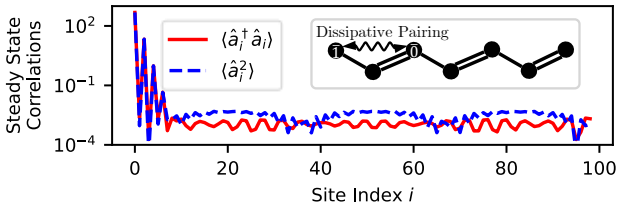

Figure 3.2: Steady state correlation functions for a 99-site SSH chain with $\delta = -0.65$. There is a single jump operator of the form of Eq. (3.6) with $\overline{0} = 4$ and $\overline{1} = 0$, and $\eta = 0.999\eta_c \sim 0.045$. The squeezing correlation functions show a pure, single-mode squeezed state exponentially localized to the edge. Inset: Schematic of the dissipatively stabilized SSH chain. A single jump operator generates a dissipative pairing interaction, selectively exciting the edge mode.

ing they will have $\tanh r_\alpha = \eta$. Thus, by spreading the two sites out over a few localization lengths ζ_L, a weak pump rate $\eta \ll 1$ can set $\tanh r_\alpha \sim 1$ for *only* the edge modes. Here, the total number of excitations in the bulk would be very small, $\langle \hat{n}_\alpha \rangle = O(\eta^2)$, whereas the number of excitations in the edge mode, as one approaches instability, will be super-exponentially enhanced and scales like: $\langle \hat{n}_\alpha \rangle = O([1 - \eta e^{(d_{\overline{0}} - d_{\overline{1}})/\zeta_L}]^{-1})$.

The upshot is that by using a single dissipative pairing interaction, we can selectively populate, squeeze and entangle edge modes of a topological bosonic band structure. Such states could be useful for applications in topological photonics [61], and are reminiscent of topological lasing states [65, 68] (which typically require complex schemes to only pump the edge states). We analyze this physics more carefully below for two prototypical topological hopping models.

3.5 SSH Chain

A paradigmatic topological model is the SSH chain [27, 28], see Fig. 3.2 inset. This is a linear, 1D lattice with staggered hopping strengths, given by the Hamiltonian:

$$\hat{H} = -J \sum_{i=1}^{N-1} (1 + (-1)^i \delta) \hat{a}_i^\dagger \hat{a}_{i+1} + h.c. \tag{3.11}$$

Such a model has been realized with bosons in a variety of experiments (e.g. [69, 70, 71, 85]). The topological regime of $\hat{H}$ admits one (two) protected edge modes if there are an odd (even) number of lattice sites, with a localization length $\zeta_L = (1+\delta)/(1-\delta)$. As $\alpha \to -1$, $\zeta_L \to 0$, and the edge modes become infinitely localized.

We consider for simplicity an odd number of lattice sites (see Appendix B for even N). This yields a single zero-energy edge mode, localized on a single sublattice. Hence, if we place the pairing dissipator on the correct sublattice, we can selectively excite just the edge mode into a single-mode squeezed vacuum with a super-exponentially enhanced squeezing parameter. The dissipative steady state for such a situation is plotted in Fig. 3.2. We thus have a resource-friendly approach for creating topologically-protected, bright non-classical squeezed light, using an SSH chain with a single, quasi-local, linear dissipator. One could imagine using the stabilized photons by weakly coupling the edge lattice site to an output waveguide, see Appendix B for more details. Note that topological features of the SSH chain are protected against disorder in the hopping coefficients up to the bulk gap $2|\delta|J$. We find that the qualitative nature of the dissipative steady state is also protected against hopping disorder over a similar scale (see Appendix B).

3.6 Hofstadter Lattice

2D topological systems admit extended boundaries, allowing one to more easily study entanglement properties. Motivated by this, we consider a finite, quarter-flux Hofstadter lattice [29]. This corresponds to a square lattice with a quarter magnetic flux quanta per plaquette (see Fig. 3.3) giving the Hamiltonian:

$$\hat{H} = \sum_{m,n} \hat{a}^\dagger_{m,n}\hat{a}_{m+1,n} + e^{i\pi m/2}\hat{a}^\dagger_{m,n}a_{m,n+1} + h.c., \tag{3.12}$$

which has been realized experimentally in Refs. [86, 87, 88].

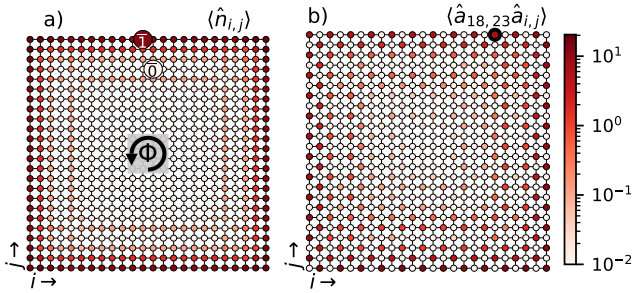

Figure 3.3: (a) is a 24×24 site Hofstadter lattice, which has uniform hopping and a quarter flux per plaquette $\Phi = \frac{1}{4}\Phi_0$. There is a single dissipator of the form of Eq. (3.6), with $\overline{1} = (11, 23)$ and $\overline{0} = (12, 20)$, and with $\eta = 0.999\eta_c \sim 0.0007$. The color corresponds to local steady state photon number, which is exponentially localized to the edges of the lattice. (b) is the same system, now showing steady state squeezing correlations between the randomly chosen edge site (18,23) and the rest of the lattice. Every edge site has exponentially enhanced squeezing with every other edge site on the same sublattice.

This Hamiltonian supports exponentially localized modes which propagate chirally around the edge [86, 87, 89] [1]. The fact that they are extended around the full edge is critical for generating long-range entanglement.

With the same prescription of adding a dissipative interaction of the form of Eq. (3.6) with $\overline{1}$ on the edge and $\overline{0}$ in the bulk, the steady state solution has exponentially localized edge photon density, with nearly all-to-all edge correlations, see Fig. 3.3. For a fixed η, these sites will obey a volume-law scaling in entanglement entropy, where maximally separated edge sites are now highly entangled, see Fig. 3.3. Having all edge sites lie on the same topological boundary is crucial for this to occur, see Appendix B for more details.

In the limit that $\eta \to \eta_c$, the steady state will be dominated by the topological edge modes approaching instability. Treating the edge as a ring, we can label these by their momenta k; the steady state has all momenta k and $k + \pi$ in a TMS vacuum. Close enough to instability, a single momentum will dominate, generating uniform edge photon densities, see Fig. 3.3a, and a "checkerboard" of correlations, see Fig. 3.3b. The checkerboard is a

1. The astute reader may be concerned that the chiral Altland-Zirnbauer class AIII is topologically trivial in 2D. However, the quarter-flux Hofstadter lattice is not gapped at half-filling, instead meeting at Dirac cones. The gaps at 1/4 and 3/4 filling have no chiral symmetry, and therefore are in class A and topological.

result of the chiral symmetry, which admits only correlations within a sublattice. The values of the correlations and densities can be understood directly from Eq. (3.10), where $\langle \hat{n}_{i,j} \rangle \sim \sinh(r_k)^2$ and $\langle \hat{a}_{i,j} \hat{a}_{i',j'} \rangle \sim \sinh(r_k)\cosh(r_k)$ are super-exponentially enhanced compared to the bulk modes. This gives an arbitrary amount of entanglement between any two edge sites on the same sublattice as $\eta \to \eta_c$. This also means that for a relatively weak dimensionless pumping ($\eta < 10^{-3}$ in Fig. 3.3), the steady state can still have a large number of photons ($O(10^2)$ in Fig. 3.3), that is completely independent of the strength of the dissipation κ compared to the Hamiltonian.

3.7 Implementation

The basic master equation is naturally suited for any circuit- or cavity-QED experimental platform that can generate tunable couplings, along with an engineered lossy mode. Quantum systems that have been able to successfully create topological photonic or phononic lattices spans superconducting circuits [88, 85], micropillar polariton cavities [69], photonic cavities [90], photonic crystals [89], ring resonators [86, 87, 91, 70, 71], and optomechanics [92, 93]. In order to generate the requisite jump operator in Eq. (3.6), one can couple the dissipation sites to an auxilliary bosonic mode $\hat{b}$ with the interaction

$$\hat{H}_I = g\hat{b}^\dagger(\hat{a}_{\overline{0}} + \eta\hat{a}^\dagger_{\overline{1}}) + h.c. \tag{3.13}$$

In the limit that the auxiliary mode $\hat{b}$ is very lossy with a loss rate $\kappa \gg g$, this gives the desired jump operator, with an effective strength $\Gamma = 4g^2/\kappa$, [94]. This allows one to easily engineer the desired reservoir with few additional resources.

3.8 Conclusions

We have demonstrated that dissipative pairing interactions lead to a previously unexplored class of instabilities in bosonic systems, where stable Hamiltonians and stable dissipation combine to give unstable dynamics. We have shown that these instabilities are incredibly sensitive to topological boundaries, providing a new mechanism to selectively excite topological edge modes without needing any momentum or frequency selectivity. Moreover, the steady state of the dynamics remains pure all the way up to the instability point, allowing one to populate the edge with an arbitrary number of zero-temperature excitations. Our ideas are compatible with a variety of different experimental platforms, and require few resources to implement.

CHAPTER 4

FUNDAMENTAL TIME-ENTANGLEMENT TRADEOFFS

This chapter contains previously-published material found in Ref. [95]. Reuse is permitted according to the copyright agreement used by *Physical Review X Quantum*.

4.1 Introduction

An exciting and powerful recent direction in quantum many-body physics is the realization that dynamical properties can be directly related to ground state entanglement features. For example, pioneering work by Hastings showed that the ground states of finite-range, gapped 1D Hamiltonians obey an entanglement area law [96]. Under certain conditions, this result can be extended to longer-range interactions [97, 98] and higher dimensions [99, 100, 101, 102, 103, 104, 105], (c.f. [106] for a review). By understanding aspects of a many-body system's energy spectrum, one can obtain extremely non-trivial information about the structure of entanglement in its ground state.

In this Chapter, we show that non-trivial connections between steady state bipartite entanglement and dynamical properties can also be established in open quantum systems supporting pure steady states. Focusing on many-body Markovian dissipative systems (described by a GKSL/Lindblad master equation [76, 77]) satisfying only weak locality constraints, we show that systems with pure, *maximally* entangled steady states necessarily exhibit dynamical isolation: there is an emergent strong symmetry that makes it impossible to prepare the entangled steady state in finite time. This phenomenon implies a vanishing of the dissipative gap.

Further, for systems with non-maximal steady state entanglement, we prove an inequality that sets a lower bound on the preparation time of the steady state. This bound shows that the time required to reach the steady state grows exponentially in the Renyi-2 entanglement

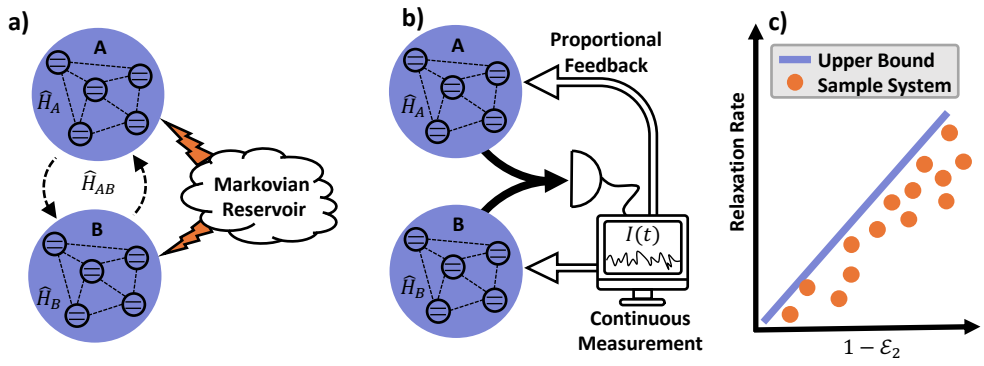

Figure 4.1: (a) Schematic showing two arbitrary systems A and B interacting dissipatively via local couplings to a common Markovian reservoir, along with arbitrary intra-system $(\hat{H}_A, \hat{H}_B)$ as well as inter-system $(\hat{H}_{AB})$ Hamiltonian interactions. We focus on cases where the dynamics leads to pure steady-states with finite entanglement. (b) The above dynamics is equivalent to a generic adaptive measurement setup: a continuous collective measurement is made of $A$and B, and the result $I(t)$ is used to drive both systems. (c) Our key result is that the relaxation rate to the steady state is bounded above by $1-\mathcal{E}_2$, where $\mathcal{E}_2$ is the scaled steady-state entanglement [c.f. Eq. (4.17)]. $(1-\mathcal{E}_2)$ is zero for maximally entangled states, indicating the dissipative gap must close in such cases.

entropy of the steady state. The general setup we consider [c.f. Fig. 4.1] also directly constrains a broad class of measurement and feedback protocols, whose unconditional dynamics result in steady state entanglement. We thus establish a fundamental trade-off between steady state entanglement generation and relaxation times for an extremely wide class of non-unitary dynamics. Note that previous work on open systems has established relations between steady state correlations and the dissipative gap [107, 108, 109]; however, unlike our work, these results only apply in the thermodynamic limit, and do not connect bipartite entanglement and relaxation times.

Our result has strong implications for the general techniques of reservoir engineering and autonomous feedback [2, 3]. Such approaches are ubiquitous in quantum information processing, and involve employing tailored dissipative processes to prepare and stabilize useful quantum steady states. Perhaps the most common kind of target states here are those with long-range entanglement (see e.g. [37, 110, 111, 23, 112, 15, 36, 113, 114, 115, 116, 117, 118, 119, 11, 12, 13, 1, 14, 15]). While extremely powerful, reservoir engineering

is only practically effective if the relevant relaxation rates are sufficiently fast (otherwise intrinsic, uncontrolled dissipative processes will corrupt the eventual steady state). Our fundamental entanglement-time trade-off directly applies to this setting. Previous work had phenomenologically seen evidence of such a trade-off in a variety of different schemes; i.e., the preparation time would diverge as the steady state was engineered to have maximal entanglement [116, 1, 117], as seen in Chapter 2. In the simplest, specific case of two qubits, this trade-off could be connected to an effective conservation of angular momentum that emerged in the maximum entanglement limit [117]. Our results establish the origin of this trade-off in the most general many-body setting, and have far-reaching implications on the design of optimal entanglement stabilization protocols. Note that for two qubits, studies have shown how to evade dynamical slowdown by using additional energy levels [113, 117]. Such an approach effectively changes the local Hilbert space dimensions (and thus the maximum possible amount of entanglement), and thus a version of our bound still applies.

One might worry that while our work sets an upper bound on timescales for dissipative remote entanglement stabilization, this bound might be extremely loose, and have little relevance to typical systems. To address this, we first solve a seemingly complex inverse problem: given a specific many-body entangled pure state of interest, how do we reverse engineer a local dissipative process that will stabilize it? We provide a very general construction that solves this challenge, and use it to construct a set of local, random Lindbladians that all stabilize a given target state. Using this ensemble of random Lindbladians, we show that the dissipative gap scales with entanglement entropy exactly as predicted by our bound. Moreover, we show analytically that the relaxation of a Haar random initial state follows the same scaling predicted by the bound. Our general reverse engineering of local dissipation compatible with a target entangled state could have a variety of other interesting applications [120].

One potential application of recent interest is designing open quantum systems which

are able to simulate finite temperature states of many-body systems (often called quantum Gibbs samplers)[121, 121, 122, 123, 120]. Our technique could be used to prepare the purified thermofield double (TFD) state, which allows one to probe finite temperature properties. Another possible use is given in Ref. [124], where our technique would be able to prepare an entangled state for optimal multi-parameter metrology.

This Chapter is organized as follows. Section 4.2 establishes our general setup, while Section 4.3 provides a rigorous statement of our main results. In Section 4.4, we show how to reverse engineer a class of local dissipative dynamics that all stabilize a given target entangled state. We combine this with random matrix theory to show that typical relaxation times scale with entanglement entropy exactly as predicted by our bound. In Section 4.5, we show that the spectra of random Lindbladians exhibit a bulk gap along with isolated midgap state(s), which are responsible for all of the slow dynamics.

4.2 Setup and definitions

4.2.1 Maximally Entangled States

We work throughout with systems having a tensor product Hilbert space $\mathcal{H} = \mathcal{H}_A \otimes \mathcal{H}_B$ (with $\dim \mathcal{H}_{A,B} = N_{A,B} < \infty$), and will be interested in pure states with entanglement between subsystems A and B. Unless otherwise stated, we will assume $N_A = N_B \equiv N$. Any state $|\psi\rangle \in \mathcal{H}$ admits a Schmidt decomposition

$$|\psi\rangle = \sum_{i=1}^{\min(N_A,N_B)} \sqrt{p_i}|i\rangle_A \otimes |i\rangle_B, \tag{4.1}$$

where the Schmidt coefficients $\sqrt{p_i}$ are taken to be real and positive without loss of generality throughout. A *maximally entangled state* for our bipartition is any state with uniform Schmidt coefficients, i.e. $\sqrt{p_i} = [\min(N_A, N_B)]^{-1/2}\ \forall i$.

The bipartite entanglement of $|\psi\rangle$ can be characterized by the Renyi-α entropy between subsystems A and B:

$$S^{(\alpha)}(|\psi\rangle) = \frac{1}{1-\alpha} \log \sum_i p_i^\alpha. \tag{4.2}$$

For a maximally entangled state $|\psi\rangle_{\max}$ (letting $N_A = N_B = N$), this gives

$$S^{(\alpha)}(|\psi\rangle_{\max}) = \log N. \tag{4.3}$$

4.2.2 Open Markovian Dynamics and Timescales

Our overarching goal is to connect steady state entanglement to dynamics. We will focus exclusively on systems whose open system dynamics is described by a Markovian master equation in Gorini-Kossakowski-Sudarshan-Lindblad (GKSL) form [77, 76]. Letting $\hat{\rho}$ be the system's density matrix, we have

$$\partial_t \hat{\rho} = -i[\hat{H}, \hat{\rho}] + \sum_{\mu=1}^{M} \mathcal{D}[\hat{L}_\mu]\hat{\rho} \equiv \mathcal{L}\hat{\rho}, \tag{4.4}$$

$$\mathcal{D}[\hat{L}_\mu]\hat{\rho} \equiv \hat{L}_\mu \hat{\rho} \hat{L}_\mu^\dagger - \frac{1}{2}\left\{\hat{L}_\mu^\dagger \hat{L}_\mu, \hat{\rho}\right\}, \tag{4.5}$$

where the Hermitian operator $\hat{H}$ is the Hamiltonian, and the M jump operators $\hat{L}_\mu$ parameterize the non-unitary evolution. We will refer to the superoperator $\mathcal{L}$ as the Lindbladian. As we discuss below, we consider situations where subsystems A and B are physically separated and only interact via local couplings to common dissipative environments. As a result, we require all jump operators to have the form:

$$\hat{L}_\mu = \hat{A}_\mu \otimes \hat{\mathbf{1}} + \hat{\mathbf{1}} \otimes \hat{B}_\mu. \tag{4.6}$$

Every Lindbladian will have at least one steady state solution $\hat{\rho}_{\rm ss}$ defined by $\mathcal{L}\hat{\rho}_{\rm ss} = 0$. Our interest here is in systems which have a pure steady state; the goal is to connect the entanglement of the steady state to dynamical timescales. We say that $\mathcal{L}$ has a maximally entangled steady state if there exists a state $|\psi\rangle$ such that $S^{(\alpha)}(|\psi\rangle) = \log N$ and $\mathcal{L}(|\psi\rangle\langle\psi|) = 0$. A steady state is unique if and only if every initial condition tends towards the steady state in the long time limit.

In most cases, we will be interested in systems where $\mathcal{L}$ is diagonalizable, and can be written as $\mathcal{L} = \sum_{\alpha=0}^{N^4-1} \lambda_\alpha |r_\alpha\rangle\rangle\langle\langle l_\alpha|$. (Here and throughout, the double bracket notation $|\hat{\rho}\rangle\rangle$ represents a vectorized density matrix.) The complete set of dissipative rates are given by the real parts of the eigenvalues $\{\lambda_\alpha\}$. We will work with the convention that $0 = \lambda_0 \geq {\rm Re}\lambda_1 \geq \cdots \geq {\rm Re}\lambda_{N^4-1}$ [125]. We define the dissipative gap

$$\Delta = -{\rm Re}\lambda_1. \tag{4.7}$$

4.2.3 Locality in Bipartite Lindbladians

When proving an area law for the ground states of gapped 1D systems, one has to first imbue the Hamiltonian with a meaningful notion of locality. We similarly must identify a relevant notion of locality in our open system dynamics. To that end, we assume that subsystems A and B are physically separated, and only interact via local couplings to common, extended Markovian reservoirs, see Fig. 4.1. For example, one might consider groups of qubits decaying into a common waveguide, or groups of atoms interacting with a common cavity mode. The locality of this setup means that before eliminating the environment to generate our master equation, its interaction with the system will be described by a Hamiltonian of the form:

$$\hat{H}_{\rm int} = \sum_{\mu=1}^{M'} \hat{R}_{A,\mu} \otimes \hat{\tilde{A}}_\mu \otimes \hat{\mathbf{1}} + \hat{R}_{B,\mu} \otimes \hat{\mathbf{1}} \otimes \hat{\tilde{B}}_\mu + {\rm H.\,c.} \tag{4.8}$$

where μ indexes interactions with the reservoir(s), and $\hat{R}_{A,\mu}$ and $\hat{R}_{B,\mu}$ are reservoir operators localized near either the A or the B subsystem, respectively. Correspondingly, $\hat{\tilde{A}}_\mu$ ($\hat{\tilde{B}}_\mu$) are subsystem A (B) operators. Note crucially that A and B *only* interact via their common coupling to the environment.

Assuming now the reservoir(s) is Markovian, we can eliminate it in the usual manner (see e.g. [126, 94]) to generate a GKSL master equation for the dynamics of $A+B$ with the constrained form of Eqs. (4.4) to (4.6), see Section C.6 for more details. In particular, each jump operator $\hat{L}_\mu$ is the sum of an A and a B operator as given in Eq. (4.6), where $\hat{A}_\mu, \hat{B}_\mu$ are local A, B operators that depend on $\hat{\tilde{A}}_\mu$ and $\hat{\tilde{B}}_\mu$ as well as reservoir properties. Even with this constraint, we have an extremely general problem. We can still have arbitrary local dissipative processes (i.e. set either $\hat{A}_\mu$ or $\hat{B}_\mu$ to 0), as well as all forms of correlated Markovian dissipation relevant to physically separated systems. Moreover, we place no constraints on the Hamiltonian $\hat{H}$ in Eq. (4.4) (as there could be arbitrary bath-induced Hamiltonian interactions between A and B).

4.2.4 Connection to measurement-feedback dynamics

The general setup described by Eqs. (4.4) and (4.5) is also directly relevant to describing dynamics where A and B interact via locality-constrained continuous measurement and feedforward (MFF) processes [127, 128, 129]. In particular, this constrained form describes the unconditional dynamics arising from a MFF protocol where one measures *sums* of A and B quantities, and then uses the results to apply local feedback control to each subsytem. To be explicit, consider the unconditional dynamics generated by making a weak continuous measurement of a Hermitian observable $\hat{M}$, and then using the measurement record to drive another Hermitian quantity $\hat{F}$. In the limit where delay can be neglected, the theory of weak continuous measurement shows that the unconditional state (i.e. averaged over all possible

measurement outcomes) evolves as: [130]

$$\partial_t \hat{\rho} = \mathcal{D}[\hat{M}]\hat{\rho} + \mathcal{D}[\hat{F}]\hat{\rho} - i[\hat{F}, \{\hat{M}, \hat{\rho}\}] = \mathcal{D}[\hat{F} - i\hat{M}]\hat{\rho} - \frac{i}{2}[\{\hat{F}, \hat{M}\}, \hat{\rho}]. \tag{4.9}$$

As long as both $\hat{M}$ and $\hat{F}$ are sums of local operators, we have a master equation that obeys the general form of Eqs. (4.4) to (4.6). For example, we could take:

$$\hat{M} = \frac{i}{2}(\hat{A} - \hat{A}^\dagger + \hat{B} - \hat{B}^\dagger) \tag{4.10}$$

$$\hat{F} = \frac{1}{2}(\hat{A} + \hat{A}^\dagger + \hat{B} + \hat{B}^\dagger) \tag{4.11}$$

In this case $\hat{F} - i\hat{M} = \hat{A} + \hat{B}$, implying the dissipator in Eq. (4.9) has the required form of Eq. (4.6) (while the last term in Eq. (4.9) is a Hamiltonian interaction which is always allowed).

Given this connection, the entanglement-time bounds we prove below directly constrain locality-constrained measurement+feedback protocols. Moreover, we stress that while we have formulated the measurement+feedback protocol without any additional Hamiltonian interactions, any Hamiltonian can always be added in without any change to our results.

4.3 Bound Statement

4.3.1 Maximally Entangled Steady States Cannot be Reached by Markovian Dynamics

It is well known that dissipative dynamics having the form of Eqs. (4.4) to (4.6) can be used to stabilize pure entangled states. Examples include the dissipative stabilization of bosonic two-mode squeezed states [43, 44, 42], qubit Bell pairs [23, 1, 116], and even more exotic states of matter in spin chains [1, 119]. Our first result is to show that all such protocols are highly constrained. If a Lindbladian $\mathcal{L}$ of the form Eqs. (4.4) to (4.6) has a pure *maximally*

entangled steady state $|\psi\rangle$ (i.e. $\mathcal{L}|\psi\rangle\langle\psi| = 0$), then this state is necessarily dynamically isolated: the projector $|\psi\rangle\langle\psi|$ becomes a conserved quantity, implying that the dissipative dynamics will never relax an arbitrary initial state into this entangled state. This necessarily implies the existence of multiple steady states and the closing of the dissipative gap. Our result here holds irrespective of further details (e.g. Hilbert space dimension, number of jump operators, form of the $\hat{A}_\mu, \hat{B}_\mu$ operators, form of $\hat{H}$, etc.).

To establish this result, note first that as $|\psi\rangle$ is a pure steady state, we necessarily have [12]

$$[\hat{H}, |\psi\rangle\langle\psi|] = \hat{L}_\mu|\psi\rangle = 0, \tag{4.12}$$

i.e., it is an eigenstate of the Hamiltonian and a dark state of each jump operator. Within the quantum jumps interpretation of our master equation [130], the dark state conditions imply that if the system is in the state $|\psi\rangle$, there is zero probability of a quantum jump evolving it into a different state.

The fact that $|\psi\rangle$ is also maximally entangled leads to a second, even stronger constraint: there will also be zero probability that a quantum jump from an arbitrary initial state $|\phi\rangle$ will produce a state with non-zero overlap with $|\psi\rangle$. To see this explicitly, we define the unnormalized "absorbing state" associated with each jump operator $\hat{L}_\mu$ to be $|\tilde{\psi}_\mu\rangle \equiv \hat{L}_\mu^\dagger|\psi\rangle$. The probability that a quantum jump induced by $\hat{L}_\mu$ will result in some initial state $|\phi\rangle$ having overlap with $|\psi\rangle$ is then $|\langle\psi|\hat{L}_\mu|\phi\rangle|^2 = |\langle\tilde{\psi}_\mu|\phi\rangle|^2$. Using the fact that $|\psi\rangle$ is a dark state, we have:

$$\langle\tilde{\psi}_\mu|\tilde{\psi}_\mu\rangle = \langle\psi|\hat{L}_\mu\hat{L}_\mu^\dagger|\psi\rangle = \langle\psi|[\hat{L}_\mu, \hat{L}_\mu^\dagger]|\psi\rangle = \langle\psi|[\hat{A}_\mu, \hat{A}_\mu^\dagger] \otimes \hat{\mathbf{1}}|\psi\rangle + \langle\psi|\hat{\mathbf{1}} \otimes [\hat{B}_\mu, \hat{B}_\mu^\dagger]|\psi\rangle. \tag{4.13}$$

Next, as $|\psi\rangle$ is also a maximally entangled state, an explicit calculation shows that the above

expression is proportional to $\mathrm{tr}[\hat{A}_\mu, \hat{A}_\mu^\dagger] + \mathrm{tr}[\hat{B}_\mu, \hat{B}_\mu^\dagger] = 0$ when $N_A = N_B$ (see Section C.1). Hence, there is zero probability for a quantum jump moving population into the entangled steady state $|\psi\rangle$. The vanishing of $|\tilde{\psi}_\mu\rangle$ also implies that the "no-jump" evolution described by $\hat{H}_{\text{eff}} = \hat{H} - (i/2)\sum_\mu \hat{L}_\mu^\dagger \hat{L}_\mu$ will never increase the population of $|\psi\rangle$. We thus have established our key result: the population of the maximally entangled steady state $|\psi\rangle$ will never change in time, and hence even given infinite time, dissipative preparation of the steady state $|\psi\rangle$ is impossible.

We can also establish this result rigorously using the notion of a strong symmetry of a Lindbladian [131]. Eq. (4.13) shows that for each jump operator $\hat{L}_\mu^\dagger|\psi\rangle = 0$. Given that $|\psi\rangle$ is also a pure steady state, it immediately follows that

$$[\hat{P}, \hat{L}_\mu] = [\hat{P}, \hat{H}] = 0 \tag{4.14}$$

where $\hat{P} = |\psi\rangle\langle\psi|$. This implies that $\hat{P}$ (the projector onto $|\psi\rangle$) generates a strong symmetry of $\mathcal{L}$ and describes a dynamically conserved charge. It thus separates the full Hilbert space into two dynamically isolated subspaces, namely $|\psi\rangle$ and its orthogonal complement. It also tells us that there must be steady state degeneracy (i.e. at least one steady state orthogonal to $|\psi\rangle$), and hence a vanishing of the dissipative gap. Our result here generalizes the discussion of [117], which discusses this phenomena in a specific two-qubit Lindbladian where the conserved quantity reduced to total angular momentum. Our generalization shows that this phenomena occurs in an extremely broad class of systems (including systems in the truly many-body limit), and that the conserved quantity is the population of the entangled steady state itself. In the 2 qubit example, a maximally entangled state $|\psi\rangle$ can be written (up to local unitaries) as a spin singlet, and so conserving the steady state is equivalent to conserving total angular momentum, connecting to the results in Ref. [117].

4.3.2 Universal Time-Entanglement Trade-Off

We now establish the second main result of this work: a fundamental trade-off in our locality-constrained dissipative dynamics between the amount of pure steady state entanglement and the timescales associated with dissipative stabilization. We find a rigorous bound that implies increased steady state entanglement leads to longer relaxation times (with the timescale diverging for maximal entanglement, as demonstrated above).

To formulate these ideas, we again consider a Lindbladian $\mathcal{L}$ of the form in Eqs. (4.4) to (4.6), which has a pure stady state $\hat{\rho}_{\text{ss}} \equiv |\psi\rangle\langle\psi|$. We now allow $\hat{\rho}_{\text{ss}}$ to have an arbitrary amount of entanglement. Consider the time evolution of an arbitrary initial state under $\mathcal{L}$, with the time dependent density matrix denoted as $\hat{\rho}_t$. We are interested in how this state relaxes towards $\hat{\rho}_{\text{ss}}$, and thus consider the fidelity $F(t)$ between these states:

$$F(t) = \left(\text{tr}\sqrt{\sqrt{\hat{\rho}_{\text{ss}}}\hat{\rho}_t\sqrt{\hat{\rho}_{\text{ss}}}} \right)^2. \tag{4.15}$$

Relaxation of an initial trivial state to the entangled steady state corresponds to $F(t)$ evolving from ~ 0 at $t = 0$ to ~ 1 at some finite time $t \sim \tau_{\text{rel}}$.

To formulate our result, consider the product basis defined by the Schmidt decomposition of our pure steady state given in Eq. (4.1). To fix a single time scale for the problem, we will non-dimensionalize the jump operators by pulling out an overall scale factor with units of frequency. This allows us to differentiate the role entanglement plays in the dynamics form the more trivial role the overall magnitude of the Lindbladian plays. I.e., we will define $|\hat{A}_\mu| \equiv \sqrt{\kappa_\mu}$ to be the magnitude of the largest matrix element of $\hat{A}_\mu$ in the Schmidt basis, so that we can write each jump operator as:

$$\hat{L}_\mu = \sqrt{\kappa_\mu}\left(\frac{\hat{A}_\mu}{|\hat{A}_\mu|} \otimes \hat{\mathbf{1}} + \hat{\mathbf{1}} \otimes \frac{\hat{B}_\mu}{|\hat{A}_\mu|} \right) \equiv \sqrt{\kappa_\mu}\hat{\tilde{L}}_\mu, \tag{4.16}$$

where $\hat{\tilde{L}}_\mu$ is unitless and κ_μ has the units of a rate. From here, we define the average rate $\overline{\kappa} = \frac{1}{M}\sum_{\mu=1}^{M}\kappa_\mu$. We will go on to show that this average rate $\overline{\kappa}$ appears naturally in the models considered and sets an overall time scale. Turning to the steady state $\hat{\rho}_{\rm ss} = |\psi\rangle\langle\psi|$, we use $S^{(2)}_{\rm ss}$ to denote its Renyi-2 entanglement entropy [c.f. Eq. (4.2)], and define $\sqrt{p_{\rm min}}$ to be its smallest Schmidt coefficient.

Finally, we introduce the scaled entanglement $\mathcal{E}_2$, a measure for the steady state entanglement based on $S^{(2)}$ that varies from 0 (no entanglement) to 1 (maximal entanglement):

$$\mathcal{E}_2 \equiv \frac{1}{1-1/N}\left(1 - e^{-S^{(2)}_{\rm ss}}\right) = \frac{1}{1-1/N}\left(1 - \sum_{j=1}^{N} p_j^2\right) \tag{4.17}$$

With these definitions in hand, we can state our key result: the growth of the fidelity $F(t)$ is rigorously bounded by a rate, whose value is directly proportional to the entanglement deficit of the steady state. Assuming first that $p_{\rm min} > 0$, we have:

$$|F(t) - F(0)| \leq \Gamma_{\rm max} t, \tag{4.18a}$$

$$\frac{\Gamma_{\rm max}}{M\overline{\kappa}} = \sqrt{2}\,(N-1)\,(p_{\rm min})^{-1}\,(1-\mathcal{E}_2)\,, \tag{4.18b}$$

where $N \equiv N_A = N_B$. A full proof of this result is presented in Section C.1. We see that the growth of the fidelity towards 1 is bounded by the rate $\Gamma_{\rm max}$, which in turn decreases linearly with the scaled entanglement $\mathcal{E}_2$. For a maximally entangled state ($\mathcal{E}_2 = 1$), $\Gamma_{\rm max}$ vanishes, thus recovering the result of the previous subsection: $F(t)$ is time independent in this case, and no dynamical stabilization of the entangled steady state is possible. For more general cases, our result provides a lower bound on the relaxation time $\tau_{\rm rel}$: $\tau_{\rm rel} \geq 1/\Gamma_{\rm max} \propto 1/(1-\mathcal{E}_2)$. At a heuristic level, for $\mathcal{E}_2 < 1$ we do not have a perfect strong symmetry and conserved quantity like the maximal-entanglement case [c.f. Eq. (4.14)]. Nonetheless, there is an "almost" conserved quantity that relaxes slowly, leading to very slow relaxation to the

steady state. This is discussed in more detail in Section C.3.

The bound in Eq. (4.18) is for the case where the steady state reduced density matrix of each subsystem is full rank; it clearly has no utility in the case where $p_{\min}$ is zero or extremely small. In these cases, an analogous, more useful bound can be derived that again constrains relaxation timescales in terms of the steady state entanglement deficit. The bound still has the form of Eq. (4.18a), but the rate $\Gamma_{\max}$ is replaced by $\Gamma'_{\max}$ (see Section C.1):

$$\frac{\Gamma'_{\max}}{\sqrt{2(N^3-N^2)}} = \left[\left(\sum_{\mu=1}^{M}|\hat{A}_\mu|\right)^2 + \left(\sum_{\mu=1}^{M}|\hat{B}_\mu|\right)^2\right](1-\mathcal{E}_2)^{1/2} \tag{4.19}$$

The rate in this bound is still decreases monotonically with increasing scaled entanglement $\mathcal{E}_2$, and vanishes as one approaches maximal entanglement $\mathcal{E}_2 = 1$.

Finally, the bounds discussed here constrain the relaxation of *any* state towards the entangled pure steady state. It thus sets a speed limit for even the optimal cases, where one has a fast-relaxing state. It is interesting to instead ask about the relaxation of a *typical* state towards the entangled steady state. We can also derive a general bound that applies to this situation. Consider that at some time t we have a Haar-random pure state of our system, $\hat{\rho}_t = \hat{U}|\phi_0\rangle\langle\phi_0|\hat{U}^\dagger$ where $\hat{U}$ is a Haar-random unitary, and $|\phi_0\rangle$ is some arbitrary fixed state. We can then derive a rigorous bound on the instantaneous change in the average fidelity $F(t)$ (see Section C.2)

$$\int_{\text{Haar}} |\partial_t F| \, \mathrm{d}\hat{U} \leq 2M\overline{\kappa}\frac{N-1}{N^2}\left(p_{\min}\right)^{-1}(1-\mathcal{E}_2) \tag{4.20}$$

We again find the same scaling with the scaled entanglement, but now with a smaller N-dependent prefactor.

Finally, the same physics that leads to the bounds in Eqs. (4.18), (4.19) and (4.20) can also be used to bound the mixing time of the Lindbladian [132], a standard timescale metric

for dissipative dynamics. This involves using inequalities between quantum fidelity and the trace distance [133]. Explicitly, if we define

$$t_{\text{mix}}(\epsilon) = \inf\{t > 0 \mid \forall \hat{\rho}, d_{\text{tr}}(e^{\mathcal{L}t}\hat{\rho}, \hat{\rho}_{\text{ss}}) \leq \epsilon\}, \tag{4.21}$$

where d_{tr} is the trace distance, then we show (see Section C.1) that

$$t_{\text{mix}}(\epsilon) \geq \frac{1-\epsilon}{\Gamma_{\text{max}}} = \frac{(1-\epsilon)M\overline{\kappa}p_{\text{min}}}{\sqrt{2}(N-1)}(1-\mathcal{E}_2)^{-1}, \tag{4.22}$$

where Γ_{max} is the rate introduced in Eq. (4.18).

Eqs. (4.18), (4.19), (4.20) and (4.22) are key results of this work. They provide a unifying explanation for phenomena seen in specific studies of a variety of different dissipative systems, all of which observed an extreme slow down of dynamics as parameters were tuned to increase the entanglement of the dissipative steady state [116, 1, 117]. Moreover, while they have been formulated for the case where both systems have the same Hilbert space dimension $N_A = N_B$, they can be easily extended to the case where this is not true. In this more general case, one can always map the problem to the case where dimensions are equal, but where one system is completely decoupled from some of its levels. One could then directly apply the bound Eq. (4.19). More importantly, such a setup is by definition never close to being maximally entangled by our definition (as it is not exploiting the full Hilbert space). See Section C.1 for more details.

4.4 Many-Body Random Lindbladians

While our entanglement-time bound in Eq. (4.18) is rigorous, it only provides a lower bound on relaxation times. There is no *a priori* reason to assume this bound is tight, or that it even qualitatively captures how relaxation timescales vary in a typical system. For example, it could be that relaxation times diverge with increasing entanglement in a manner that is

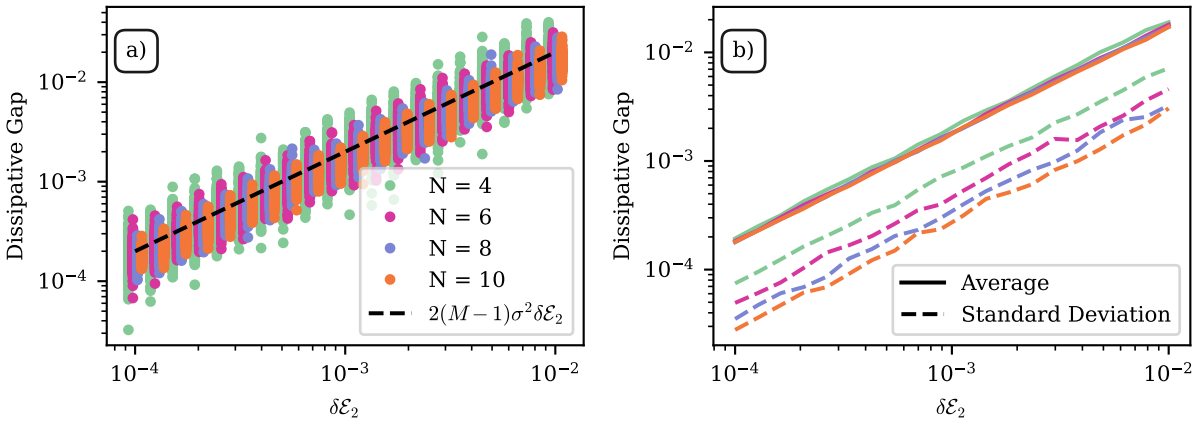

Figure 4.2: (a) Dissipative gap of random Lindbladians stabilizing a random pure state with a fixed entanglement $\delta\mathcal{E}_2$ [c.f. Eq. (4.25)], for varying system size constructed using Eq. (4.24). Recall that $\delta\mathcal{E}_2$ decreases monotonically with increasing entanglement and is zero for a maximally entangled state. Here, each A_μ matrix that is used to construct our dissipators is sampled from the Ginibre ensemble of random matrices with variance σ. For each system size and entanglement value, we plot results for 100 random Lindbladians. Different values of N are offset horizontally to avoid overlap. (b) Average and standard deviation of data in (a) for a fixed system size and entanglement. The average gap is $2(M-1)\sigma^2\delta\mathcal{E}_2$ and independent of system size. The standard deviation also scales linearly with $\delta\mathcal{E}_2$ and falls off as N increases.

much worse than the predictions of our bound.

To address these issues, in this section we study relaxation times in an ensemble of random Lindbladians having the form of Eqs. (4.4) to (4.6), that all have a pure steady state having some *fixed* value of the scaled entanglement $\mathcal{E}_2$ [c.f. Eq. (4.17)]. We can then ask about the statistics of relaxation times in this ensemble, and how they vary as we change the steady state entanglement.

4.4.1 Reverse engineering dissipative dynamics compatible with a target entangled state

To proceed, we consider a system with fixed local Hilbert space dimension N for each subsystem, and start by picking a particular (perhaps randomly chosen) pure steady state $|\psi\rangle$ specified by its Schmidt coefficients $\sqrt{p_j}$ [c.f. Eq. (4.1)]. These coefficients can be used to define a single system operator $\hat{\Psi}$, which is nothing but the square root of the reduced steady state density matrix for each subsystem:

$$\hat{\Psi} \equiv \sum_i \sqrt{p_i}|i\rangle\langle i| = \sqrt{\hat{\rho}_A} = \sqrt{\hat{\rho}_B} \tag{4.23}$$

where $|i\rangle$ are states in the Schmidt basis for the entangled state $|\psi\rangle$, and $\hat{\rho}_A = \text{tr}_B|\psi\rangle\langle\psi|$, $\hat{\rho}_B = \text{tr}_A|\psi\rangle\langle\psi|$. In what follows, we assume that all Schmidt coefficients are non-zero, i.e. $\hat{\Psi}$ is full rank.

The next step is to construct a dissipative dynamics of the form of Eqs. (4.4) to (4.6) that has the chosen pure state $|\psi\rangle$ as a steady state. We focus on the simple case where there is no Hamiltonian, and thus the problem reduces to finding one or more jump operators $\{\hat{L}_\mu\}$ such that $\hat{L}_\mu|\psi\rangle = 0$, and where each jump operator is the sum of an operator acting on just one subsystem: $\hat{L}_\mu = \hat{A}_\mu + \hat{B}_\mu$. Our approach is to first pick arbitrary system-A operators $\hat{A}_\mu$ for each jump operator. The dark state conditions then uniquely determine the form of

the corresponding system B operator in each $\hat{L}_\mu$. Letting A_μ, B_μ and Ψ denote the $N \times N$ matrix representation of these operators in the Schmidt basis, we have:

$$(\hat{A}_\mu \otimes \hat{\mathbf{1}} + \hat{\mathbf{1}} \otimes \hat{B}_\mu)|\psi\rangle = 0 \implies B_\mu = -\Psi A_\mu^T \Psi^{-1}. \tag{4.24}$$

Our construction here provides an extremely general way to construct a large number of dissipative dynamics that will stabilize a particular chosen pure entangled steady state. The construction guarantees that for a particular jump operator, the operators $\hat{A}_\mu$ and $-\hat{B}_\mu$ are isospectral. As a result, the kernel of a single jump operator $\hat{L}_\mu$ necessarily has a dimension $\geq N$, see Section C.1. Having a unique steady state will thus require at least two jump operators (chosen so that the desired steady state $|\psi\rangle$ spans the intersection of their kernels). Alternatively, one could remedy this problem by introducing an appropriate Hamiltonian to the dynamics.

We note that that the construction here (where B operators can be viewed as the modular conjugation of A operators) has a close connection to certain formulations of quantum detailed balance (i.e. KMS detailed balance [134, 135] and hidden-time reversal symmetry [136]), as well as to the theory of coherent quantum absorbers [111, 137]. The construction is also reminiscent of the construction of the Petz recovery map [138], and formal constructions of Hamiltonians that have thermofield double states as their ground state [139].

4.4.2 Entanglement-time trade-offs and dissipative gap scaling in random many-body dissipative dynamics

We now use our state-to-dynamics construction to assess whether the general time - entanglement bound in Eq. (4.18) tells us anything about typical relaxation times. For a given chosen steady state entanglement $\mathcal{E}_2$, we first construct an ensemble of entangled pure states $|\psi_\alpha\rangle$ all having the same $\mathcal{E}_2$. For each state, we then use our construction to generate a

random Lindblad master equation having two jump operators that will stabilize this state. This involves first picking two random $N \times N$ matrices A_1, A_2, and then using Eq. (4.24) to pick the corresponding B matrices. These matrices then define the jump operators $\hat{L}_1, \hat{L}_2$. We draw each A matrix from the complex random Ginibre ensemble: each matrix element is a Gaussian random variable with $\mathbb{E}[(A_\mu)_{ij}] = 0$ and $\mathbb{E}[(A_\mu)^*_{ij}(A_\nu)_{kl}] = \sigma^2 \delta_{\mu\nu}\delta_{ik}\delta_{jl}$. As we have no Hamiltonian contribution to our dynamics, the variance σ^2 plays no role except setting an overall timescale for the dynamics. That is to say, we can always choose to set $\sigma = 1$ by absorbing it into κ_μ as defined in Eq. (4.16). In this way, we can separate the dimensionful quantity κ_μ from the dimensionless slowdown due to the entanglement entropy. Another way of putting it is to observe that, if we let $\mathcal{L}_\sigma$ be a Lindbladian sampled from the random ensemble where each matrix element of A has variance σ, then $\mathcal{L}_\sigma = \sigma^2 \mathcal{L}_{\sigma=1}$. Hence, if we normalize the Lindbladian to fix a time scale, the factors of σ^2 drop out, and can therefore be set to unity without loss of generality. Note that this is only true because there is no Hamiltonian, otherwise σ would control the strength of the dissipative dynamics relative to the coherent dynamics.

In Fig. 4.2, we show results obtained by numerically implementing this procedure for system sizes N ranging from 4 to 10. We plot the dissipative gap (c.f. Eq. (4.7)) for each constructed random Lindbladian, as a function of their steady state entanglement $\mathcal{E}_2$. We stress that each realization here involves both randomly constructing a pure entangled steady state, and a dissipative dynamics that will stabilize this state. The dissipative gap Δ characterizes the slowest relaxation process in our system, and hence we might expect that $\Delta \sim \Gamma_{\max}$, where $\Gamma_{\max}$ is the rate appearing in our general bound Eq. (4.18). We see that there is a striking linear scaling of the average dissipative gap with $\mathcal{E}_2$, $\Delta \propto 1 - \mathcal{E}_2$. This is exactly the dependence predicted by our general bound for $\Gamma_{\max}$. While the prefactor of the scaling does not match the system-size dependence predicted by our bound, we see that the general trade-off between entanglement and relaxation times in this class of unstructured

many-body Lindbladians is quantitatively in agreement with Eq. (4.18).

Further, these results are not contingent on our use of the complex Ginibre ensemble to construct our random dissipators. As shown in Section C.2, constructions based on other, physically motivated random ensembles also show analogous scaling.

Turning to the prefactor of the average dissipative gap scaling with $1 - \mathcal{E}_2$, the bound states that it cannot grow faster than N^2. However, as shown in Fig. 4.2(b), we numerically find that, for randomly sampled Lindbladians, it appears to be independent of N. Further, we see that the fluctuations of the dissipative gap about its average decrease significantly even for modest increases in N. At this point, we stress that this does not imply that the bound is not tight, as it must account for *all possible Lindbladians*, whereas in Fig. 4.2, we consider only the more constrained set of *average* or *random Lindbladians*. In fact, in the next subsection, we will give a specific example of a system that relaxes much more quickly than the Haar random examples, but still satisfies the bound. To truly prove whether or not the bound is tight requires either finding a tighter bound, or finding a model system that saturates it, which we leave to future works.

However, we can analytically show that the Haar random case should have a prefactor that is independent of system size: first, define the deviation from maximal entanglement

$$\delta\mathcal{E}_2 \equiv \frac{N-1}{N}\left(1 - \mathcal{E}_2\right). \tag{4.25}$$

Then, assume that we have M random dissipators constructed as above, and that for a fixed $\mathcal{E}_2$ the Schmidt coefficients p_j are chosen randomly subject to normalization $\sum_j p_j = 1$ and $\mathcal{E}_2$ is fixed [c.f. Eq. (4.17)]. To leading order in $\delta\mathcal{E}_2$, one can show (see Section C.2):

$$\mathbb{E}\left[\int_{\text{Haar}} |\partial_t F| \, \mathrm{d}U\right] = 2M\sigma^2\delta\mathcal{E}_2, \tag{4.26}$$

where $\mathbb{E}[\bullet]$ is an average both over matrices A_μ as well as Schmidt coefficients p_j. We now

have a scaling of a typical relaxation rate that is still proportional to $(1 - \mathcal{E}_2)$, but with an N-independent prefactor.

We expect that Eq. (4.26) will give a good estimate of the dissipative gap Δ, except for the correction that $M \to M - 1$. The reason for this is that, due to the condition Eq. (4.24), a single jump operator generates N steady states, and so the dissipative gap is by definition zero when $M = 1$. Despite this, the dynamics can still increase the fidelity to the chosen steady state, hence Eq. (4.26) is nonzero even when $M = 1$. To account for this difference between the dissipative gap and the rate of change of the fidelity, we expect that the average dissipative gap scales as

$$\mathbb{E}[\Delta] = 2(M - 1)\sigma^2 \delta\mathcal{E}_2. \tag{4.27}$$

This is in good agreement with the behaviour of the average dissipative gap shown in Fig. 4.2.

Note that for the Lindbladians considered here, we find that the dissipative gap accurately predicts long-time relaxation to the steady state. It is well known that there exist examples where this correspondence can fail [140, 141, 142], for example in systems exhibiting so-called "skin-effects" (see e.g. [143, 144, 145, 146, 147, 148, 149]). Note that even for cases where the dissipative gap is not reflective of relaxation, our general bound Eq. (4.18) remains valid: it directly constrains the dynamics of the fidelity $F(t)$ (a physically observable quantity), without any assumptions on how the dissipative gap is related to the decay of observables.

4.4.3 Typical versus best case relaxation rates

As noted above, it is unclear whether or not the bound stated in Eq. (4.18) is tight, as the random systems sampled from the given distribution seem to relax roughly N^2 times more slowly than the bound predicts is the fastest possible rate. However, we stress that there is nothing contradictory: the bound in Eq. (4.18) must account for all possible Lindbladians

subject to the locality constraint, whereas in the random case, the systems are much less general.

For example, by adding back in more structure than is present in the randomly sampled Lindbladians, we can construct a model that, while not saturating the bound, does have a prefactor that is $\mathcal{O}(N)$, in between the one given in the bound and the Haar random case.

Consider a Lindbladian $\mathcal{L}_1$ acting on a Hilbert space with local dimension d, which has a steady state Renyi-2 entanglement entropy $S_1^{(2)}$ and a dissipative gap Δ_1. We can enlarge the Hilbert space in a trivial way by tensoring together n copies of the same steady state, which evolve under the Lindbladian

$$\mathcal{L} = \sum_{i=1}^{n} \hat{\mathbf{1}}^{\otimes i-1} \otimes \mathcal{L}_1 \otimes \hat{\mathbf{1}}^{\otimes n-i} \tag{4.28}$$

The steady state entanglement entropy (taking a bipartition that splits each copy) is now $S_{\text{ss}}^{(2)} = nS_1^{(2)}$ by additivity. Thus, the deviation of the scaled entanglement from its maximum value scales as

$$1 - \mathcal{E}_2 = \frac{N}{N-1}\left(e^{-S_{\text{ss}}^{(2)}} - \frac{1}{N}\right) = \frac{1}{1-d^{-n}}\left(e^{-nS_1^{(2)}} - d^{-n}\right), \tag{4.29}$$

which decays exponentially with n. It thus follows from Eq. (4.26) that the instantaneous rate of change in fidelity between a Haar random state and the steady state is decaying *exponentially* in the number of copies n. However, by construction, the dissipative gap in this system is independent of n, suggesting no slow down with increasing system size. This lack of slow down is however consistent with the larger prefactor in our more general bound in Eq. (4.18).

This example shows that a general bound must have a prefactor that grows with N at least as $\mathcal{O}(N/\log(N))$. The large deviation between this example and the Haar random models

can be attributed to the highly structured form of the Lindbladian. Stated succinctly, the eigenvectors of the Lindbladian are now very far from being related to Haar-random states. All of the eigenvectors of Eq. (4.28) are completely unentangled between copies, and so approximating them with a Haar random state is unsuccessful.

4.5 Beyond the slowest relaxation rate: structure of the Lindbladian spectra

4.5.1 Bulk Gap and Midgap States

The results of the previous section show that for random, unstructured dissipative dynamics that is locality-constrained and which has a pure steady state, the scaling of the dissipative gap with steady state entanglement matches the predictions of our general bounds in Eqs. (4.18) and (4.20). In this section, we turn to another question: does increasing steady state entanglement only lead to the formation of at most a handful of slow relaxation modes, or does it imply that an extensive number of relaxation modes become slow? This is a question about the full spectrum of our Lindbladian, and not just the dissipative gap. Through numerical investigation, we find that the first scenario holds: strong steady state entanglement leads to the formation of a unique slow mode, whereas the vast majority of relaxation modes exhibit no slow down. We find that for a variety of different random Lindbladians, the spectrum of relaxation rates exhibit what we term a "bulk gap", where almost every mode has an $\mathcal{O}(\overline{\kappa})$ decay rate regardless of the slow down associated with large steady state entanglement. However, there also always exists a single, isolated "midgap" state, which decays extremely slowly and is responsible for all of the long-time slow dynamics.

To provide context for this result, we first recall known results for the spectral properties of completely unstructured random Lindbladians (i.e. dynamics that do not have the locality and purity constraints of our general setting). Consider a general Lindbladian for a system

with an N dimensional Hilbert space:

$$\mathcal{L}\hat{\rho} = \sum_{\mu,\nu=1}^{N} K_{\mu\nu} \left(\hat{F}_\mu \hat{\rho} \hat{F}_\nu^\dagger - \frac{1}{2} \left\{ F_\nu^\dagger \hat{F}_\mu, \hat{\rho} \right\} \right), \tag{4.30}$$

where $K_{\mu\nu}$ is the complex positive semi-definite $N \times N$ "Kossakowski matrix". We take $K = NGG^\dagger / \operatorname{tr}(GG^\dagger)$, with the matrix G sampled from the complex Ginibre ensemble (unit variance of matrix elements). The operators $\{\hat{F}_\mu\}$ form an orthonormal traceless basis of SU(N).

For this general setup, it can be shown that the average dissipative gap scales as $1 - 2/N$ [150]. For large N the average gap becomes N-independent, a scaling that will match almost all relaxation modes in our more structured dissipative problem. However, the additional constraints we impose in our general setup (entangled pure steady state, local form of dissipators) leads to the formation of a single extremely slow mode as entanglement is increased, i.e. a "midgap state", see Fig. 4.4(a). It is this single slow mode that is responsible for the slow relaxation described by our bounds. It is also interesting to note that the midgap state(s) are purely a result of the entanglement and locality constraints, they never show up in the completely random Lindbladians considered in Ref. [150].

Heuristically, this behaviour matches our general picture [c.f. Eq. (4.14)] that as steady state entanglement increases, we have the emergence of an almost-conserved quantity, the projector onto the steady state. This separates the Hilbert space into two subspaces. One naively expects fast dynamics within each of these subspaces, with a single slow rate corresponding to mixing between the subspaces (see Section C.3 for more details). This picture matches the results of our numerics. One can picture the steady state and midgap state(s) as forming a quasi-stable, slowly relaxing "slow manifold" whereas the rapidly decaying modes above the bulk gap are an effective "fast manifold". One could imagine tracing out the rapidly decaying states above the bulk gap to understand the slow dynamics within the

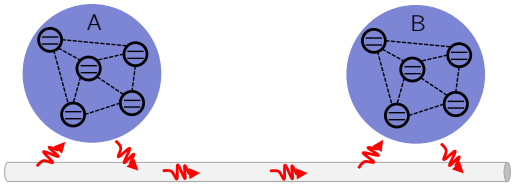

Figure 4.3: Schematic showing two systems A and B that are coupled via a Markovian chiral (i.e. directional) waveguide, thus realizing a cascaded quantum system. The A system is "upstream", and its dynamics are unaffected by B (whereas B is indeed affected by A).

midgap states(s); see, e.g. Ref. [151]. It is especially interesting to note, though, that in this case the slow manifold contains only a handful of modes, whereas the fast manifold is growing exponentially with N.

4.5.2 Prethermalization and local relaxation

Given this hierarchy of relaxation rates, it is interesting to ask what kind of observables relax slowly via the midgap state, and which relax quickly. Previous work on specific non-random models suggests that observables local to one subsystem tend to relax on fast $\mathcal{O}(\overline{\kappa})$ time scales, whereas non-local intersystem correlations relax slowly (recall that in Fig. 2.2 in Chapter 2, the local density relaxes quickly whereas the total parity relaxes much more slowly).

In order to study this, we want a system where we can independently look at the relaxation rate of the full $A-B$ system, as well as trace out one subsystem and look at the spectra of the other subsystem, which controls local observables. This can be achieved by constructing a unidirectional or cascaded [152, 153, 154] quantum system following the so-called "Coherent Quantum Absorber" (CQA) approach [111], see Fig. 4.3. Such a system still has the basic struture of our generic setup, where dissipative interactions between A and B are generated from local couplings to a common bath. Now, however, these interactions are directional: A influences B, but not vice-versa.

To achieve this directionality, and still have the dynamics stabilize a chosen pure entan-

gled steady state, we chose the matrices A_μ [c.f. Eq. (4.24)] in each jump operator so that they obey the constraint equation:

$$A_\mu = \Psi A_\mu^T \Psi^{-1}, \tag{4.31}$$

where Ψ is defined via the steady state as per Eq. (4.23). This condition corresponds to imposing an effective classical detailed balance condition (see Section C.4). We also add a Hamiltonian to our system $\hat{H}_{\text{CQA}}$ that combines with each dissipator to enforce directionality, see Section C.4. Note that previously, we used Eq. (4.24) to define a dissipator given an arbitrary matrix A_μ; now, Eq. (4.31) also gives a constraint on which A_μ are allowed. Using both Eqs. (4.24) and (4.31) also tells us that $A_\mu = -B_\mu$, thus determining the form of each jump operator. Using this construction, we find that the dynamics of system A is given by

$$\begin{aligned} \text{tr}_B[\partial_t \hat{\rho}] &= \text{tr}_B \left[-i[\hat{H}_{\text{CQA}}, \hat{\rho}] + \sum_\mu \mathcal{D}[\hat{A}_\mu + \hat{B}_\mu]\hat{\rho} \right] \\ &= -i[\hat{H}_A, \hat{\rho}_A] + \sum_\mu \mathcal{D}[\hat{A}_\mu]\hat{\rho}_A \equiv \mathcal{L}_A \hat{\rho}_A, \end{aligned} \tag{4.32}$$

where $\hat{\rho}_A \equiv \text{tr}_B \hat{\rho}$. It thus follows that every eigenvalue of the system A Lindbladian $\mathcal{L}_A$ is also an eigenvalue of the full Lindbladian $\mathcal{L}$. Moreover, all observables on the A system relax according to the spectrum of $\mathcal{L}_A$, whereas correlations between the two systems relax on a timescale governed by the gap of $\mathcal{L}$. Note that because of Eq. (4.31), the Lindbladian $\mathcal{L}_A$ necessarily satisfies classical detailed balance (also known as GNS detailed balance) [136, 155].

In Fig. 4.4(b), we numerically sample a random distribution of Schmidt coefficients $\{p_i\}$, and constrain A_μ to obey the detailed balance condition Eq. (4.31). We also add the requisite Hamiltonian, making the system completely directional. Numerically, we observe that the full Lindbladian acting on both A and B has a small dissipative gap $\Delta \sim \overline{\kappa}\delta\mathcal{E}_2$, as predicted

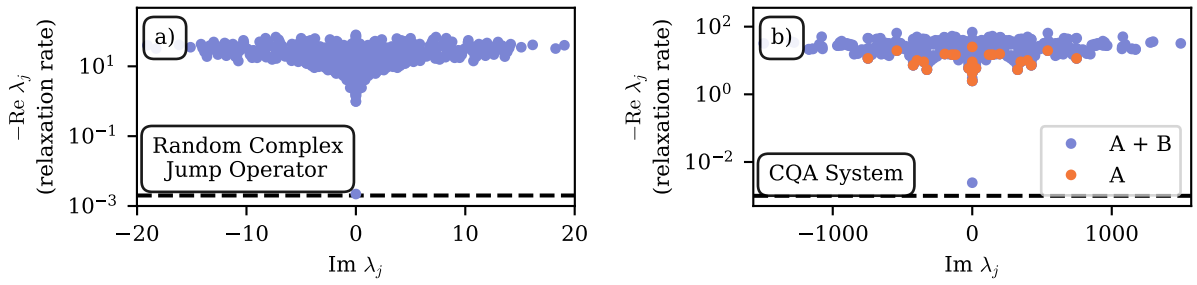

Figure 4.4: (a) Spectrum of a realization of a random Lindbladian on a bipartite system, using the construction of Section 4.4.1. Each jump operator is constructed by drawing the matrix A_μ from the complex Ginibre ensemble with variance σ; this then determines B_μ via Eq. (4.24). (b) Spectrum of a realization of a random Lindbladian constructed so that the interaction between A and B is necessarily directional (see Fig. 4.3 and Eq. (4.31)). Blue points show the spectrum of the full Lindbladian $\mathcal{L}$, and orange points of the Lindbladian $\mathcal{L}_A$ describe system-A only dynamics. When looking at $\mathcal{L}_A$ alone, there is no emergent slow mode, and the dissipative gap is large. In both (a) and (b) the local dimension $N = 5$, there are $M = 2$ independent jump operators, and a pure, random steady state with fixed $\delta\mathcal{E}_2 \equiv 10^{-3}$ [c.f. Eq. (4.25)]. In both (a) and (b) the black dashed line shows $2(M-1)\sigma^2\delta\mathcal{E}_2$ [c.f. Eq. (4.26)], and the steady state ($\lambda_0 = 0$) is not shown.

by the bound and consistent with a random jump operator as in Fig. 4.4(a). However, if we instead consider the spectrum of $\mathcal{L}_A$, the Lindbladian of system A alone [c.f. Fig. 4.3], the dissipative spectrum exhibits a large dissipative gap $\Delta \sim \overline{\kappa}$. This is in line with the results of Ref. [155], which studies the spectral properties of random Lindbladians satisfying classical (GNS) detailed balance. This separates the dynamics into two regimes. The first is a "prethermal" regime characterized by the $\mathcal{O}(\overline{\kappa})$ bulk gap; during this time, local observables can relax to their steady state values as evidenced by the upstream system not experiencing slowdown. However, intersystem correlations and entanglement approach their steady state values on exponentially longer time scales characterized by the true dissipative gap, see Fig. 4.4. This is in line with previously observed open system dynamics with highly entangled steady states (that are not necessarily directional); e.g., the example given in Chapter 2.

4.5.3 Multiple slow modes

Our discussion of Lindbladian spectra has so far focused on cases where, apart from our constraints on locality and having a pure entangled stead state, the dynamics is essentially unstructured. The slow-down of dynamics associated with increasing entanglement in this case can be attributed to a the emergence of a single slow mode. We now ask how this situation is modified when our Lindbladian has some additional structure. We find regimes where now multiple slow modes (midgap states) arise due to increasing steady state entanglement.

Consider the case where we also have a notion of spatial locality *within* both the A and B subsystems. For example, consider two n qubit spin chains denoted A and B, with local XXZ Hamiltonians governed by the master equation $\partial_t\hat{\rho} = -i[\hat{H}_{\mathrm{XXZ}}, \hat{\rho}] + \mathcal{L}_{\mathrm{diss}}$ with

$$\begin{aligned}\hat{H}_{\mathrm{XXZ}} = &\sum_{s=A,B}\sum_{i=1}^{n-1} J\left(\hat{\sigma}^{+}_{s,i}\hat{\sigma}^{-}_{s,i+1} + \mathrm{H.\,c.}\right) \\ &+ \sum_{s=A,B}\mathrm{sgn}(s)\sum_{i=1}^{n-1} J_z\hat{\sigma}^{z}_{s,i}\hat{\sigma}^{z}_{s,i+1}, \end{aligned} \tag{4.33}$$

$$\mathcal{L}_{\mathrm{diss}} = \mathcal{D}[u\hat{\sigma}^{-}_{A,1} + v\hat{\sigma}^{+}_{B,1}] + \mathcal{D}[u\hat{\sigma}^{-}_{B,1} + v\hat{\sigma}^{+}_{A,1}]. \tag{4.34}$$

Here, we take $\mathrm{sgn}(A) = -\mathrm{sgn}(B) = 1$ and $u^2 + v^2 = 1$. This models two spins chains being driven by two-mode squeezed vacuum light at their boundary, and in the limit $J_z = 0$ has been considered as a method of entanglement generation [23, 118, 119] and is identical to the model considered in Chapter 2. This system has a pure steady state, and thus is an example of the general class of dynamics [c.f. Eqs. (4.4) to (4.6)] that we consider. The steady state can be found exactly (c.f. [119] and Chapter 2), and is independent of J, J_z:

$$|\psi\rangle_{\mathrm{ss}} = \bigotimes_{i=1}^{n}\left[\sqrt{1-v^2}|0\rangle_{A,i}|0\rangle_{B,i} + (-1)^i v|1\rangle_{A,i}|1\rangle_{B,i}\right]. \tag{4.35}$$

It follows that the steady state entanglement is controlled by v.

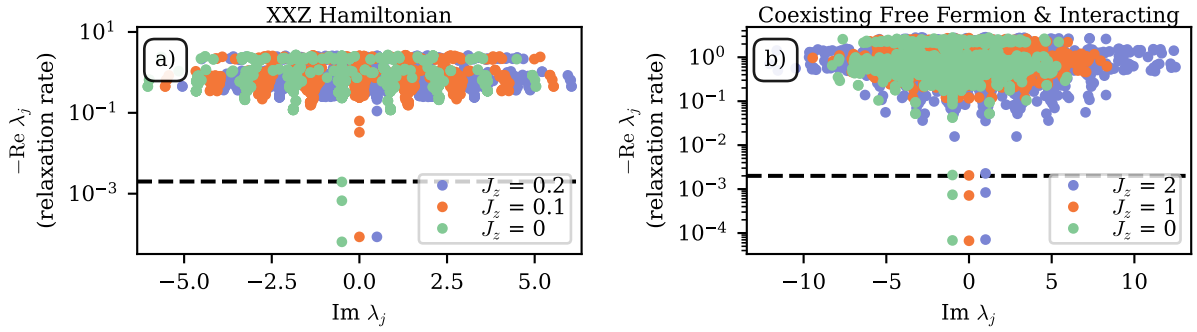

Figure 4.5: (a) Lindbladian spectra for the master equation for two $n = 3$ qubit spin chains given by the XXZ Hamiltonian Eq. (4.33) and local boundary dissipation Eq. (4.34) for varying values of the intrachain ZZ interaction J_z, with $J = 1$. Note whenever $J_z > 0$ (and the Hamiltonian is no longer mappable to free fermions), all but one of the midgap states move into the bulk spectra. (b) Lindbladian spectra for the master equation for two $n = 3$ qubit spin chains given by $\hat{H} = \hat{H}_{\parallel} + \hat{H}_{\perp}$ [c.f. Eqs. (4.36) and (4.37)] and local boundary dissipation Eq. (4.34) for varying values of the interchain ZZ interaction J_z. Note this Hamiltonian always supports ballistic dynamics and the slow modes are robust to interactions. In both (a) and (b) the steady state entanglement is fixed to be $\delta\mathcal{E}_2 = 10^{-3}$ and the black dashed line is at $2(M-1)\delta\mathcal{E}_2$. Different values of J_z are offset horizontally to avoid overlap.

This is system is clearly more structured than the completely random examples studied in the previous subsections. As such, one might expect that the Lindbladian spectrum would be very different, with potentially many more slow modes emerging when the steady state has high entanglement. Surprisingly, for generic parameters this is not the case, see Fig. 4.5: one still gets a single slow mode.

However, the special case where $J_z = 0$ the situation is very different. For this parameter choice the local Hamiltonian Eq. (4.33) is equivalent to a free fermion Hamiltonian, and we find the emergence of *multiple* slow modes for strong entanglement, see Fig. 4.5. Note that while the Hamiltonian alone can be mapped to non-interacting particles, the full dissipative dynamics still corresponds to an interacting fermionic problem (see [1] for more details). As such, it is surprising at first glance that the non-interacting nature of the Hamiltonian alone leads to such differences in the dissipative spectrum. Moreover, we observe numerically that

the number of slow modes is exactly equivalent to n, the number of qubits in each chain, and hence is extensive in system size.

To see that the free fermion dynamics is truly the cause of having multiple slow modes, we can consider a more complicated local Hamiltonian introduced in Ref. [156] which exhibits both free-fermion sectors of the Hilbert space, as well as diffusive sectors, see Section C.5. Specifically, consider the master equation $\partial_t \hat{\rho} = -i[\hat{H}, \hat{\rho}] + \mathcal{L}_{\text{diss}}$ with $\mathcal{L}_{\text{diss}}$ defined as in Eq. (4.34) and $\hat{H} = \hat{H}_{\parallel} + \hat{H}_{\perp}$ with

$$\hat{H}_{\parallel} = J \sum_{i=1}^{n-1} \sum_{s=A,B} \hat{\sigma}^{+}_{s,i} \hat{\sigma}^{-}_{s,i+1} + \text{H. c.}, \tag{4.36}$$

$$\hat{H}_{\perp} = \sum_{i=1}^{n} J \left(\hat{\sigma}^{x}_{A,i} \hat{\sigma}^{x}_{B,i} + \hat{\sigma}^{y}_{A,i} \hat{\sigma}^{y}_{B,i} \right) + J_z \hat{\sigma}^{z}_{A,i} \hat{\sigma}^{z}_{B,i}. \tag{4.37}$$

Here, $\hat{H}_{\parallel}$ is equivalent to the XXZ Hamiltonian in Eq. (4.33) at the free fermion point $J_z = 0$. $\hat{H}_{\perp}$ couples the two chains together to form a two-rung ladder. Recall that a direct Hamiltonian coupling between subsystems A and B is allowed by our general locality constraint, and does not impact the validity of our time-entanglement bounds. One can again show that the steady state is pure and given by Eq. (4.35). Moreover, by plotting the dissipative spectra, we observe that there are still n slow modes separate from the bulk spectra, just as in the completely free case, see Fig. 4.5.

4.6 Conclusion

In this paper, we have established a set of relations between pure steady state entanglement and relaxation dynamics for a class of many-body open quantum systems, where two systems A and B have locality-constrained dissipative interactions (i.e. all dissipators are sums of local operators). We find that such a system can never have a unique, maximally entangled steady state. Further, we demonstrated that this result is a special case of a more general

bound, which says that the time to reach the steady state is bounded below by how close that state is to being maximally entangled.

We further explored this bound in the context of random Lindbladians satisfying our constraints, demonstrating that our bound accurately predicted the scaling of the dissipative gap with the steady state entanglement. We also considered the Lindbladian spectra of such models, finding that for large entanglement, they generically have a bulk gap accompanied by extremely slow midgap state(s), the number of which we conjecture is related to whether or not the Hamiltonian is mappable to free fermions.

We believe that these results provide new insight into dissipative entanglement generation. They are directly relevant to quantum reservoir engineering schemes targeting remote entanglement, and helps explain a number of previous results that observed a trade-off between entanglement and preparation time in various specific systems. In future work, it would be interesting to explore further whether such entanglement-time constraints also apply to more general situations (e.g. extended many body systems where one could try to connect entanglement and relaxation times for different choices of regions A and B).

CHAPTER 5

USING ADAPTIVE DYNAMICS TO CIRCUMVENT TRADE-OFFS

This chapter contains previously-published material found in Ref. [157]. Reuse is permitted according to the copyright agreement used by *Physical Review Letters*.

5.1 Introduction

There is renewed interest in using the power of non-unitary time evolution to prepare complex entangled states of quantum many-body systems. Protocols based on measurements and classical feedback [158, 159], as well as on using engineered dissipation [2, 3], have received considerable theoretical and experimental attention. Of particular interest are stabilization schemes whose dynamics have unique, highly-entangled steady states. Such schemes have numerous advantages over more conventional approaches, and are particularly intriguing when the goal is establishing large amounts of remote entanglement [111, 23, 113, 116, 117, 118, 119, 11, 12, 13, 1, 14, 15].

For all non-unitary stabilization protocols, it is crucial both to have a useful steady state, as well as a relaxation rate that is fast. If relaxation is too slow, then other unwanted dissipative dynamics will invariably degrade the final stabilized state. For dissipative remote entanglement stabilization, a variety of different schemes all suffer from a basic time-entanglement tradeoff: the more entangled the steady state, the slower the relaxation [113, 116, 1, 117, 119, 160]. In Chapter 4, we unified these results, proving a fundamental time-entanglement bound that constrains a wide set of local dissipative stabilization protocols. In particular, the stabilization timescale diverges for maximally entangled states.

These studies raise a natural question: can we use additional resources to speed up

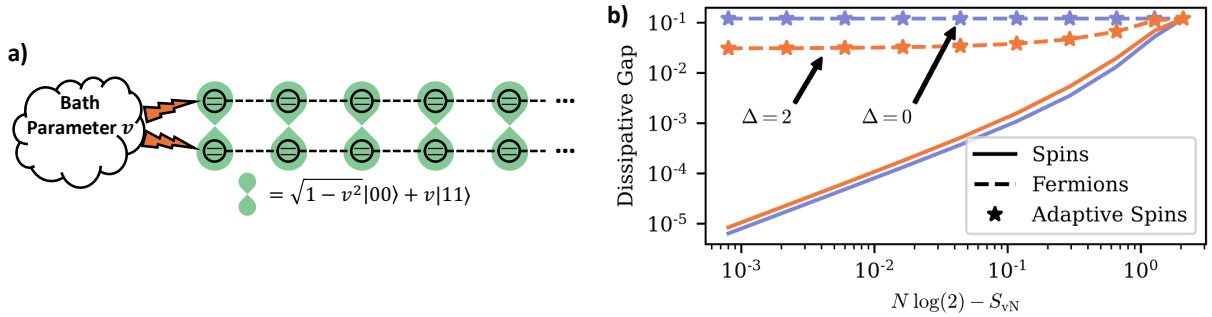

Figure 5.1: a) Schematic showing two chains of n qubits/ fermions each that only interact via coupling to a common engineered bath at the boundary. Tuning the bath parameter v tunes the steady state interchain entanglement $S_{\mathrm{vN}} \leq N \log 2$. b) Dissipative gap vs S_{vN} for $2n = 6$ total fermions (dashed lines), spins (solid lines) and adaptive spins (stars). Qubits exhibit a dramatic slowdown with increasing entanglement, fermions do not. Dynamics is given by Eqs. (5.4) and (5.5) (fermions), Eqs. (4.34) and (5.6) (spins), with $J = \Gamma = 1$, and interaction $\Delta = 0$ (blue) or $\Delta = 2$ (orange). The adaptive spin protocol (given by Eqs. (5.6) and (5.12)) mimics the fermionic model, with no entanglement induced slowdown.

entanglement stabilization? One method is to use only a subset of the total available Hilbert space, so as to never try to reach the maximal amount of entanglement [117]. If instead one wants to use only spin degrees of freedom and fully prepare the maximal number of Bell pairs, we show that this is possible in many settings by using a minimal kind of adaptive dynamics.

Adaptive dynamics whereby one does measurement and feedback on a quantum system has been explored both theoretically (e.g., [130, 161, 162, 163, 164, 165]) as well as experimentally (e.g., [166, 167, 168, 169, 170, 171]) where it as been successful in preparing quantum states or phases.

We start with the realization that simple fermionic entanglement stabilization schemes are not limited by the time-entanglement tradeoff that plagues most qubit schemes. Formally, the fact that spatially distinct fermionic operators need not commute means that the results in Chapter 4 do not apply. More physically, fermionic statistics provide a kind of built-in non-locality that is, surprisingly, a resource for entanglement stabilization. We show that

the basic ingredients that give fermions an advantage can be mimicked in qubit systems with local interactions augmented by a minimal classical memory that time-correlates subsequent quantum jumps. This dramatically accelerates the preparation of maximally entangled states (as well as spin squeezed states), both in time-continuous schemes, as well as in discrete circuits (see Fig. 5.1).

5.2 Fermions evade slowdown

We start by recapping the result of Chapter 4. Consider a system defined on a bipartite Hilbert space $\mathcal{H} = \mathcal{H}_A \otimes \mathcal{H}_B$ with local Hilbert space dimension $\dim \mathcal{H}_A = \dim \mathcal{H}_B = N$. We assume that the subsystems are physically separated, but interact with a common Markovian reservoir that mediates intersystem interactions (c.f. Fig. 5.1). The system density matrix is then described by a Lindblad master equation $\partial_t \hat{\rho} = \mathcal{L}\hat{\rho}$ whose form satisfies

$$\mathcal{L} = -i[\hat{H}, \bullet] + \sum_{\mu} \mathcal{D}[\hat{L}_\mu], \tag{5.1}$$

$$\hat{L}_\mu = \hat{A}_\mu \otimes \hat{\mathbf{1}} + \hat{\mathbf{1}} \otimes \hat{B}_\mu. \tag{5.2}$$

Here, $\mathcal{D}[\hat{L}]\hat{\rho} = \hat{L}\hat{\rho}\hat{L}^\dagger - \frac{1}{2}\{\hat{L}^\dagger\hat{L}, \hat{\rho}\}$. The sum-of-locals form in Eq. (5.2) reflects the locality constraint on the system-bath coupling [95]. Next, suppose $\mathcal{L}$ has a pure steady state $\hat{\rho}_{\rm ss} = |\psi\rangle\langle\psi|$, i.e. $\mathcal{L}\hat{\rho}_{\rm ss} = 0$. An initial state $\hat{\rho}_0$ evolves as $\hat{\rho}_t = e^{\mathcal{L}t}\hat{\rho}_0$ and its fidelity to the steady state is $F(t) = \left(\mathrm{tr}\sqrt{\sqrt{\hat{\rho}_{\rm ss}}\hat{\rho}_t\sqrt{\hat{\rho}_{\rm ss}}}\right)^2$. Defining $S^{(2)}_{\rm ss}$ to be the steady state Renyi-2 entanglement entropy between subsystems A and B, Ref. [95] shows that $|\partial_t F(t)|$ is bounded above by $\Gamma_{\rm max} \propto \delta\mathcal{E}_2$ where $\delta\mathcal{E}_2 = \left(e^{-S^{(2)}_{\rm ss}} - \frac{1}{N}\right)$ is a measure of how close the state is to being maximally entangled. This implies that the relaxation rate vanishes as the steady state entanglement approaches its maximal value.

Given this general result for spins, one might assume it also applies to fermionic systems. There is, however, a loophole: as fermions satisfy canonical *anti*-commutation relations,

operators localized to the A system need not commute with ones localized on the B system. Formally, the theorem of Ref. [95] assumes a tensor product Hilbert space. This is violated by fermions, as they live in the exterior algebra $\mathcal{H} = \mathcal{H}_A \wedge \mathcal{H}_B$ (the totally antisymmetrized part of the tensor product space [172]). This structure implies a subtle kind of non-locality, something that becomes more explicit if we map a given fermionic dynamics to qubits. For example, the Jordan-Wigner transformation maps qubit operators $\hat{\sigma}^+, \hat{\sigma}^-$ to fermionic creation and annihilation operators $\hat{c}, \hat{c}^\dagger$ via

$$\hat{c}_i = \left(\prod_{j=1}^{i-1} \hat{\sigma}_j^z \right) \hat{\sigma}_i^- . \tag{5.3}$$

The Pauli string $\left(\prod_{j=1}^{i-1} \hat{\sigma}_j^z\right)$ captures the non-local essence of the canonical fermionic anti-commutation relations. Hence, what appeared to be a local fermionic dissipative interaction (i.e. satisfying Eq. (5.2)) will in general look highly non-local when mapped to qubits.

We now show that this effective non-locality can be used as a resource to speed up fermionic entanglement generation. Consider two fermionic tight-binding chains with hopping J, locally coupled to a Markovian bath at their left boundaries with a coupling rate Γ (see Fig. 5.1). The bath is constructed so that it creates pairing correlations between the boundary sites (for other examples of linear-in-fermion jump operators, see e.g. [13, 173]). The Lindbladian is $\mathcal{L} = -i[\hat{H}_\mathrm{f}, \bullet] + \mathcal{L}_\mathrm{f}$, with

$$\hat{H}_\mathrm{f} = \sum_{s=A,B} \mathrm{sgn}(s) \left[\sum_{i=1}^{n-1} J \hat{c}_{s,i}^\dagger \hat{c}_{s,i+1} + \frac{\Delta}{2} \hat{n}_{s,i} \hat{n}_{s,i+1} \right] + \mathrm{H.\,c.}, \tag{5.4}$$

$$\mathcal{L}_\mathrm{f} = \Gamma \mathcal{D}[u\hat{c}_{A,1} + v\hat{c}_{B,1}^\dagger] + \Gamma \mathcal{D}[u\hat{c}_{B,1} - v\hat{c}_{A,1}^\dagger]. \tag{5.5}$$

Here, $\hat{n}_\alpha = \hat{c}_\alpha^\dagger \hat{c}_\alpha$, $u^2 + v^2 = 1$, and $\mathrm{sgn}(A) = -\mathrm{sgn}(B) = 1$. This is the same model considered in Chapter 2 when $\Delta = 0$. This master equation explicitly obeys the locality constraint of Eq. (5.2) (i.e. jump operators are sums-of-locals). There is a unique, pure steady

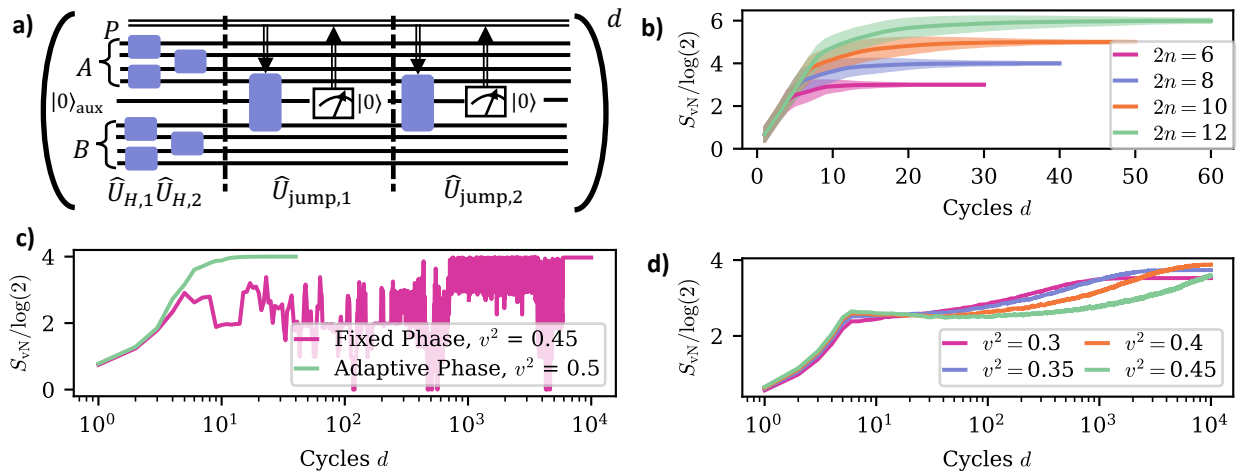

Figure 5.2: a) Brickwork adaptive circuit that allows for rapid entanglement stabilization by mimicking fermionic dynamics of Eqs. (5.8) and (5.9). Solid black lines: qubits, double black lines: classical single-bit memory, blue rectangles: unitary gates [c.f. Eqs. (5.10) and (5.11)]. Each cycle is repeated d times. b) Average entanglement dynamics for the adaptive circuit with $v^2 = 0.5$, generating n perfect bell pairs. S_{vN} is the von Neumann entanglement entropy between the A and B chains measured at the end of the cycle; solid lines shows average values over 1000 runs, and shaded area shows one standard deviation. c) Entanglement dynamics over a single trajectory for the adaptive circuit (green), as well as the non-adaptive variant where P is fixed over the full run (pink). d) Average entanglement dynamics for a non-adaptive circuit with $2n = 8$ and variable v^2. Each line is averaged over 2500 runs. In both b) and d) the system begins in the product state $|\psi\rangle = \otimes_{j=1}^{2n+1}|0\rangle$ with $P = 1$. For all plots, $J = 1$ in $\hat{U}_{H,1}$ and $\hat{U}_{H,2}$.

state given by $|\psi\rangle = \prod_{i=1}^{n} \left(u - v\hat{c}^{\dagger}_{A,i}\hat{c}^{\dagger}_{B,i}\right)|0\rangle$ where $|0\rangle$ is the joint fermionic vacuum [1]. As $u \to v$, the steady state of this system becomes maximally entangled, but the dissipative gap is independent of u, v and remains $\mathcal{O}(\Gamma)$. The relaxation timescale is thus independent of the amount of steady state entanglement, and this fermionic system has no entanglement-time tradeoff, see Fig. 5.1. Even for $\Delta \neq 0$ (i.e. $\hat{H}_{\mathrm{f}}$ is now interacting), there is no slow down. The steady state is unchanged, and the dissipative gap does not close with increasing steady-state entanglement, see Fig. 5.1.

To emphasize that the fermionic nature of the above system was crucial, consider the behaviour of the analogous qubit setup, which is a pair of anisotropic XXZ spin chains with boundary pairing dissipation:

$$\hat{H}_{\mathrm{s}} = \sum_{s=A,B} \mathrm{sgn}(s) \left[\sum_{i=1}^{n-1} J\hat{\sigma}^{+}_{s,i}\hat{\sigma}^{-}_{s,i+1} + \frac{\Delta}{2}\hat{\sigma}^{z}_{s,i}\hat{\sigma}^{z}_{s,i+1}\right] + \mathrm{H.\,c.}, \tag{5.6}$$

$$\mathcal{L}_{\mathrm{s}} = \mathcal{D}[u\hat{\sigma}^{-}_{A,1} + v\hat{\sigma}^{+}_{B,1}] + \mathcal{D}[u\hat{\sigma}^{-}_{B,1} + v\hat{\sigma}^{+}_{A,1}]. \tag{5.7}$$

The master equation governed by $\mathcal{L} = -i[\hat{H}_{\mathrm{s}}, \bullet] + \mathcal{L}_{\mathrm{s}}$ also has a pure, entangled steady state given by n dimerized pairs of spins: $|\psi\rangle = \prod_{i=1}^{n} \left(u - v\hat{\sigma}^{+}_{A,i}\hat{\sigma}^{+}_{B,i}\right)|0\rangle$ in exact analogue to the fermions. However, the dissipative gap closes as predicted by the bound [95], see Fig. 5.1. We are thus left with the conclusion that the effective non-locality inherent in fermionic dissipative evolution can be a resource for entanglement stabilization: they can completely evade the slowdown that is fundamental to analogous qubit setups.

5.3 Fermion-inspired adaptive dynamics

Surprisingly, we now show that knowing about the exceptional behaviour of fermionic dissipative models can be used to modify qubit models in a way that preserves locality, but dramatically speeds up entanglement stabilization. Note first that adding dissipators with

a jump operator of the form $\hat{L} = \hat{A} \otimes \hat{B}$ can circumvent the bound of Ref. [95], as this no longer satisfies the locality condition Eq. (5.2). However, it is not *a priori* obvious what sort of dissipators should be added for speeding up the dynamics while preserving the steady state entanglement.

Our study of fermions, however, provides a recipe for what to do: mimic the fermionic dynamics. The most naive way to do this would be to directly implement the needed string operators in order to realize Eqs. (5.4) and (5.5) with qubits:

$$\hat{H} = J \sum_{s=A,B} \mathrm{sgn}(s) \sum_{i=1}^{n-1} \hat{\sigma}^{+}_{s,i} \hat{\sigma}^{-}_{s,i+1} + \mathrm{H.\,c.} \tag{5.8}$$

$$\hat{L}_1 = u\hat{\sigma}^{-}_{A,1} - v\hat{\sigma}^{+}_{B,1}(-1)^{\hat{n}}, \quad \hat{L}_2 = u\hat{\sigma}^{-}_{B,1}(-1)^{\hat{n}} - v\hat{\sigma}^{+}_{A,1}, \tag{5.9}$$

with $\mathcal{L} = -i[\hat{H}, \bullet] + \mathcal{D}[\hat{L}_1] + \mathcal{D}[\hat{L}_2]$. Here, $\hat{n}$ is the total Z magnetization in both chains $\hat{n} = \frac{1}{2}\sum_{s,i}(\hat{\sigma}^{z}_{s,i} + 1)$. This qubit model will evade slow-down, as it is equivalent to the fermion master equation Eqs. (5.4) and (5.5) under a Jordan-Wigner transformation (with $\Delta = 0$ for simplicity), [1]. However, because of the string operators, it corresponds to a long-range dissipative interaction between the chains that would be extremely difficult to engineer. We will thus consider an alternate route.

Note that in Eq. (5.9), the parity operator $\hat{P} \equiv (-1)^{\hat{n}}$ is the only object that violates our locality constraint. Further note that it yields a weak symmetry of the dynamics: $[\hat{H}, \hat{P}] = \{\hat{L}_i, \hat{P}\} = 0$, [131]. More explicitly, the Hamiltonian conserves parity, and each quantum jump simply flips it sign. This suggests a strategy: by starting in a definite parity state and then tracking the number of jumps that have occurred, we can treat $P = \langle \hat{P} \rangle$ as a *classical variable*. We can use this variable to update the dynamics, by setting a phase in the system-bath coupling to match its value. In doing so, we eliminate the need to engineer an explicit long-range interaction between the chains. Instead, we have an example of an adaptive protocol. We stress that this "fermion-inspired" protocol is able to exponentially improve

the preparation time of the steady state, while requiring the absolute minimal resource of a single bit classical memory necessary to evade the bounds set in [95].

While such an adaptive protocol may seem non-trivial to engineer in a time-continuous open quantum system, it can be done very efficiently via a measured unitary circuit. Adaptive quantum circuits have been shown to be extremely powerful in other contexts, including entanglement generation [163, 164, 165] and topological ground state preparation [174, 175, 176]. While the power of adaptive circuits is often tied to the use of long-range classical communication, this is not part of our scheme; nonetheless, we still obtain a dramatic advantage. For our setup, we assume that at $t = 0$ we are in a state of fixed parity. The Hamiltonian interaction can be implemented using two unitaries in a brickwork structure [see Fig. 5.2(a)]:

$$\begin{aligned}\hat{U}_{H,1} &= \exp\left(-iJ\sum_{s=A,B}\sum_{i=1}\hat{\sigma}^{+}_{s,2i-1}\hat{\sigma}^{-}_{s,2i} - \text{H. c.}\right),\\ \hat{U}_{H,2} &= \exp\left(-iJ\sum_{s=A,B}\sum_{i=1}\hat{\sigma}^{+}_{s,2i}\hat{\sigma}^{-}_{s,2i+1} - \text{H. c.}\right),\end{aligned} \tag{5.10}$$

which are independent of the classical parity variable P. To implement the quantum jumps, we use two other unitaries as well as an auxilliary qubit $\hat{\sigma}_{\text{aux}}$:

$$\begin{aligned}\hat{U}_{\text{jump},1} &= \exp\left(-i\hat{\sigma}^{+}_{\text{aux}}\left[u\hat{\sigma}^{-}_{A,1} - vP\hat{\sigma}^{+}_{B,1}\right] - \text{H. c.}\right),\\ \hat{U}_{\text{jump},2} &= \exp\left(-i\hat{\sigma}^{+}_{\text{aux}}\left[u\hat{\sigma}^{-}_{B,1} - vP\hat{\sigma}^{+}_{A,1}\right] - \text{H. c.}\right).\end{aligned} \tag{5.11}$$

We imagine initializing the auxiliary qubit in $|0\rangle$ and then acting with $\hat{U}_{\text{jump},1}$. Then we perform a projective measurement on the auxiliary qubit in the computational basis. If the site is still in $|0\rangle$ then no jump occurred and we do nothing. If the site is now in $|1\rangle$, then we acted one time with $\hat{L}_1$, and so we have done a single jump. We update the parity $P \to -P$, and then reset the auxiliary qubit. We repeat the same process with $\hat{U}_{\text{jump},2}$. This type of

measurement and reset operation is a well known method to simulate Lindblad dynamics on a unitary circuit (see e.g. [177, 178, 179]). However, using it within this kind of adaptive setting (where the subsequent unitary evolution is updated based on the presence or absence of a jump) was not considered.

The above gates define one layer of an adaptive circuit [see Fig. 5.2(a)] which implements a time-discretized version of the fermionic master equation on the spins, and therefore can converge to the proper steady state without being constrained by time-entanglement trade-offs. By tracking parity and using it to adapt the dynamics, we are effectively trading a long range spatial interaction for a minimal kind of non-Markovian dynamics (using a single-bit classical memory). The entanglement dynamics of this circuit (averaged over measurement outcomes) is shown in Fig. 5.2(b), where we always start from an all-down product state. The bipartite entanglement entropy saturates to a maximal value in a time that grows *linearly* with system size, even for $v^2 = 0.5$ when the fixed point of the circuit generates n perfect bell pairs (a maximally entangled state). It thus evades the general time-entanglement bound of Ref. [95]. The difference in dynamics is even more remarkable at the single trajectory level: we find that for any given stochastic trajectory, the entanglement entropy increases monotonically with time, see Fig. 5.2(c). We can understand this mechanistically by thinking of the dissipation as injecting entanglement into the system: by flipping the phase of each injected Bell pair, it is impossible to inadvertently remove entanglement from the system, see Appendix D for more details. Moreover, in Appendix D, we show this is surprisingly robust to measurement errors.

To emphasize the importance of the adaptive dynamics, we can compare against a circuit that is identical except that the relative phase P is not updated, but instead held constant in time. For any value of $v^2 \neq 0.5$, the resulting dynamics still converges to the same entangled state as the adaptive protocol, but on a much longer time scale, one that diverges as $v^2 \to 0.5$. This is shown in Fig. 5.2(d). The striking difference in dynamics can also

be seen at the trajectory level, where instead of growing monotonically the entanglement entropy rapidly fluctuates in both directions before finally reaching the fixed point on an exponentially longer time scale, see Fig. 5.2(c).

Additionally, we find that this scheme is surprisingly robust to measurement errors in the auxiliary qubit, see Appendix D for details.

5.4 Time continuous adapative dynamics

Our circuit-based adaptive protocol can be directly generalized to a continuous-time, fully autonomous stabilization scheme by simply promoting the classical memory used above to a quantum degree of freedom. Here, we will use the operator $\hat{\sigma}^z_P$ of a single auxiliary qubit to effectively track jumps and to update the phase of the dissipator accordingly. We thus consider a modified Lindblad master equation for our double spin-chain system, where the jump operators in Eq. (5.9) are now:

$$\begin{aligned} \hat{L}_1 &= \hat{\sigma}^x_P(u\hat{\sigma}^-_{A,1} + v\hat{\sigma}^+_{B,1}\hat{\sigma}^z_P), \\ \hat{L}_2 &= \hat{\sigma}^x_P(u\hat{\sigma}^-_{B,1}\hat{\sigma}^z_P + v\hat{\sigma}^+_{A,1}). \end{aligned} \tag{5.12}$$

Each jump now flips the state of the P qubit, and its state also determines the phase of the dissipators as needed. We find that the master equation generated by these dissipators and the Hamiltonian in Eq. (5.8) can rapidly stabilize an entangled state, completely evading the general time-entanglement bound of Ref. [95], see Fig. 5.1. One appealing way to understand this is that the P spin acts like a classical memory, making the effective dynamics of the spin chains non-Markovian (and hence making the general bound inapplicable). While we have focused on a specific setup, the construction here can be used to accelerate any scheme using dissipators of the form in Eq. (5.2). The result is dissipative stabilization of arbitrary pure many-body entangled states without any time-entanglement tradeoff. Moreover, we show that this is possible using a minimal non-local resource of a single auxiliary qubit coupled

to each system.

5.5 Accelerated spin squeezing

Our approach can also accelerate dissipative stabilization schemes very different from those in Eqs. (5.6) and (5.7). For example, consider dissipative preparation of a spin squeezed state of N two level systems (collective spin operators $\hat{S}^{x,y,z} = \sum_{i=1}^{N} \hat{\sigma}_i^{x,y,z}$). The master equation

$$\partial_t \hat{\rho} = \Gamma \mathcal{D}[\hat{S}^+ + \tanh(r)\hat{S}^-]\hat{\rho} \tag{5.13}$$

conserves total angular momentum S_{tot}, and in the maximum S_{tot} subspace (and for N even) has a unique, pure spin squeezed steady state. For large r, this state has a Wineland parameter that exhibits Heisenberg limited scaling: $\xi_R^2 \equiv N\langle(\hat{S}^x)^2\rangle/|\langle\hat{S}\rangle|^2 \propto 2/(N+2)$[1], see [180, 181, 182]. This scheme also has a slow-down problem, and a time-squeezing tradeoff: as r increases, the dissipative gap (relaxation rate) is observed to vanish as $\sim e^{-4r}$. The reason for this slow down is different than the spin chains, in that it is not directly related to entanglement. Instead, it is a result of a general constraint on dissipative preparation of low fluctuation states. In fact, recalling the fidelity to the steady state $F(t)$, for a Lindbladian with a jump operator $\hat{L}$, one can show that[2]

$$\partial_t F \leq \langle(\hat{L} + \hat{L}^\dagger)^2\rangle - \langle\hat{L} + \hat{L}^\dagger\rangle^2, \tag{5.14}$$

1. We also note that for this particular state, a Ramsey measurement is in fact optimal, and so the Quantum Fisher Information $\mathcal{F}_Q$ can be simply related to the Wineland Parameter via $\mathcal{F}_Q = N/\xi_R^2$. See Appendix D for more details.

2. While this expression does not obviously reflect the gauge invariance $\hat{L} \to e^{i\phi}\hat{L}$, it can be shown that, because the steady state is pure and annihilated by the jump operator, the variance of the real part of $\hat{L}$ is invariant under multiplication by a phase. See Appendix D for more details.

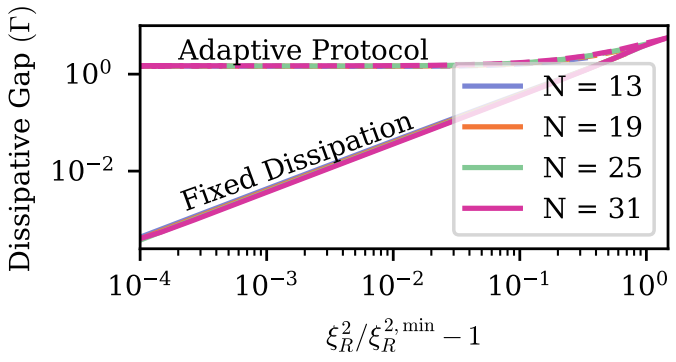

Figure 5.3: Dependence of the dissipative gap on the amount of squeezing. Each curve shows a fixed system size N, where the x-axis parameterizes how close the steady state Wineland squeezing parameter ξ_R^2 is compared to its minimal value $\xi_R^{2,\min}$, and is tuned using the squeezing parameter r. Solid lines correspond to the standard protocol with fixed dissipation [c.f. Eq. (5.13)], and dashed lines are the adaptive protocol where the phase flips after every jump.

and so the time scale is bounded by the fluctuations in the real part of the jump operator. In this case, because $\hat{L} + \hat{L}^\dagger \propto \hat{S}^x$ is being squeezed, it causes the dynamics to slow down. See Appendix D for details.

We can use the above fermion-inspired methods to modify and accelerate the dynamics here in a manner than preserves the steady state squeezing. It is rather unintuitive that this works - it means that after every jump, the squeezing axis switches from $\hat{S}^x \leftrightarrow \hat{S}^y$. It seems like half the time, the jump operator is actually trying to stabilize the wrong steady state. However, as can be seen in Fig. 5.3, this dramatically increases the relaxation rate. This is reminiscent of the quantum Mpemba effect, where starting farther away from the steady state allows you to reach it more quickly [183, 184, 185].

In order to actually implement this, one approach would be to use the "discrete-time" method. If dissipative squeezing is achieved via red- and blue-sideband drives on a cavity [181], then one can keep track of the quantum jumps by doing single photon detection on the cavity output field. Then, one can update the jump operator $\mathcal{D}[\hat{S}^+ + \tanh(r)\hat{S}^-] \leftrightarrow$

$\mathcal{D}[\hat{S}^+ - \tanh(r)\hat{S}^-]$ every time a photon is detected by toggling the phase of the drive, see Appendix D for details. Alternatively, the continuous-time approach would use the modified master equation

$$\partial_t \hat{\rho} = \Gamma \mathcal{D}\left[\hat{\sigma}^x_{\text{aux}}\left(\hat{S}^+ + \hat{\sigma}^z_{\text{aux}} \tanh(r)\hat{S}^-\right)\right]\hat{\rho}. \tag{5.15}$$

Here, $\hat{\sigma}^z_{\text{aux}}$ corresponds to an auxiliary qubit degree of freedom. Surprisingly, either method can significantly improve the time scale on which squeezing occurs: the dissipative gap remains $\mathcal{O}(\Gamma)$ even for arbitrarily large r and maximal squeezing.

5.6 Conclusion

We have demonstrated how an extremely minimal kind of adaptive dynamics can be used to dramatically speed up the stabilization of highly entangled many-body states. This includes the generation of remote entanglement, as well as the stabilization of spin squeezed states. Our protocols do not need long-range interactions, but nonetheless take direct inspiration from fermionic stabilization protocols, which are surprisingly immune from time-entanglement tradeoffs due to a subtle kind of in-built non-locality. In future work, it would be interesting to explore whether similar adaptive protocols could be used to speed up the preparation of other metrologically useful states.

This chapter concludes the first part of this dissertation on reservoir engineering. In the remaining chapters, we will shift focus to instead consider techniques to understand more generic open many body systems, and ways to efficiently simulate them.

CHAPTER 6

SIMULATION OF SPIN CHAINS USING A STOCHASTIC UNRAVELING

This chapter contains previously-published material found in Ref. [186]. Reuse is permitted according to the copyright agreement used by *Physical Review X Quantum*.

6.1 Introduction

One dimensional spin chains are paradigmatic models in theoretical physics, informing our understanding of a plethora of phenomena, including transport [187, 188], quantum phase transitions [189, 190], and entanglement dynamics [191, 192, 96]. Extending these systems to an open systems context with driving and dissipation gives rise to a wealth of new effects, and is also crucial for understanding the many-body dynamics of many NISQ-era quantum simulation platforms, where coupling to the environment can never be neglected [193]. For some 1D spin models, the Hamiltonian can be solved exactly via a Jordan-Wigner mapping to a system of free fermions [30]. However, adding even innocuous-looking forms of dissipation (e.g. local spin relaxation) can break the integrability of the system, as the linear spin operators appearing in dissipators pick up non-trivial Jordan-Wigner strings. Hence, outside of a handful of models that have been solved exactly (see e.g. [194, 195, 196]), describing the effects of even simple dissipative processes can require an exponential computational overhead.

In this work, we will present a new technique to efficiently simulate a class of Markovian dissipative spin chains which are non-trivial, in the sense that they cannot be mapped to quadratic fermionic master equations. We focus primarily on 1D systems where the Hamiltonian is equivalent to free-fermions, but the presence of Jordan-Wigner strings in the dissipative terms makes the system no longer free; however, we will relax this constraint

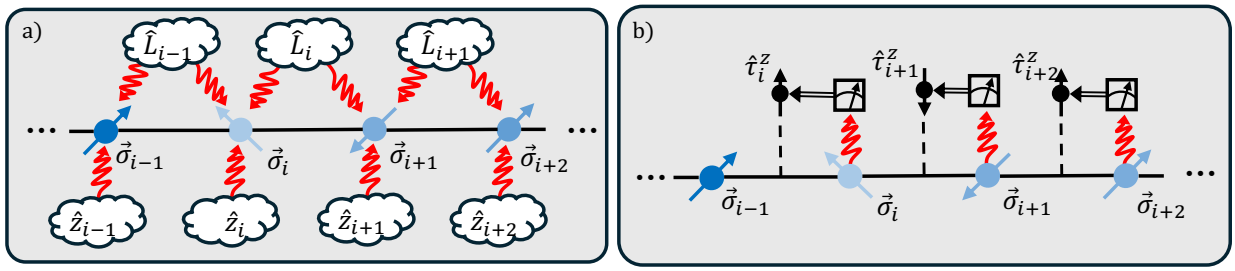

Figure 6.1: a) Schematic of the class of models simulable using our techniques: a 1D spin chain with linear dissipation that is local or correlated between sites (jump operators $\hat{z}_i$ or $\hat{L}_i$, respectively), and a Hamiltonian with anisotropic XY nearest-neighbor exchange and possibly non-uniform local Z fields. Upon a Jordan-Wigner transformation, due to non-trivial string operators in the dissipators, the system is mapped to a fermionic model inequivalent to free fermions. b) We can interpret the action of the string operators in the dissipation as a measurement and feedback process, where following each jump, a local $\mathbb{Z}_2$ gauge field undergoes a classical bit flip.

later to show the technique can also work on a broader class of systems, even including a 2D model.

Our method is based on an exact stochastic unraveling of the master equation, chosen so that each individual trajectory is a time-dependent fermionic Gaussian state. This provides an efficient means for computing the dynamics of observables, even though the average state is not a Gaussian state and the full dynamics isn't free fermion. Our method possesses many advantageous features: it has provable convergence results, has a computational complexity that scales only polynomially in the number of spins, and is free of any sign problems because it samples from only physical trajectories [197]. Because our technique is not limited to low-entanglement states (indeed, Gaussian states can have arbitrarily high amounts of entanglement), we believe our method can compliment existing simulation techniques that rely on area laws to achieve polynomial scaling.

The magic underlying our approach is that for a class of interesting master equations, we can find a stochastic unraveling that directly maps to a kind of fermionic measurement-plus-feedback dynamics, see Fig. 6.1. In this mapping, non-trivial string operators are now interpreted as feedback unitaries that follow a quantum jump, with each unitary having the

simple form of a Gaussian gauge transformation. Using this correspondence, we show that our technique is equivalent to a noisy $\mathbb{Z}_2$ gauge theory where the gauge fields are *classically* dynamical (i.e. they always have definite values), see Fig. 6.1. This has the benefit of both making the dynamics efficient to simulate, as well as providing direct physical insights into the effect that string operators have on the dynamics that would not be as easy to elucidate from other simulation techniques. This also allows us to also expand the technique beyond simple 1D spin chains to more complicated $\mathbb{Z}_2$ gauge theories, such as the Kitaev Honeycomb in 2D [198].

The remainder of this Chapter is organized as follows: in Section 6.2, we introduce open spin chains and briefly review previously known results on simulation complexity. Then, in Section 6.3, we present the most general type of spin system which we are able to simulate efficiently, and present two different algorithms loosely based on either interpreting the dynamics as being in the Heisenberg or Schrödinger picture. In Section 6.4, we give a few initial examples of models we can solve. We study the melting of anti-ferromagnetic order in a 1D XX spin chain with loss, we look at the dynamics and steady state of a dissipative Ising model, we study many-body subradiant decay in a 1D chain of emitters, and finally we sketch how this can applied to the 2D Kitaev honeycomb. Finally, in Section 6.5, we present a generalization of our technique to generic, open fermion models where the interaction is not a Jordan-Wigner string or inspired by an underlying spin model.

6.2 Open Spin Chains: Previous Work

There has been significant previous work studying open quantum spin chains, both numerically and exactly, which we will give an extremely brief outline of here. The goal will be to set the context for our solution technique, and outline how the new class of models we can solve fits into the space of previously known results.

We will be interested exclusively in Gorini-Kossakowski-Sudarshan-Lindblad (GKSL)

form master equations, which represent the most generic possible completely positive, trace preserving, Markovian quantum master equations [76, 77]. These have the form

$$\partial_t \hat{\rho} = -i[\hat{H}, \hat{\rho}] + \sum_i \hat{L}_i \hat{\rho} \hat{L}_i^\dagger - \frac{1}{2}\{\hat{L}_i^\dagger \hat{L}_i, \hat{\rho}\}, \tag{6.1}$$

where $\hat{H}$ is the Hamiltonian of the system, and the collection of operators $\hat{L}_i$ are "jump" operators describing the interaction with a Markovian environment. We will study primarily 1D spin chains by mapping them to fermions via the Jordan-Wigner (JW) transformation [30]. If we have a set of spin-1/2 operators $\hat{\sigma}_i^{x,y,z}$ indexed by a lattice position $i = 1, \ldots, N$, then we can define a set of canonical fermion annihilation operators

$$\hat{\sigma}_i^- = \left(\prod_{j=1}^{i-1} (-1)^{\hat{c}_j^\dagger \hat{c}_j} \right) \hat{c}_i \equiv \hat{\Pi}_{i-1} \hat{c}_i, \tag{6.2}$$

where $\hat{\sigma}_i^- = (\hat{\sigma}_i^x + i\hat{\sigma}_i^y)/2$. These fermions obey the canonical anti-commutation relations $\{\hat{c}_i, \hat{c}_j\} = \{\hat{c}_i^\dagger, \hat{c}_j^\dagger\} = 0$ and $\{\hat{c}_i, \hat{c}_j^\dagger\} = \delta_{ij}$. The product of fermion parity operators $\hat{\Pi}_i$ are called JW strings.

By using such a mapping, one can directly relate the simulability of a spin problem to whether or not it maps onto a simulable system of fermions, which has been well studied in the literature [199, 200, 173]. Considering first the coherent (Hamiltonian) dynamics, the set of nearest neighbor spin interactions that map to quadratic Hamiltonians of the fermion operators are of the form:

$$\begin{aligned} \hat{H} &= \sum_i \frac{\Delta_i}{2} \hat{\sigma}_i^z - J_i \hat{\sigma}_i^+ \hat{\sigma}_{i+1}^- - \tilde{J}_i \hat{\sigma}_i^+ \hat{\sigma}_{i+1}^+ + \text{H. c.} \\ &= \sum_i \Delta_i \hat{c}_i^\dagger \hat{c}_i + J_i \hat{c}_i^\dagger \hat{c}_{i+1} + \tilde{J}_i \hat{c}_i^\dagger \hat{c}_{i+1}^\dagger + \text{H. c.}, \end{aligned} \tag{6.3}$$

where $\Delta_i \in \mathbb{R}$ and $J_i, \tilde{J}_i \in \mathbb{C}$. The dynamics of any Gaussian state (see Section E.1 for

definitions of Gaussian states/operators) under a quadratic Hamiltonian remains Gaussian, and therefore time evolving the state can be reduced to time evolving the covariance matrix of the Gaussian state. This reduces the problem of evolving an exponentially large state vector or density matrix, to the dramatically simpler problem of evolving a polynomially-large covariance matrix.

When adding in dissipation and again mapping to fermions, for a Gaussian state to remain Gaussian, we again need the Hamiltonian to be quadratic in fermions. However, we also require that each jump operator $\hat{L}_i$ be linear in fermion creation/annihilation operators. One can immediately see that this will be problematic when starting from the spin problem: linear spin operators pick up a JW string under mapping to fermions, and so time evolution with linear spin operators does not preserve Gaussianity. For example, simple loss modeled by a jump operator $\hat{L}_i = \hat{\sigma}_i^-$ maps to $\hat{L}_i = \hat{\Pi}_{i-1}\hat{c}_i$. Moreover, as the string operators $\hat{\Pi}_i$ are extremely non-local, the resulting interactions in the fermionized model would appear to be very long range and hence intractable.

There are a few circumstances in which spin chains (with quadratic Hamiltonians) remain efficiently simulable in the presence of dissipation. If the jump operators are quadratic and Hermitian (like the terms appearing in Eq. (6.3), an example being dephasing noise), then the dynamics are equivalent to a classically stochastic quadratic Hamiltonian [126, 94, 130].Specifically, in these scenarios the state is not Gaussian, but the equation of motion for $2r$-point correlation functions close on themselves for all r, making them efficiently simulable [201, 202]. When noise is sufficiently strong, it can damp out long range correlations such that the system undergoes a percolation transition and then becomes simulable [203, 204]. However, outside of these particular cases, there is no efficient and exact method for simulating what happens when the jump operators have strings.

6.3 Stochastic Simulation Method

6.3.1 Stochastic Unraveling of the Master Equation

In this section, we will outline a new simulation technique which extends the set of efficiently simulable spin models. Specifically, we will demonstrate how to simulate a class of models where the non-Hermitian Hamiltonian encoded in Eq. (6.1) maps to an operator quadratic in JW fermions, but where fermionic interactions arise through string operators associated with the quantum jump terms. We stress that the techniques presented below are numerically *exact* - given sufficient averaging they recover unbiased expectation values of the time continuous master equation. This is true regardless of the relative strength of the noise and whether or not it is classical. Moreover, the technique is entirely agnostic to the total amount of entanglement in the system.

We study systems with Hamiltonians of the form Eq. (6.3) and jump operators which can be written as sums of 2-local linear spin operators:

$$\begin{aligned}\hat{L}_i &= l_{i,1}\hat{\sigma}_i^- + l_{i,2}\hat{\sigma}_i^+ + l_{i,3}\hat{\sigma}_{i+1}^- + l_{i,4}\hat{\sigma}_{i+1}^+ \\ &= \hat{\Pi}_i(-1)^{\hat{c}_i^\dagger \hat{c}_i}\left(l_{i,1}\hat{c}_i + l_{i,2}\hat{c}_i^\dagger\right) + \hat{\Pi}_i\left(l_{i,3}\hat{c}_{i+1} + l_{i,4}\hat{c}_{i+1}^\dagger\right) \\ &= \hat{\Pi}_i\left(l_{i,1}\hat{c}_i - l_{i,2}\hat{c}_i^\dagger + l_{i,3}\hat{c}_{i+1} + l_{i,4}\hat{c}_{i+1}^\dagger\right) \equiv \hat{\Pi}_i\hat{L}_i', \end{aligned} \tag{6.4}$$

where $l_{i,j} \in \mathbb{C}$ are arbitrary, possibly time-dependent, coefficients. With this constraint the only non-quadratic interaction terms in the fermionic representation of the master equation arise via the overall JW string operator in the jump operators $\hat{L}_i$. It is crucial that we can factor out a single string operator, which is why we are limited to 2-local jumps.

We will make this class of systems efficiently simulable by rewriting the master equation as a stochastic average. We will unravel the master equation in the "quantum jumps" picture. We can group together the commutator and the anti-commutator in Eq. (6.1) to form the

non-Hermitian effective Hamiltonian $\hat{H}_{\text{eff}} = \hat{H} - \frac{i}{2}\sum_i \hat{L}_i^\dagger \hat{L}_i - \langle \hat{L}_i^\dagger \hat{L}_i \rangle$. We next introduce the stochastic equation of motion [126, 94, 130]

$$d|\psi\rangle = -i\hat{H}_{\text{eff}}|\psi\rangle dt + \sum_i \left(\frac{\hat{L}_i}{\sqrt{\langle \hat{L}_i^\dagger \hat{L}_i \rangle}} - 1 \right) |\psi\rangle d\xi_i, \tag{6.5}$$

where $d\xi_i \in \{0, 1\}$ is a point process with mean $\overline{d\xi_i} = \langle \hat{L}_i^\dagger \hat{L}_i \rangle dt$, which implicitly depends on the state at a time t. We can interpret the dynamics governed by Eq. (6.5) as the state evolving under the non-Hermitian Hamiltonian $\hat{H}_{\text{eff}}$, with this smooth evolution interrupted with discrete quantum jumps: at each instant in time, with a probability $\langle \hat{L}_i^\dagger \hat{L}_i \rangle dt$, the system undergoes a discrete jump defined by the jump operator $\hat{L}_i$. Note that this time evolution generically does not preserve the norm of $|\psi\rangle$ because $\hat{H}_{\text{eff}} \neq \hat{H}_{\text{eff}}^\dagger$.

The first crucial observation that we make is that as we have constrained our jump operators to have the form $\hat{L}_i = \hat{\Pi}_{i-1}\hat{L}'_i$ where $\hat{\Pi}_{i-1}$ is a string operator and $\hat{L}'_i$ is a linear fermionic operator, then $\hat{L}_i^\dagger \hat{L}_i = (\hat{L}'_i)^\dagger \hat{L}'_i$. It follows that the the effective Hamiltonian $\hat{H}_{\text{eff}}$ is a quadratic fermionic operator. This in turn implies that all of the complexity in the dynamics of each individual stochastic trajectory arises from the finite "jumps": the continuous time evolution under the effective Hamiltonian is purely Gaussian. We will show below that the situation is even more favourable: because of the specific way string operators appear (i.e. they are exponentials of quadratic fermion operators), they will also be easily simulable. Specifically, we will show that each jump operator maps Gaussian states to Gaussian states. We can thus view the jump process as Gaussian feedback where we apply a conditional Gaussian transformation conditioned on whether or not a quantum jump occurred, see Fig. 6.1.

We will use this observation to derive two techniques to efficiently simulate the master equation. The first is roughly based on a "Heisenberg Picture" interpretation, where we directly solve for the time evolution of operators instead of the state. This method provides

an appealing intuitive picture of the effect of the interactions encoded in the strings. The algorithm has a computational complexity that is polynomial in the number of spins, but still turns out not to be the most efficient way to simulate the dynamics. The second is based on a "Schrödinger Picture" interpretation, where the state itself is dynamic, and is more numerically efficient than the Heisenberg picture interpretation. In the remainder of this Chapter we provide intuition and examples of the different types of models that can be simulated, and in Section E.2 we give the most general 1D spin chain model that can be simulated with our technique. Moreover, the technique can be extended to higher dimensional systems in certain cases, see Section 6.4.4.

Before proceeding, we note that Ref. [205] derived a result on Lindblad dynamics that applies to a *subset* of our general class of simulable models. If we restrict attention to models where the Hamiltonian is strictly (fermionic) number conserving, and dissipation only involves loss, then Ref. [205] provides a method for computing the spectral decomposition of the Liouvillian (using its lower-triangular, block-diagonal structure). The spectrum can be obtained from $\hat{H}_{\text{eff}}$ alone, and this can then be used to recursively calculate eigenmodes. We stress that this result does not apply to the more general class of models we consider, where the Hamiltonian need not conserve excitation number, and where dissipation can involve particle loss and addition. Even in the more restricted loss-only setting, our approach remains extremely valuable, as using the results of Ref. [205] to compute the dynamics of observables still results in an exponentially hard problem (see Section E.3 for more details).

6.3.2 Heisenberg Picture

On any given stochastic trajectory, the system evolves under $\hat{H}_{\text{eff}}$, punctuated by quantum jumps. Consider time-evolution from $t = 0$ until $t = t_f$ starting from a pure state $|\psi\rangle$, during which a specific trajectory undergoes m quantum jumps. We index these jumps with $j = 1, \ldots, m$, and use $\hat{L}_{i_j}$ to denote the jump operator corresponding to jump j at lattice

site i_j occuring at time t_j. For this specific trajectory, the expectation value of an arbitrary observable $\hat{O}$ at time $t = t_f$ takes the form:

$$\langle \hat{O} \rangle (t_f) = \langle \psi | \hat{V}^\dagger(t_f, t_0) \hat{O} \hat{V}(t_f, t_0) | \psi \rangle / \mathcal{N}(t), \tag{6.6}$$

$$\hat{V}(t_f, t_0) = e^{-i\hat{H}_{\text{eff}}(t_f - t_m)} \hat{L}_{i_m} e^{-i\hat{H}_{\text{eff}}(t_m - t_{m-1})} \dots e^{-i\hat{H}_{\text{eff}}(t_2 - t_1)} \hat{L}_{i_1} e^{-i\hat{H}_{\text{eff}} t_1} \tag{6.7}$$

where $\mathcal{N}(t)$ corresponds to state normalization. To help elucidate the structure here, we introduce the set of operators $\hat{P}_j = \hat{\Pi}_{i_1} \hat{\Pi}_{i_2} \dots \hat{\Pi}_{i_j}$ (i.e. the product of string operators associated with jumps $1, 2, ..., j$). We define the Heisenberg picture time evolution for an operator under the non-Hermitian Hamiltonian evolution as:

$$\partial_t \hat{O}_{\text{unnorm}} = i \left(\hat{H}^\dagger_{\text{eff}} \hat{O}_{\text{unnorm}} - \hat{O}_{\text{unnorm}} \hat{H}_{\text{eff}} \right), \tag{6.8}$$

$$\partial_t \mathcal{N} = \partial_t \langle \hat{\mathbf{1}} \rangle = i \langle \hat{H}^\dagger_{\text{eff}} - \hat{H}_{\text{eff}} \rangle, \tag{6.9}$$

where $\hat{O} = \hat{O}_{\text{unnorm}} / \mathcal{N}$.

We next introduce a time-dependent non-Hermitian Hamiltonian whose form is set by the pattern of jumps occurring along a specific trajectory of interest:

$$\hat{H}'_{\text{eff}}(t) = \begin{cases} \hat{H}_{\text{eff}} & 0 < t < t_1 \\ \hat{P}_j \hat{H}_{\text{eff}} \hat{P}_j & t_j < t < t_{j+1} \end{cases}, \tag{6.10}$$

with $t_{m+1} \equiv t_f$. Note crucially that as each string operator $\hat{\Pi}_i$ is a Gaussian unitary (i.e., an exponential of quadratic fermion operators), so are the $\hat{P}_j$ operators. It follows that for any trajectory, the corresponding $\hat{H}'_{\text{eff}}(t)$ is a quadratic fermionic operator for all times. With these definitions, our expectation value takes the convenient form:

$$\langle \hat{O} \rangle (T) = \langle \psi | (\hat{L}')^\dagger_{i_1}(t_1) \dots (\hat{L}')^\dagger_{i_m}(t_m) (\hat{P}_m \hat{O} \hat{P}_m)(t_f) \hat{L}'_{i_m}(t_m) \dots \hat{L}'_{i_1}(t_1) | \psi \rangle / \mathcal{N}(t). \tag{6.11}$$

Recall that the $\hat{L}'_j$ are our jump operators *without* the overall string-operator prefactor (c.f. (6.4)), and note that the Heisenberg-picture operators here evolve according to the trajectory-dependent non-Hermitian Hamiltonian $\hat{H}'_{\text{eff}}(t)$

We see that we have a string of time-evolved operators, where each $\hat{L}'_{i_j}(t_j)$ will be linear in fermionic raising and lowering operators (as it is a linear-in-fermion operator evolved under a *quadratic* Hamiltonian). This is a very tractable structure as long as our initial state $|\psi\rangle$ is Gaussian: it corresponds to computing an out-of-time-order correlator (OTOC) of a *Gaussian state*, which can be done efficiently. More explicitly, as each $\hat{L}'_{i_j}(t_j)$ is linear in fermion operators, this OTOC can be efficiently computed by diagonalizing $\hat{H}_{\text{eff}}$ and then computing a Pfaffian, see Chapter 8 for details. This gives the expectation value for the observable $\hat{O}$ over a single stochastic trajectory; the observable for the master equation can be computed by averaging over the trajectories. Overall, this can be done with asymptotic computational complexity $\mathcal{O}(N^7T^2)$ where N is the number of spins in the chain and T is the total simulation time, proving that observables can be efficiently simulated, see Chapter 8 for more details.

Eq. (6.10) for our time-dependent conditional Hamiltonian has a straightforward interpretation: after each quantum jump, we flip some of the signs in the effective Hamiltonian based on the position of the jump, and this modified Hamiltonian then governs the evolution until the next jump. These sign-flips directly correspond to the string operators effecting a position-dependent gauge transformation $\hat{c}_j \to -\hat{c}_j$ for all of the sites to the left of the jump. We thus obtain a useful intuitive picture for the action of the string operators in the dissipators: they drive a kind of time-dependent disorder that is correlated with the location of the jumps.

We can make the above picture more explicit by gauging the weak $\mathbb{Z}_2$ symmetry in the problem. We first introduce a set of auxiliary spins $\hat{\tau}_i^\alpha$ ($\alpha = x, y, z$) in each jump operator

of our original spin master equation via:

$$\hat{L}_{i,G} = \hat{\tau}_i^x \left(l_{i,1}\hat{\sigma}_i^- + l_{i,2}\hat{\sigma}_i^+ + l_{i,3}\hat{\sigma}_{i+1}^- + l_{i,4}\hat{\sigma}_{i+1}^+ \right). \tag{6.12}$$

The auxiliary spins do not appear in the Hamiltonian. Since $\hat{\tau}_i^x$ is a strongly conserved quantity, they have no impact on the dynamics. Now, when we map to fermions, we find that

$$\hat{H}_G = \sum_i \Delta_i \hat{c}_i^\dagger \hat{c}_i + \hat{\tilde{\tau}}_i^z \left(J_i \hat{c}_i^\dagger \hat{c}_{i+1} + \tilde{J}_i \hat{c}_i^\dagger \hat{c}_{i+1}^\dagger \right) + \text{H. c.}, \tag{6.13}$$

$$\hat{\tilde{\tau}}_i^z \equiv (i\hat{\gamma}_{\tau,i}\hat{\bar{\gamma}}_{\tau,i}), \tag{6.14}$$

$$\hat{L}_{i,G} = \hat{\gamma}_{\tau,i} \left(l_{i,1}\hat{c}_i - l_{i,2}\hat{c}_i^\dagger + l_{i,3}\hat{c}_{i+1} + l_{i,4}\hat{c}_{i+1}^\dagger \right), \tag{6.15}$$

where $\hat{\gamma}_{\tau,i}, \hat{\bar{\gamma}}_{\tau,i}$ are Majorana fermions. The gauge factors $\hat{\tilde{\tau}}_i^z$ that now appear in the Hamiltonian controls the sign of the interaction on each bond [206], and are dynamical due to the dissipation. However, upon a stochastic unraveling, the dynamics of the $\hat{\tilde{\tau}}_i^z$ become completely classical, because the jump terms all commute or anticommute with the local gauge degrees of freedom

$$[\hat{L}_{i,G}, \hat{\tilde{\tau}}_j^z] = 0 \quad \forall i \neq j, \tag{6.16}$$

$$\{\hat{L}_{i,G}, \hat{\tilde{\tau}}_i^z\} = 0. \tag{6.17}$$

Hence, we can treat the gauge degrees of freedom as numbers $\hat{\tilde{\tau}}_i^z = \pm 1$ that are classically updated after each jump. This is just another way of rewriting Eq. (6.10) where instead of the Hamiltonian being time-dependent, there is instead a classically dynamical gauge field fluctuating between $1 \leftrightarrow -1$ after each quantum jump.

It is also interesting to point out that this interpretation of a conditional gauge transformation being applied by each quantum jump is an interesting type of non-reciprocal feedback

identified in [207], where each jump applies a unitary gate on a different subsystem. This interpretation will prove useful in later sections to understand some of the specific models we consider, and how they differ from their free fermion counterparts. Moreover, this interpretation allows us to generalize the simulation technique to higher dimensional $\mathbb{Z}_2$ gauge theories, for example the Kitaev honeycomb, which we show can be simulated with noise in Section 6.4.4.

6.3.3 Schrödinger Picture

While the previous Heisenberg-picture formulation provides useful intuition in terms of effective time-dependent disorder, it is not the most efficient way to do simulations. We now present things in the Schrödinger picture, where only the state vector changes in time. To achieve this, we make use of a second key observation: despite the string operator prefactor, the action of each jump operator $\hat{L}_i$ [c.f. Eq. (6.4)] maps Gaussian states into Gaussian states. To see this, we will decompose it into two factors, and show that each is Gaussianity-preserving. First, we can consider the string operator $\hat{\Pi}_i$. This is trivially Gaussian, as it can equivalently be written as $\hat{\Pi}_i = \exp(i\pi \sum_{j=1}^{i} \hat{c}_j^\dagger \hat{c}_j)$, which is just a time evolution unitary generated by a quadratic Hamiltonian. The remaining factor $\hat{L}_i'$ in our jump operator is linear in fermionic raising and lowering operators. Acting with such linear fermionic operators also maps Gaussian states into Gaussian states (see Section E.1 for details).

We assume throughout that our initial state is Gaussian. Since the state $|\psi\rangle$ remains Gaussian along each individual trajectory (as defined in Eq. (6.5)), it suffices to only keep track of its covariance matrix. It will be useful to do this in a Majorana basis, we hence define:

$$\hat{\gamma}_{2i-1} = \hat{c}_i + \hat{c}_i^\dagger, \tag{6.18}$$

$$\hat{\gamma}_{2i} = i(\hat{c}_i - \hat{c}_i^\dagger), \tag{6.19}$$

such that $\{\hat{\gamma}_i, \hat{\gamma}_j\} = 2\delta_{ij}$. We then define the $2N \times 2N$ covariance matrix as

$$\Gamma_{ij} = \langle \hat{\gamma}_i \hat{\gamma}_j \rangle. \tag{6.20}$$

Our problem thus reduces to computing the evolution of $\Gamma_{ij}(t)$ along each trajectory, due both to $\hat{H}_{\text{eff}}$ and the discrete quantum jumps. Consider first the no-jump evolution. If we allow $\hat{H}_{\text{eff}}$ to be a general quadratic Hamiltonian defined by an antisymmetric matrix H:

$$\hat{H}_{\text{eff}} = \sum_{ij} H_{ij} \hat{\gamma}_i \hat{\gamma}_j, \tag{6.21}$$

then we can define $X = 4iH$ the generator of the dynamics of Γ via the non-linear equation of motion

$$\partial_t \Gamma = \Gamma X - X^* \Gamma + \frac{1}{2} \Gamma (X^* - X) \Gamma. \tag{6.22}$$

When $\hat{H}_{\text{eff}}$ is Hermitian, then $X = X^*$ and we recover the standard equations of motion for the fermionic covariance matrix. The nonlinear term encodes the fact the Hamiltonian is not Hermitian, and the state norm is changing.

Next, we include the effects of quantum jumps. Note that a given JW string operator $\hat{\Pi}_m$ can be written as

$$\hat{\Pi}_m = i^m \prod_{j=1}^{m} \hat{\gamma}_{2j-1} \hat{\gamma}_{2j}. \tag{6.23}$$

If we write the non-string part of each jump operator as

$$\hat{L}'_i = \sum_j l_{ij} \hat{\gamma}_j, \tag{6.24}$$

then following a jump involving $\hat{L}_i$, the state goes from $|\psi\rangle \to |\psi'\rangle = \hat{L}_i|\psi\rangle/\sqrt{\langle \hat{L}_i^\dagger \hat{L}_i\rangle}$. The covariance matrix after the jump is defined as $\Gamma'_{mn} = \langle\psi'|\hat{\gamma}_m\hat{\gamma}_n|\psi'\rangle$. We can write this covariance matrix in terms of the pre-jump covariance matrix Γ_{mn}:

$$\Gamma'_{mn} = \frac{\sum_{kl} l^*_{ik} l_{il} \langle \hat{\gamma}_k \hat{\Pi}_i \hat{\gamma}_m \hat{\gamma}_n \hat{\Pi}_i \hat{\gamma}_l\rangle}{\sum_{kl} l^*_{ik} l_{il} \langle \hat{\gamma}_k \hat{\gamma}_l\rangle}, \tag{6.25}$$

where the expectations values are with respect to the state pre-jump. This can be simplified greatly by noticing that as $\hat{\Pi}_i$ is a string of Majorana's, it either commutes or anticommutes with $\hat{\gamma}_m$ and $\hat{\gamma}_n$, depending on the sign of $m-2i$. We can collect all of these phases together and define

$$\eta^i_m = \begin{cases} -1 & m \leq 2i \\ +1 & m > 2i \end{cases}, \tag{6.26}$$

such that

$$\hat{\Pi}_i \hat{\gamma}_m = \eta^i_m \hat{\gamma}_m \hat{\Pi}_i. \tag{6.27}$$

Formally, these phases are keeping track of the conditional gauge transformations being introduced by the string operators. In Section 6.3.2 we introduced gauge operators $\hat{\tilde{\tau}}^z_m$, here we can observe that $\langle \hat{\tilde{\tau}}^z_m\rangle \to \eta^i_m \langle \hat{\tilde{\tau}}^z_m\rangle$ following a quantum jump at a site i. Using these phase variables, we find:

$$\begin{aligned} \Gamma'_{mn} &= \frac{\sum_{kl} l^*_{ik} l_{il} \eta^i_m \eta^i_n \langle \hat{\gamma}_k \hat{\gamma}_m \hat{\gamma}_n \hat{\gamma}_l\rangle}{\sum_{kl} l^*_{ik} l_{il} \langle \hat{\gamma}_k \hat{\gamma}_l\rangle} \\ &= \frac{\sum_{kl} l^*_{ik} l_{il} \eta^i_m \eta^i_n (\Gamma_{km}\Gamma_{nl} + \Gamma_{kl}\Gamma_{mn} - \Gamma_{kn}\Gamma_{ml})}{\sum_{kl} l^*_{ik} l_{il} \Gamma_{kl}}. \end{aligned} \tag{6.28}$$

Hence, this gives us a simple way to update the covariance matrix of the conditional state

after a given quantum jump. Note that the string operators enter this update rule through the phase factors $\eta^i_m \eta^i_n$. This corresponds to the effective unitary "feedback" operation occurring after each fermionic jump (see Fig. 6.1).

Eqs. (6.22) and (6.28) completely specify how to evolve the covariance matrix along a particular stochastic trajectory. We can conveniently combine these rules into a single stochastic equation of motion for the covariance matrix:

$$\begin{aligned} \mathrm{d}\Gamma_{mn} = &\left(\Gamma X - X^*\Gamma + \frac{1}{2}\Gamma(X^* - X)\Gamma\right)_{mn} \mathrm{d}t \\ &+ \sum_i \left(\frac{\sum_{kl} l^*_{ik} l_{il} \eta^i_m \eta^i_n (\Gamma_{km}\Gamma_{nl} + \Gamma_{kl}\Gamma_{mn} - \Gamma_{kn}\Gamma_{ml})}{\sum_{kl} l^*_{ik} l_{il} \Gamma_{kl}} - \Gamma_{mn}\right) \mathrm{d}\xi_i. \end{aligned} \tag{6.29}$$

As before, the $\mathrm{d}\xi_i$ are independent, nonlinear point processes that depend on the current state of the system, satisfying $\mathrm{d}\xi_i^2 = \mathrm{d}\xi_i$ and $\overline{\mathrm{d}\xi_i} = \langle \hat{L}_i^\dagger \hat{L}_i \rangle \, \mathrm{d}t$.

In Chapter 8 we provide an explicit simulation algorithm using these equations that works in $\mathcal{O}(N^4)$ time, and in Section E.4 we show that for bounded observables (i.e. Pauli strings) the sampling complexity required to get convergence is bounded and independent of system size. We stress that our equations and the corresponding numerical technique is exact, and not the result of any approximations. In particular, it is agnostic to the total amount of entanglement in the system.

6.3.4 Constraints on dynamics

While the above stochastic techniques are more computationally friendly, we can in principle recast Eq. (6.29), the stochastic equation of motion for our covariance matrix, as a deterministic equation for a probability distribution $p(\Gamma, t)$ on the space of possible covariance matrices. Using this distribution, we could write down the exact density matrix at all times

as

$$\hat{\rho}(t) = \int p(\Gamma, t)\hat{\rho}_\Gamma \, \mathrm{d}\Gamma, \tag{6.30}$$

where $\hat{\rho}_\Gamma$ is the unique Gaussian state with covariance matrix Γ. We derive the Fokker-Planck equation governing $p(\Gamma, t)$ in Section E.5. It has a rather unwieldy structure due the point-process noise; in particular, it is not local in the space of covariance matrices.

The form of Eq. (6.30) also provides crucial insights into generic features of the class of models we study. Even though we are able to describe master equations that correspond to non-free fermions (i.e. where Gaussian initial states can evolve to non-Gaussian states), the dynamics is inherently constrained: the state at all times can be viewed as a *classical mixture* of Gaussian states, described by a classical probability distribution $p(\Gamma, t)$. We note that a similar class of states was recently studied for very different reasons in [208]; the motivation here was to simulate a class of interacting fermionic lattice models with strong dephasing. This mixture-of-Gaussians represents a highly constrained state space. For example, the only pure states in this space are simple Gaussian states.

We note that this is the same class of states that one would get after time evolving with a classically stochastic quadratic Hamiltonian, which is one way to model quadratic, Hermitian fermionic jump operators. However, despite living in the same state space, we stress that a classically stochastic free Hamiltonian admits significantly simpler dynamics than our particular class of stochastic spin models. A stochastic quadratic Hamiltonian can be modeled by the following equation of motion for the covariance matrix Γ:

$$\partial_t \Gamma = -(X_0\Gamma - \Gamma X_0) \, \mathrm{d}t - \sum_i (X_i\Gamma - \Gamma X_i) \, \mathrm{d}W_i. \tag{6.31}$$

Here, $\mathrm{d}W_i$ are independent Wiener increments, $X_0 = 4iH$ is the static generator of the dynamics, and $X_i = 4iL_i$ are the matrices corresponding to the Hermitian jump operators.

This is a very simple set of dynamics, where everything is linear, and the noise is a simple Wiener process independent of the state. This can be contrasted with Eq. (6.29), where the equation of motion becomes non-linear in Γ, and the noise itself is a non-linear point process that depends on the state, greatly increasing the complexity of the problem.

Our results also imply that all information on the evolved state (at any time) is encoded in $4N^2$ stochastic degrees of freedom. This should be contrasted against a generic state, which requires one to specify 4^N degrees of freedom, and alternatively a truly Gaussian state which has $4N^2$ *deterministic* degrees of freedom. Note that a polynomial number of stochastic degrees could still encode an exponential amount of information, if there are an exponential number of non-trivial moments of the distribution function $p(\Gamma, t)$. However, even in this extreme case, the information is encoded in a more convenient manner. In particular $(2n)-$point correlation functions are encoded in $n^{th}-$order moments, and are insensitive to higher-order moments. Further, we never need to calculate any given moment larger than order $2N$ (as this is the longest irreducible string of Majorana operators), and so any individual Pauli string is encoded efficiently in the distribution. There are an exponentially large number of these Pauli strings, and so we cannot access *all* information efficiently, but we can access *arbitrary* information efficiently.

Finally, we can also use our equations to derive a useful deterministic but approximate equation of motion for the trajectory-averaged covariance matrix $\bar{\Gamma}$. One simply takes the stochastic average of Eq. (6.22), making a first moment approximation (i.e. replacing each factor of Γ_{jk} with its average on the RHS). This gives the following approximate equation for the trajectory-averaged covariance matrix (i.e., the covariance matrix of the unconditional state):

$$\partial_t \bar{\Gamma}_{mn} = (\bar{\Gamma} X - X \bar{\Gamma}^*)_{mn} + \sum_{ikl} l^*_{ik} l_{il} (\eta^i_m \eta^i_n - 1)(\bar{\Gamma}_{km}\bar{\Gamma}_{nl} + \bar{\Gamma}_{kl}\bar{\Gamma}_{mn} - \bar{\Gamma}_{kn}\bar{\Gamma}_{ml}). \tag{6.32}$$

While not immediately obvious, this approximation equation matches what one would obtain

using a more standard second-cumulant approximation on equations of motion obtained directly from the full fermionic master equation (see Section E.6 for details).

6.4 Numerical Results

In this section we highlight the power of our general method by applying it to understand three paradigmatic examples of open spin chains. While we focus on 1D examples here, we stress that our technique can also be applied to certain higher-dimensional models (see Section 6.4.4). The three examples we study correspond to open spin models where a JW mapping results in non-trivial strings in the dissipators. In each case, if one simply ignores the strings, one is left with a quadratic fermionic Lindbladian where the physics is easily understood. The question is then to understand how the inclusion of strings change the physics, i.e. how is the spin system different from the corresponding free fermion system. In our examples, the strings will lead to large changes in either the dynamics or the steady state of the system. In the first two examples (AFM order melting and subradiance), we will look at how the addition of the string operators can speed up the approach to the steady state via effective scattering interactions, even if the steady state is trivial vacuum with or without the presence of the string operators. In the final example (an open Ising chain) we will see how the strings can actually affect the steady state observables and effective temperature of the steady state distribution.

6.4.1 AFM Order Melting in XX Chains

Our first example is perhaps simplest and seemingly most trivial kind of open spin chain: an XX chain where there is uniform local loss on each site. This would correspond to a chain of qubits with nearest neighbor couplings, with each qubit having a finite T_1 decay time. The system evolves under the master equation given in Eq. (6.1), with

$$\hat{H} = -\frac{J}{2}\sum_{i=1}^{N-1}\left(\hat{\sigma}_i^x\hat{\sigma}_{i+1}^x + \hat{\sigma}_i^y\hat{\sigma}_{i+1}^y\right), \tag{6.33}$$

$$\hat{L}_i = \sqrt{\kappa}\hat{\sigma}_i^-. \tag{6.34}$$

This system has a unique steady state given by the spin polarized state $|\uparrow\rangle^{\otimes N}$. Furthermore, because the total magnetization is a weak symmetry, we can characterize the time scale for the decay of the total magnetization by observing that if we define $\hat{n} = \frac{1}{N}\sum_{i=1}^{N}\hat{\sigma}_i^+\hat{\sigma}_i^-$, then this decays with a simple exponential to zero:

$$\langle\hat{n}\rangle(t) = e^{-\kappa t}\langle\hat{n}\rangle(0). \tag{6.35}$$

This decay profile is identical to what one would find for the dynamics of total density in the corresponding free fermion model, i.e. a tight-binding chain with singe-particle loss on each site:

$$\hat{H} = -J\sum_{i=1}^{N-1}\hat{c}_i^\dagger\hat{c}_{i+1} + \text{H. c.}, \tag{6.36}$$

$$\hat{L}_i = \sqrt{\kappa}\hat{c}_i. \tag{6.37}$$

Hence, at first glance, it is tempting to conclude that both the free fermion and spin system (i.e. fermions with strings in the dissipator) are equally trivial. Surprisingly, even in this maximally simple model, there are local, extensive observables where the spins and fermions have dramatic differences in their dynamics. As the average total density is not sensitive to the strings, we instead look at how non-zero Fourier components of the average excitation density decay. In particular, we focus on Néel or anti-ferromagnetic (AFM) order, defined

as the $k = \pi$ component of density:

$$\hat{A} = \frac{1}{N}\sum_{i=1}^{N}(-1)^i(1 - 2\hat{c}_i^\dagger \hat{c}_i) = \frac{1}{N}\sum_{i=1}^{N}(-1)^i \hat{\sigma}_i^z. \tag{6.38}$$

We consider a scenario where the system is initialized at $t = 0$ into the Néel state so as to maximize $\langle \hat{A} \rangle$. We then study how this order decays to zero. In the case where the dynamics are given by free fermions, in the thermodynamic limit, we can solve for this exactly. Defining momentum space annihilation operators as

$$\hat{\tilde{c}}_k = \frac{1}{\sqrt{N}}\sum_i e^{ijk}\hat{c}_j, \tag{6.39}$$

the AFM order (assuming infinite boundary conditions) is given by

$$A(t) = \int_{-\pi}^{\pi} \langle \hat{\tilde{c}}_k^\dagger \hat{\tilde{c}}_{k+\pi} \rangle \frac{\mathrm{d}k}{2\pi}, \tag{6.40}$$

where we define $A(t) = \langle \hat{A} \rangle(t)$. For free fermions, the integrand has an overall decay at rate κ, and an oscillation set by the energy difference of the momentum states k and $k + \pi$. This yields

$$A(t) = \int_{-\pi}^{\pi} e^{4iJ\cos(k)t - \kappa t}\frac{\mathrm{d}k}{2\pi} = e^{-\kappa t} J_0(|4Jt|), \tag{6.41}$$

where J_0 is the Bessel function. The overall exponential decay here just corresponds to the decay of the total particle density. More interesting is the Bessel function envelope, which is the result of the interplay between the coherent Hamiltonian dynamics and the initial Néel ordering. The simple form here relies on the fact that momentum is conserved (see Section E.7). At long times, the Bessel function decays like $t^{-1/2}$, giving a power law behavior decay in the scaled correlation $A(t)/e^{-\kappa t}$.

We can now turn to the spin model, and again ask how the AFM order decays starting from an initial Néel state. The dynamics now is far more complicated, as the strings in the loss dissipators play a non-trivial role. In particular, they allow scattering between different fermionic k modes, disrupting the simple dynamics of the purely fermionic model. Results for a $N = 100$ site spin chain using our simulation method are shown in Fig. 6.2, where we plot the scaled AFM order $A(t)/e^{-\kappa t}$. While for short times the spin and fermion models show similar behavior (not surprising as few jump have occurred), for larger times $\kappa t \gtrsim 1$ the two systems have very different behavior. In particular, the decay of the scaled AFM order for the spin model is $\propto 1/t$, and hence faster than the powerlaw decay $1/\sqrt{t}$ found in the simple fermion model. The difference persists for a large range of times, until a longer timescale where boundaries become relevant.

We can develop intuition for this result and even make approximate quantitative estimates by starting with the Heisenberg/OTOC formulation of the spin-system evolution, where the spins look like the fermions, except every time there is a quantum jump, the sign of one of the bonds in the Hamiltonian flips its sign, leading to a kind of time-dependent disorder. A very crude way of trying to model this is to consider a fermionic system with static disorder, e.g. a Hamiltonian of the form

$$\hat{H} = \sum_i J_i \hat{c}_i^\dagger \hat{c}_{i+1} + \text{H. c.}, \tag{6.42}$$

where the $J_i \in \{J, -J\}$ are random variables. To get an idea of the decay dynamics, we could fix the disorder level to mimic times in our spin model where $\mathcal{O}(N)$ jumps have occurred. This would be accurate for $\kappa t \gtrsim 1$, which is where the spins and free fermions diverge. In our approximate fermionic model, we can imagine that the disorder will generate some dephasing of the coherence between the k and $k + \pi$ momentum modes that determines the AFM order. Further, we expect that this dephasing rate will depend on the group velocity of the quasiparticles involved, for the simple reason that for some fixed evolution time, "fast

moving" modes will experience more of the spatial disorder than slow moving modes. This motivates an ansatz for the Néel order of the form:

$$\langle \hat{\tilde{c}}_k^\dagger \hat{\tilde{c}}_{k+\pi} \rangle \sim e^{-4iJ\cos(k)t - \kappa t - 4\alpha^2 J^2 \sin^2(k) t^2}, \tag{6.43}$$

where α is some unitless parameter dependent on the correlation length of the noise and $4J^2\sin^2(k)t^2 = (\nu_g t)^2$ is the distance squared a wavepacket with momentum k has propagated in time t.

Using this form, our disordered fermionic model will have a faster decay of the Néel order than the disorder free case, because of the effective dephasing. We find the decay follows (see Section E.7 for more details):

$$A(t) \sim e^{-\kappa t}\frac{\cos(Jt)}{t}. \tag{6.44}$$

The faster power-law decay of $1/t$ is in very good agreement with the full numerics for our spin model as shown in Fig. 6.2, indicating that at least for this model, the effective disorder picture provides good intuition for how spins are different from simple free fermions.

6.4.2 Subradiance

Our approach is not limited to purely local dissipative processes, but can also describe dissipation correlated across adjacent sites. This motivates our second example: a 1D XX spin chain where now we have correlated loss on neighboring sites. This setup can be viewed as a minimal model for studying subradiant decay in an ordered array of 1D emitters, a topic that has received considerable recent interest (see e.g. [209, 210, 211, 212, 213, 214, 215, 216]). At a basic level, subradiance corresponds to the existence of certain spin-wave modes that have highly suppressed radiative decay due to destructive interference. Such subradiant physics has been studied in the context of a quantum memory for light [217, 218], as well

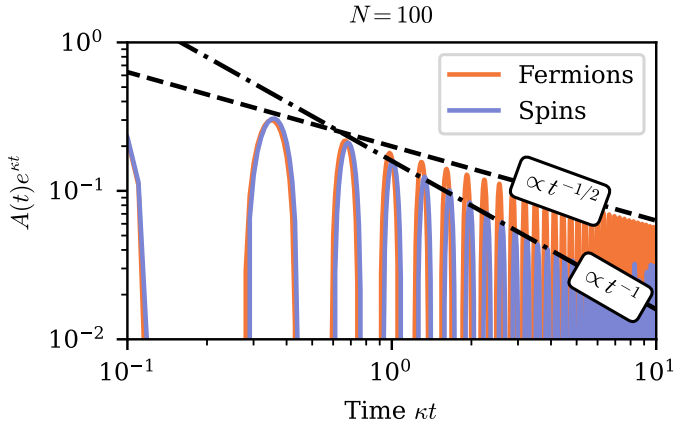

Figure 6.2: Here we plot the time dynamics of the AFM order parameter melting for either a 1D spin chain [c.f. Eqs. (6.33) and (6.34)] or free fermions [c.f. Eqs. (6.36) and (6.37)]. The fermion curve corresponds to the analytical solution in the thermodynamic limit given by the Bessel function [c.f. Eq. (6.41)], and the spins are found for an $N = 100$ spin chain with open boundary conditions averaged over 50,000 trajectories.

as having shown suprising fermion-like correlation patterns [211]. While this physics is well understood when there is only a single excitation, the physics with multiple excitations is far more complicated and remains an open problem. Our model and simulation technique provide a setting to study this phenomena with many excitations, in a manner that is numerically exact.

Our minimal model for subradiance corresponds to a master equation of the form in Eq. (6.1) with:

$$\hat{H} = -\frac{J}{2}\sum_{i=1}^{N-1} \hat{\sigma}_i^x \hat{\sigma}_{i+1}^x + \hat{\sigma}_i^y \hat{\sigma}_{i+1}^y, \tag{6.45}$$

$$\hat{L}_i = \sqrt{\kappa}(\hat{\sigma}_i^- + \hat{\sigma}_{i+1}^-). \tag{6.46}$$

We note that the 1D subradiant models studied in Refs. [209, 210, 211, 212, 213, 214, 215, 216], describing ordered arrays of emitters, are derived from a microscopic light-matter interaction, and yield long-range Hamiltonian and dissipative interactions. In contrast, all our

interactions are nearest-neighbor. There are nonetheless qualitatively many similar features between our models. All models exhibit a dissipative gap (slowest relaxation rate) that closes in the thermodynamic limit. In our model this gap closing scales as N^{-2} whereas the microscopically-motivated models show a stronger dependence $\propto N^{-3}$. Further, both in our model and the more microscopic models, there is a set of single-excitation subradiant modes indexed by an integer j, with the slow decay rates growing as $\Gamma_j \propto j^2$.

Our correlated decay model will have a trivial steady state solution of the vacuum, but the dynamics are greatly altered by the correlation in the dissipation. The free-fermion equivalent of this model (i.e. the spin model written in terms of JW fermions, but with all string operators dropped) has the form

$$\hat{H} = -J \sum_{i=1}^{N-1} \hat{c}_i^\dagger \hat{c}_{i+1} + \text{H. c.}, \tag{6.47}$$

$$\hat{L}_i = \sqrt{\kappa}(\hat{c}_i - \hat{c}_{i+1}). \tag{6.48}$$

$\hat{H}_{\text{eff}}$ (which is the same for both models) is diagonalized using momentum modes, resulting in:

$$\hat{H}_{\text{eff}} = 2\sum_k (J\cos(k) - i\kappa \sin^2(k/2))\hat{c}_k^\dagger \hat{c}_k. \tag{6.49}$$

Hence, in the thermodynamic $N \to \infty$ limit, there is a specific momentum mode $k = 0$ that never decays. At the single excitation level, this "subradiant state" persists forever with periodic boundary conditions, and for times quadratic in the system size for open boundary conditions. This also leads to anomalous (non-exponential) scaling of local observables in time, due to the fact that the dissipative gap closes at $k = 0$ (i.e., this momentum mode is undamped).

For concreteness, we imagine starting from the completely-filled state (all qubits in their

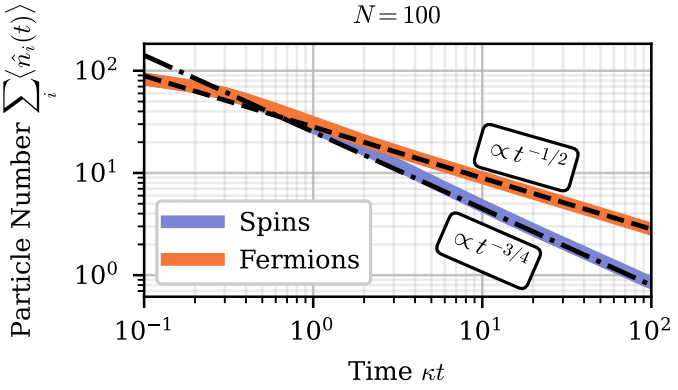

Figure 6.3: Comparison of the subradiant master equation for spins [c.f. Eqs. (6.45) and (6.46)] and fermions [c.f. Eqs. (6.47) and (6.48)] with $J = \kappa = 1$. The free fermion line is given by the analytical expression in Eq. (6.50) and asymptotically scales as $t^{-1/2}$ (dashed black line). The spins are found using the stochastic averaging technique in the Schrödinger picture and represents an average of 10,000 trajectories of $N = 100$ spins. The local spin number density numerically fits a different power law scaling of $t^{-3/4}$ (dash-dot black line).

excited state), and ask how the total number of excitations $n(t)$ relaxes. For the case of free fermions, there is no scattering between different momentum modes, and so the total density in the thermodynamic limit scales as (see Section E.8):

$$\langle \hat{n} \rangle(t) = \int_{-\pi}^{\pi} \frac{\mathrm{d}k}{2\pi} e^{-2\kappa t \sin^2(k/2)} = e^{-2\kappa t} I_0(2\kappa t), \tag{6.50}$$

where I_0 is the modified Bessel function. Asymptotically, this gives a scaling law of the form $\langle \hat{n} \rangle(t)|_{t\to\infty} \sim (4\pi\kappa t)^{-1/2}$, see Section E.8 for details. The slow power-law decay directly follows from fact that long wavelength modes with wavevectors k close to $k = 0$ have very slow decay rates $\propto k^2$. Not surprisingly, this result has no dependence on the strength of the exchange coupling J.

Turning now to the spin model (which corresponds to fermions with string operators in the dissipators), the dynamics will in general be more complicated. One might expect that the above scaling will be modified by the effective interactions encoded by the strings,

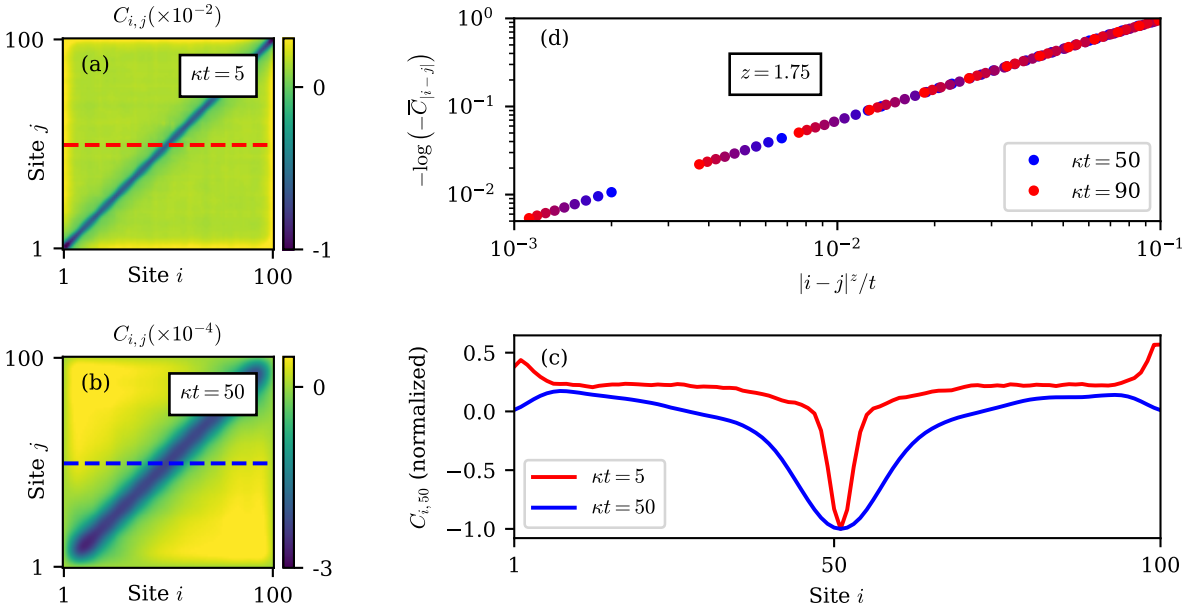

Figure 6.4: (a) and (b) show the connected density-density correlation functions $C_{i,j}$ as defined in Eq. (6.51) for the subradiant spin model. The spins are initialized in the all up state, and then the correlation pattern is shown after $\kappa t = 5$ (a) or $\kappa t = 50$ (b). Note the correlations are primarily local, with some boundary effects clearly visible at $\kappa t = 50$. (c) shows the line cuts from (a) and (b) though $i = 50$ in the center of the chain. Each curved is normalized independently such that $C_{50,50} = -1$. As time progresses, the size of the exchange-correlation hole is growing, which can be seen comparing the two line-cuts. (d) shows the logarithm of the windowed averaged correlation function $-\log\left(\overline{C}_{|i-j|}\right)$ [c.f. Eq. (6.53)], plotted for $50 \leq \kappa t \leq 90$ in steps of $\kappa t = 5$. For free fermions, this is simply $|i-j|^2/(2t)$ [see Section E.8], giving a dynamical exponent $z = 2$. We observe scaling collapse for the spins with $z = 1.75$. In all plots $N = 100$ lattice sites, and $J = \kappa = 1$, and data is averaged over 10,000 trajectories.

as now spin waves (i.e. fermionic k modes) are not conserved but can undergo scattering. Similar to free fermions, a single excitation prepared in the subradiant mode will not decay (as in this case interactions play no role). As soon as one has multiple excitations, we expect strong differences. At a heuristic level, interaction-induced scattering can scatter particles from $k = 0$ into finite-k modes, providing a new decay pathway out of the subradiant state.

In Fig. 6.3 we show results for the decay of the average density for a chain of $N = 100$ spins, starting from the full excited state and for $J = \kappa$. We see that the spin model exhibits a faster decay that the free fermion model: at long times, the decay follows a power law $\langle \hat{n}(t) \rangle \propto (\kappa t)^{-3/4}$, as opposed to the $1/\sqrt{t}$ behavior of free fermions [1]. Here, we again highlight the power of our technique: because there is only loss in the system, the Lindbladian for the free fermions and the spins have an *identical spectrum* [205]. The Lindbladian spectrum alone is thus not enough to understand the different decay behavior. Because the dissipative gap closes as a function of k, the profile of the Lindbladian eigenmodes is crucial to understanding the long-time power law relaxation in the thermodynamic limit, which we are able to do using only polynomial resources.

In Section E.8, we show that by running a simulation where we add random telegraph noise to the sign of the couplings in $\hat{H}_{\text{eff}}$, we can recover the $t^{-3/4}$ power law scaling. This follows from our intuition that the string operators act as conditional gauge transformations, and by adding in random fluctuations to these gauge fields we can qualitatively understand the dynamics of the system, similarly to how adding disorder gave us a qualitative picture of the AFM-order melting in Section 6.4.1. Unlike in the previous section, though, we take the signs of the Hamiltonian couplings to fluctuate in time during the dynamics instead of just inserting static disorder. The reason for this is that, because the subradiant model is gapless, the probability for a jump to occur $\sum_i \langle \hat{L}_i^\dagger \hat{L}_i \rangle$ is not decaying exponentially, and so we cannot assume that all jumps happen roughly instantaneously. Instead, there is a

1. We note that in Ref. [219], the authors also observed a change in the power law compared to free fermions in a different collective spin model, which has purely unidirectional interactions.

non-trivial probability of a jump at any point in the dynamics, giving the telegraph process.

In order to explore this behavior, it was crucial to be able to simulate very long spin chains, in order to properly distinguish the short time dynamics from the long time dynamics. By using a chain of $N = 100$ lattice sites, we are able to show power law scaling over 2 decades during which there is greater than 1 excitation in the system (on average) [see Fig. 6.3].

We note that previous work numerically studying subradiance in 1D spin chains did not observe that there was any change in the power law scaling of the mean excitation density with time: Ref. [211] observed that mean particle number for a subradiant spin model decayed in time as $t^{-1/2}$ like the free fermions, whereas we observe $t^{-3/4}$. One possible explanation for this discrepancy is that the model studied in Ref. [211] was different than the particular subradiant model we study here, being significantly more collective in both the dissipation and the Hamiltonian interactions. Alternatively, it is also possible that they would also have seen a change in the power-law scaling of the mean density if they had been able to simulate larger system sizes, as we study here, which is closer to the thermodynamic limit. It remains an open question how generic the observed power-law scaling is in other subradiant spin models.

In addition to just having access to the covariance matrix, we also have access to higher weight correlation functions. In previous studies of subradiance, the approximate "fermionization" of the dynamics has been explored by studying the connected density-density correlation function

$$C_{i,j} = \langle \hat{n}_i \hat{n}_j \rangle - \langle \hat{n}_i \rangle \langle \hat{n}_j \rangle, \tag{6.51}$$

where $\hat{n}_i = (\hat{\sigma}_i^z + 1)/2$ is the fermion number density. These density-density correlations were previously discussed in Ref. [211], where they saw the presence of exclusion-like correlation patterns one would expect from a free-fermion state. However, whereas they could look qualitatively at the correlation pattern and see fermion-like behavior, we have a large enough

system and long enough times to extract more quantitative data. This correlator can be calculated extremely easily in terms of our fermionized dynamics, because $\hat{\sigma}_i^z$ is quadratic, and comes with no JW string.

For a system of purely free fermions (neglecting all string operators) the time dynamics of the connected correlation can be calculated explicitly in the long time limit (see Section E.8 for details):

$$\frac{C_{i,j}}{\langle \hat{n}_i \rangle \langle \hat{n}_j \rangle}(\kappa t \gg |i-j|) = -e^{-|i-j|^2/2\kappa t}. \tag{6.52}$$

Such a pattern of correlation shows a fermionic exchange correlation hole due to Pauli exclusion. Moreover, it has a time dependent length scale $l \sim (\kappa t)^{1/2}$, or in other words there is a dynamical exponent $z = 2$ for the size of the hole, signaling a diffusive process. This can be understood intuitively in the momentum-space picture by noting that in the long time limit, the state is roughly a Gaussian centered around $k = 0$, with a variance in the wavevector scaling like $t^{-1/2}$. Inverting this RMS wavevector in turn gives a length scale, which exactly sets the spatial size of the exchange correlation hole. This would mean that we expect the length scale might go as $l \sim 1/\langle \hat{n} \rangle$ more generally.

We can now ask what happens in the case of the spin system, which is shown in Fig. 6.4. In Fig. 6.4(a) and (b) we see a strong correlation-exchange hole appearing at both $\kappa t = 5$ and $\kappa t = 50$, showing the Fermi-like behavior of the 1D subradiant spin chain. Moreover, looking at the line cuts in Fig. 6.4(c) we can see that the hole is growing in time, as was expected from the free-fermion system. To be more quantitative on how the exchange correlation hole is growing, let's define the following averaged quantity:

$$\overline{C_d} = \sum_{\substack{s \le i,j \le N-s \\ |i-j|=d}} \frac{C_{i,j}}{\langle \hat{n}_i \rangle \langle \hat{n}_j \rangle}. \tag{6.53}$$

I.e., we average over a fixed separation $|i-j|=d$, but stay at least s lattice sites away from the edges to mitigate the boundary effects. For the free fermions in the bulk, this should just be $\overline{C}_d^{\text{free}} \sim -\exp(-d^2/2\kappa t)$. In Fig. 6.4(d) we plot the logarithm of this quantity for a system with $N = 100$ lattice sites and $s = 20$ lattice sites, and find a scaling collapse with with a superdiffusive dynamical exponent $z = 1.75$, which is different from the free fermion dynamical exponent. Moreover, if we used the naive free fermion picture that the length scale $l \sim 1/\langle\hat{n}\rangle$, this would imply the length scale should be $l \sim t^{3/4}$, which in turn would imply $z = 4/3 \neq 1.75$ which is incorrect. The role the interactions coming from the strings play is incredibly non-trivial, and affects the dynamical behavior of the exchange-correlation hole. This again stresses the fact that just because the entire spectrum is known, it is still not enough to understand the dynamical phenomenon of the model.

We note that in Ref. [220], they study a class of dissipative free-fermion models that exhibit a tunable dynamical exponent. However none of them are given by 1.75.

6.4.3 Open Ising Model

A final system we can consider is an open Ising model with transverse field:

$$\hat{H} = \sum_i J\hat{\sigma}_i^x\hat{\sigma}_{i+1}^x + h\hat{\sigma}_i^z, \tag{6.54}$$

$$\hat{L}_i = \sqrt{\kappa}\hat{\sigma}_i^-. \tag{6.55}$$

This model is distinct from the previous two as it has a non-trivial steady state solution. Moreover, if we consider the analogous free fermion model (where we drop the string opera-

tors in the jumps):

$$\hat{H} = \sum_i J(\hat{c}_i + \hat{c}_i^\dagger)(\hat{c}_{i+1} - \hat{c}_{i+1}^\dagger) + 2h\hat{c}_i^\dagger \hat{c}_i, \tag{6.56}$$

$$\hat{L}_i = \sqrt{\kappa}\hat{c}_i, \tag{6.57}$$

then these two master equations will have different steady state solutions. Hence, we can compare directly the impact of the strings on the steady state as opposed to dynamics, as we have done previously.

In order to access steady state quantities using our simulation technique, we initialize the state to an arbitrary Gaussian state (for instance, the vacuum), and then perform time evolution until observables of interest saturate and stop changing in time.

In previous attempts to study the dissipative Ising model, one technique that has been used is a so-called "Generalized Gibbs Ensemble" (GGE) Ansatz [221, 222, 223], where it is assumed that the state remains diagonal in the energy eigenbasis of the closed system eigenmodes. A related, less restrictive approximation, is to just make the approximation that the density matrix is Gaussian, and therefore one can use Wick's theorem. As discussed in Section 6.3.4, this actually is equivalent to assuming that the higher moments of the distribution function are all trivial. Such an approximation is well justified in the limit where the dissipation is vanishingly weak [224, 223]. We also find numerically that it tends to do well when the fixed point is Gaussian, like the previous two examples. However, for this model, when all parameters $J, h, \kappa = \mathcal{O}(1)$, this approximation will qualitatively fail. This can be seen in Fig. 6.5, where we initialize a completely spin polarized state, and then observe the time dynamics of the average local excitation density, the average nearest neighbor Ising correlation, and the energy density. Interestingly, the mean field theory and the free fermions tend to be quite close together, whereas the spins have a significantly greater value of the nearest neighbor correlation function, and also a significantly smaller

average energy density. In fact, if one were to associate the steady state energy density with a temperature, the free fermions and the mean field solution would both have an effective negative temperature, where as the spins relax to a steady state with a positive temperature (energy density smaller than the infinite temperature state). This lower temperature is due almost exclusively to a significantly greater average anti-ferromagnetic correlation than the free fermion solution. If we define the AFM correlation as

$$\overline{X_i X_{i+1}} = \frac{1}{N-1} \sum_{i=1}^{N-1} \langle \hat{\sigma}_i^x \hat{\sigma}_{i+1}^x \rangle, \tag{6.58}$$

then for the spins, this value is roughly 5 times greater than for the free fermions in the steady state, see Fig. 6.5. The stronger correlations can be understood from the mean field phase diagram (see Section E.9 for more details), which predicts a second order phase transition in the AFM correlation at the parameters we have chosen. Hence, the mean-field value of the correlation would be nearly zero, which is what is seen from the second cumulant expansion as well as the free fermions in Fig. 6.5. However, as was predicted for much smaller system sizes in Ref. [225], the actual spin system doesn't have a sharp transition from ferromagnet to paramagnet, but instead a slow roll off of the nearest neighbor correlations, which is why the actual spin system still has a large amount of correlation.

We also note that the fact that the mean field is qualitatively unable to predict expectation values in this model highlights the power of our numerically exact technique. We believe that the reason mean-field fails in this case is because the steady state of the system can be extremely non-Gaussian. Essentially, we can imagine that the different individual trajectories are able to diffuse out over the space of all Gaussian states. This is in contrast to the previous two models studied, where the steady state was Gaussian. Hence, because the dynamics are forced to begin and end in a Gaussian state, they never "spread out" very much in the Gaussian state space, which is why the second cumulant expansion is fairly successful in capturing qualitatively some of the dynamics, as is shown in Section E.8.

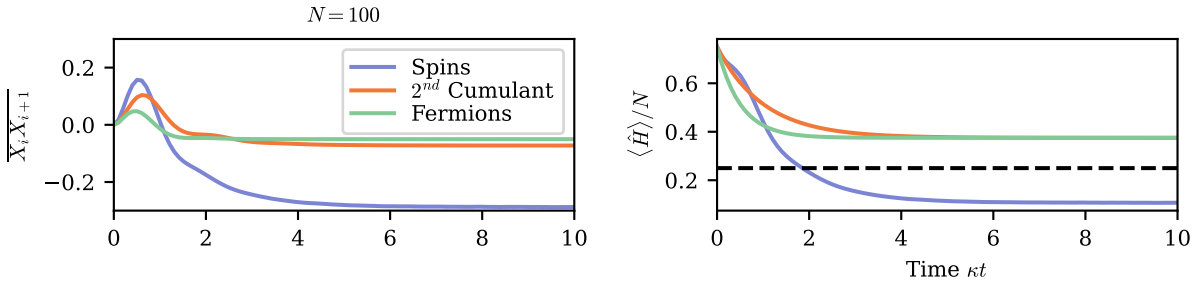

Figure 6.5: Here, we compare the dynamics of the mean value of the XX interaction $\overline{X_i X_{i+1}}$ is defined in Eq. (6.58) and the average energy is $\langle \hat{H} \rangle / N = J \langle \hat{C} \rangle + \Delta \langle \hat{n} \rangle$. We can observe that for all these operators the actual dynamics (blue) differs qualitatively from both the 2nd cumulant expansion (orange) as well as the free fermions (green). The black dashed line corresponds to the infinite temperature energy density $h/2$. Here, we have taken $J = \kappa = 1$, $h = 0.5$ with $N = 100$ lattice sites and for the spins we average of 10,000 trajectories.

In addition to this, the full numerical technique has access to more information than just the quantum steady state, if one takes the unraveling as being physically motivated as opposed to simply a computational tool. For example, if instead of the loss being the result of some simple relaxation process of the spins into the environment, we instead imagine that each spin is being continuously monitored to see whether or not it has decayed, then each trajectory corresponds to an individual measurement record [126, 94, 130]. If we now try and ask questions about observables which are not linear in the density matrix, we will get different answers if we look at observables of the averaged state vs averaging over the observable on each trajectory.

One such example is the entanglement entropy. The density matrix after averaging over trajectories will generically be a mixed state, and so to discuss entanglement entropy requires looking at mixed state entanglement monotones [226]. However, each stochastic trajectory remains pure, and so we can meaningfully discuss the entanglement entropy of a given trajectory using more standard means, for example, the Renyi entropies. Of course, before we do so, it is important to ask exactly what we wish to take the entanglement entropy of: we are trying to understand a spin state, but we have used a highly non-local transformation

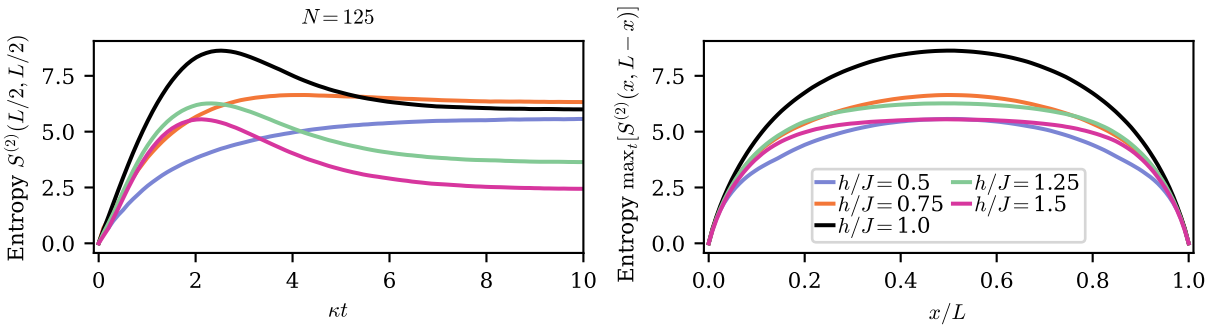

Figure 6.6: We look at the entanglement entropy on a trajectory level for the open Ising model with $J/\kappa = 10$ and variable h/J. We take $N = 125$ lattice sites, and average over 1,000 trajectories, and also quench from an initial product state of all spins down. In the upper plot, we study the bipartite entanglement entropy as a function of time, where when h/J is below the transition, it appears the entanglement is monotonic in time, but it peaks at some early time near the phase transition. In the lower plot, we show Page curves where for each bipartition we look at where the entanglement is maximal as a function of time.

to map it into fermions in order to understand it. *A priori*, the entanglement entropy of the Gaussian fermion state has no relation to the underlying spin model, since the JW is not local. However, as we show in Section E.10, if we take "good" bipartitions, the entanglement entropy is actually the same. Here, a good bipartition is one where $A = \{i | 1 \leq i \leq m\}$ and $B = \{i | m < i \leq N\}$ for some chain of length of N, where the ordering is defined by the Jordan-Wigner transformation.

Given this, we can ask how the average bipartite entanglement entropy of each trajectory changes as we tune through the closed system phase transition, and see whether or not the open system is still sensitive to the closed system critical point. This is shown in Fig. 6.6, where we plot the Renyi-2 entropy for varying values of h/J. It appears that when $h/J \lesssim 1$, the entanglement grows monotonically in time before saturating to a steady state value, whereas when $h/J \gtrsim 1$ the entanglement peaks at early times. Moreover, if we look at what the maximal amount of entanglement achieved over all times, the most entanglement seems to be near the closed system phase transition $h/J \sim 1$, and for the system sizes probed the entanglement at this point does not appear to obey an area law.

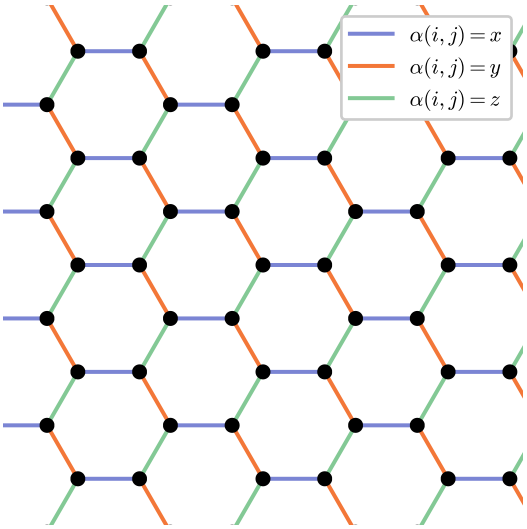

Figure 6.7: Kitaev Honeycomb model as described in Eq. (6.59)

6.4.4 2D Model

We have so far exclusively focused on spin chains in a single spatial dimension, as they generically can be transformed into free fermions using the JW transformation. However, there are certain 2D spin models that also have a representation in terms of free fermions, and can thus be extended to open models amenable to our unraveling technique. As an example, consider the Kitaev Honeycomb [198], a 2D spin model on a hexagonal lattice defined by the Hamiltonian

$$\hat{H} = \sum_{\langle i,j \rangle} J_{\alpha(i,j)} \hat{\sigma}_i^{\alpha(i,j)} \hat{\sigma}_j^{\alpha(i,j)}, \tag{6.59}$$

where $\langle i,j \rangle$ is a sum over nearest neighbors, and $\alpha(i,j) \in \{x,y,z\}$ depending on the orientation of the bond (see Fig. 6.7).

This model can be solved by defining on each lattice site 4 Majorana fermions $\hat{c}, \hat{\gamma}^\alpha$

(comprising 2 degrees of freedom per lattice site) by

$$\hat{\sigma}_i^\alpha = i\hat{c}_i\hat{\gamma}_i^\alpha. \tag{6.60}$$

There is an extra degree of freedom per lattice site, which is fixed by defining the condition:

$$\hat{\sigma}^x\hat{\sigma}^y\hat{\sigma}^z = i \implies \hat{c}\hat{\gamma}^x\hat{\gamma}^y\hat{\gamma}^z = 1. \tag{6.61}$$

Now, we can rewrite the Hamiltonian in the form:

$$\hat{H} = \sum_{\langle i,j\rangle} iJ_{\alpha(i,j)} \left(i\hat{\gamma}_i^{\alpha(i,j)}\hat{\gamma}_j^{\alpha(i,j)}\right)\hat{c}_i\hat{c}_j. \tag{6.62}$$

For the moment, this does not look significantly better than it was before: we have a 4-point fermion interaction, which cannot be generically solved. However, if we define the gauge field $\hat{A}_{ij}$ via

$$\hat{A}_{ij} = i\hat{\gamma}_i^{\alpha(i,j)}\hat{\gamma}_j^{\alpha(i,j)}, \tag{6.63}$$

then it is not difficult to check that $[\hat{A}_{ij}, \hat{A}_{kl}] = 0$ for all sets of nearest neighbors $\langle i,j\rangle$ and $\langle k,l\rangle$. Further, these operators all commute with the Hamiltonian. Thus, we can take $\hat{A}_{i,j} \to A_{ij} = \pm 1$ to be a static background field and write down an effective quadratic theory for the $\hat{c}$ operators via

$$\hat{H} = \sum_{\langle i,j\rangle} iJ_{\alpha(i,j)}A_{ij}\hat{c}_i\hat{c}_j. \tag{6.64}$$

Hence, if the system is initialized as a Gaussian state in terms of the $\hat{c}$ operators, then time evolution under this Hamiltonian will keep it Gaussian at all later times, making it efficiently simulable.

Now, we can consider adding dissipative terms that are local in terms of spin operators that preserve the simulability of the system. For each bond of our lattice, we define the generalized correlated dephasing operators:

$$\hat{L}_{ij} = l_{ij}^1 \hat{\sigma}_i^{\alpha(i,j)} + l_{ij}^2 \hat{\sigma}_j^{\alpha(i,j)}, \tag{6.65}$$

where the constants $l_{ij}^{1,2}$ can be complex. If these constants are all real, then this corresponds to a classically stochastic Hamiltonian with local fields driven by white noise. Further, the local fields do not commute with the gauge operators, so this stochastic Hamiltonian would not be solvable with free fermions. Static local fields have previously been studied perturbatively [198], as they open a gap in the portion of the phase diagram with non-Abelian anyons. However, we show now that the techniques in the main text apply to this model.

First note that

$$\hat{L}_{ij}^\dagger \hat{L}_{ij} = |l_{ij}^1|^2 + |l_{ij}^2|^2 + 2\mathrm{Re}\left(l_{ij}^1 (l_{ij}^2)^*\right) \hat{\sigma}_i^{\alpha(i,j)} \hat{\sigma}_j^{\alpha(i,j)}, \tag{6.66}$$

$$\begin{aligned} \implies \hat{H}_{\text{eff}} &= \hat{H} - \frac{i}{2} \sum_{\langle i,j \rangle} \hat{L}_{ij}^\dagger \hat{L}_{ij} \\ &= \sum_{\langle i,j \rangle} \left[J_{\alpha(i,j)} - i\mathrm{Re}\left(l_{ij}^1 (l_{ij}^2)^*\right) \right] \hat{\sigma}_i^{\alpha(i,j)} \hat{\sigma}_j^{\alpha(i,j)} \\ &\equiv \sum_{\langle i,j \rangle} i \tilde{J}_{\alpha(i,j)} A_{ij} \hat{c}_i \hat{c}_j, \end{aligned} \tag{6.67}$$

and so the effective Hamiltonian remains quadratic with new, complex coupling constants $\tilde{J}_{\alpha(i,j)} = J_{\alpha(i,j)} - i\mathrm{Re}\left(l_{ij}^1 (l_{ij}^2)^*\right)$. A non-Hermitian Hamiltonian of this form was also studied in Ref. [227]. However, they study *only* the non-Hermitian Hamiltonian and completely ignore the quantum jumps. We stress that the no-jump evolution described by $\hat{H}_{\text{eff}}$ is only relevant to the experimentally-daunting situation where each bond is continuously monitored, and one post-selects on no-jump events. It is not relevant to our (more general)

situation of interest where dissipative effects arise from couplings to unmonitored environments. Moreover, $\hat{H}_{\text{eff}}$ is trivially solvable as it is completely equivalent to free fermions; the full Lindbladian including the jumps cannot be mapped onto free fermions, which is what we are interested in studying. To do this, the next question to ask is whether or not the system remains Gaussian under a quantum jump. To address this, we write our jump operators using the previously-introduced Majorana representation:

$$\hat{L}_{ij} = il^1_{ij}\hat{c}_i\hat{\gamma}_i^{\alpha(i,j)} + il^2_{ij}\hat{c}_j\hat{\gamma}_j^{\alpha(i,j)}. \tag{6.68}$$

Naively, it appears that dissipation generated by such jump operators will not preserve Gaussianity, as they are a linear combination of two quadratic operators.

The crucial observation will be that each $\hat{\gamma}_i^{\alpha(i,j)}, \hat{\gamma}_j^{\alpha(i,j)}$ anti-commutes with the local gauge field:

$$\{\hat{\gamma}_i^{\alpha(i,j)}, \hat{A}_{ij}\} = \{\hat{\gamma}_j^{\alpha(i,j)}, \hat{A}_{ij}\} = 0. \tag{6.69}$$

Hence, when we consider an unraveling, we can think of the action of $\hat{\gamma}_i^{\alpha(i,j)}, \hat{\gamma}_i^{\alpha(i,j)}$ as simply locally flipping the sign of the gauge field, sending the *classical variable* $A_{ij} \to -A_{ij}$. To see this more clearly, note that for each bond we can define a Dirac fermion $\hat{a}_{ij}$:

$$\hat{a}_{ij} = \frac{1}{2}\left(\hat{\gamma}_i^{\alpha(i,j)} + i\hat{\gamma}_j^{\alpha(i,j)}\right). \tag{6.70}$$

We can then explicitly write down the wavefunction for the two different values of the local gauge field as

$$|A_{ij} = -1\rangle = |0\rangle, \quad |A_{ij} = 1\rangle = \hat{a}^\dagger_{ij}|0\rangle, \tag{6.71}$$

where $|0\rangle$ is defined as the Dirac fermion vacuum such that $\hat{a}_{ij}|0\rangle = 0$. Using this explicit

basis, we can then compute that

$$\hat{\gamma}_i^{\alpha(i,j)}|A_{ij}=-1\rangle = -i\hat{\gamma}_j^{\alpha(i,j)}|A_{ij}=-1\rangle = |A_{ij}=1\rangle, \tag{6.72}$$

$$\hat{\gamma}_i^{\alpha(i,j)}|A_{ij}=1\rangle = i\hat{\gamma}_j^{\alpha(i,j)}|A_{ij}=1\rangle = |A_{ij}=-1\rangle. \tag{6.73}$$

And so (up to a phase) both $\hat{\gamma}_i^{\alpha(i,j)}$ and $\hat{\gamma}_i^{\alpha(i,j)}$ simply flip $\hat{A}_{ij}$ from one eigenstate to the other eigenstate.

Thus, the action of the jump operator on the state can be understood as moving the state to a different gauge sector. Hence, we can *classically* keep track of the binary variables A_{ij}, as the operators $\hat{A}_{ij}$ will always have a definite value. Every time there is a quantum jump, we first must update the classical bit value for A_{ij}, and then we compute the action of the following effective jump operator:

$$\hat{L}'_{ij} = il^1_{ij}\hat{c}_i - (-1)^{(A_{ij}+1)/2} l^2_{ij}\hat{c}_j, \tag{6.74}$$

which are linear and therefore preserve Gaussianity. The sign $(-1)^{(A_{ij}+1)/2}$ encapsulates the relative phase accumulated in Eqs. (6.72) and (6.73) where A_{ij} is evaluated pre-jump. Thus, we can imagine that the jump operators are exactly (up to possibly a relative phase) their free-fermion counter parts, along with the fact that every time we do a jump, we update the gauge fields (which also change the Hamiltonian). This is in exact analogy to the 1D case, where we interpret the JW strings as updating the local gauge field at the site of the jump.

6.5 Generalizations

6.5.1 Fermions

The stochastic numerical technique introduced in Section 6.3 was formulated in order to try and study spin systems that had been Jordan-Wigner transformed into fermions with JW

strings. However, there is no reason that it could not be applied directly to a fermionic model that doesn't arise from a spin problem originally (see Refs. [228, 229, 230] for examples of fermionic master equations where the fact that trajectories remain Gaussian was exploited for simulation). Instead of thinking about string operators, we can instead consider any jump operator of the form of a unitary $\hat{U}$ multiplied by a Majorana-linear:

$$\hat{L}_i = \hat{U}_i \sum_j l_{ij} \hat{\gamma}_j. \tag{6.75}$$

In this case, we have that $\hat{L}_i^\dagger \hat{L}_i = \sum_{jk} l_{ij}^* l_{ik} \hat{\gamma}_j \hat{\gamma}_k$ is quadratic, and therefore $\hat{H}_{\text{eff}}$ will still be quadratic in the Majorana operators.

The only other requirement is that the unitary operator $\hat{U}_i$ is Gaussian - i.e., it maps quadratic operators to quadratic operators. In the case of the OTOC picture, this means that one can push the unitary onto $\hat{H}_{\text{eff}}(t)$ that is updated after every jump, and it will remain quadratic. Further, we can also use the state update picture because then the full jump operator remains Gaussian.

If $\hat{U}_i$ does not preserve Gaussianity, then obviously the state-update picture is not valid, because the state doesn't remain Gaussian over each trajectory. One might be tempted to think that we could instead use the OTOC picture, where now we just have to calculate a much longer OTOC by leaving the unitaries in the expectation value instead of gauging them into $\hat{H}_{\text{eff}}$. However, unless the unitaries can be written as a single Majorana string (in which case they would be Gaussian anyways), each expectation value for a given observable would require calculating a number of Pfaffians that grows exponentially in the number of jumps, and the number of jumps will be extensize in the system size. Therefore, this reverts us to non-polynomial scaling, and cannot be done.

Thus, the most general type of jump operator that can be simulated efficiently is one where $\hat{U}_i$ is Gaussian. It is interesting to note that Gaussianity is a gauge dependent choice:

an arbitrary unitary rotation the jump operators $\hat{L}_i \to \sum_j V_{ij}\hat{L}_j$ (with V a unitary matrix) *does not* affect the unconditional dynamics of the master equation, but it can affect the individual trajectories. For this reason, although the specific unraveling of a master equation is non-unique, there can still be an "incorrect choice": a linear combination of Gaussian unitaries need not be a Gaussian unitary. In the spin examples, this can be seen from the fact that taking arbitrary linear combinations of 2-local jump operators need not be 2-local anymore.

6.5.2 Bosons

Let's define the set of bosonic operators $\hat{a}_i$ that obey the canonical commutation relations $[\hat{a}_i, \hat{a}_j^\dagger] = \delta_{ij}$ and $[\hat{a}_i, \hat{a}_j] = [\hat{a}_i^\dagger, \hat{a}_j^\dagger] = 0$. We can similarly consider systems where the jump operator can be written as, for example, $\hat{L}_i = \hat{U}_i\hat{a}_i$, such that $\hat{H}_{\text{eff}}$ is a quadratic operator and therefore efficiently simulable. In some sense, though, this is a fundamentally different question from the fermions, because linear bosonic operators *do not* preserve Gaussianity.

Therefore, in order to try and simulate this, it would require working in the OTOC picture. However, we are then left with the problem that, for a Gaussian bosonic state, computing a high-weight observable is equivalent to computing a *hafnian*, and not a *pfaffian* as it is for fermions. While the Pfaffian can be computed efficiently in polynomial time, the Hafnian is #P-complete, and classically intractable - this underlies the complexity of Gaussian Boson Sampling [231]. Hence, this problem remains intractable.

Thus, the only problem we could actually simulate for bosons is the case where $\hat{L}_i = \hat{U}_i$ is a unitary operator that preserves the Gaussianity in the state. This, though, is equivalent to stochastically applying a Gaussian unitary channel, which is trivially solvable, as the equations of motion for 2-point correlation functions close on themselves.

6.6 Discussion

We have introduced a new simulation technique for open quantum systems, with special application to spin chains. Our technique leverages the fact that many models which are interacting at the level of the master equation can be made non-interacting after performing a stochastic unraveling. We show that initially Gaussian states time evolve into states which are non-Gaussian, but can be written as a positive probability distribution over the Gaussian states, which can then be classically sampled from efficiently. This technique opens new avenues in exploring open quantum systems that is not constrained to be either Gaussian or having low-entanglement. Our technique allows access to arbitrary system observables without affecting complexity, even non-local and non-linear ones such as the entanglement entropy.

We have given three concrete examples of 1D spin chains that can now be studied efficiently for large system sizes. First, we observed AFM order parameter melting in an XX chain with local loss, where we saw that the string operators generate effective noise on the Hamiltonian bonds. Next, we studied subradiance in a 1D spin chain with nearest neighbor correlated loss. We observed that, despite not changing the actual spectrum, the effective scattering interactions generated by the string operators can cause faster power-law relaxation to the vacuum than in the case of free fermions. This can be understood by noting that the population in the slowest relaxing modes is no longer conserved, and can be scattered into more quickly relaxing ones. Finally, we have looked at the 1D Ising model with transverse field and single particle loss in the direction of the transverse field. This model has a non-trivial steady state solution which is itself non-Gaussian, and distinct from the steady state one would find if ignoring the string operators. We find that our technique is able to make quantitative predictions about both dynamics as well as the non-Gaussian steady state of this system in regimes where simple approximations (e.g., GGE) fail qualitatively.

We believe that in addition to the simple models outlined above, our technique paves

the way to further understanding open 1D spin chains. Our technique not only allows one to numerically probe relevant models, but it also gives insights and intuition as to the effect that string operators can have on the dynamics and steady state of the master equation.

Finally, the technique is not fundamentally limited to only one dimensional systems; as noted this also allows the simulation of the Kitaev honeycomb in 2D. In particular, the technique seems well suited to any free $\mathbb{Z}_2$ gauge theory in arbitrary dimensions, and exploring other higher dimensional models could prove fruitful. Another interesting future direction would be to utilize the non-uniqueness of stochastic unravelings, to see if there are alternative unravelings that are either more optimal numerically [232], or provide different physical insights into the dynamics.

CHAPTER 7

INSIGHTS INTO DECOHERED CRITICALITY

This chapter contains material that can be found on the arXiv preprint server in Ref. [233].

7.1 Introduction

State-of-the-art quantum simulators [234, 235, 236, 237, 238, 239] and quantum processors [240, 241, 242, 243, 244] have made rapid progress in their ability to prepare complex quantum states. This include states with topological order and long-range entanglement [234, 235, 241, 236, 238, 244], and scale-invariant quantum critical states which appear at quantum phase transitions [240, 242, 243, 237, 239]. Unavoidable noise and dissipation imply that the dynamics of these systems is necessarily non-unitary, motivating a host of new fundamental questions concerning how novel quantum states behave in out-of-equilibrium settings, and the basic nature of mixed state phases of matter [245, 246, 247, 248, 249, 250]. Recent works have studied the robustness of topologically ordered states to noise [251, 252, 250, 249, 253, 254], as well as the effect of non-unitary dynamics on critical ground states [255, 256, 257, 258, 259, 260, 261]. While these works reveal a host of interesting physics, they have primarily studied quantities that are well-suited to theoretical techniques like CFT, but that are extremely challenging for experiments. These include quantities nonlinear in the system density matrix (which require multiple copies of the system to measure) [257], and quantities post-selected on measurement outcomes [256, 258, 259] (which generally incur an exponential sampling overhead). It would be extremely interesting to study how non-unitary evolution of non-trivial topological or critical states impacts simple observable quantities, and what insights these provide into the nature of the resulting non-equilibrium state.

In this work, we address these questions through a detailed study of the critical ground state of the 1D transverse-field Ising model (TFIM) subject to local, Markovian Pauli noise.

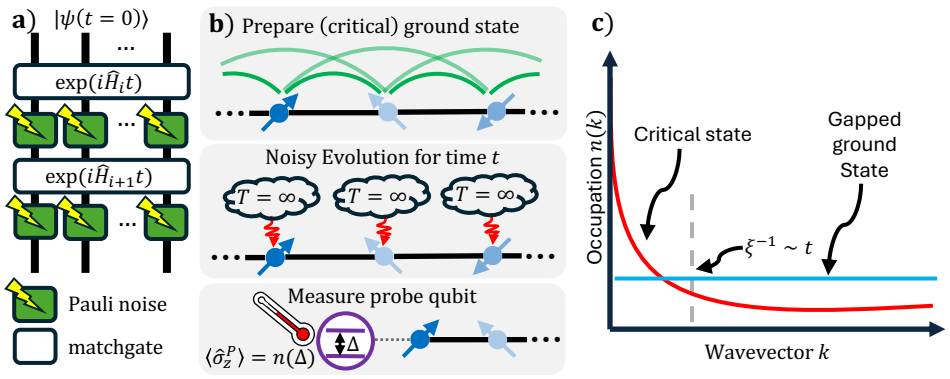

Figure 7.1: a) Schematic of a matchgate circuit with Pauli noise. Despite non-trivial fermionic strings, such circuits can be efficiently simulated using our technique. b) Experimental protocol where one first prepares a critical ground state, then decoheres the state under noisy evolution, then finally uses a probe qubit with tunable splitting Δ to measure the frequency-dependent effective temperature. c) Example quasiparticle excitation density as a function of wavevector for either a decohered critical ground state (red) or gapped ground state (blue). The critical state roughly follows a Fermi-Dirac distribution up to a length scale ξ^{-1} which grows linearly with the total time of the decoherence process as depicted in b).

Our focus is on unconditional evolution (no post-selection), and on standard observables that are linear in the density matrix. One might immediately fear that in this setting, nothing interesting can happen, as it is well-known that local noise channels cannot change critical properties: spin correlation functions must decay with the same power law as they did without the application of dissipation. Surprisingly, we show that this is not the full story. While spin correlators have an unchanged algebraic decay, we show that noise causes fermionic correlators (which are also critical in the ground state) to immediately develop a length scale (i.e. they now decay exponentially). Hence, after decoherence, the spins remain critical, whereas the fermions do not.

We further show that this dichotomy has measurable consequences: it leads to a novel non-equilibrium state whose low-energy physics is described by an effective time-dependent temperature. This is surprising, as Markovian Pauli noise corresponds to an infinite-temperature, infinite-bandwidth environment; such environments typically do not lead to finite-temperature

thermal equilibrium states. The emergent temperature we find is directly tied to criticality: it does not arise if one starts with a non-critical ground state. We also show that this effective temperature can be easily probed experimentally, using a single frequency-tunable probe qubit that is weakly coupled to the chain (see Fig. 7.1). While our focus here is on the TFIM, we suspect that the basic mechanism we describe could apply to more general critical ground states exposed to decoherence, thus representing a new kind of emergent non-equilibrium state. To support this claim, we show that all of the features identified in the TFIM are also present in a critical XX chain in the zero magnetization sector.

Our results rely on a technical innovation that has implications well beyond our decohered TFIM model. The questions we are interested in are not naturally suited to the CFT techniques in, e.g., Ref. [257]; also, naive master equation simulations are not feasible, as the dynamics when written in terms of Jordan-Wigner (JW) fermions now has non-trivial strings. We circumvent these issues by using an exact solution to the dynamics of matchgate circuits [262, 263] subject to arbitrary Pauli noise, see Fig. 7.1. We build on the results presented in Chapter 6, which introduced a new stochastic averaging technique for a class of dissipative spin chain models. We show that for Pauli noise, one can obtain closed-form solutions for the time-evolution of arbitrary observables by exactly resumming the trajectories due to the classical nature of the noise. We note that aspects of this were previously observed in Ref. [264]; however, we are able to give a more intuitive understanding of the underlying physical mechanisms. Moreover, we are able to get exact solutions for observables in systems with periodic boundary conditions where the Hamiltonian is formally interacting. This technique allows one to go beyond the standard setting of decohered topological or critical states, and consider situations where both the decoherence and Hamiltonian evolution are simultaneously acting on the system.

The remainder of this Chapter is organized as follows: In Section 7.2, we present our derivation for the exact solution for matchgate circuits with Pauli noise. In Section 7.3,

we introduce the specific model we will consider, namely an Ising model with decoherence in the X and Y directions. In Section 7.4, we identify the physical phenomena that result from applying the decoherence channel to the Ising critical state when there are no coherent dynamics. Further, we propose a simple experiment that would be able to observe the effects. In Section 7.5.0, we compare the results found in Section 7.4 to the case where the initial condition is shifted away from the Ising critical point (but still with no coherent dynamics). In Section 7.6, we explain how to compute the exact solution for the dynamics in the presence of a Hamiltonian with periodic boundary conditions, and use this to show data when there are both coherent and incoherent dynamics. In Section 7.7, we compare our results with other common noise channels. Finally, in Section 7.8.0, we compare the results from the decohered critical TFIM to a decohered critical XX model.

7.2 Exact Solution for matchgate Circuits with Pauli Noise

We begin by showing that, for any matchgate circuit with Pauli noise, the evolution of observables can be computed exactly and efficiently. This was first shown in Ref. [264]; here, we present an alternative proof. To fix terminology, we will define a unitary matchgate circuit as a circuit where every unitary operator can be understood as the free evolution of a collection of fermionic modes [262, 263]. In other words, there exists a mapping from qubits to free fermions such that every unitary maps Gaussian fermionic states to Gaussian fermionic states. For example, any unitary operator $\hat{U} = \exp(i\theta\hat{H})$ acting on a set of spin-1/2's generated by a Hamiltonian $\hat{H}$ of the form

$$\hat{H} = \sum_i J_i^1 \hat{\sigma}_i^+ \hat{\sigma}_{i+1}^- + J_i^2 \hat{\sigma}_i^+ \hat{\sigma}_{i+1}^+ + \Delta_i \hat{\sigma}_i^z + \text{H. c.} \tag{7.1}$$

can be written exactly as a quadratic free fermion model using a Jordan-Wigner (JW) transformation [30]. If we define a set of canonical fermion modes $\hat{c}_i$ via

$$\hat{\sigma}_i^- = \left(\prod_{j<i} (-1)^{\hat{c}_j^\dagger \hat{c}_j} \right) \hat{c}_i, \tag{7.2}$$

then we can rewrite the Hamiltonian as

$$\hat{H} = \sum_i J_i^1 \hat{c}_i^\dagger \hat{c}_{i+1} + J_i^2 \hat{c}_i^\dagger \hat{c}_{i+1}^\dagger + 2\Delta_i \hat{c}_i^\dagger \hat{c}_i + \text{H. c.} \tag{7.3}$$

We are interested in studying matchgate models subject to additional non-unitary processes that correspond to Pauli noise (including cases with higher-weight Pauli operators that describe correlated noise). Returning to a discrete time picture, this general class of problems would have evolution in each time-step (i.e. each layer) described by e.g. $\hat{\rho}(t+\delta t) = \hat{U}\mathcal{K}[\hat{\rho}]\hat{U}^\dagger$ where $\hat{U} = \exp(i\hat{H}\delta t)$ denotes the unitary matchgate evolution, and the noise channel $\mathcal{K}$ is defined by

$$\mathcal{K}[\hat{\rho}] = \sum_{s \in \{0,1\}^{2n}} p_s \hat{K}_s \hat{\rho} \hat{K}_s^\dagger, \tag{7.4}$$

$$\hat{K}_s = \prod_{i=0}^{n-1} (\hat{\sigma}_i^x)^{s_{2i}} (\hat{\sigma}_i^z)^{s_{2i+1}}, \tag{7.5}$$

where $\sum_s p_s = 1$. The choice of $\hat{U}$, $\mathcal{K}$ could of course vary from layer to layer. An example of such a circuit is depicted in Fig. 7.1. Note that Pauli noise is particularly relevant to near term experiments, as even when the physical hardware has a more complicated error model, experiments often employ Pauli twirling (or randomized compiling) so that all of the errors can be modeled as a Pauli channel [265].

At the outset, the combination of matchgate circuits and Pauli noise is no longer obviously simulable. While each ingredient can be efficiently simulated on their own, they rely on

different techniques that would seem to be incompatible. As noted, the unitary dynamics can be mapped onto free fermions because the dynamics preserve the Gaussianity of the fermionic state. However, the noise operators do not map to simple operators under JW, and moreover the noise does not preserve Gaussianity of the density matrix. Alternatively, Pauli noise preserves Cliffords, and therefore can be efficiently simulated as a Clifford circuit. However, matchgate circuits can inject an arbitrary amount of non-stabilizerness (or magic) [1], and so this immediately breaks simulability of the dynamics as a Clifford circuit.

Progress was made on this problem in Chapter 6, where it was shown that, while the state does not remain Gaussian under the noisy evolution, it can be written as a convex sum of Gaussian states [268, 269]. As a result, dynamics can be efficiently described using a stochastic equation of motion for the fermionic covariance matrix.

Here, we make further progress by noting that, when the noise is Pauli, the above stochastic equation of motion can be *exactly* re-averaged. Intuitively, the reason this is possible is because the noise is in some sense classical. Each trajectory can be thought of as a random kick model [270, 271], where at each point in time there is a probability to apply a random Pauli operator. Importantly, though, the probability of applying a "kick" is independent of the quantum state, allowing one to re-sum them.

If we define Majorana modes $\hat{\gamma}_{2m} = \hat{c}_m + \hat{c}_m^\dagger, \hat{\gamma}_{2m+1} = i(\hat{c}_m - \hat{c}_m^\dagger)$ and a covariance matrix $\Gamma_{mn} = \langle \hat{\gamma}_m \hat{\gamma}_n \rangle$, then we can show that the evolution of the covariance matrix under the noise channel $\mathcal{K}$ is given by

$$(\mathcal{K}_{\text{cov}}[\Gamma])_{mn} = f_{mn}(\vec{p})\Gamma_{mn}. \tag{7.6}$$

We have denoted $\mathcal{K}_{\text{cov}} : \mathbb{C}^{2N\times 2N} \to \mathbb{C}^{2N\times 2N}$ as the induced map between covariance

1. This is because the T-gate $\hat{T} = \exp(i\pi\hat{\sigma}^z/8)$ is in fact a matchgate, and so any amount of magic can be present in a matchgate circuit [266]. We stress that this does not mean that matchgates are universal, as they do not include the entire Clifford group. There is a different notion of "fermionic magic" which requires a pure non-Gaussian resource state to make matchgates universal [267].

matrices derived from the quantum channel $\mathcal{K}$. The constants $f_{mn} \in \mathbb{R}$ can be calculated exactly for any (Pauli) noise model. We derive this expression for arbitrary Pauli noise in Section F.1, and also show explicitly how to calculate the constants f_{mn}.

The simplicity of Eq. (7.6) reveals two surprises. The first is that the covariance matrix updates close on themselves, despite the fact that the state does not remain Gaussian. The second surprise is that not only do the moments close on themselves, but in the Majorana basis $\mathcal{K}_{\text{cov}}$ is diagonal: following an arbitrary Pauli noise channel, the two-point function $\langle \hat{\gamma}_m \hat{\gamma}_n \rangle$ depends only on its previous value and the noise strength, and not on any other correlation function. In general, this holds for all higher moments written in the Majorana basis.

To give a concrete example, the primary noise model we study is given by equal strength spatially uniform dephasing in the X and Y directions, where

$$\mathcal{K}[\hat{\rho}] = \prod_i \mathcal{K}_{i,x}[\mathcal{K}_{i,y}[\hat{\rho}]], \tag{7.7}$$

$$\mathcal{K}_{i,\alpha}[\hat{\rho}] = p\hat{\sigma}_i^\alpha \hat{\rho} \hat{\sigma}_i^\alpha + (1-p)\hat{\rho}. \tag{7.8}$$

For this particular channel, the constants f are given by (see Section F.1)

$$f_{mn}(p) = \begin{cases} (1-2p)^{2|\lfloor m/2 \rfloor - \lfloor n/2 \rfloor|} & \lfloor m/2 \rfloor \neq \lfloor n/2 \rfloor \\ (1-2p)^{2(1-\delta_{mn})} & \lfloor m/2 \rfloor = \lfloor n/2 \rfloor \end{cases}. \tag{7.9}$$

This result allows us to calculate arbitrary observables exactly for all times.

Moreover, we show that the result can be generalized to the continuous time version of the problem with a Lindblad generator as opposed to a finite noise channel. Given any Hamiltonian of the form of Eq. (7.1) and Pauli noise, we are also capable of simulating a

time continuous process described by a Lindblad master equation [76, 77]:

$$\partial_t \hat{\rho} = -i[\hat{H}, \hat{\rho}] + \sum_{s \in \{0,1\}^{2n}} \gamma_s \mathcal{D}[\hat{K}_s]\hat{\rho}, \tag{7.10}$$

where $\mathcal{D}[\hat{z}]\hat{\rho} \equiv \hat{z}\hat{\rho}\hat{z}^\dagger - \frac{1}{2}\{\hat{z}^\dagger\hat{z}, \hat{\rho}\}$, and we have reused the definition of $\hat{K}_s$ as given in Eq. (7.5).

We note that the fact that fermionic correlation functions close on themselves under matchgates with Pauli noise was previously observed in Ref. [264] via explicit calculation. However, by beginning from the stochastic trajectories and then reaveraging them, we also get an intuitive understanding for why this is the case, as well as get mroe information about the structure of the quantum state. Specifically, we know that it must be able to be written as a convex sum of Gaussians, which will prove extremely useful later when we consider periodic boundary conditions.

7.3 Transverse Field Ising Model in a Noisy Magnetic Field

The model we wish to study here is a transverse field Ising model subject to spatially uniform noise. We consider a Hamiltonian with an Ising interaction in the X direction, and a transverse field in the Z direction:

$$\hat{H} = \sum_i -J\hat{\sigma}_i^x\hat{\sigma}_{i+1}^x + g\hat{\sigma}_i^z. \tag{7.11}$$

We choose to study this system because it can be exactly solved using the techniques outlined above in Section 7.2, as well as admits a phase transition at $|g/J| = 1$, allowing us to study how critical states behave in the presence of noise exactly. Unless otherwise noted, we will work in the thermodynamic limit, in which case the Hamiltonian can be diagonalized in

terms of plane wave momentum modes (see Section F.2):

$$\hat{H} = \sum_k \epsilon_k \hat{\beta}_k^\dagger \hat{\beta}_k, \tag{7.12}$$

$$\hat{\beta}_k = \cos(\theta_k/2)\hat{d}_k + i\sin(\theta_k/2)\hat{d}_{-k}^\dagger, \tag{7.13}$$

where $\tan\theta_k = \frac{J\sin(k)}{g - J\cos(k)}$ and $\epsilon_k = 2\sqrt{J^2 + g^2 - 2gJ\cos(k)}$. Here, $\hat{d}_k$ is a fermion momentum mode with momentum k: $\hat{d}_k = \frac{1}{\sqrt{N}}\sum_j e^{ijk}\hat{c}_j$.

When $|g/J| = 1$, the spectrum becomes gapless for the long wavelength $k = 0$ mode. Moreover, the ground state at this point has long-range order, characterized by an algebraically decaying spatial correlation function. In the Majorana basis (for $m \leq n$)

$$\langle \hat{\gamma}_{2m}\hat{\gamma}_{2n+1}\rangle = \frac{2i}{\pi}\frac{1}{1-2(m-n)}, \tag{7.14}$$

$$\langle \hat{\gamma}_{2m}\hat{\gamma}_{2n}\rangle = \langle \hat{\gamma}_{2m+1}\hat{\gamma}_{2n+1}\rangle = 0. \tag{7.15}$$

We want to understand the fate of the critical properties of this model in the presence of noise. Motivated by the previous literature on decohered and measurement altered critical states [258, 259, 257], we consider the case where one first prepares the critical ground state, and then applies only the noise channel with no coherent (Hamiltonian) dynamics. We couple each spin to a local Markovian reservoir described by an equal probability of flipping the spin from up to down or down to up. This is given by the Lindblad equation

$$\mathcal{L}_{XY} = \sum_i \mathcal{D}[\hat{\sigma}_i^-] + \mathcal{D}[\hat{\sigma}_i^+] = \frac{1}{2}\sum_i \mathcal{D}[\hat{\sigma}_i^x] + \mathcal{D}[\hat{\sigma}_i^y]. \tag{7.16}$$

$$\partial_t\hat{\rho} = -i\theta[\hat{H},\hat{\rho}] + \gamma\mathcal{L}_{XY}\hat{\rho}. \tag{7.17}$$

We define the binary variable $\theta \in \{0,1\}$ which sets the coherent dynamics to be either "on" or "off"; unless otherwise specified, we consider the case where $\theta = 0$ so there is

noise-only dynamics (however, we consider $\theta = 1$ in Section 7.6). Eq. (7.16) describes a set of independent, infinite temperature, infinite bandwidth reservoirs. Equivalently, this describes driving each spin with a classically stochastic magnetic field in the X and Y directions that is identical and independent on each lattice site. Evolution under the master equation Eq. (7.17) (with $\theta = 0$) for a time t is identical to applying the noise channel defined in Eq. (7.7) with $p = (1 - e^{-\gamma t/2})/2$. We are not in principle limited to considering spatially or temporally uniform dephasing, nor did the strength of the dephasing in the X and Y directions need be equivalent, but it was chosen for simplicity and by experimental motivation.

Despite the fact that this is an interacting many body spin model, we are able to get *exact, closed form* expressions for the dynamics of *all* correlation function of the fermionic operators, see Section F.2 for more details. The equation of motion for the two-point correlation functions is given by:

$$\partial_t \langle \hat{\gamma}_{2m} \hat{\gamma}_{2n+1} \rangle = -\gamma(|m-n| + \delta_{mn}) \langle \hat{\gamma}_{2m} \hat{\gamma}_{2n+1} \rangle. \tag{7.18}$$

$$\implies \langle \hat{\gamma}_{2m} \hat{\gamma}_{2n+1} \rangle(t) = \frac{2i}{\pi} \frac{e^{-(\gamma|m-n|+\delta_{mn})t}}{1-2(m-n)}. \tag{7.19}$$

This takes a surprisingly simple form; however, we again stress that even though the equations of motion for the two point functions close on themselves, the state will generally evolve to something *highly* non-Gaussian. Using Wick's theorem to try to calculate higher point correlation functions could result in values that diverge exponentially from their true values, see Section F.1.3.

7.4 Decohered Critical Phenomena

In this section, we will try to understand the effect of just noise ($\theta = 0$) on an initial critical state.

7.4.1 Emergent length scale

Using the exact solution for the equation of motion of the fermionic degrees of freedom, we can now ask what physical understanding we can get from this model. One of the most striking things that emerges immediately from the form of Eq. (7.19) is that the fermions have an emergent length scale for any time $t > 0$, given by

$$\xi_F = \frac{1}{\gamma t} \tag{7.20}$$

The reason that this is surprising is that the initial state was scale invariant, and the noise channel we applied is local and finite depth, which cannot create a length scale from a scale invariant state [2] . This apparent tension is resolved by noting that the actual spins never develop a length scale. For example, the correlations in the Ising direction obey

$$\langle \hat{\sigma}^x_m \hat{\sigma}^x_n \rangle \sim |m-n|^{-1/4} e^{-\gamma t}. \tag{7.21}$$

This provides an interesting juxtaposition: on the one hand the physical spins are scale invariant, but on the other hand the degrees of freedom which diagonalize the Hamiltonian do develop a length scale which is tending to zero as a function of time.

Given that any real experiment will measure the spins as opposed to the fermionic operators, a natural question is whether this emergent length is ever observable or experimentally relevant. As we will show, it is in fact observable with an extremely simple experimental apparatus by probing a kind of "effective temperature".

2. This is because Pauli noise can be described by a unitary interaction with an ancilla qubit that is then traced out. Because this is a finite depth channel, it is impossible to alter any features of the long-range correlations characteristic of critical states.

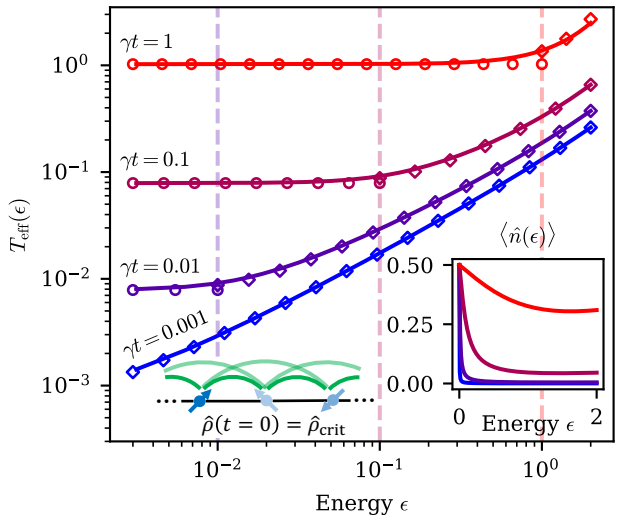

Figure 7.2: Effective temperature $T_{\text{eff}}(\epsilon)$ of the decohered critical Ising ground state. For all curves, the initial condition is the ground state of the Hamiltonian in Eq. (7.11) at $g = J = 1$. One then applies the decoherence channel (Eqs. (7.16) and (7.17) with $\theta = 0$); different curves correspond to different times γt as indicated. For longer evolution times, one sees clearly the emergence of a constant effective temperature at low energies. Solid lines are the exact $T_{\text{eff}}(\epsilon)$ (c.f. Eq. (7.25)). Open circles (diamonds) are the approximation given in Eq. (7.26) for the long (short) times. Vertical dashed lines denote the energy where the approximation switches its functional form. Inset: quasiparticle occupation corresponding to the T_{eff} in the main plot, using Eq. (7.24).

7.4.2 Effective temperature

As noted above, the length scale is emergent only when looking at the fermionic degrees of freedom and not the physical spins. While the spins may be the natural microscopic degree of freedom, the energetics are naturally described by the fermions since they describe the quasiparticle excitations above the ground state. Despite the fact that there is no Hamiltonian dynamics, knowledge of the Hamiltonian is encoded in the initial state which has knowledge of the quasiparticle excitations. This motivates looking at an observable with energy resolution to try and see this length scale. The simplest such observable is the expectation value of the quasiparticle number at a given energy/wavevector.

We can define the set of number operators $n_k = \langle \hat{\beta}_k^\dagger \hat{\beta}_k \rangle$ and ask how they evolve in time

under the applied noise (c.f. Eqs. (7.16) and (7.17) with $\theta = 0$). Now, before performing the explicit calculation, there is reason to believe that the structure of the noise coupled with a critical state can lead to extremely counter-intuitive effects. For a real model in thermal equilibrium at some temperature T, low energy modes will be more populated than high energy modes. In our setting the noise is perfectly Markovian, and so one might assume it does not care at all about the energy of the modes it is exciting. However, because of the string operators, the noise is sensitive to long-range correlations: the longer distance the correlation function, the more strongly the noise couples [c.f. Eq. (7.18)]. This implies the noise is sensitive to distance, or equivalently momentum, which in turn gives a path to energy selectivity while still being infinitely broadband. Moreover, because the long-range order of the critical state stems from the spatial structure of the low-energy modes, this gives a mechanism by which the low-energy modes are preferentially excited by a broadband source, mimicking a true temperature.

Before considering the full time dynamics, it is informative to consider both the limit $|k|/(\gamma t) \ll 1$ and $|k|/(\gamma t) \gg 1$. Equivalently, this is the same as asking if the fermionic length scale $\xi_F = (\gamma t)^{-1}$ is longer or shorter than a given wavelength $\propto |k|^{-1}$. For short times, the length scale is still longer than the wavelength, and we find that (see Section F.2.1):

$$n_k(t) = \frac{2}{\pi}\left(\frac{J}{\epsilon_k} + \frac{\epsilon_k}{8J}\right)\gamma t + \mathcal{O}(\gamma t/|k|)^3. \tag{7.22}$$

Since we are considering a long-wavelength expansion $k \ll 1$, then $\epsilon_k/J \ll 1$ and the rate at which quasiparticles are being injected by the noise scales inversely with their energy, in line with our intuition that the noise couples most strongly to the low energy modes. In the opposite limit of long time where the length scale is much shorter than the wavelength, we

have that

$$n_k(t) = \frac{1}{2} + \frac{\epsilon_k}{4\pi J}(1 - e^{-\gamma t} - \coth(\gamma t/2)) + \mathcal{O}\left(\frac{|k|}{\gamma t}\right)^3. \tag{7.23}$$

Note that for long times, $(1 - e^{-\gamma t} - \coth(\gamma t/2)) = -3e^{-\gamma t} + \mathcal{O}(e^{-\gamma t})^2$. This implies that at long times, we have exponential relaxation at a rate γ which is the same for all modes, but they behave as if they are relaxing from an energy dependent initial condition of $1/2 - 3\epsilon_k/(4\pi J)$.

Both the long and short time dynamics can be understood heuristically by thinking about the interplay between the noise and the fermionic length scale ξ_F. When the length scale $\xi_F \gg k^{-1}$ the wavelength, then the noise couples extremely strongly to this wavevector, and so the population grows faster than one would expect, like $1/\epsilon_k$. Very heuristically, we can think of this as a two-step relaxation process. First, at very short times there is some initial heating that depends strongly on the nature of the long range order and is very sensitive to the energy of a given quasiparticle mode. This process is cutoff when the length scale is less than the wavelength of the quasiparticle, $\xi_F \lesssim |k|^{-1}$. After this, there is uniform relaxation to infinite temperature at a rate independent of the energy, but with the initial fast dynamics leaving an imprinted "initial condition" of the exponential relaxation. It is this initial imprint (which scales roughly linearly with energy) that gives rise to the effective temperature.

The full closed form solution for the dynamics at all times is given by (see Section F.2.1):

$$\begin{aligned} n_k(t) = &-\frac{i}{\pi}\cosh(t/2)\left[\tanh^{-1}\left(e^{(-i|k|-\gamma t)/2}\right) - \tanh^{-1}\left(e^{(i|k|-\gamma t)/2}\right)\right] \\ &+ \frac{1}{\pi}|\sin(k/2)|(1 - e^{-\gamma t}) + \frac{1}{2}. \end{aligned} \tag{7.24}$$

Given a value of the quasiparticle population, we can use this to define a kind of effective

temperature that depends on both time and energy by asking, given a quasiparticle density, what temperature would this correspond to in an equilibrium system. This temperature is defined by

$$T_{\text{eff}}(k,t) = \frac{\epsilon_k}{\log(1-n_k) - \log(n_k)}. \tag{7.25}$$

We can use the previously derived approximations for the limiting behavior of n_k [c.f. Eqs. (7.22) and (7.23)] to find the limiting behavior of the effective temperature (see Fig. 7.2):

$$T_{\text{eff}}(k,t) \sim \begin{cases} \pi J \frac{e^{2\gamma t} - e^{\gamma t}}{3e^{\gamma t} - 1} & \gamma t \gtrsim |k| \\ -4\epsilon_k \log^{-1}\left[\left(\frac{\epsilon_k}{2J} + \frac{J}{\epsilon_k}\right)\frac{\gamma t}{\pi}\right] & \gamma t \lesssim |k| \end{cases}. \tag{7.26}$$

Note that for long times, when the length scale $\xi_F < |k|^{-1}$, then the effective temperature becomes effectively independent of the energy/momentum and the system looks as if it has reached a thermal equilibrium. In this way, one can directly observe the length scale by measuring the "temperature" as a function of momentum and seeing at what wavevector the system begins to look nonequilibrium. A sketch of how this experiment might work is given in Fig. 7.1 as well as the inset of Fig. 7.6. To probe the particle density as a function of energy, one can attach a probe qubit, denoted by operators $\hat{\sigma}_P^{x,y,z}$ to the edge of the Ising model with a weak XX coupling:

$$\hat{H} = \frac{\Delta}{2}\hat{\sigma}_z^P + \hat{H}_{\text{Ising}} + \lambda(\hat{\sigma}_P^+ \hat{\sigma}_1^- + \text{H. c.}), \tag{7.27}$$

where $\hat{H}_{\text{Ising}}$ is the Hamiltonian in Eq. (7.11). In the limit that the coupling is extremely weak $\lambda \ll J$, then only quasiparticles with an energy exactly at the probe qubit splitting Δ can tunnel in, and so the effective dynamics can be described by rates $\Gamma_{\uparrow,\downarrow}$ for the probe qubit to flip from down to up or up to down, respectively, which depend only on the coupling strength λ and the quasiparticle density at the energy Δ. In the long time limit, the probe

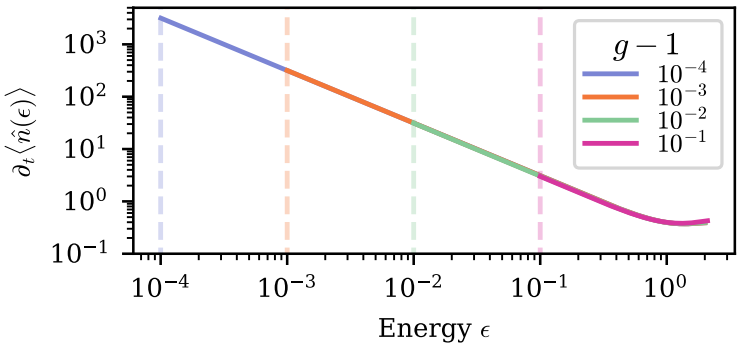

Figure 7.3: Instantaneous rate of change of the quasiparticle number at $t = 0$ as a function of energy under the decoherence channel Eqs. (7.16) and (7.17) with $\theta = 0$. The initial condition is the ground state of the Ising model Eq. (7.11) for the given value of g with $J = 1$. Vertical dashed lines denote the corresponding energy gap.

qubit will equilibrate so that the number of quasiparticles is encoded in the expectation value of $\hat{\sigma}_P^z$ (see Section F.4.1)

$$\langle \hat{\sigma}_P^z \rangle (t \to \infty) = (2n_k - 1), \quad \epsilon_k = \Delta. \tag{7.28}$$

Thus, if one simply performed thermometry on the probe qubit and asked its "temperature" given the splitting frequency Δ and the population imbalance, one would exactly recover $T_{\text{eff}}(\Delta)$ of the Ising model, as desired. More details can be found in Section F.4.

This protocol is reminiscent of schemes to cool many-body systems by extracting energy into an ancilla at a fixed frequency [272, 273, 243, 274, 275]; the difference here is that we work in a regime where instead of attempting to actually extract a large amount of energy, we are in a regime where the actual energy transfer is small enough to be negligible to the original system, as we aren't trying to cool the system and instead are trying to probe the state.

7.4.3 Divergent quasiparticle production

The emergence of a temperature comes after applying the noise channel for a relatively long time, so that the fermionic length scale ξ_F becomes comparable to a handful of lattice sites. We instead now consider what phenomena can be seen in the extremely short time limit. The most extreme short time data is the derivative $\partial_t n_k$ in the ground state. The reason to believe that this quantity might prove interesting is that, when the state is critical, we know the noise causes a sharp jump in the QP number. In fact, one can show that to leading order in ϵ_k (see Section F.2.4)

$$\partial_t n_k|_{t=0} = \frac{2\gamma}{\pi\epsilon_k} + \mathcal{O}(\epsilon_k^0). \tag{7.29}$$

This scaling is shown in Fig. 7.3, where the inverse scaling of the derivative with the energy is immediately apparent. Such a divergence in the derivative at short times manifests in a total particle number that, starting from the critical state, behaves as (see Section F.2.4):

$$n = \int \frac{\mathrm{d}k}{2\pi} n_k \sim \begin{cases} -\frac{1}{\pi^2}\gamma t \log \gamma t & \gamma t \ll 1 \\ \frac{1}{2} - \frac{38}{9\pi^2} e^{-\gamma t} & \gamma t \gg 1 \end{cases}. \tag{7.30}$$

This divergence is in keeping with the notion that critical states are very fragile to noise: defects are created super-linearly at short times. At long times, it also exactly mimics the notion that there is a quick "jump" followed by uniform relaxation.

Because the total quasiparticle number grows superlinearly at short times, this reflects another experimental signature of coupling the noise to a critical state. Moreover, it is again experimentally measurable. Instead of weakly coupling a probe, an even simpler protocol is imagined: after applying the noise, one turns the Ising Hamiltonian back on, and performs an adiabatic ramp from the critical point ($g/J = 1$) to either the perfect ferromagnet ($g/J = 0$) or the perfect paramagnet ($g/J = \infty$). If one ramps to the paramagnet, then projectively

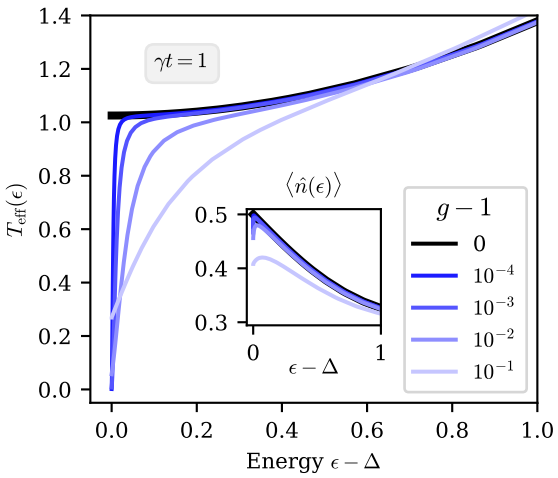

Figure 7.4: Effective temperature of the decohered ground state away from the critical point. $\Delta = 2|g-1|$ corresponds to the energy gap, and $\epsilon - \Delta$ the energy above the gap. The initial condition is the ground state of the Ising model Eq. (7.11) for the given value of g with $J = 1$. The state is given by time evolution under Eqs. (7.16) and (7.17) with $\theta = 0$ for a time $\gamma t = 1$. Solid black lines ($g - 1 = 0$) denotes the critical point as depicted in Fig. 7.2 for comparison. Inset: quasiparticle densities corresponding to the effective temperature in the main plot.

measuring Z on every lattice site and counting how many spins are in the $|\uparrow\rangle$ state gives the number of QPs (see Section F.4). Alternatively, ramping to the ferromagnet, projectively measuring in the X basis, and counting domain walls also gives the number of QPs.

7.5 Dynamics away from the critical point

In this section, we will compare the decohered critical state to decoherence applied to a gapped ground state. We will still only consider evolution under the noise only dynamics Eqs. (7.16) and (7.17) with $\theta = 0$.

7.5.1 Lack of emergent temperature

We have seen that applying the infinite temperature noise channel to the critical ground state induces an effective temperature up to a length scale ξ_F. We now ask how important it was that the initial condition was a critical state having long range order. Intuitively, one

might expect that the dynamics will be quite different if the initial state already has a length scale. The sudden "jump" in quasiparticle number at small wavevector and short times was directly due to the fact that there was long range order and the noise could couple extremely strongly to these low frequency modes. When the system is gapped, this is no longer the case.

This intuition is supported by the exact calculations for the Ising model, which can be seen in Fig. 7.4, where the effective temperature is plotted for varying value of $g/J - 1$ after decohering for a time $\gamma t = 1$. We note that, even after moving only slightly away from the critical point to $g = 1.1J$, the lightest curve in the plot, the effective temperature for low energies looks extremely different than that of the critical ground state. Instead of being flat as a function of energy, it is now growing linearly for small energies, making it highly nonequilibrium.

7.5.2 Logarithmically diverging quasiparticle production

Recall from Section 7.4.3 that when initializing the quantum state exactly at the critical point, then the noise channel injects QPs at a rate that is diverging at short times. Intuitively, this is a result of the fact that exactly at $t = 0$, the quantum state has algebraically decaying correlation functions. Since the noise strength is growing linearly with separation, these two effects ultimately cause a divergence. Alternatively, when the initial condition is no longer critical, the correlations decay exponentially and therefore we expect the rate at which quasiparticles are being injected should be bounded. We wish to understand the leading order behavior of $\partial_t n|_{t=0}$ as a function of $g - 1$, working in units where $J = 1$. When $g = 1$ we know this value must diverge, but it is informative to understand how this works.

This value can be represented by the following momentum space integral (see Section F.2):

$$\partial_t n|_{t=0} \sim \int_{-\pi}^{\pi} \frac{\mathrm{d}k}{2\pi} \int_{-\pi}^{\pi} \frac{\mathrm{d}k'}{2\pi} \frac{\sin^2([\theta_k - \theta'_k]/2)}{(k - k')^2}. \tag{7.31}$$

which is valid for all values of $g-1$. As expected, this quantity can only diverge directly at the critical point, as the integrand is strictly bounded above by $(1-g)^{-2}/4$. Utilizing the exact solution, one can show that to leading order

$$\partial_t n|_{t=0} = -\frac{\gamma}{\pi^2}\log(g-1) + \mathcal{O}(g-1)^0. \tag{7.32}$$

Therefore, the rate at which QP are being injected into the system is diverging logarthmically as one approaches the critical point. This is incredibly intuitive when looking at Fig. 7.3, where one can see that the energy resolved QP number is being injected at a rate $\sim 1/\epsilon$. Integrating this over all energy, recalling the flat density of states at low energy and that the gap is set by $g-1$ gives a logarthmic divergence.

Together, the lack of temperature and lack of divergence highlights the fact that there is an extremely nontrivial interplay between criticality and noise. Decohered critical states effectively thermalize under local Markovian noise in a way that gapped ground states do not. We believe this is a result of the nature of how noise can couple to scale invariant states that is distinctly different from how it couples to states with exponentially decaying correlations. Moreover, we posit that this result may be more general than just the transverse-field Ising model, and instead reflect characteristics of more general decohered critical models. Given generic local noise operators, if the low energy excitations are described by long-wavelength fluctuations then the noise will be able to degrade these correlations much more quickly than short range correlations. This heuristic does not depend on the microsopic details of the Ising model, and it would be of interest to see if this holds more generally (which we explore briefly in Section 7.8.0). Additionally, it could point to an interesting experimental signature of criticality.

7.6 Noise With Coherent Dynamics

In this section, we will compare the results derived in Section 7.4 to the case where there are also coherent Hamiltonian dynamics. This can be done either in a time continuous process or as a discrete circuit of interleaved coherent dynamics with discrete noise channels as depicted in Fig. 7.1. We will consider the time-continuous version here for simplicity and take dynamics given by Eqs. (7.16) and (7.17) with $\theta = 1$.

In the case that there are both coherent dynamics and noise, we no longer have closed form expressions for the time traces of the quasiparticle number; however, there are still closed expressions for the equations of motion of the fermionic two point functions, and we can access very large system sizes using numerics. In order to understand how these curves converge in the thermodynamic limit, it is important to attempt to mitigate boundary effects that should be asymptotically irrelevant to the bulk physics.

In order to do this, the boundary conditions we impose will be relevant. In fact, in Section F.1 we show that while the low energy physics with periodic boundary conditions (PBC) converge as N^{-1}; when there are open boundary conditions (OBC) it only converges as $N^{-1/2}$. Therefore, it is often preferable to work directly with PBC. There is some subtlety here, though, as the PBC Hamiltonian is interacting:

$$\begin{aligned}\hat{H}_{\text{PBC}} &= -J\hat{\sigma}_1^x\hat{\sigma}_N^x - J\sum_{i=1}^{N-1}\hat{\sigma}_i^x\hat{\sigma}_{i+1}^x + g\sum_{i=1}^{N}\hat{\sigma}_i^z \\ &= J(\hat{c}_N^\dagger - \hat{c}_N)(\hat{c}_1 + \hat{c}_1^\dagger)\hat{\Pi} - J\sum_{i=1}^{N-1}(\hat{c}_i^\dagger - \hat{c}_i)(\hat{c}_{i+1} + \hat{c}_{i+1}^\dagger) + 2g\sum_{i=1}^{N}\hat{c}_i^\dagger\hat{c}_i, \end{aligned} \tag{7.33}$$

where $\hat{\Pi} = \prod_{i=1}^{N}(-1)^{\hat{c}_i^\dagger\hat{c}_i} = \prod_{i=1}^{N}\hat{\sigma}_i^z$ is the total parity operator. This is also the $\mathbb{Z}_2$ symmetry of the Ising Hamiltonian and is a weak symmetry of the noisy dynamics [131].

Now, because the Hamiltonian is formally interacting, operators do not naively have closed equations of motion, and specifically the result in Ref. [264] will not apply. However,

we are still able to make progress by understanding the nature of the state as a convex sum of Gaussians.

The first step is to observe that, while the Hamiltonian is interacting, the interaction comes from a conserved quantity $[\hat{H}_{\mathrm{PBC}}, \hat{\Pi}] = 0$. Therefore, we can replace the operator $\hat{\Pi}$ with its expectation value and diagonalize the Hamiltonian in the different parity sectors. When there are an even number of quasiparticles, then $\hat{\Pi} = 1$ and so $\hat{H}_{\mathrm{PBC}}$ is a free-fermion Hamiltonian with anti-periodic boundary conditions (APC); i.e., one can imagine threading a $\phi = \pi$ flux through the loop. On the other hand, when there are an odd number of quasiparticles, then $\hat{\Pi} = -1$, and so $\hat{H}_{\mathrm{PBC}}$ is again free and has PBC.

Therefore, the covariance matrix dynamics are still simple and can be solved exactly in each parity sector. The next step is to realize that, while the noise can change parity, it can never generate coherences between different parity sectors. This is in keeping with fermion super-selection rules, and formally is a result of the fact that parity is a weak symmetry of the dynamics. Therefore, we can observe that, not only can the state be written as a convex sum of Gaussians, it can also be written as a convex sum of each fixed parity sector. Specifically, if we consider a pure state $|\Gamma\rangle$ as a Gaussian free-fermion state with covariance matrix Γ, then its parity is given by $\mathrm{Pf}(\Gamma)$ where $\mathrm{Pf}(\bullet)$ stands for the Pfaffian. We can write the total density matrix at all times in the form:

$$\hat{\rho}(t) = \hat{\rho}_+(t) + \hat{\rho}_-(t), \tag{7.34}$$

$$\hat{\rho}_\pm(t) = \sum_{\Gamma|\mathrm{Pf}(\Gamma)=\pm 1} p_\pm(\Gamma, t)|\Gamma\rangle\langle\Gamma|. \tag{7.35}$$

Here, $\hat{\rho}_\pm$ are (unnormalized) fixed parity convex sums of Gaussians with probability distributions over the space of covariance matrices given by $p_\pm$. We can use these to define even

and odd covariance matrices $\Gamma_\pm$ given by

$$(\Gamma_\pm)_{mn} = \text{tr}(\hat{\rho}_\pm \hat{\gamma}_m \hat{\gamma}_n). \tag{7.36}$$

Now, to understand what the noise does, we can observe that it will mix the even and odd parity sectors into each other. Specifically, if there is a finite depth channel with local probability p to perform a parity-reversing jump, then we can observe that the total channel can be written as

$$\mathcal{K}[\hat{\rho}] = (1-p)\mathcal{K}_+[\hat{\rho}] + p\mathcal{K}_-[\hat{\rho}], \tag{7.37}$$

where $\mathcal{K}_\pm[\bullet] = \sum_i \hat{K}_{i,\pm} \bullet \hat{K}_{i,\pm}^\dagger$ with $[\hat{K}_{i,+}, \hat{\Pi}] = 0$ commuting with parity, and $\{\hat{K}_{i,-}, \Pi\} = 0$ anticommuting. Given the local noise model we have been considering of equal probability X and Y dephasing, then $\hat{K}_{i,+}$ are proportional to all strings of Paulis of even length, and vice versa for $\hat{K}_{i,-}$ and odd length strings because all jumps flip parity. Because the jump probabilities after separating into even and odd sectors remain independent of the state, it is still possible to exactly re-sum the stochastic equations of motion generated under these trajectories, which is explained in more detail in Section F.1. Moreover, we can show that the overall effect is that the coupling rates between the two parity sectors is weakly dependent on system size because the probability of having an even or odd length string depends weakly on the total number of lattice sites. Overall, if previously the covariance matrix Γ_{mn} obeyed the equation of motion $\partial_t \Gamma_{mn} = -\gamma f_{mn} \Gamma_{mn}$ where γ is a rate. Once we consider separately the different parity sectors we find that this gives the channel:

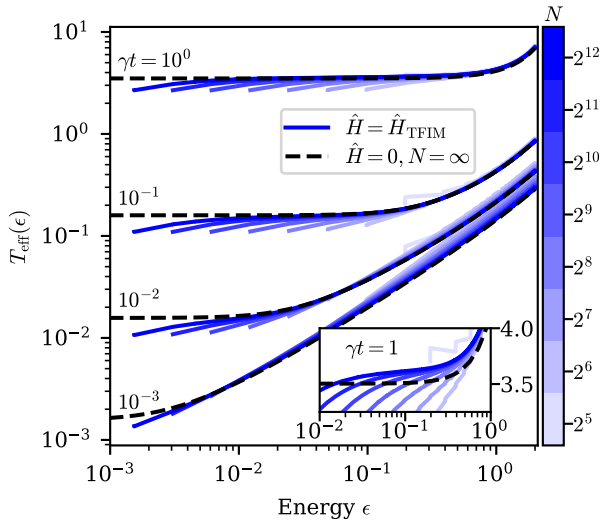

Figure 7.5: Interplay between coherent and incoherent dynamics, where the initial condition is the critical ground state. The blue curves show time evolution under the master equation Eqs. (7.16) and (7.17) with $\theta = 1$ for system sizes varying from $N = 32$ (lightest) to $N = 4096$ (darkest), with periodic boundary conditions. The black dashed curves show time evolution under the master equation Eq. (7.17) with $\theta = 0$ in the thermodynamic limit $N = \infty$ [c.f. Fig. 7.2]. Inset: zoomed in details for $\gamma t = 1$.

$$\begin{pmatrix} (\Gamma_+)_{mn} \\ (\Gamma_-)_{mn} \end{pmatrix}(t) = e^{-\gamma N t} \begin{pmatrix} \cosh(\gamma t(N - f_{mn}) & \sinh(\gamma t(N - f_{mn}) \\ \sinh(\gamma t(N - f_{mn}) & \cosh(\gamma t(N - f_{mn}) \end{pmatrix} \begin{pmatrix} (\Gamma_+)_{mn} \\ (\Gamma_-)_{mn} \end{pmatrix}(0). \tag{7.38}$$

We can check that if there are no other dynamics, then

$$[(\Gamma_+)_{mn} + (\Gamma_-)_{mn}](t) = e^{-\gamma f_{mn} t}[(\Gamma_+)_{mn} + (\Gamma_-)_{mn}](0), \tag{7.39}$$

recovering the previous results. However, this will not hold exactly when $\Gamma_\pm$ evolve under different Hamiltonian dynamics.

Now that we understand how to solve periodic boundary conditions, we can consider

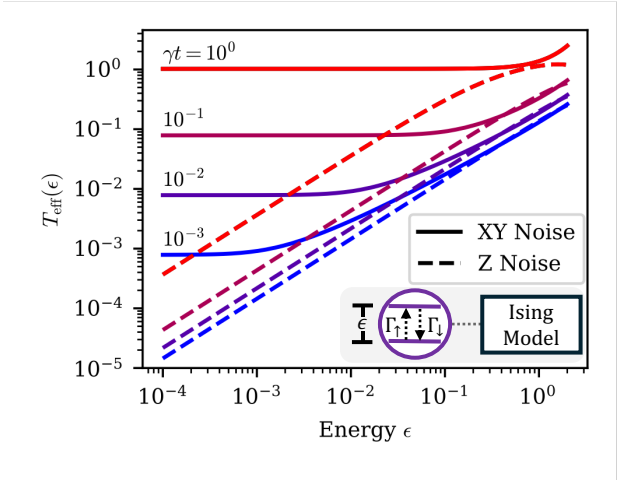

Figure 7.6: Effective temperature as shown in Fig. 7.2 of the decohered ground state of the critical Ising model with $g = J$ for variable decoherence time $\gamma t \in \{0.001, 0.01, 0.1, 1\}$. Solid lines denote decoherence in the X and Y directions [c.f. Eq. (7.16)] identical to the data in Fig. 7.2. Dashed lines show decoherence for the same time in the Z direction [c.f. Eq. (7.40)]. Inset: experimental technique to measure the temperature using a type of noise spectroscopy. The probe qubit (purple) with a splitting Δ is weakly coupled to the Ising chain, which induces incoherent transitions at a rate $\Gamma_{\uparrow/\downarrow}$.

what happens under the combined coherent and noisy channels. This is shown in Fig. 7.5, for system size varying from $N = 32$ to $N = 4096$. Each blue curve is initialized at the critical ground state, and then evolves under the critical Ising Hamiltonian and noise. The black dashed curves are the closed form results in Eq. (7.24) when there is only noise. One can observe that the curves with the coherent Hamiltonian dynamics are asymptotically converging to something qualitatively similar to the noise only dynamics, but there are some small quantitative differences, as can be seen in the inset. One can also see that the low energy physics is converging extremely slowly in system size, even though the high energy QP numbers converge rapidly.

7.7 Other Noise Types

Here, we will briefly consider alternative decoherence channels, and see the effect they have on the phenomena we have observed both at and away from the critical point. We will again

only consider pure noise dynamics where $\theta = 0$.

7.7.1 Transverse field noise

First, we consider the more commonly studied noise model corresponding to decoherence in the Z direction [276, 277, 278]. An equivalent description of this is the case where the transverse field is subject to Markovian, spatially uncorrelated classical noise. This is given by the master equation

$$\partial_t \hat{\rho} = \gamma \sum_i \mathcal{D}[\hat{\sigma}_i^z]\hat{\rho}. \tag{7.40}$$

Upon performing the JW transformation, this maps to noise generated by the operators $\hat{L}_i = \hat{c}_i^\dagger \hat{c}_i$. This is a known class of simulable fermionic models, as the jump operators are fermion bilinears and Hermitian, and does not require our technique to solve [173].

Because the noise is quite simple in terms of the energy eigenmodes, the effect is has is also simple. Specifically, it generates a length scale for *neither the spins nor the fermions* as it is local in both representations. This simplicity allows one to observe that (see Section F.2.2):

$$n_k(t) = n_k(\infty)(1 - e^{-\gamma t}), \tag{7.41}$$

where $n_k(\infty) \neq \frac{1}{2}$ now because the local Z magnetization is a conserved quantity and so the system does not equilibrate to infinite temperature. As one would expect, the fact that there is no length scale generated and the noise is local in the QP picture means that the phenomenology is quite different from the XY noise previously examined. In Fig. 7.6, one can see that there is never an emergent notion of temperature, as now the noise is truly agnostic to the spectrum of the Hamiltonian even at the critical point.

We posit that, in some sense, the Z noise is more fine-tuned than the XY noise. For one thing, the Z-parity generates the $\mathbb{Z}_2$ symmetry of the Hamiltonian, and so the transverse

field direction plays a special role. Moreover, one would imagine that in a general critical state with long range order, it would be difficult to construct local operators that couple only to QP bilinears with no higher powers.

7.7.2 Free fermion dissipation

The final type of noise we will consider is "free fermion" noise, where one simply drops the JW strings. This is evolution under the master equation

$$\partial_t \hat{\rho} = \gamma \sum_i \mathcal{D}[\hat{c}_i]\hat{\rho} + \mathcal{D}[\hat{c}_i^\dagger]\hat{\rho}. \tag{7.42}$$

This noise model is even simpler, as the entire Lindbladian is quadratic in the fermionic operators and Gaussian states remain Gaussian for all time. It is tempting to hope that this might be qualitatively similar to the original noise model Eq. (7.16). However, because the strings are responsible for the emergent length scale, the physical dynamics will be radically different. In fact, one can compute exactly that the quasiparticle density, for any value of g in the initial condition, will evolve as

$$n_k(t) = \frac{1}{2}(1 - e^{-2\gamma t}), \tag{7.43}$$

which is completely independent of wavelength and energy. Similarly to the case of Z-dephasing noise, this will never develop a length scale or a temperature that is independent of energy. Even more surprisingly, under the free fermion dissipation the spins will actually generate a length scale. This can be seen immediately by noting that there is a duality

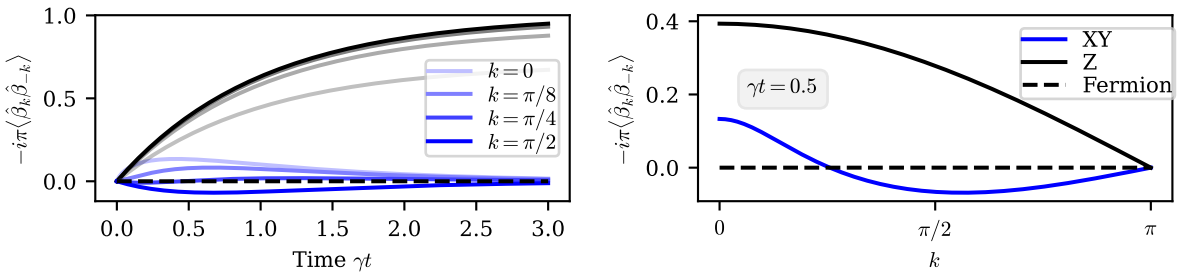

Figure 7.7: Quasiparticle coherences $C_{k,-k} = \langle\hat{\beta}_k\hat{\beta}_{-k}\rangle$ as a function of time (upper plot) and momentum (lower plot). The initial condition is the critical ground state $g/J = 1$. Blue curves show time evolution under the master equation Eq. (7.17) with $\theta = 0$. Solid black curves show time evolution under the master equation Eq. (7.40) and dashed black curves show time evolution under the master equation Eq. (7.42)

relating spin observables under fermion noise to fermion observables under spin noise.

7.7.3 Coherences

In addition to the quasiparticle density, the only other two point correlation function allowed by translational invariance is the coherence $C_k = \langle\hat{\beta}_k\hat{\beta}_{-k}\rangle$. This parameter has three distinct behaviors for all three types of noise we have considered. Beginning with XY noise [c.f. Eq. (7.16)] we note that the steady state is infinite temperature, and so they must be identically zero at long times. Further, we find that they vary significantly with the value of k, and for $k = 0$ then $C^{XY}_{k=0}(t) = -\frac{i}{2\pi}(\gamma t)\log(\gamma t) + \mathcal{O}(\gamma t)$ grows superlinearly at short times. The exact functional form valid for all (k, t) is derived explicitly in Section F.2.3. We can compare this to the case where one drops the string operators, and instead considers free-fermion noise [c.f. Eq. (7.42)]. In this case, the coherences are identically zero for all k and all times: $C^{\text{ff}}_k(t) = 0$, in stark contrast to the spin noise. In this case, all of the generated coherences is a result of the interactions coming from the strings. Finally, as an intermediate case we can consider Z dephasing [c.f. Eq. (7.40). Here, the steady state is no longer infinite temperature, and so the coherences actually saturate to a constant value: $C^Z_k(t) = \frac{i}{\pi}\text{sgn}(k)\cos(k/2)(1 - e^{-\gamma t})$, although the rate is k-independent.

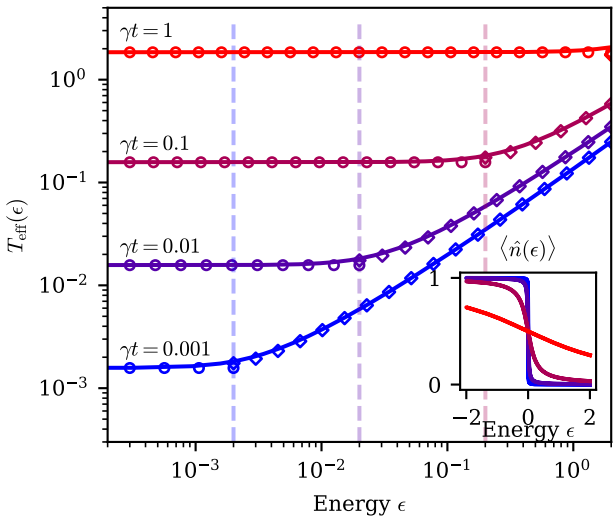

Figure 7.8: Effective temperature for the dephased XX model in the zero magnetization sector. Initial condition is the ground state, evolved under the XY noise channel for times $\gamma t \in \{0.001, 0.01, 0.1, 1\}$. Solid lines correspond to the exact solution in Eq. (7.48). Circle and diamond markers correspond to the long and short time expansions, respectively, given in Eq. (7.50). Vertical lines correspond to the cutoff for the approximation due to the length scale. Inset gives the quasiparticle densities.

7.8 Critical XX Model

We show here that the main features found for a decohered critical ground state of the TFIM (namely the emergence of an effective temperature at low energies) can also arise in other models. Specifically, we will now consider applying the same noise channel to an XX spin chain:

$$\hat{H}_{\text{XX}} = -\frac{J}{2} \sum_{i=1}^{N-1} \hat{\sigma}_i^x \hat{\sigma}_{i+1}^x + \hat{\sigma}_i^y \hat{\sigma}_{i+1}^y, \tag{7.44}$$

$$\partial_t \hat{\rho} = \gamma \mathcal{L}_{\text{XY}} \hat{\rho}, \tag{7.45}$$

where $\mathcal{L}_{\text{XY}}$ is defined in Eq. (7.16). We will work with the ground state in the zero-magnetization sector. Note that while the CFT for the TFIM is given by free Majoranas with a central charge $c = 1/2$, for this XX model, the critical theory is the Luttinger liquid

CFT with $c = 1$. We show below that despite this difference in central charge, the physics of the emergent temperature in the decohered state is largely the same.

This Hamiltonian can be diagonalized in terms of the plane wave fermionic modes $\hat{H}_{\mathrm{XX}} = -2J\sum_k \cos(k)\hat{d}_k^\dagger \hat{d}_k$, see Section F.3 for more details. As noted above, we work with the ground state in the zero magnetization sector, a state determined by:

$$\langle \hat{d}_k^\dagger \hat{d}_k \rangle_{\mathrm{GS}} = \begin{cases} 1 & |k| < \pi/2 \\ 0 & |k| > \pi/2 \end{cases}. \tag{7.46}$$

In real space, this state has critical long-range correlations given by [see Section F.3]:

$$\langle \hat{c}_m^\dagger \hat{c}_n \rangle_{\mathrm{GS}} = \frac{\sin\left(\frac{\pi}{2}(m-n)\right)}{\pi(m-n)}. \tag{7.47}$$

Using the new quasiparticle operators $n_k = \langle \hat{n}_k \rangle = \langle \hat{d}_k^\dagger \hat{d}_k \rangle$, we can again calculate explicitly

$$n_k(t) = \frac{1}{2} + \frac{\operatorname{arccot}(e^{-ik+\gamma t}) + \operatorname{arccot}(e^{ik+\gamma t})}{\pi}. \tag{7.48}$$

From here, we can again calculate the short and long time expansions to find that

$$n_k(t) = \begin{cases} n_k(0) + \frac{2J}{\pi\epsilon_k}\gamma t & \gamma t \lesssim |k| \\ \frac{1}{2} - \frac{\epsilon_k}{J\pi} e^{-\gamma t} & \gamma t \gtrsim |k| \end{cases}. \tag{7.49}$$

Just as in the case with the TFIM, there is a kind of two stage relaxation: first the particle number grows very quickly at a rate inversely proportional to its energy. After this, every mode undergoes constant relaxation, but the initial jump has been imprinted as a kind of initial condition.

We can use these to calculate the temperature, and we again find that for long times/short

wavevectors there is an emergent effective temperature constant in energy [see Section F.3]

$$T_{\text{eff}}(k,t) \sim \begin{cases} \frac{\pi J}{2}\sinh(\gamma t) & \gamma t \gtrsim |k| \\ |\epsilon_k| \log^{-1}\left(\frac{\pi|\epsilon_k|}{2J\gamma t}\right) & \gamma t \lesssim |k| \end{cases}. \tag{7.50}$$

This scaling is confirmed in Fig. 7.8, where one can see qualitatively identical behavior to that seen in the TFIM model (compare to Fig. 7.2).

Finally, we can also calculate how the overall quasiparticle changes at short times. Now, because we are considering the model in the zero-magnetization sector, the total quasiparticles number does not change in time. However, we can instead consider the imbalance between positive and negative energy particles. We will define

$$n_{\epsilon>0} = \int_{\pi/2}^{\pi} \langle \hat{d}_k^\dagger \hat{d}_k \rangle \frac{\mathrm{d}k}{\pi} + \int_{-\pi}^{-\pi/2} \langle \hat{d}_k^\dagger \hat{d}_k \rangle \frac{\mathrm{d}k}{\pi}, \tag{7.51}$$

the particle density in positive energy modes. To leading order in time, this behaves as

$$n_{\epsilon>0} = -\frac{2}{\pi^2}\gamma t \log(\gamma t), \tag{7.52}$$

and so the particle number in positive energy modes is indeed growing superlinearly at short times, matching the TFIM, c.f. Eq. (7.30). Interestingly, the prefactor differs by a factor of 2 which is the same factor by which the central charges differ.

All together, this provides strong evidence that the features identified for the TFIM and XX models could extend more generally to other critical states.

7.9 Discussion

In this Chapter, we have used an exact solution to matchgate circuits with Pauli noise to analytically probe the time dynamics of a quantum critical state under spatially uniform,

Markovian dephasing noise. We have shown that, despite the fact that the noise was infinite bandwidth and infinite temperature, there is an emergent notion of temperature at intermediate time scales coming from the interactions in the noisy dynamics.

This emergent temperature effect is intimately related to the fact that, even though the spins remain scale invariant, the underlying quasiparticle excitations described by the Jordan-Wigner fermions develop a time-dependent length scale. We confirmed that this behavior is not specific to the TFIM and extends to other decohered critical states in 1D. However, it would be extremely interesting to see if it persists in higher dimensional or non-integrable models.

Moreover, we have just begun to scratch the surface of the interplay between coherent dynamics and noise and there is still much to do in understanding how noise impedes unitary evolution in many-body systems near critical points. It would be extremely interesting to use the techniques developed here to try and gain either numerical or analytical insights into the effect of noise on the Kibble-Zurek mechanism or other adiabatic preparation mechanisms where one can see competition between unitary dynamics attempting to build long length scales while dissipation tries to shrink them. Such results could provide immediate insights into numerous noisy simulation experiments in the near term.

CHAPTER 8

COMPUTATIONAL TECHNIQUES

This chapter contains previously-published material found in Ref. [186]. Reuse is permitted according to the copyright agreement used by *Physical Review X Quantum*. This chapter also contains material that can be found on the arXiv preprint server in Ref. [233].

8.1 Introduction

The goal of this Chapter is to give a more pedagogical review of the simulation techniques presented in Chapters 6 and 7. Specifically, the goal of this Chapter is that it would provide a guide on how to implement the numerical techniques we have developed in this dissertation in actual software. We will begin by studying the stochastic equation of motion presented in Chapter 6 in both the "Schrödinger" and the "Heisenberg" picture. After this, we will discuss how one is able to implement the exact re-summed dynamics from Chapter 7 in the form of a matchgate + Pauli circuit.

We will work to write explicit algorithms in pseudo-code so that they can be directly written into the preferred language if desired. Some subroutines we will take for granted, especially standard linear algebra subroutines such as matrix diagonalization or matrix multiplication that can be taken directly from any number of open-source libraries.

We will also discuss the scaling of these algorithms in terms of computational complexity. As a caveat, we also note that the main bottleneck will often simply be the computational complexity of matrix multiplication. Because matrix multiplication is a highly parallelizable task, it is often possible to reduce computational complexity at the cost of more resources. Finally, we will also assume that memory is not a limiting factor when computing computational complexity and take it to be essentially infinite (although all algorithms considered use polynomial memory resources).

8.2 Stochastic Time Evolution

In this section, we will detail the algorithms necessary to time evolve operators using the stochastic unraveling techniques from Chapter 6. For historical reasons[1], we will begin with what we refer to as the "Heisenberg" picture, despite not being the most efficient numerical implementation. Following this, we will show the "Schrödinger picture" which is much more computationally efficient. However, both methods will scale polynomially in the number of qubits.

8.2.1 Heisenberg Picture

Algorithm 1: Compute covariance from Pfaffian, complexity $\mathcal{O}(N^5M + N^2M^3)$

Data: Matrix A of dimension $2M + 2$
Result: Matrix $\Gamma(t)$ of dimension $2N$
$\Gamma \leftarrow 0_{2N,2N}$; /* Initialize to the zero matrix */
for $m = 0$ **to** $2N - 1$ **do**
  for $n = 0$ **to** $2N - 1$ **do**
    for $k = 0$ **to** $M - 1$ **do**
      $A_{M,k} \leftarrow \langle \gamma_m(t) L^\dagger_{x_k}(t_k) \rangle$; /* Update A to compute Γ_{mn} */
      $A_{M+1,k} \leftarrow \langle \gamma_n(t) L^\dagger_{x_k}(t_k) \rangle$;
    end
    for $k = M + 2$ **to** $2M + 1$ **do**
      $A_{M,k} \leftarrow \langle \gamma_m(t) L_{x_{2M+2-k}}(t_{2M+2-k}) \rangle$
      $A_{M+1,k} \leftarrow \langle \gamma_n(t) L_{x_{2M+2-k}}(t_{2M+2-k}) \rangle$;
    end
    $A_{M,M+1} \leftarrow \langle \gamma_m(t)\gamma_n(t) \rangle$;
    $A \leftarrow (A - A^T)/2$;
    $\Gamma_{mn} \leftarrow \mathrm{Pf}(A)$;
  end
end

1. The real reason being that this method was found first. It also gives a much clearer connection to the gauge theory interpretation (c.f. Chapter 6), although this is irrelevant for numerical implementation.

The goal will be an efficient method to compute expectation values of the following form:

$$\langle \hat{O} \rangle(T) = \langle \psi | (\hat{L}')^{\dagger}_{i_1}(t_1) \dots (\hat{L}')^{\dagger}_{i_m}(t_m)(\hat{P}_m \hat{O} \hat{P}_m)(t_f) \hat{L}'_{i_m}(t_m) \dots \hat{L}'_{i_1}(t_1) | \psi \rangle / \mathcal{N}(t). \tag{8.1}$$

We will define $\{\hat{\gamma}_m | m = 1, \dots, 2N\}$ as Majorana operators. We will assume that $\hat{O} = \hat{\gamma}_m \hat{\gamma}_n$ is a two-point fermion correlation function. We will also discuss how this can be extend to more general observables, but all of the two point correlation functions are a minimal requirement.

Recall that we have the following definition from Chapter 6:

$$\hat{L}'_i = \sum_{j=1}^{2N} l_{ij} \hat{\gamma}_j. \tag{8.2}$$

Further, the generator of the time evolution is given by

$$\hat{H}(t) = \sum_{i,j=1}^{2N} h_{ij}(t) \hat{\gamma}_i \hat{\gamma}_j, \tag{8.3}$$

where h_{ij} is an antisymmetric matrix, that will be updated following every jump. We will define $\Gamma(t) = \langle \hat{\gamma}_m \hat{\gamma}_n \rangle(t)$ the set of two point functions at a time t. Now, we can calculate the probability to perform a jump between a time t and $t + \mathrm{d}t$ by noting that

$$p_i = \langle \hat{L}_i'^{\dagger} \hat{L}'_i \rangle \, \mathrm{d}t = \sum_{j,k=1}^{2N} l^*_{ij} l_{jk} \Gamma_{jk} \, \mathrm{d}t = \left(l^* \Gamma l^T \right)_{ii} \, \mathrm{d}t, \tag{8.4}$$

$$p_{\text{jump}} = \sum_i p_i = \ \mathrm{tr}(l^* \Gamma l^T) \, \mathrm{d}t. \tag{8.5}$$

Here, the notation $(AB)_{ij}$ is the i, j matrix element of the matrix $C = AB$. That is to say, $(AB)_{ij} = \sum_k A_{ik} B_{kj}$. In algorithms, we will often leave values written in this form, where the added complexity of matrix multiplication is implicit and assumed to be worst-case

scenario $\mathcal{O}(N^3)$, where $N = \dim(A)$.

There are a few interlocking pieces for running the algorithm. Let's assume we start at time $t = 0$, and we take n_{steps} discrete time steps of size $\mathrm{d}t$ such that $n_{\text{steps}}\ \mathrm{d}t = T$ where T is the total evolution time of interest. We need to build up the following pieces: firstly, we need to calculate stochastically a distribution of jumps along with the times they occur. We will assume that we index this as

$$t_{\text{jump}} = \{t_i : i = 1, \ldots, M\} \subset [0, n_{\text{steps}}] \cap \mathbb{Z}, \tag{8.6}$$

$$x_{\text{jump}} = \{x_i : i = 1, \ldots, M\} \subset [0, N] \cap \mathbb{Z}, \tag{8.7}$$

which we interpret as the quantum jump $\hat{L}'_{x_i}$ occurs at time $t = t_i$. Note that because we have discretized both time and space, both x_{jump} and t_{jump} are both *ordered* subsets of integers, and the elements in x_{jump} can repeat.

Next, we can use these sets to define the evolution unitaries as a function of time. Let's suppose we begin with a Hamiltonian $\hat{H}_0 = \hat{H}(t = 0)$. Then we have the initial unitary given by

$$\hat{U}_0 = \exp(i\hat{H}_0\ \mathrm{d}t). \tag{8.8}$$

Every time there is a quantum jump, we perform a gauge transformation of the Hamiltonian. Let's define the following set of jump unitary operators (where we use the convention that operators without hats are the induced maps on $\mathbb{C}^{2N\times 2N}$ the space of covariance matrices):

$$U_{\text{jump}} = \{U_x : x = 1, \ldots, N\}, \tag{8.9}$$

$$(U_x)_{i,j=0}^{2N-1} = \delta_{ij} \times \begin{cases} 1 & i \geq 2x \\ -1 & i < 2x \end{cases}. \tag{8.10}$$

Note here that we have taken the matrix element entries to be zero-indexed and that conjugating by this matrix is equivalent to performing a gauge transformation. Hence, we have well defined update rules:

$$U(t, t + \ \mathrm{d}t) = \left(\prod_{i:t_i<t} U_{x_i} \right) U_0 \left(\prod_{i:t_i<t} U_{x_i} \right)^{\dagger}. \tag{8.11}$$

where $U(t, t+\delta t)$ is the infinitesimal generator taking us from $t \to t + \ \mathrm{d}t$. Note the product is over all integers i such that $t_i < t$. Also, all $U \in U_{\text{jump}}$ mutually commute, so the ordering is irrelevant but we should interpret this as being time ordered. Finally, let's compute the propagator $U(t, 0) \equiv U_t$. This can be understood as

$$U_t = \prod_{i:t_i<t} U(t_i, t_i + \ \mathrm{d}t), \tag{8.12}$$

where again the product should be interpreted as time ordered. Now, the last thing we require is to understand how to compute the covariance matrix at time t. Observe that the form of Eq. (8.1) is the expectation value of a string of Majorana operators in a Gaussian state, and so it can be calculated as a Pfaffian. In general, let's recall that

$$L_{x_i}(t_i) = U_{t_i} L_{x_i}(0) = \sum_{m,n=1}^{2N} l_{x_i,m} (U_{t_i})_{mn} \hat{\gamma}_n. \tag{8.13}$$

Therefore, we can write that

$$\begin{aligned} \langle L_{x_i}(t_i) L_{x_j}(t_j) \rangle &= (l U_{t_i} \Gamma_0 U_{t_j}^T l^T)_{x_i,x_j}, \\ \langle L_{x_i}(t_i)^{\dagger} L_{x_j}(t_j) \rangle &= (l^* U_{t_i} \Gamma_0 U_{t_j}^T l^T)_{x_i,x_j}, \\ \langle L_{x_i}(t_i)^{\dagger} \gamma_m(t) \rangle &= (l^* U_{t_i} \Gamma_0 U_t^T)_{x_i,m}, \end{aligned} \tag{8.14}$$

where Γ_0 is the covariance matrix in the initial condition. The remainder of the relevant

correlators can be found using complex conjugation. Therefore, we can note that, if there have been M jumps, then

$$\langle (\hat{L}')^{\dagger}_{i_1}(t_1)\dots(\hat{L}')^{\dagger}_{i_m}(t_M)\gamma_m(t)\gamma_n(t)\hat{L}'_{i_M}(t_m)\dots\hat{L}'_{i_1}(t_1)\rangle = \mathrm{Pf}(A_{mn}), \tag{8.15}$$

where A is a $(2M+2)\times(2M+2)$ skew symmetric matrix whose elements are pairwise correlators which we have already calculated in Eq. (8.14). From a complexity standpoint, note that for all the different A_{mn} (when we change the two point function in the middle $\hat{O} = \hat{\gamma}_m\hat{\gamma}_n$) the majority of the matrix elements are the same, as they are correlators between the jumps. The only elements that change as a function of m, n are the $4M$ elements that are correlations between the jumps and γ_m, γ_n. Moreover, because they show up in complex conjugate pairs, we only need to calculate $2M$ of them. Hence, if we keep the A matrix in memory, we only need to calculate $\mathcal{O}(M)$ new elements when we switch out which observable we are calculating.

A similar argument goes for when adding a new jump operator. The majority of the matrix elements have already been calculated, and there is no need to calculate them again. Simply augment the size of A and repeat.

Now we understand how to proceed explicitly. First, we initialize empty sets $x_{\mathrm{jump}}, t_{\mathrm{jump}}$ and we compute U_0 via matrix exponentiation. Further, we construct the set of N matrices to define the set U_{jump}. We will define $M(t)$ to be the total number of jumps that has occurred up to time step t (though we will usually drop the explicit time dependence and just call this variable M). We will define the total integration time T. We proceed by repeating the following steps n_{steps} times:

1. Calculate the covariance matrix at time step t using Eqs. (8.14) and (8.15) from the matrix A. Use this to calculate and save any observables of interest. This has complexity

$\mathcal{O}(N^5M + N^2M^3)$ [2], see Algorithm 1.

2. Decide whether or not to perform a jump using the distribution in Eqs. (8.4) and (8.5) stochastically. If we perform a jump, update $x_{\text{jump}}, t_{\text{jump}}$. This has complexity $\mathcal{O}(N^3)$, see Algorithm 2.

3. Calculate $U_{t+\ \mathrm{d}t}$ using Eq. (8.12). This has complexity $\mathcal{O}(N^3)$, see Algorithm 3.

4. Update the matrix A using Eq. (8.14). This has complexity $\mathcal{O}(MN^3)$, see Algorithm 4.

Repeating these steps n_{steps} times gives a single stochastic time evolution. Finally, we will repeat this n_{traj} times to get average values. Summing over all of the steps, we can see that the total complexity for a single time increment is $\mathcal{O}(N^5M + N^2M^3)$. From here, we note that we require a time step $\mathrm{d}t = \mathcal{O}(1/N)$ so that the average number of jumps per time step is much less than one. Hence, $n_{\text{steps}} = \mathcal{O}(TN)$ where T is the total simulation time. From here, we can note that M, the number of jumps that have occurred up to time t is growing linearly in time, so the complexity of each step is also growing linearly in time. Summing over all of them, we find that

$$\sum_{t=1}^{\mathcal{O}(NT)} M^\alpha = \mathcal{O}(NT)^{\alpha+1}. \tag{8.16}$$

Therefore the complexity of the entire algorithm is $\mathcal{O}(N^7T^2 + N^6T^4)$. While not incredible, this at least gives a proof of principle that simulation in polynomial time is possible.

8.2.2 Schrödinger Picture

In this section, we will provide an alternative to the previous algorithms, where we directly increment the state. Because we update the state as opposed to computing observable

2. Note, we take as given that matrix multiplication, exponentiation, as well as taking the Pfaffian are all implemented via stanrd libraries with a complexity that grows as the third power of the matrix dimension.

Algorithm 2: Compute jump decision, complexity $\mathcal{O}(N^3)$

Data: Covariance matrix Γ, current time t
Result: Updated jump list
$B \leftarrow l^* \Gamma l^T \, \mathrm{d}t$; `/* Define matrix` B `*/`
$p_{\text{list}} \leftarrow \{\emptyset\}$; `/* Initialize to the emptyset */`
$p \leftarrow 0$;
$jump \leftarrow$ `False` ; `/* Default to no jump occuring */`
for $i = 0$ **to** $N - 1$ **do**
  $p_{\text{list}} \leftarrow p_{\text{list}} \cup \{B_{ii}\}$;
  $p \leftarrow p + B_{ii}$;
end
$r \leftarrow$ `Rand()` ; `/* random variable between zero and one */`
if $p > r$ **then**
  $t_{\text{jump}} \leftarrow t_{\text{jump}} \cup \{t\}$; `/* Append current time */`
  $r_2 \leftarrow$ `Rand()` ;
  $a \leftarrow 0$;
  $c \leftarrow 0$;
  while $a < r_2$ **do**
    $c \leftarrow c + 1$; `/* select jump location */`
    $a \leftarrow a + (p_{\text{list}})_i$;
  end
  $x_{\text{jump}} \leftarrow x_{\text{jump}} \cup \{c\}$; `/* Append new jump operator */`
  $jump \leftarrow$ `True` ;
end
if $p \leq r$ **then**
  $jump \leftarrow$ `False` ;
end

Algorithm 3: Update unitary, complexity $\mathcal{O}(N^3)$

Data: Previous unitary U_t, $U(t - \mathrm{d}t, t)$, $jump$ variable from Algorithm 2
Result: New Unitary $U_{t+\mathrm{d}t}$
if $jump =$ ***True*** **then**
  $V \leftarrow (U_{\text{jump}})_{(x_{\text{jump}})_{M+1}}$; `/* Gauge transform of most recent jump */`
  $U(t, t + \mathrm{d}t) \leftarrow V U(t - \mathrm{d}t, t) V$; `/* Conjugate update matrix */`
else
  $U(t, t + \mathrm{d}t) \leftarrow U(t - \mathrm{d}t, t)$;
end
$U_{t+\mathrm{d}t} \leftarrow U(t, t + \mathrm{d}t) U_t$; `/* Update time evolution operator */`

Algorithm 4: Update A, complexity $\mathcal{O}(MN^3)$

Data: Previous matrix A of dim $2M+2$, x_{jump}, $jump$ variable from Algorithm 2
Result: New Unitary $U_{t+\ \mathrm{d}t}$
if $jump =$ `True` **then**
  $M_{new} \leftarrow M+1$;
  $A_{new} \leftarrow 0_{2M_{new}+2,2M_{new}+2}$; `/* A increases in dim by 2 */`
  for $i = 0$ **to** $M-1$ **do**
    for $j = 0$ **to** $M-1$ **do**
      $(A_{new})_{ij} = A_{ij}$; `/* Insert old values to new matrix */`
    end
    for $j = M+1$ **to** $2M+1$ **do**
      $(A_{new})_{i,j+2} = A_{ij}$; `/* Insert old values to new matrix */`
    end
  end
  for $j = 0$ **to** M_{new} **do**
    $(A_{new})_{M_{new},j} \leftarrow \langle L_{x_{M_{new}}}(t_{M_{new}})^\dagger L^\dagger_{x_j}(t_j)\rangle$; `/* Compute new values */`
    $(A_{new})_{M_{new}+3,j} \leftarrow \langle L_{x_{M_{new}}}(t_{M_{new}}) L^\dagger_{x_j}(t_j)\rangle$;
  end
  for $j = M_{new}+3$ **to** $2M_{new}+2$ **do**
    $(A_{new})_{M_{new},j} \leftarrow \langle L_{x_{M_{new}}}(t_{M_{new}})^\dagger L_{x_{2M_{new}+2-j}}(t_{2M_{new}+2-j})\rangle$
    $(A_{new})_{M_{new}+3,j} \leftarrow \langle L_{x_{M_{new}}}(t_{M_{new}}) L_{x_{2M_{new}+2-j}}(t_{2M_{new}+2-j})\rangle$;
  end
  $A_{new} \leftarrow (A_{new} - A^T_{new})$; `/* Antisymmetrize */`
else
  $A_{new} \leftarrow A$; `/* If no jump, do nothing */`
end

correlations, we call this the "Schrödinger" picture algorithm. As we will see, it will be much more efficient. The basic idea is to directly integrate the stochastic differential equation [c.f. Eq. (6.29)]:

$$\begin{aligned} \mathrm{d}\Gamma_{mn} = &\left(\Gamma X - X^*\Gamma + \frac{1}{2}\Gamma(X^* - X)\Gamma\right)_{mn} \mathrm{d}t \\ &+ \sum_i \left(\frac{\sum_{kl} l^*_{ik} l_{il} \eta^i_m \eta^i_n (\Gamma_{km}\Gamma_{nl} + \Gamma_{kl}\Gamma_{mn} - \Gamma_{kn}\Gamma_{ml})}{\sum_{kl} l^*_{ik} l_{il} \Gamma_{kl}} - \Gamma_{mn}\right) \mathrm{d}\xi_i. \end{aligned} \tag{8.17}$$

We will take as inputs the matrices X and l. Many of the algorithms we already have can be simply reused, such as computing the jump probability and selecting a jump. The basic idea will be as follows:

1. Use a Runge-Kutta 4^{th} order integration to time evolve under the deterministic dynamics. This has complexity $\mathcal{O}(N^3)$, see Algorithm 5.

2. Decide whether or not to perform a jump using the distribution in Eqs. (8.4) and (8.5) stochastically. This has complexity $\mathcal{O}(N^3)$, see Algorithm 2.

3. Perform a jump. This has complexity $\mathcal{O}(N^3)$, see Algorithm 6.

Algorithm 5: RK4 Integration, complexity $\mathcal{O}(N^3)$

Data: Matrix X and Γ, increment $\mathrm{d}t$
Result: New covariance Γ
Function `Step`$(X,\ \Gamma)$**:**
  return $\Gamma X - X^*\Gamma + \frac{1}{2}\Gamma(X^* - X)\Gamma$;
$k_1 \leftarrow$`Step`$(X,\ \Gamma)$;
$k_2 \leftarrow$`Step`$(X,\ \Gamma + k_1\ \mathrm{d}t/2)$;
$k_3 \leftarrow$`Step`$(X,\ \Gamma + k_2\ \mathrm{d}t/2)$;
$k_4 \leftarrow$`Step`$(X,\ \Gamma + k_3\ \mathrm{d}t)$;
$\Gamma_{new} \leftarrow \Gamma + (k_1 + 2k_2 + 2k_3 + k_4)\ \mathrm{d}t/6$;

As one can see, this is much more efficient, and the entire algorithm runs with complexity $\mathcal{O}(N^4 T)$ (as again $n_{\text{steps}} = \mathcal{O}(NT)$). Moreover, this is completely limited by matrix

Algorithm 6: State update after jump, complexity $\mathcal{O}(N^3)$

Data: Matrices Γ, l, jump location x, jump gauge transform U_x, jump probability p_x
Result: New covariance Γ

```
G ← l*Γ ;
for m = 0 to 2N − 1 do
    for n = 0 to 2N − 1 do
        Γ_{m,n} ← Γ_{m,n} + (G_{x,m} G*_{x,n} − G*_{x,m} G_{x,n})/p_x ;    /* Insert new values */
    end
end
Γ ← U_x Γ U_x ;                                   /* Perform Gauge transformation */
```

multiplication, which is massively parallelizable. Hence, with enough resources this can be significantly reduced.

Finally, as a last note we will comment that for any observable with bounded operator size independent of N, standard Hoeffding bounds tell us that, to fixed additive error, the number of stochastic samples required does not increase with system size. Moreover, one can simultaneously compute any observable that scales at most as N^3 complexity without affecting the asymptotic performance. Examples include the entire covariance matrix, the entanglement entropy, and up to N^3 different connected correlation functions (e.g. all N^2 connected density-density correlation functions).

8.3 Re-summed Time Evolution

In this section, we will outline the algorithms and techniques developed in Chapter 7 and Ref. [233] on numerical implementations that do not require stochastic averaging.

We will begin by calculating the explicit time dynamics for a general matchgate circuit with Pauli noise. This boils down to solving the equation of motion [c.f. Chapter 7]:

$$\partial_t \Gamma_{mn} = -i[H, \Gamma]_{mn} - f_{mn}\Gamma_{mn}. \tag{8.18}$$

The one relevant subtlety here is that the coefficients f_{mn} grow linearly with system size, and so unless the time step is extremely small, this quickly becomes numerically unstable. Therefore, what we will do instead is compute the Trotterized dynamics for a short time increment $\mathrm{d}t$. Then, we can compute the dynamics for both the coherent and incoherent dynamics independently. That is to say, if we define the coherent and incoherent linear channels on the covariance matrix

$$\mathcal{L}_{\mathrm{coh}}[\Gamma] = -i[H, \Gamma], \tag{8.19}$$

$$\mathcal{L}_{\mathrm{inc}}[\Gamma]_{mn} = -f_{mn}\Gamma_{mn}. \tag{8.20}$$

Then we can approximate the total channel $\mathcal{L} = \mathcal{L}_{\mathrm{coh}} + \mathcal{L}_{\mathrm{inc}}$ as

$$e^{\mathcal{L}t} = \lim_{n\to\infty} \left(e^{\mathcal{L}_{\mathrm{coh}}t/2n} e^{\mathcal{L}_{\mathrm{inc}}t/n} e^{\mathcal{L}_{\mathrm{coh}}t/2n}\right)^n. \tag{8.21}$$

For finite n, then we can define $\mathrm{d}t = t/n$, where the total error scales as $n\ \mathrm{d}t^3$, implying that to make this small we need $n = \mathcal{O}(t^{3/2})$. We can calculate both the incoherent and coherent channels explicitly by noting that

$$e^{\mathcal{L}_{\mathrm{coh}}\ \mathrm{d}t/2}\Gamma = U_{\ \mathrm{d}t/2}\Gamma U^{\dagger}_{\ \mathrm{d}t/2}, \tag{8.22}$$

$$U_{\ \mathrm{d}t/2} = e^{-iH\ \mathrm{d}t/2}, \tag{8.23}$$

$$\left(e^{\mathcal{L}_{\mathrm{inc}}\ \mathrm{d}t}\Gamma\right)_{mn} = e^{-f_{mn}\ \mathrm{d}t}\Gamma_{mn}. \tag{8.24}$$

Using this, we can construct an algorithm for a single discrete time step $\mathrm{d}t$, see Algorithm 7, which has complexity $\mathcal{O}(N^3)$, again set by matrix multiplication. Now, however, because the step size does not need to scale with N, we have an overall complexity $N^3T^{3/2}$. Moreover, no sampling overhead is required.

Algorithm 7: Pauli noise time step, complexity $\mathcal{O}(N^3)$

Data: Matrices Γ, f, U
Result: New covariance Γ
Function `coh`$(\Gamma,\ U_{\ \mathrm{d}t/2})$**:**
  return $U_{\ \mathrm{d}t/2}\Gamma U^{\dagger}_{\ \mathrm{d}t/2}$;
Function `inc`$(\Gamma,\ f)$**:**
  $\Gamma_{new} \leftarrow 0_{2N,2N}$;
  for $m = 0$ **to** $2N-1$ **do**
    for $n = 0$ **to** $2N-1$ **do**
      $(\Gamma_{new})_{m,n} \leftarrow e^{-f_{m,n}}\Gamma_{m,n}$;
    end
  end
  return Γ_{new} ;
$\Gamma \leftarrow$ `coh`$(\Gamma,\ U_{\ \mathrm{d}t/2})$;
$\Gamma \leftarrow$ `inc`$(\Gamma,\ f\ \mathrm{d}t)$;
$\Gamma \leftarrow$ `coh`$(\Gamma,\ U_{\ \mathrm{d}t/2})$;

8.4 Sources of Error

Here, we will consider the dominant sources of error, and what parameters can be tuned to minimize them. There are two important sources of error. Errors that occur within a given trajectory, and those that occur from sampling. Sampling errors are discussed in Section E.4, but we will repeat them here for completeness. Let's define an observable O

$$O : \mathcal{H} \to \mathbb{R} \tag{8.25}$$

is a map from the Hilbert space of quantum states[3] to the real numbers. This generalizes to complex numbers by taking the real and imaginary parts. We will assume that O is bounded from both above and below, so that $\lambda_1 < O(|\psi\rangle) < \lambda_2$ for all $|\psi\rangle \in \mathcal{H}$. Examples include any expectation value of any operator, any Renyi entropy, the purity, etc. These are all (non-)

3. Here, we only include pure quantum states as this is what is relevant for us, since every trajectory is pure. However, the discussion that follows also generalizes trivially to maps $O : \mathcal{H}^{\otimes 2} \to \mathbb{R}$ from density matrices to numbers.

linear maps from state vectors to numbers that are bounded both above and below. Next, we will define

$$O' = \frac{2}{\lambda_2 - \lambda_1} O. \tag{8.26}$$

In this case, the function O' has a variance that is bounded above by 1. Now, because the stochastic simulation algorithms are unbiased estimators of the quantum state, then we can apply the Hoeffding bound. That is to say, if we compute n_{traj} stochastic trajectories, and we get a sample distribution $\{O'(|\psi_1\rangle), \ldots O'(|\psi_{n_{\text{traj}}}\rangle)\}$, then for any $\epsilon > 0$ we have that

$$P(|O'_{\text{act}} - \mathbb{E}[O']| > \epsilon) \leq 2 \exp\left(-\frac{n_{\text{traj}} \epsilon^2}{2}\right), \tag{8.27}$$

$$\mathbb{E}[O'] \equiv \frac{1}{n_{\text{traj}}} \sum_{i=1}^{n_{\text{traj}}} O'(|\psi_i\rangle), \tag{8.28}$$

where O'_{act} is the true value. Hence, if wants to know the value O'_{act} to within an error ϵ with probability $1 - \delta$, then this requires a number of samples:

$$n_{\text{traj}} \geq \frac{2 \log(2\delta^{-1})}{\epsilon^2}. \tag{8.29}$$

In turn, this implies that if one wishes to know the original observable O_{act} to within an error ϵ with probability $1 - \delta$, this requires

$$n_{\text{traj}} \geq \frac{(\lambda_2 - \lambda_1)^2 \log(2\delta^{-1})}{2\epsilon^2}. \tag{8.30}$$

Hence, for any *intensive* observable (that has a finite value in the thermodynamic limit), such as the energy density, any local observable, correlation functions, etc., then the required number of samples is independent of the system size, and only depends on the desired precision. This allows us to now observe that the total computational complexity to learn

any bounded observable to additive error ϵ with probability of at least $1-\delta$ of an open spin chain of N qubits evolved for time T has a worst-case computational complexity of

$$\mathcal{O}\left(\frac{N^4 T \log(2\delta^{-1})}{\epsilon^2}\right). \tag{8.31}$$

The second relevant type of error are those that occur within a given trajectory. These come from the discretization of time. For the coherent dynamics, if they are implemented via a p^{th} order Trotter formula or time integrator (Eq. (8.21) is the 2^{nd} order Trotter formula and RK4 in Algorithm 5 is a 4^{th} order time integration method), then the error will generically be

$$\epsilon = \mathcal{O}(T\ \mathrm{d}t^p), \tag{8.32}$$

where $\mathrm{d}t$ is the time increment size, and so one can improve the error by either using a higher order approximation (making p larger) or by using a smaller step size (making $\mathrm{d}t$ smaller).

Another relevant error comes from the jump statistics in the unraveling method. That is to say, we are making the approximation that the number of jumps that occur in any given time step $[t, t+\ \mathrm{d}t)$ is either 0 or 1. The probability of any jump occuring is $\langle \hat{L}_i^\dagger \hat{L}_i \rangle\ \mathrm{d}t$, and is therefore extensive in system size. For simplicity, let's assume Poissonian statistics, and define

$$\bar{\lambda} = \frac{1}{N}\langle \hat{L}_i^\dagger \hat{L}_i \rangle, \tag{8.33}$$

where $\bar{\lambda}$ is an intensive variable. Then we have the probability to have exactly zero or one

quantum jumps in a time step $\mathrm{d}t$ is given by

$$P_0 = \prod_i e^{-\langle \hat{L}_i^\dagger \hat{L}_i \rangle \ \mathrm{d}t} = e^{-N\bar{\lambda} \ \mathrm{d}t}, \tag{8.34}$$

$$P_1 = \sum_j \langle \hat{L}_j^\dagger \hat{L}_j \rangle \ \mathrm{d}t e^{-\langle \hat{L}_j^\dagger \hat{L}_j \rangle \ \mathrm{d}t} \prod_{i \neq j} e^{-\langle \hat{L}_i^\dagger \hat{L}_i \rangle \ \mathrm{d}t} = (N\bar{\lambda} \ \mathrm{d}t) e^{-N\bar{\lambda} \ \mathrm{d}t}. \tag{8.35}$$

The probability to have more than one jump is then

$$P_{>1} = 1 - P_0 - P_1 = \mathcal{O}(N\bar{\lambda} \ \mathrm{d}t)^2. \tag{8.36}$$

Hence, for this error to be small, we need that $\mathrm{d}t = \mathcal{O}(N^{-1})$. Hence, we need the time step to be small compared to system size if we are doing stochastic time evolution.

We note that the p^{th} order time integration error implies that

$$\mathrm{d}t = \frac{T}{n_{\text{steps}}} = \mathcal{O}(T^{-1/p}) \implies n_{\text{steps}} = \mathcal{O}(T^{1+1/p}), \tag{8.37}$$

and that the jump statistics require

$$\mathrm{d}t = \frac{T}{n_{\text{steps}}} = \mathcal{O}(N^{-1}) \implies n_{\text{steps}} = \mathcal{O}(NT). \tag{8.38}$$

This implies that the jump statistics will dominate unless $T > \mathcal{O}(N^p)$, or that time is growing superlinearly in system size. This tends not to be the relevant regime, which is why we assumed that $n_{\text{steps}} = \mathcal{O}(NT)$ in Section 8.2. However, if time is growing superlinearly in N, then the computational complexity can change to properly minimize discretization errors. Ideally, one would want to characterize how expectation values scale as one changes $\mathrm{d}t$, and make it small enough so as to get good convergence.

8.5 Conclusion

We presented a number of different techniques to simulate open quantum many body systems with computational complexity that grows polynomially in system size. We gave two different methods to compute the time evolution using stochastic unravelings, the more optimal version scaling as $\mathcal{O}(N^4T)$ where N is the linear size of the spin chain and T is a dimensionless integration time. Moreover, we also gave an algorithm to simulate the dynamics for Pauli noise that does not require stochastic unraveling and has complexity $\mathcal{O}(N^3T^{3/2})$. Finally, we explained the dominant sources of errors and their scaling with different tunable simulation parameters, and how one can minimize them.

CHAPTER 9

CONCLUSIONS AND DISCUSSION

In this dissertation, we have provided new understanding into the nature of the non-equilibrium steady states and dynamics of open many-body systems.

In the first part, we began by highlighting ways in which a dissipative quantum environment can prepare interesting and useful many-body quantum states. We gave exact solutions for how a structured local bath can dissipatively prepare volume law entanglement in a 1D spin chain in Chapter 2, as well as methods to selectively prepare and entangle topological edge modes in 1 and 2 dimensional cavity arrays in Chapter 3. In Chapter 4, we uncovered a fundamental tradeoff between the amount of entanglement in the steady state and the preparation time scale for any local, Markovian quantum channel. Quite surprisingly, we showed that one can circumvent these bounds using adaptivity or non-Markovianity in Chapter 5. We showed that one only requires a single-bit classical memory in order to prepare a maximally entangled state in finite time, and gave an explicit construction of how one can do this in a discrete circuit. These results give insight into the nature of how steady state properties can give information on dynamical properties in open quantum systems, and vice versa. Moreover, it implies that non-Markovianity can be an extremely powerful resource in the dissipative preparation of quantum many-body states. This is reminiscent and complementary to the well-known results in closed systems where measurement and feedback can be a powerful tool in preparing long-range entanglement. It motivates further study on the utility of classical and quantum memory in the bath to gain further insights into the kind of quantum states that can be prepared and stabilized subject to local constraints.

In the second part, we switched focus to instead try and understand both computationally and analytically the effect of common noise models in many-body physics. In all of the cases we consider, the noise formally makes the system interacting, and so a brute force attempt to compute observables will generically incur an exponential overhead in computational

resources. In Chapter 6, we circumvent this problem by noting that there is a way to remove the interaction by performing a stochastic unraveling of the master equation, similarly to the way that a Hubbard-Stratonovich transformation can formally decouple interactions in the closed system setting. Alternatively, one can think of this as a way of more efficiently packing data: to describe the entire master equation requires knowing 4^N coefficients. We show that these can instead be encoded in N^2 classical random variables, where the information is efficiently stored in the moments of the distribution. Because the distribution is known to be positive, we can sample from it efficiently as well giving a much simpler way to access the quantities of interest, which scales polynomially with system size. In Chapter 7, we show that for a more restrictive class of noise models, one can analytically average this distribution to get exact and closed form equations of motion for arbitrary observables. We use this powerful tool to study the effect of noise on quantum critical states, finding novel emergent phenomena such as an emergent notion of temperature, as well as a new kind of non-equilibrium phase of matter where some operators remain scale-invariant while others are gapped out.

We also note that all of the models that we are able to solve either analytically or via stochastic sampling have a subtle relation to $\mathbb{Z}_2$ gauge theories. In this picture, it naively looks like there is a coupling between the matter and gauge fields, but upon unraveling the gauge fields always update classically. This understanding implies that there is a large class of noisy simulable $\mathbb{Z}_2$ gauge theories, opening the door to numerical and analytical insights into the way that noise interacts with, for example, topologically ordered quantum materials. This could be a powerful technique in understanding everything from the fundamental properties of mixed state topological order, to very practical applications of decoding thresholds in quantum memories. We have only begun to scratch the surface of what can be understood from these new techniques.

APPENDIX A

APPENDIX TO CHAPTER 2

A.1 Fermions

In Chapter 2, we show that when equipped with the appropriate chiral symmetry, the fermionic master equation has a unique, pure steady state. In this section, we provide a detailed proof for this result. Recall the Hamiltonian and jump operators:

$$\hat{H}_F = \sum_{i,j=1}^{2N} H_{ij}\hat{c}_i^\dagger \hat{c}_j = \sum_{\alpha=1}^{N} \epsilon_\alpha (\hat{d}_\alpha^\dagger \hat{d}_\alpha - \hat{d}_{-\alpha}^\dagger \hat{d}_{-\alpha}), \tag{A.1}$$

$$\hat{\beta}_L = u\hat{c}_{\overline{0}} - ve^{i\phi}\hat{c}_{\overline{1}}^\dagger. \tag{A.2}$$

Our strategy is to find a new set of Bogoliubov energy eigenmodes so that the dissipator $\hat{\beta}_L$ cools these modes into their joint vacuum in the steady state limit. In the following, we first show that the Hamiltonian is invariant under a set of Bogoliubov transformations if it has a built-in chiral symmetry, and then discuss conditions for the system to have the desired pure steady state.

A.1.1 General Model

We assume that our system has $2N$ sites, and a chiral symmetry, $\hat{\mathcal{C}}$, such that $\hat{\mathcal{C}}\hat{H}_F\hat{\mathcal{C}}^\dagger = -\hat{H}_F$. This means there are $2N$ eigenmodes, and they come in pairs of energy $\pm\epsilon_\alpha$, where $\hat{\mathcal{C}}\hat{d}_\alpha\hat{\mathcal{C}}^{-1} = \hat{d}_{-\alpha}$. Hence, we can label our eigenmodes $\hat{d}_{\pm\alpha}^\dagger$, where $\alpha = 1, \ldots, N$, and $d_{\pm\alpha}^\dagger$ creates a mode with energy $\pm\epsilon_\alpha$. We will define the unitary transformation $\hat{c}_i = \sum_\alpha \psi_\alpha[i]\hat{d}_\alpha$ to go between position space and energy eigenmode space. We will posit that our system

has the steady state solution $|\psi\rangle_{ss}$ of the form

$$|\psi\rangle_{ss} = \prod_{\alpha>0}(u_\alpha + v_\alpha \hat{d}^\dagger_\alpha \hat{d}^\dagger_{-\alpha})|0\rangle, \tag{A.3}$$

where $|0\rangle$ is the joint vacuum of all of the energy eigenmodes, and $u_\alpha, v_\alpha \in \mathbb{C}$ are yet to be determined constants such that $|u_\alpha|^2 + |v_\alpha|^2 = 1$, to maintain normalization. It is evident by construction that this is a zero energy eigenstate of the Hamiltonian. We can now observe that

$$\begin{aligned}
\hat{\beta}_L|\psi\rangle_{ss} &= (u\hat{c}_{\overline{0}} - ve^{i\phi}\hat{c}^\dagger_{\overline{1}}) \prod_{\alpha>0}(u_\alpha + v_\alpha \hat{d}^\dagger_\alpha \hat{d}^\dagger_{-\alpha})|0\rangle \\
&= \sum_\gamma (u\psi_\gamma[\overline{0}]\hat{d}_\gamma - ve^{i\phi}\psi^*_\gamma[\overline{1}]\hat{d}^\dagger_\gamma) \prod_{\alpha>0}(u_\alpha + v_\alpha \hat{d}^\dagger_\alpha \hat{d}^\dagger_{-\alpha})|0\rangle \\
&= \sum_{\gamma>0} \prod_{\alpha\neq\gamma} (u_\alpha + v_\alpha \hat{d}^\dagger_\alpha \hat{d}^\dagger_{-\alpha}) \\
&\quad \times (u\psi_\gamma[\overline{0}]\hat{d}_\gamma + u\psi_{-\gamma}[\overline{0}]\hat{d}_{-\gamma} - ve^{i\phi}\psi^*_\gamma[\overline{1}]\hat{d}^\dagger_\gamma - ve^{i\phi}\psi^*_{-\gamma}[\overline{1}]\hat{d}^\dagger_{-\gamma})(u_\gamma + v_\gamma \hat{d}^\dagger_\gamma \hat{d}^\dagger_{-\gamma})|0\rangle \\
&= \sum_{\gamma>0} \prod_{\alpha\neq\gamma} (u_\alpha + v_\alpha \hat{d}^\dagger_\alpha \hat{d}^\dagger_{-\alpha}) \\
&\quad \times (uv_\gamma\psi_\gamma[\overline{0}]\hat{d}^\dagger_{-\gamma} - uv_\gamma\psi_{-\gamma}[\overline{0}]\hat{d}^\dagger_\gamma - u_\gamma ve^{i\phi}\psi^*_\gamma[\overline{1}]\hat{d}^\dagger_\gamma - u_\gamma ve^{i\phi}\psi^*_{-\gamma}[\overline{1}]\hat{d}^\dagger_{-\gamma})|0\rangle \\
&= \sum_{\gamma>0} \prod_{\alpha\neq\gamma} (u_\alpha + v_\alpha \hat{d}^\dagger_\alpha \hat{d}^\dagger_{-\alpha}) \\
&\quad \times \left[(uv_\gamma\psi_\gamma[\overline{0}] - u_\gamma ve^{i\phi}\psi^*_{-\gamma}[\overline{1}])\hat{d}^\dagger_{-\gamma} - (uv_\gamma\psi_{-\gamma}[\overline{0}] + u_\gamma ve^{i\phi}\psi^*_\gamma[\overline{1}])\hat{d}^\dagger_\gamma\right]|0\rangle.
\end{aligned} \tag{A.4}$$

If this is a steady state, then it must be zero. Hence, we will require that

$$uv_\gamma\psi_\gamma[\overline{0}] - u_\gamma ve^{i\phi}\psi^*_{-\gamma}[\overline{1}] = uv_\gamma\psi_{-\gamma}[\overline{0}] + u_\gamma ve^{i\phi}\psi^*_\gamma[\overline{1}] = 0. \tag{A.5}$$

This equation will have solutions if, and only if

$$\frac{\psi_\gamma[\overline{0}]}{\psi_{-\gamma}[\overline{0}]} = -\frac{\psi^*_{-\gamma}[\overline{1}]}{\psi^*_\gamma[\overline{1}]}. \tag{A.6}$$

This sets a constraint on both the placement of $\overline{0}, \overline{1}$, as well as on the overall chiral symmetry. Assuming Eq. (A.6) holds, we can define

$$u_\gamma = \frac{u\psi_\gamma[\overline{0}]}{N_\gamma}, \tag{A.7}$$

$$v_\gamma = \frac{ve^{i\phi}\psi^*_{-\gamma}[\overline{1}]}{N_\gamma}, \tag{A.8}$$

$$N_\gamma = \sqrt{u^2|\psi_\gamma[\overline{0}]|^2 + v^2|\psi^*_{-\gamma}[\overline{1}]|^2}, \tag{A.9}$$

where N_γ enforces normalization. These allow us to define the Bogoliubov modes

$$\hat{\beta}_\gamma = u_\gamma \hat{d}_\gamma - v_\gamma \hat{d}^\dagger_{-\gamma}, \tag{A.10}$$

$$\hat{\beta}_{-\gamma} = u_\gamma \hat{d}_{-\gamma} + v_\gamma \hat{d}^\dagger_\gamma. \tag{A.11}$$

We can then rewrite the Hamiltonian nicely as

$$\hat{H}_F = \sum_{\gamma>0} \epsilon_\gamma (\hat{\beta}^\dagger_\gamma \hat{\beta}_\gamma - \hat{\beta}^\dagger_{-\gamma}\hat{\beta}_{-\gamma}). \tag{A.12}$$

Note that $\hat{\beta}_{\pm\gamma}|\psi\rangle_{ss} = 0$, meaning the steady state is the joint vacuum of all of the Bogoliubov modes, and also a 0 energy eigenstate. We can now observe that

$$\begin{aligned}
\hat{\beta}_L &= u\hat{c}_{\overline{0}} - ve^{i\phi}\hat{c}^\dagger_{\overline{1}} = \sum_\gamma u\psi_\gamma[\overline{0}]\hat{d}_\gamma - ve^{i\phi}\psi^*_\gamma[\overline{1}]d^\dagger_\gamma \\
&= \sum_{\gamma>0} u\psi_\gamma[\overline{0}]\hat{d}_\gamma + u\psi_{-\gamma}[\overline{0}]\hat{d}_{-\gamma} - ve^{i\phi}\psi^*_\gamma[\overline{1}]d^\dagger_\gamma - ve^{i\phi}\psi^*_{-\gamma}[\overline{1}]d^\dagger_{-\gamma} \\
&= \sum_{\gamma>0} N_\gamma\left[u_\gamma\hat{d}_\gamma + u_\gamma x_\gamma^{-1}\hat{d}_{-\gamma} + x_\gamma^{-1}v_\gamma d^\dagger_\gamma - v_\gamma d^\dagger_{-\gamma}\right] \\
&= \sum_{\gamma>0} N_\gamma\left[\hat{\beta}_\gamma + x_\gamma^{-1}\hat{\beta}_{-\gamma}\right],
\end{aligned} \tag{A.13}$$

where we have defined $x_\gamma = \psi_\gamma[\overline{0}]/\psi_{-\gamma}[\overline{0}]$, the ratio in Eq. (A.6). For an $A \leftrightarrow B$ hopping model, we can work in a gauge where $x_\gamma = 1$, reproducing the result in Chapter 2. Thus, we can see that the jump operator $\hat{\beta}_L$ cools all of the Bogoliubov modes with a rate fixed by the overlap of the eigenmodes with the dissipation sites, encoded in N_γ. Thus, the steady state will always be uniquely the joint vacuum of the modes $\hat{\beta}_\gamma$, whenever there are no eigenmodes dark to the dissipation sites. The original Hamiltonian had a $U(1)^{2N}$ gauge symmetry, which came from rotating the phases individually of any of the eigenmodes. In a very specific way, the jump operator has broken that gauge freedom to be just $U(1)^N$, as now the relative phase between the positive and negative eigenmodes is fixed in the definition of the Bogoliubov modes. This dissipative symmetry breaking is also apparent in Eq. (A.5), which can only be satisfied for a fixed phase reference between positive and negative eigenmodes. The steady state is Gaussian, and can be characterized by its correlation matrices. In energy eigenmode space, it is simply

$$\langle\hat{d}^\dagger_\alpha\hat{d}_\gamma\rangle = |v_\alpha|^2\delta_{\alpha\gamma}, \qquad \langle\hat{d}_\alpha\hat{d}_\gamma\rangle = u_\alpha v_\gamma\ \mathrm{sgn}(\alpha)\delta_{\alpha,-\gamma}, \tag{A.14}$$

where sgn is the sign function.

Finally, we can immediately observe that the decay rates are set by N_γ, which depends on the overlap of the eigenmodes with the dissipation sites. The dissipative gap, or the slowest decay rate, is therefore determined by $\min_\gamma |N_\gamma|^2$. Normalization tells us this scales like at best $1/N^2$ when the modes are approximately evenly distributed across the lattice, and possibly much worse if the modes are highly localized.

A.1.2 A - B Hopping Models

A very simple, and general model that satisfies the condition in Eq. (A.6) is a lattice that can be divided into two, equal size sublattices, denoted A, B, such that the Hamiltonian $\hat{H}_F$ only allows hopping between the sublattices. For example, any nearest neighbor hopping model on a square lattice can be described this way, where the sublattices are comprised of every other lattice site (or a checkerboard-like pattern in higher dimensions). Now, in this case, we have the chiral symmetry, as mentioned in Chapter 2:

$$\hat{\mathcal{C}} : \hat{c}_i \to \begin{cases} -\hat{c}_i & i \in A \\ \hat{c}_i & i \in B \end{cases}, \tag{A.15}$$

which sends the Hamiltonian $\hat{H}_F \to -\hat{H}_F$. Now, if we let $\overline{0} \in A, \quad \overline{1} \in B$, then we can observe that $\psi_\gamma[\overline{0}] = -\psi_{-\gamma}[\overline{0}]$ and $\psi_\gamma[\overline{1}] = \psi_{-\gamma}[\overline{1}]$, immediately satisfying the constraint Eq. (A.6). We can rewrite the Hamiltonian, as a matrix equation, by defining $\vec{c} = (\hat{c}_1, \ldots \hat{c}_{2N})^T$ where sites $1, \ldots, N \in A$ and $N+1, \ldots 2N \in B$, to get

$$\hat{H}_F = (\vec{c}\,)^\dagger \begin{pmatrix} 0 & V \\ V^\dagger & 0 \end{pmatrix} \vec{c}, \tag{A.16}$$

with V some generic matrix encoding the hopping. One chiral symmetry, $\hat{\mathcal{C}}$, is written above, which simply sends $A \to -A$ and $B \to B$. However, any Hamiltonian with 1 chiral symmetry

in fact has an infinite $U(1)^{2N}$ family of chiral symmetries, since we can send $\hat{d}_\alpha \mapsto e^{i\phi_\alpha}\hat{d}_{-\alpha}$ where the phase is a free, $U(1)$ gauge symmetry for each eigenmode. Now, the correlators in Eq. (A.14) tell us the preferred chiral symmetry should be antisymmetric, as is required by fermionic statistics. Hence, we can define a new chiral symmetry $\hat{S} : \hat{d}_\alpha \mapsto \ \mathrm{sgn}(\alpha)\hat{d}_{-\alpha}$. If we now express this in real space, just like the Hamiltonian, we get that

$$S = \begin{pmatrix} 0 & U \\ -U^\dagger & 0 \end{pmatrix}, \tag{A.17}$$

where U is a unitary $N \times N$ matrix. Now, since this a chiral symmetry, we can conclude that $U^\dagger V U^\dagger = V^\dagger$. This is equivalent to stating that U is the unique, unitary matrix defined by the right polar decomposition of V. I.e., we can rewrite V uniquely as $V = WU$ where W is Hermitian. We should think of U as being a map of the eigenmodes of V, which live on the A lattice, to the eigenmodes of $V^\dagger$, which live on the B lattice, and $U^\dagger$ being the inverse mapping. Because $V, V^\dagger$ have the same spectrum, it makes sense to pair up equal energy eigenmodes. The steady state entanglement structure will then dissipatively pair the two sets of eigenmodes completely through the matrix U. The Hermitian part, W, sets the spectrum, and also determines the constants u_α, v_α.

Now, in the case that $V = V^\dagger$, this reduces to the case in Chapter 2 where we have a mirror symmetry of the lattice. Hence, we know $U = 1$ and so we can immediately read off that the entanglement structure will be the identity, pairing lattice sites reflected to each other by the mirror symmetry. We were able to read off this steady state without solving any of the dynamics, completely through symmetry arguments.

We can now calculate the log negativity, an entanglement monotone, to see that this does indeed obey a volume law. Here, we will define the new modes $\hat{\gamma}_\alpha^\pm = \frac{1}{\sqrt{2}}(\hat{d}_\alpha \pm \hat{d}_{-\alpha})$. These have the nice property of overlapping with only a single sublattice (and are in fact the

eigenmodes of $VV^\dagger$ and $V^\dagger V$, respectively). We can now rewrite the steady state nicely as

$$|\psi\rangle_{ss} = \prod_{\alpha>0} (u_\alpha - v_\alpha(\hat{\gamma}_\alpha^+)^\dagger(\hat{\gamma}_\alpha^-)^\dagger)|0\rangle. \tag{A.18}$$

Now, it is very easy to see that all of the entanglement is between, and not within, the sublattices. The log negativity can now easily be calculated as

$$E_N = \sum_{\alpha>0} \log_2(1 + 2|u_\alpha v_\alpha|), \tag{A.19}$$

which clearly grows linearly with system size.

A.1.3 Fermion Examples

In Chapter 2, we have given the fermionic example of the rainbow state, but more complicated, and higher dimensional lattice models can also create pure, entangled steady states. As mentioned in Chapter 2, many exotic lattice models exhibit the necessary symmetry conditions, including the Hofstader lattice with a quarter flux and the Su-Schriefer-Heeger model, [16].

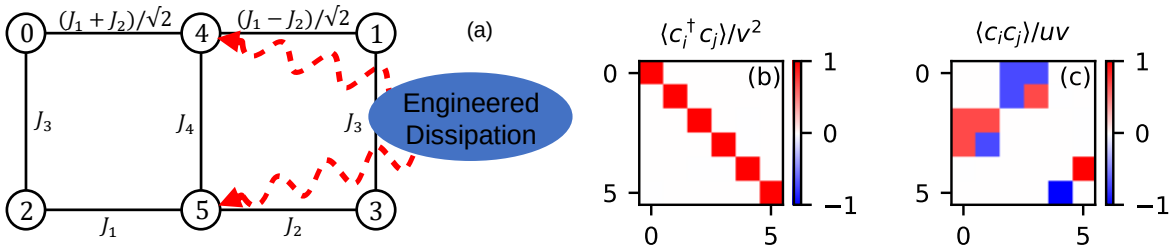

Figure A.1: (a) A 2D nearest neighbor hopping Hamiltonian with two sites coupled to an engineered reservoir. With certain constraints on the hopping amplitudes, the steady state is a pure entangled state with a non-rainbow form. Pictured are 7 possible bonds; $J_1, \ldots, J_4$ are all free parameters, with the remaining 3 constrained by the symmetry conditions. (b) The correlators $\langle \hat{c}_i^\dagger c_j \rangle = v^2 \delta_{ij}$ as expected. (c) The anomalous correlators show Bell state entanglement between the two sites coupled to the dissipation, but sites $0, 1$, are entangled with superpositions of sites $2, 3$.

For one example of a more complex steady state that is not a rainbow, see Fig. A.1. However, note that there is some constraint on the complexity of the correlations we can produce. Any steady state will always be a "generalized" rainbow state, in the sense that correlators always exactly swap two sublattice modes. In a true rainbow state, these modes are individual lattice sites, but they can be more complicated looking in real space [15, 114].

A.2 Qubit Steady State

In Chapter 2, we have shown that a spin version of the general master equation also has a pure, unique steady state. There, we focused on the rainbow, but here we will derive the result in complete generality. Again using a master equation of the form of Eq. (3.2), the

spin system has Hamiltonian and dissipators:

$$\hat{H}_S = -\sum_{i=1}^{2N} J_i \hat{\sigma}_i^+ \hat{\sigma}_{i+1}^- + \text{H. c.}, \tag{A.20}$$

$$\hat{\beta}_L = u\hat{\sigma}_k^- - v\hat{\sigma}_{k+1}^+. \tag{A.21}$$

We take site $2N+1 \equiv 1$ and the spin counterpart of vacuum state $|0\rangle$ via the relation $\hat{\sigma}_k^-|0\rangle \equiv 0$. This gives open boundary conditions if $J_{2N} = 0$, and periodic boundary conditions otherwise. The site k is arbitrary.

A.2.1 Existence

To calculate the steady state solution, we will transform to the fermion model via the Jordan-Wigner transformation (defining fermion number operators $\hat{n}_j \equiv \hat{c}_j^\dagger \hat{c}_j$)

$$\hat{\sigma}_i^- = (-1)^{\sum_{j=k+1}^{i} \hat{n}_j} \hat{c}_i, \tag{A.22}$$

The string operators are chosen such that the fermionic version of the Hamiltonian is quadratic everywhere but on the two sites connected to the dissipation:

$$\hat{H}_S = \sum_{i \neq k} J_i \hat{c}_i^\dagger \hat{c}_{i+1} - J_k \hat{c}_k^\dagger \hat{c}_{k+1} (-1)^{\hat{N}} + \text{H. c.}, \tag{A.23}$$

where $\hat{N} = \sum_i \hat{n}_i$ is the total number operator. The jump operator in Eq. (A.21) then becomes

$$\hat{\beta}_L = -(u\hat{c}_k (-1)^{\hat{N}} - v\hat{c}_{k+1}^\dagger). \tag{A.24}$$

Since phases of Lindblad jump operators do not enter the dynamics, we will drop the overall minus sign henceforth.

Consider the state

$$|\psi\rangle_{ss} = \prod_{\alpha>0} (u_\alpha + v_\alpha d_\alpha^\dagger d_{-\alpha}^\dagger)|0\rangle, \tag{A.25}$$

where $d_\alpha^\dagger$ are the energy eigenmodes of Eq. (A.23) in the even parity sector; i.e., when we replace $(-1)^{\hat{N}}$ with 1. Now, the first thing to observe is that $\hat{N} = \sum_i \hat{c}_i^\dagger \hat{c}_i = \sum_\alpha \hat{d}_\alpha^\dagger \hat{d}_\alpha$, since the energy eigenmodes $\hat{d}_\alpha$ are related to the real space operators by a unitary transformation. Further, since the fermionic steady state is completely paired, the parity operator $(-1)^{\hat{N}}$ will always have eigenvalue 1 acting on the steady state; i.e. $(-1)^{\hat{N}}|\psi\rangle_{ss} = |\psi\rangle_{ss}$. Thus, in the steady state, we can replace $(-1)^{\hat{N}}$ with 1, telling us the state identified above is trivially steady under the fermionic representation of the spin master equation in Eqs. (A.20) and (A.21).

A.2.2 Uniqueness

In the following, we will prove that the steady state identified above via the Jordan-Wigner transformation is also unique. To do this, we must first observe that the parity operator $(-1)^{\hat{N}}$ is a weak symmetry of the dynamics. Now, the Hamiltonian is number conserving, so it is clear that $[(-1)^{\hat{N}}, \hat{H}_S] = 0$. Parity anticommutes with $\hat{c}_i^{(\dagger)}$, so we can observe that

$$\begin{aligned}
&\mathcal{D}[\hat{\beta}_L]\left((-1)^{\hat{N}}\hat{\rho}(-1)^{\hat{N}}\right) \\
&= \frac{1}{2}\left(2\hat{\beta}_L(-1)^{\hat{N}}\hat{\rho}(-1)^{\hat{N}}\hat{\beta}_L^\dagger - \hat{\beta}_L^\dagger\hat{\beta}_L(-1)^{\hat{N}}\hat{\rho}(-1)^{\hat{N}} - (-1)^{\hat{N}}\hat{\rho}(-1)^{\hat{N}}\hat{\beta}_L^\dagger\hat{\beta}_L\right) \\
&= \frac{1}{2}\left(2(-1)^{\hat{N}}\hat{\beta}_L\hat{\rho}\hat{\beta}_L^\dagger(-1)^{\hat{N}} - (-1)^{\hat{N}}\hat{\beta}_L^\dagger\hat{\beta}_L\hat{\rho}(-1)^{\hat{N}} - (-1)^{\hat{N}}\hat{\rho}\hat{\beta}_L^\dagger\hat{\beta}_L(-1)^{\hat{N}}\right) \\
&= (-1)^{\hat{N}}\left(\mathcal{D}[\hat{\beta}_L]\hat{\rho}\right)(-1)^{\hat{N}}.
\end{aligned} \tag{A.26}$$

This, along with commuting with the Hamiltonian, gives us

$$\mathcal{L}[(-1)^{\hat{N}}\hat{\rho}(-1)^{\hat{N}}] = (-1)^{\hat{N}}\mathcal{L}[\hat{\rho}](-1)^{\hat{N}}, \tag{A.27}$$

which is the definition of a weak symmetry. This means that in the steady state, there are no coherences between positive and negative parity states [131], and so it makes sense to decompose this into two different systems - one with $(-1)^{\hat{N}} = 1$ (even parity) and one with $(-1)^{\hat{N}} = -1$ (odd parity).

If we define $\hat{P}_{\text{ev}}$ as the projector into the even parity subspace, we know that by the chiral symmetry arguments in Appendix A.1 (Eq. (A.12)), we can rewrite the even-parity Hamiltonian $\hat{P}_{\text{ev}}\hat{H}_S\hat{P}_{\text{ev}}$ as a sum over the Bogoliubov modes $\sum_\alpha \epsilon_\alpha \hat{\beta}_\alpha^\dagger \hat{\beta}_\alpha$, meaning it conserves these modes. Next, define $\hat{\tilde{\beta}}_A = u\hat{c}_k - v\hat{c}_{k+1}^\dagger$ and $\hat{\tilde{\beta}}_B = u\hat{c}_{k+1} + v\hat{c}_k^\dagger$, its orthogonal compliment. Here, $\hat{\tilde{\beta}}_A$ corresponds to the jump operator $\hat{\beta}_L$ in the even subspace.

Next, observe that

$$\hat{P}_{\text{ev}}\hat{H}_S\hat{P}_{\text{ev}} - (1-\hat{P}_{\text{ev}})\hat{H}_S(1-\hat{P}_{\text{ev}}) = -2J_k\hat{c}_k^\dagger\hat{c}_{k+1} + \text{H. c.} = -2J_k\hat{\beta}_A^\dagger\hat{\beta}_B + \text{H. c.}, \tag{A.28}$$

where $(1-\hat{P}_{\text{ev}})$ projects into the odd parity space. Thus, while $\hat{P}_{\text{ev}}\hat{H}_S\hat{P}_{\text{ev}}$ conserves Bogoliubov excitations, $(1-\hat{P}_{\text{ev}})\hat{H}_S(1-\hat{P}_{\text{ev}})$ may not. This is because $\hat{\tilde{\beta}}_B$ is a sum of both $\hat{\beta}_\gamma$ and $\hat{\beta}_\gamma^\dagger$.

Now, $\hat{\tilde{\beta}}_A$ is the jump operators in the even parity sector. In the odd parity sector, the jump operators is

$$-\hat{\tilde{\beta}}_A' = u\hat{c}_k + v\hat{c}_{k+1}^\dagger = (u^2-v^2)\hat{\tilde{\beta}}_A + 2uv\hat{\tilde{\beta}}_B^\dagger, \tag{A.29}$$

and so we see that the jump operator in the odd-parity section is a linear combination of both heating and cooling. When $u \neq v$, the odd parity section has both heating and cooling

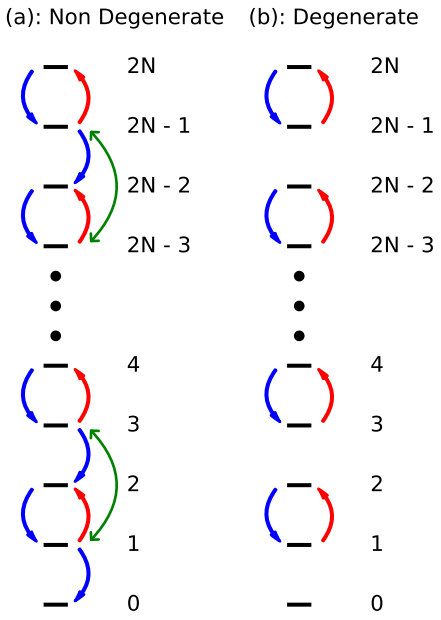

Figure A.2: Plotted are the set of $2N+1$ possible values for the number of Bogoliubov modes excited, where the m^{th} state level has degeneracy $\binom{2N}{m}$. (a) shows for the non degenerate case where the steady state is unique and corresponds to the vacuum state at the bottom of the tower. The blue arrows show cooling, the red heating, and the green are Hamiltonian interactions. The arrows on the left of the tower begin in even parity states, and the ones on the right side begin in odd parity states. (b) shows the same, except now $u = v$ with a symmetric lattice. This corresponds to odd parity states having only heating and no Hamiltonian interactions, creating $N + 1$ steady states that exist in the manifold spanned by $\{2m, 2m - 1\}$ Bogoliubov excitations.

elements, while the even parity sector is strictly cooling. If we construct a tower of Hilbert spaces labeled by the number of Bogoliubov excitations from 0 to $2N$, then we can break the dynamics down into even and odd parity sections. When the parity is even, the Hamiltonian conserves the number of excitations, and the dissipation only allows for cooling. In the odd parity section, the Hamiltonian can create and destroy pairs of excitations - connecting the levels $2m + 1 \to 2m - 1, 2m + 3$, and the dissipation allows for both heating and cooling of single excitations, connecting the level $2m + 1 \to 2m, 2m + 2$. Thus, we can see that every

level in the tower can decay to another level except for the manifold with no Bogoliubov excitations. Hence, the unique steady state is the Bogoliubov vacuum, see Fig. A.2a.

A.2.3 Steady State Degeneracy

If the Hamiltonian obeys a mirror symmetry, then it turns out that $\hat{\tilde{\beta}}_B$ can be expressed solely as a sum over $\hat{\beta}_\gamma$; hence the odd parity Hamiltonian becomes Bogoliubov number conserving. Then, exactly when $u = v$, we have that the odd-parity section is *purely* heating, since in that limit we have $\hat{\tilde{\beta}}'_A = -\hat{\beta}^\dagger_B$. Since $\hat{H}$ conserves Bogoliubov number, we know that if you start with $2m$ Bogoliubov modes, then the dynamics can take you into the space with $2m-1$ excitations through the purely cooling jump operator. Then, you enter the odd parity section, and so now the dynamics can only take you into the space with $2m$ excitations, through the purely heating jump operator. This creates a set of $N+1$ isolated manifolds; numerically, we find there are exactly $N+1$ steady states. Further, we know that each steady state must be an incoherent mixture of having $2m$ and $2m-1$ Bogoliubov excitation, or having exactly zero Bogoliubov excitations. Hence, the only *pure* steady state is the Bogoliubov vacuum. Finally, we can see that the only way to end up in the Bogoliubov vacuum is to start there since $\text{ceil}(N_{\text{Bog}}/2)$ is conserved, where ceil rounds up to the nearest integer, and N_{Bog} is the number of Bogoliubov excitations, see Fig. A.2b. This emergent degeneracy is the cause for the long time scale dynamics observed in Chapter 2.

A.2.4 Qubits in 2D

It was shown in Appendix A.1.3 that the fermions relaxed into pure states regardless of lattice dimension. It is not immediately clear whether or not this would work for qubits, though. To identify the qubit steady state, we relied heavily on using the Jordan-Wigner transformation from the qubits into non-interacting fermions. In a 2D lattice, there is no way for the Jordan-Wigner string operators to drop out of the fermion Hamiltonian, meaning

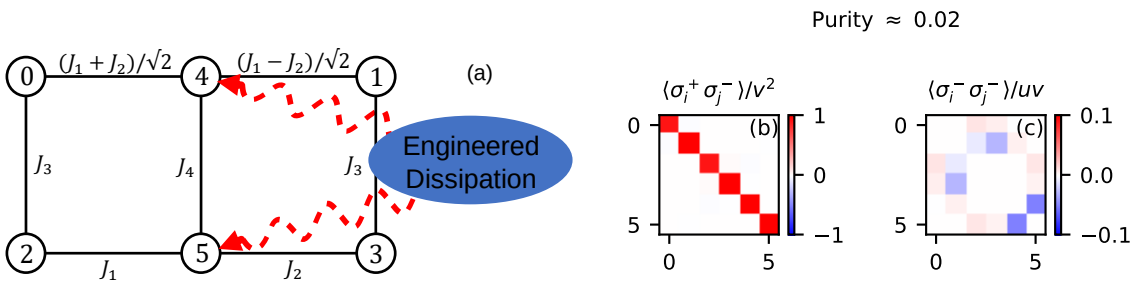

Figure A.3: (a) A 2D nearest neighbor XY spin Hamiltonian with two sites coupled to an engineered reservoir. The master equation in identical to that in Fig. A.1, where we have simply replaced $\hat{c}_i^{(\dagger)} \to \hat{\sigma}_i^{\pm}$. (b) and (c) show the spin correlators in the steady state, and also notes that the purity in the steady state $\mathrm{tr}(\rho^2) \approx 0.02$. Despite being the same lattice structure as the fermion in Fig. A.1, the steady state is no longer pure and has vastly different anomalous correlators.

the qubits will always be represented by interacting fermions. For this reason, one does not get the same steady state when going from 2D fermions to 2D qubits. A very simple way to see this is shown in Fig. A.3, where we repeat the exact same structure shown in Fig. A.1, but use spin operators in place of fermionic ones. The steady state is no longer pure, and the anomalous correlators of the qubits $\langle \hat{\sigma}_i^- \hat{\sigma}_j^- \rangle$ are very different than those of the fermions $\langle \hat{c}_i \hat{c}_j \rangle$.

A.3 Experimental Implementation

A.3.1 Sideband Driving

The correlated dissipator required in our scheme can be readily generated by coupling the two qubits to a single lossy cavity mode (i.e. an engineered reservoir), and driving the appropriate sideband processes. There are various possible ways to implement the sideband driving: one could either drive the coupling strengths between the qubits and the cavity, or modulate the qubit frequency. Here we present a protocol that makes use of qubit frequency modulation, which can be realized via, e.g., flux tunable transmon qubits.

We consider two qubits (Pauli operators $\hat{\sigma}_1^z$ and $\hat{\sigma}_2^z$) coupled to a lossy cavity mode

(annihilation operator $\hat{a}$, frequency ω_c, loss rate κ). The qubit 1 (2) has resonance frequency ω_1 (ω_2) and is coupled to the cavity mode with coupling strength g_1 (g_2), and we drive the frequencies of qubits 1 and 2 at the red and blue sideband frequencies $\omega_r = \omega_1 - \omega_c$ and $\omega_b = \omega_2 + \omega_c$, respectively (Fig. A.4). The system Hamiltonian in the lab frame is given by

$$\hat{H} = \omega_c \hat{a}^\dagger \hat{a} + \frac{1}{2}(\omega_1 + \xi_1 \omega_r \cos(\omega_r t))\hat{\sigma}_1^z + \frac{1}{2}(\omega_2 + \xi_2 \omega_b \cos(\omega_b t))\hat{\sigma}_2^z + (\hat{a} + \hat{a}^\dagger)(g_1 \hat{\sigma}_1^x + g_2 \hat{\sigma}_2^x). \tag{A.30}$$

$\xi_{1,2}$ are dimensionless drive strengths. Going into the rotating frame defined by the unitary transformation

$$\hat{\mathcal{U}} = \exp\left\{-i\omega_c t \hat{a}^\dagger \hat{a} - \frac{i}{2}[\omega_1 t + \xi_1 \sin(\omega_r t)]\hat{\sigma}_1^z - \frac{i}{2}[\omega_2 + \xi_2 \sin(\omega_b t)]\hat{\sigma}_2^z\right\}, \tag{A.31}$$

the rotating frame Hamiltonian $\hat{H}'$ is given by

$$\begin{aligned}
\hat{H}' &= \hat{\mathcal{U}}^\dagger \hat{H} \hat{\mathcal{U}} - i\hat{\mathcal{U}}^\dagger \dot{\hat{\mathcal{U}}} \\
&= g_1 \left(e^{-i\omega_c t}\hat{a} + e^{i\omega_c t}\hat{a}^\dagger\right) e^{-i\omega_1 t - i\xi_1 \sin(\omega_r t)} \hat{\sigma}_1^- + \text{H. c.} \\
&\quad + g_2 \left(e^{-i\omega_c t}\hat{a} + e^{i\omega_c t}\hat{a}^\dagger\right) e^{-i\omega_2 t - i\xi_2 \sin(\omega_b t)} \hat{\sigma}_2^- + \text{H. c.}
\end{aligned} \tag{A.32}$$

Making use of the identity

$$e^{i\xi \sin(\omega t)} = \sum_{n=-\infty}^{\infty} J_n(\xi) e^{in\omega t}, \tag{A.33}$$

where $J_n(\xi)$ are Bessel functions, we can rewrite the rotating frame Hamiltonian as

$$\hat{H}' = \left(e^{-i\omega_c t}\hat{a} + e^{i\omega_c t}\hat{a}^\dagger\right) \sum_{n=-\infty}^{\infty} \left[g_1 J_n(\xi_1) e^{-i(\omega_1 + n\omega_r)t} \hat{\sigma}_1^- + g_2 J_n(\xi_2) e^{-i(\omega_2 + n\omega_b)t} \hat{\sigma}_2^-\right] + \text{H. c.} \tag{A.34}$$

Since we drive the qubits at sideband resonances $\omega_r = \omega_1 - \omega_c$ and $\omega_b = \omega_2 + \omega_c$, the rotating terms are resonant when $n = -1$. We can rewrite this as

$$\hat{H}' = \hat{a}^\dagger(g_1'\hat{\sigma}_1^- + g_2'\hat{\sigma}_2^+) + \text{H. c.} + \hat{V}(t), \tag{A.35}$$

where $g_i' = J_{-1}(\xi_i)g_i$ $(i = 1, 2)$, and $\hat{V}(t)$ contains only rapidly oscillating terms at frequencies $\omega \gg g_1', g_2'$. Therefore, we can make the standard rotating wave approximation, and treat $\hat{V}(t)$ as a perturbation of order the coupling strength divided by the oscillation frequency, and neglect it [279, 280]. This approximation has also been shown to match experiment extremely well [281].

Now that we have found the appropriate Hamiltonian for our system, we can consider the dissipative dynamics. We have considered the cavity mode $\hat{a}$ is leaky with a loss rate κ, which can be expressed using a master equation of the form of Eq. (3.2):

$$\dot{\hat{\rho}} = -i[\hat{H}', \hat{\rho}] + \kappa\mathcal{D}[\hat{a}]\hat{\rho}. \tag{A.36}$$

From here, we trace out the cavity, leaving an effective master equation for only the spins. To do this we will assume that $\kappa \gg g_1', g_2'$, meaning that the cavity is highly damped. Using standard elimination techniques [94, 282], we are then left with the effective dynamics for $\hat{\chi} = \text{tr}_{\text{cav}}\hat{\rho}$:

$$\dot{\hat{\chi}} = \frac{4g^2}{\kappa}\mathcal{D}[\hat{L}]\hat{\chi}, \tag{A.37}$$

$$\hat{L} = u\hat{\sigma}_1^- + v\hat{\sigma}_2^+, \tag{A.38}$$

where $g^2 = g_1'^2 + g_2'^2$ and $u = g_1'/g, v = g_2'/g$. This generalizes the result in [40], and

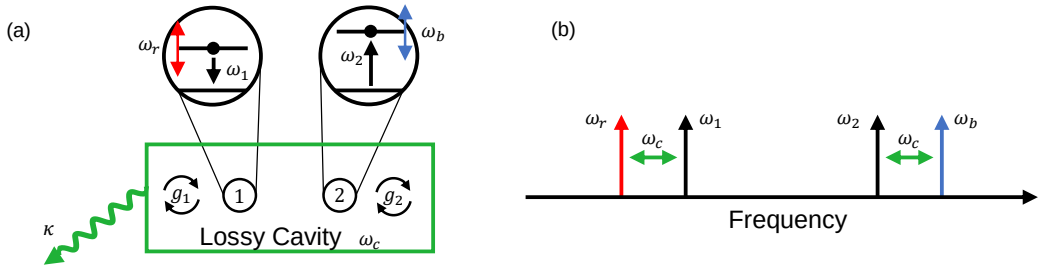

Figure A.4: (a) By placing two qubits $1, 2$ with frequencies $\omega_{1,2}$ in a lossy cavity with frequency ω_c and decay rate κ, then modulating the qubit frequencies with red and blue sidebands $\omega_{r,b}$, we can engineer the desired dissipation. (b) Shows a schematic of the necessary frequencies needed for the design.

agrees exactly in the case $v^2 = 0$. Intuitively, the effective dynamics tell us that the only resonant interactions where the cavity gains a photon is either when spin 1 loses a photon or spin 2 gains a photon. Therefore, if we assume the cavity is highly damped and almost always in the ground state, whenever it loses a photon, it means that one of those two resonant processes occurred, but we have lost the "which spin" information. This gives the coherent sum of the two operators. The rate $\frac{4g^2}{\kappa}$ can be derived from a simple Fermi's golden rule calculation, as is shown in [40].

A.3.2 Additional Dissipation

We now consider the robustness of our steady state in the presence of additional local dissipation. In Fig. A.5, we consider the effects of local relaxation (dephasing) with a strength γ_{rel} (γ_ϕ) by plotting the concurrence between pairs of sites $(l, -l)$. In all of the plots, the engineered dissipation couples to the first bond with a strength Γ, and the Hamiltonian has hopping strength $J = \Gamma$. The master equation is now given by

$$\mathcal{L}[\hat{\rho}] = -i[\hat{H}, \hat{\rho}] + \Gamma \left(\mathcal{D}[\hat{\beta}_A] + \mathcal{D}[\hat{\beta}_B] \right) \hat{\rho} + \sum_i \mathcal{D}[\hat{L}_i^\alpha] \hat{\rho}, \tag{A.39}$$

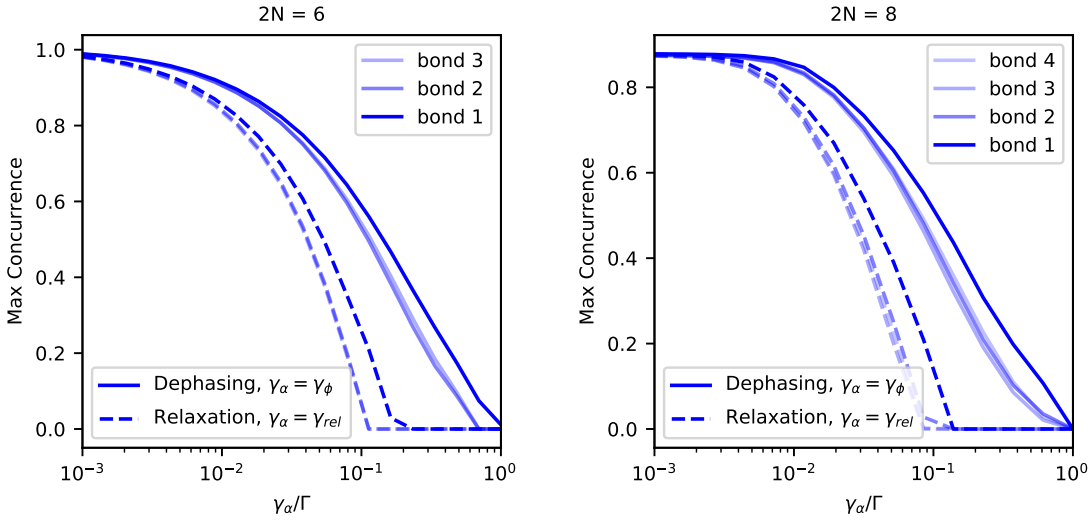

Figure A.5: Shown is the concurrence across the 'rainbows' of the rainbow state with additional dephasing and relaxation for a 6 (left) and 8 (right) site lattice. Note that the first bond, coupled directly to the engineered dissipator, is more persistent, and the other two are identical, despite being different distances from the reservoir.

where the qubit lattice Hamiltonian $\hat{H}$ and the dissipator $\hat{\beta}_L$ is again given by

$$\hat{H} = J\sum_j \hat{\sigma}_j^+\hat{\sigma}_{j+1}^- + \text{H. c.}, \quad \hat{\beta}_L = u\hat{\sigma}_{-1}^- + v\hat{\sigma}_1^+. \tag{A.40}$$

The local dephasing (relaxation) dissipator $\hat{L}_i^\alpha$ for $\alpha = \phi$ ($\alpha = \text{rel}$) are given by

$$\hat{L}_i^\phi = \sqrt{\gamma_\phi}\hat{\sigma}_i^z, \quad \hat{L}_i^{\text{rel}} = \sqrt{\gamma_{\text{rel}}}\hat{\sigma}_i^-. \tag{A.41}$$

We choose u, v to maximize concurrence on each of the entanglement bonds, starting from the 1st, innermost bond, to the Nth, outermost bond in a $2N$ particle lattice.

Taking data from a recent publication characterizing a flux-tunable transmon qubit array [36], we can estimate the capability of current experiments to perform our protocol. We will assume the transmon qubits are flux-tunable from $2\pi\times 3.5-6$ GHz, with $\gamma_{\text{rel}}/2\pi \sim 4-8$kHz and $\gamma_\phi/2\pi \sim 40-80$kHz, and tunnel coupling of up to $J/2\pi \sim 10$MHz. We will take the

lossy cavity to couple to the qubits with strength of $g/2\pi = 15 - 20$ MHz, and have a decay rate $\kappa/2\pi \sim 10$ MHz.

With these parameters, assuming a qubit frequency of 4.75 GHz and a cavity frequency of 2.75 GHz, we get red and blue sideband frequencies of $\omega_{r(b)} = 2(7.5)$ GHz. Given the tunable range of the qubits, the maximum amplitude of the drives is 1.25GHz, giving $\zeta_{1(2)} \approx 0.63(0.17)$. This gives the maximal values of $g'_{1(2)} \approx 5.95(1.66)$MHz. This would give an upper bound of $g_{\text{eff}} \approx 6$ MHz. It would therefore be very reasonable to have Γ_{eff} on the order of a few MHz, making $\gamma_\phi/\Gamma_{\text{eff}} \sim O(10^{-2})$ and $\gamma_{\text{rel}}/\Gamma_{\text{eff}} \sim O(10^{-3})$. From Fig. A.5, we can see that this would put an 8 qubit chain within reach of current experiments.

APPENDIX B

APPENDIX TO CHAPTER 3

B.1 Loss-induced instability in 2-site models

We can investigate unconventional instabilities just at the 2 mode level. As alluded to in Chapter 3, the dissipative pairing interaction can be thought of as local loss under the proper change of frame. Consider a jump operator:

$$\hat{L}/\sqrt{\kappa} = \hat{a} + \eta\hat{b}^\dagger, \tag{B.1}$$

where we assume $\eta < 1$ unless specified otherwise. We can make a two-mode squeezing transformation, and define new modes

$$\hat{a}' = \frac{1}{\sqrt{1-\eta^2}}(\hat{a} + \eta\hat{b}^\dagger), \tag{B.2}$$

$$\hat{b}' = \frac{1}{\sqrt{1-\eta^2}}(\hat{b} + \eta\hat{a}^\dagger). \tag{B.3}$$

One can easily check that these obey the canonical commutation relations, and now $\hat{L} = \sqrt{\kappa(1-\eta^2)}\hat{a}'$, giving local loss. However, such a transformation will generically generate active parametric amplifier terms if one starts from a particle-conserving detuning Hamiltonian:

$$\hat{a}^\dagger\hat{a} + \hat{b}^\dagger\hat{b} = \frac{1}{1-\eta^2}(\hat{a}'^\dagger - \eta\hat{b}')(\hat{a}' - \eta\hat{b}'^\dagger) + \frac{1}{1-\eta^2}(\hat{b}'^\dagger - \eta\hat{a}')(\hat{b}' - \eta\hat{a}'^\dagger) \tag{B.4}$$

$$= \hat{a}'^\dagger\hat{a}' + \hat{b}'^\dagger\hat{b}' - \frac{2\eta}{1-\eta^2}\left(\hat{a}'\hat{b}' + \hat{a}'^\dagger\hat{b}'^\dagger\right). \tag{B.5}$$

We believe that the frame presented in Chapter 3 is a more intuitive way to understand the dynamics, since all of the steady state features can be read off from the eigenmodes of

a passive, hopping Hamiltonian. When we work instead in the frame of the local loss, the importance of the Hamiltonian eigenmodes is no longer as immediate. However, if one insists on working in this frame, we can still explore dynamical instabilities. We can rewrite such a stable parametric amplifier Hamiltonian as:

$$\hat{H} = \Delta(\hat{a}^\dagger \hat{a} + \hat{b}^\dagger \hat{b}) + \lambda(\hat{a}^\dagger \hat{b}^\dagger + \hat{a}\hat{b}). \tag{B.6}$$

When positive parameters satisfy $\lambda < \Delta$, this Hamiltonian can be diagonalized via a Bogoliubov transformation with eigenmode energies $\pm\sqrt{\Delta^2 - \lambda^2}$, describing stable oscillatory dynamics. Now, let's add some local loss, but only to a single cavity mode. The mode amplitudes thus satisfy linear equations of motion ($a \equiv \langle \hat{a} \rangle, a^* \equiv \langle a^\dagger \rangle$, etc.):

$$\partial_t \begin{pmatrix} a \\ b^* \end{pmatrix} = \begin{pmatrix} -i\Delta - \kappa & -i\lambda \\ i\lambda & i\Delta \end{pmatrix} \begin{pmatrix} a \\ b^* \end{pmatrix}. \tag{B.7}$$

Then we find that the eigenvalues of this new problem are $-\frac{\kappa}{2} \pm i\sqrt{\left(\Delta - i\frac{\kappa}{2}\right)^2 - \lambda^2}$. Interestingly enough, one of these always has a positive real part. Moreover, if we consider the more general scenario that we damp both modes with rates κ_a, κ_b, then, defining the sum and difference $\kappa = \frac{\kappa_a + \kappa_b}{2}$ and $\delta\kappa = \frac{\kappa_a - \kappa_b}{2}$, one can show that instability arises whenever:

$$\frac{\delta\kappa^2}{\kappa^2} \geq \frac{\kappa^2 + \Delta^2 - \lambda^2}{\kappa^2 + \Delta^2}. \tag{B.8}$$

Note that this matches our intuition in all the limits we currently have considered: if $\kappa_a = 0$ or $\kappa_b = 0$, then $\kappa = |\delta\kappa|$, and so we *always* have instabilities, since the RHS is always less than 1. If instead we take $\kappa_a = \kappa_b$, then we simply have the standard par-amp instability point at $\lambda^2 = \Delta^2 + \kappa^2$.

This is a seemingly simple instability, that can be seen just at the level of 2×2 matrices.

However, it is still surprising, as we have taken a stable Hamiltonian, added to it some local loss, and made it unstable.

To understand more physically the instability mechanism, it is useful to look at the limiting regimes where either the Hamiltonian or the dissipative terms becomes the dominant contribution. For concreteness, we focus on the completely unbalanced case, where $\kappa_b = 0$. When κ_a is sufficiently small, we can think of it perturbatively as splitting the two eigenmodes. However, the eigenoperators are two-mode squeezed by the Hamiltonian, so for one of the eigenmodes, the loss on mode a acts effectively as cooling, and for the other as heating, giving us instability. When instead κ_a becomes dominant, we could adiabatically eliminate a to obtain an effective single-mode model consisting of b. In this latter case, it is straightforward to see that b experiences effective heating, since the two original modes are parametrically coupled, again leading to instabilities.

Now, let's consider a dissipative interaction generated by the jump operator $\hat{L}/\sqrt{2\kappa} = \hat{a} + \eta\hat{b}^\dagger$. Then adding to this a beam-splitter Hamiltonian $J_1(\hat{a}^\dagger\hat{b} + \hat{b}^\dagger\hat{a})$ and a Hermitian parametric amplifier $J_2(\hat{a}^\dagger\hat{b}^\dagger + \hat{a}\hat{b})$, we get a dynamical matrix of the form:

$$\partial_t \begin{pmatrix} a \\ a^* \\ b \\ b^* \end{pmatrix} = \begin{pmatrix} -\kappa & 0 & iJ_1 & -iJ_2 + \kappa\eta \\ 0 & -\kappa & iJ_2 + \kappa\eta & -iJ_1 \\ iJ_1 & -iJ_2 - \kappa\eta & \kappa\eta^2 & 0 \\ iJ_2 - \kappa\eta & -iJ_1 & 0 & \kappa\eta^2 \end{pmatrix} \begin{pmatrix} a \\ a^* \\ b \\ b^* \end{pmatrix}. \tag{B.9}$$

It is interesting to note that if we instead work in the quadratures-like basis $\hat{q}_a^\pm = (e^{i\phi}\hat{a} \pm \hat{a}^\dagger)/\sqrt{2}$ and $\hat{q}_b^\pm = (\pm\hat{b} + e^{i\phi}\hat{b}^\dagger)/\sqrt{2}$ where $\cos\phi = \frac{J_2}{J_1}$, then we can rewrite the dynamical

matrix as

$$\partial_t \begin{pmatrix} q_a^+ \\ q_b^+ \\ q_a^- \\ q_b^- \end{pmatrix} = \begin{pmatrix} -\kappa & J_\Delta + \kappa\eta & 0 & -2iJ_2 \\ -J_\Delta - \kappa\eta & \kappa\eta^2 & 2iJ_2 & 0 \\ 0 & 0 & -\kappa & -J_\Delta + \kappa\eta \\ 0 & 0 & J_\Delta - \kappa\eta & \kappa\eta^2 \end{pmatrix} \begin{pmatrix} q_a^+ \\ q_b^+ \\ q_a^- \\ q_b^- \end{pmatrix}. \tag{B.10}$$

We have defined $J_\Delta \equiv \sqrt{J_1^2 - J_2^2}$. This dynamical matrix can be equivalently rewritten as

$$\begin{pmatrix} -\frac{\kappa}{2}(1+\eta^2) & J_\Delta + \kappa\eta & 0 & -2iJ_2 \\ -J_\Delta - \kappa\eta & \frac{\kappa}{2}(1+\eta^2) & 2iJ_2 & 0 \\ 0 & 0 & -\frac{\kappa}{2}(1+\eta^2) & -J_\Delta + \kappa\eta \\ 0 & 0 & J_\Delta - \kappa\eta & \frac{\kappa}{2}(1+\eta^2) \end{pmatrix} - \frac{\kappa}{2}(1-\eta^2)\hat{\mathbf{1}}, \tag{B.11}$$

where we straightforwardly see the $\mathcal{PT}$-dimer structure in the upper-left and lower-right blocks. Hence, a bit of algebraic manipulation tells us we get an exceptional point (EP) when

$$\eta = \pm\left(1 - \sqrt{\frac{2}{\kappa}}(J_1^2 - J_2^2)^{1/4}\right), \tag{B.12}$$

so that we can always find a value of η to realize an EP whenever $J_1^2 > J_2^2$, which occurs at $-\kappa(1-\eta^2)/2$. Further, tuning past the EP, we reach an instability point at:

$$\eta = \frac{\sqrt{\kappa^2 + J_1^2 - J_2^2} - \kappa}{\sqrt{J_1^2 - J_2^2}}, \tag{B.13}$$

as can be seen in Fig. B.1.

We now consider replacing the correlated dissipation with uncorrelated heating and cooling on the two sites. This would be equivalent to setting $\kappa\eta = 0$, while leaving $\kappa\eta^2$ unchanged

in Eq. (B.11), which simply shifts the EP to the point where $\frac{\kappa}{2}(1+\eta^2) = \sqrt{J_1^2 - J_2^2}$. However, this also means that if $\frac{2}{\kappa}\sqrt{J_1^2 - J_2^2} < 1$, the EP disappears under the uncorrelated dissipation, but remains robust for the correlated case. This can be seen in Fig. B.1.

Another interesting case to consider is instead of a beam-splitter and parametric amplifier, let's consider just a detuned beam-splitter interaction. By setting $J_2 = 0$ in Eq. (B.11), we see that when the detuning is zero, then we would expect an EP. One can show that adding the dissipative interaction makes the EP robust to any detuning, and without it any detuning immediately destroys the EP.

We can similarly write down the dynamical matrix for the case without dissipative interaction, as

$$\partial_t \begin{pmatrix} a \\ a^* \\ b \\ b^* \end{pmatrix} = \begin{pmatrix} -\kappa + i\delta & 0 & iJ & \kappa\eta \\ 0 & -\kappa - i\delta & \kappa\eta & -iJ \\ iJ & -\kappa\eta & \kappa\eta^2 - i\delta & 0 \\ -\kappa\eta & -iJ & 0 & \kappa\eta^2 + i\delta \end{pmatrix} \begin{pmatrix} a \\ a^* \\ b \\ b^* \end{pmatrix}, \tag{B.14}$$

where J denotes the beam-splitter strength, and δ detuning between the modes. Interestingly, Eq. (B.14) actually can have two exceptional points, which occur at

$$\frac{\eta^2}{(\eta^2-1)^2} = \frac{16J^4 + \kappa^4 + 32J^2\delta^2 + 8\kappa^2\delta^2 + 16\delta^4 - 8J^2\kappa^2}{64J^2\kappa^2}, \quad \text{and} \quad \frac{\eta^2}{(\eta^2-1)^2} = \frac{\delta^2}{4J^2}. \tag{B.15}$$

When $\delta \neq 0$, these exceptional points remain. This can be seen in Fig. B.1. Without the dissipative interaction, and only incoherent gain and loss, the dynamical matrix takes the

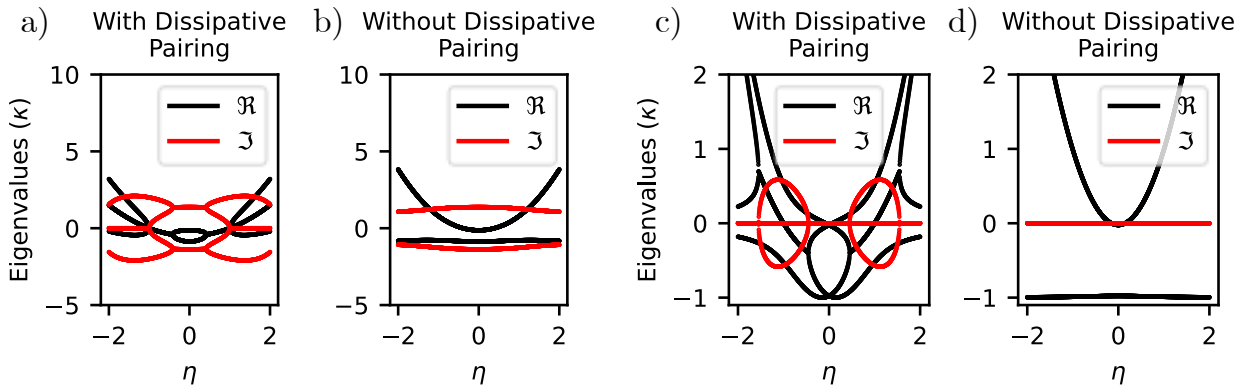

Figure B.1: a) and b) show the real and imaginary spectra for the dynamical matrix with a beamsplitter ($J_1 = 0.25\kappa$) plus parametric amplifier ($J_2 = 0.2\kappa$) interaction subject to (a) dissipative pairing on the two modes and (b) incoherent gain and loss. Observe that since $\frac{2}{\kappa}\sqrt{J_1^2 - J_2^2} = 0.3$ is less than unity, panel b) depicting uncorrelated dissipation does not have an EP, but the case with correlated dissipation does. c) and d) show the spectra of the dynamical matrix for a detuned beamsplitter Hamiltonian, subject to (c) dissipative pairing on the two modes and (d) incoherent gain and loss. Note that the left exhibits 4 exceptional points (half coming from the $\eta \to -\eta$ symmetry) while the right exhibits none. We have chosen $J = \kappa = \delta = 1$.

block diagonal form:

$$\partial_t \begin{pmatrix} a \\ b \end{pmatrix} = \begin{pmatrix} -\frac{\kappa}{2}(1+\eta^2) + i\delta & iJ \\ iJ & \frac{\kappa}{2}(1+\eta^2) - i\delta \end{pmatrix} \begin{pmatrix} a \\ b \end{pmatrix} - \frac{\kappa}{2}(1-\eta^2)\mathbf{1} \begin{pmatrix} a \\ b \end{pmatrix}, \quad \text{(B.16)}$$

where we can directly conclude that we create a $\mathcal{PT}$ dimer and exceptional point if, and only if, we are at zero detuning. Thus, the dissipative interaction generated by the correlated noise makes the EP robust to detuning. This can be seen in Fig. B.1.

An interesting corollary of our analysis is that two coupled modes subject to unbalanced loss will undergo an EP when the coupling is equal to half the difference of the loss rates. This system cannot, though, ever become unstable.

B.2 3 Site Model Dynamical Matrix and Stability Analysis

Recall our three site Hamiltonian and jump operator:

$$\hat{H} = J_1 \hat{a}^\dagger \hat{b} + J_2 \hat{b}^\dagger \hat{c} + h.c., \tag{B.17}$$

$$\hat{L} = \sqrt{\kappa}(\hat{a} + \eta \hat{c}^\dagger). \tag{B.18}$$

This Hamiltonian has the unnormalized normal modes

$$\hat{d}_0 = J_2 \hat{a} - J_1 \hat{c}, \tag{B.19}$$

$$\hat{d}_\pm = J_1 \hat{a} \pm \sqrt{J_1^2 + J_2^2}\hat{b} + J_2 \hat{c}, \tag{B.20}$$

which have energies $0, \pm\sqrt{J_1^2 - J_2^2}$. We will call these the dark mode and bright modes, respectively. The time dynamics of the expectation value of an operator $\langle \hat{O} \rangle$ is given by:

$$\partial_t \langle \hat{O} \rangle = i\langle [\hat{H}, \hat{O}] \rangle + \frac{1}{2}\langle \hat{L}^\dagger [\hat{O}, \hat{L}] + [\hat{L}^\dagger, \hat{O}]\hat{L} \rangle. \tag{B.21}$$

This gives the semi-classical dynamical matrix for the mode operators expectation values ($a = \langle \hat{a} \rangle, a^* = \langle a^\dagger \rangle$, etc.):

$$\partial_t \begin{pmatrix} a \\ b \\ c \\ a^* \\ b^* \\ c^* \end{pmatrix} = -i \begin{pmatrix} -i\frac{\kappa}{2} & J_1 & 0 & 0 & 0 & -i\frac{\kappa}{2}\eta \\ J_1 & 0 & J_2 & 0 & 0 & 0 \\ 0 & J_2 & i\frac{\kappa}{2}\eta^2 & i\frac{\kappa}{2}\eta & 0 & 0 \\ 0 & 0 & -i\frac{\kappa}{2}\eta & -i\frac{\kappa}{2} & -J_1 & 0 \\ 0 & 0 & 0 & -J_1 & 0 & -J_2 \\ i\frac{\kappa}{2}\eta & 0 & 0 & 0 & -J_2 & i\frac{\kappa}{2}\eta^2 \end{pmatrix} \begin{pmatrix} a \\ b \\ c \\ a^* \\ b^* \\ c^* \end{pmatrix}. \tag{B.22}$$

Before we calculate the stability conditions for this matrix, we can gain some intuition by performing a simple perturbative calculation. If we know the eigenvectors and eigenvalues of a normal matrix M satisfy $M|n\rangle = \epsilon_n|n\rangle$, and we are interested in the spectrum of $M + \delta M$, then to first order, this is simply $\epsilon_n + \langle n|\delta M|n\rangle$. For stability, we only care about the real part, and so we can simply calculate $\langle n|\delta M + \delta M^\dagger|n\rangle$. For our system, the dissipative interaction is *Hermitian*, so to leading order it doesn't affect the stability conditions at all. Hence, we can just focus on the local heating and cooling rates in the perturbative analysis, which tells us that for the bright modes, we expect a relaxation rate proportional to $\kappa(J_1^2 - \eta^2 J_2^2)$, and for the dark mode a relaxation rate proportional to $\kappa(J_2^2 - \eta^2 J_1^2)$. If either is negative, the system would be dynamically unstable, giving rise to exponential growth, which occurs exactly at the point $|\eta| > |J_1/J_2|$ for the bright modes, and $|\eta| > |J_2/J_1|$ for the dark mode, reproducing the values quoted in Chapter 3.

To show that these are actually the instability points for all κ, we must go beyond this leading order calculation. Fortunately, we can observe that, because the dissipation is confined to a single sublattice, flipping the sign of the other sublattice - that is $\hat{b} \to -\hat{b}$, is equivalent to sending $J_i \to -J_i$ (in this sense, the dissipator respects the chiral sublattice symmetry of the Hamiltonian). Next, because the Hamiltonian terms are all imaginary, and the dissipative terms all real, complex conjugation $a \to a^*$, etc, also sends $J_i \to -J_i$. In other words, the map $a \to a^*, b \to -b^*, c \to c^*$ constitutes a symmetry of the full dynamical matrix. This allows us to block diagonalize in terms of the quadratures $x_a = \langle \hat{a} + \hat{a}^\dagger\rangle/\sqrt{2}, p_b = i\langle \hat{b}^\dagger - b\rangle/\sqrt{2}$ and $x_c = \langle \hat{c} + \hat{c}^\dagger\rangle/\sqrt{2}$:

$$\partial_t \begin{pmatrix} x_a \\ p_b \\ x_c \end{pmatrix} = -i \begin{pmatrix} -i\frac{\kappa}{2} & iJ_1 & -i\frac{\kappa}{2}\eta \\ -iJ_1 & 0 & -iJ_2 \\ i\frac{\kappa}{2}\eta & iJ_2 & i\frac{\kappa}{2}\eta^2 \end{pmatrix} \begin{pmatrix} x_a \\ p_b \\ x_c \end{pmatrix}. \tag{B.23}$$

We can analytically calculate the spectrum of Eq. (B.23), as the roots of the characteristic

equation of the dynamical matrix (setting $\kappa = 2$ for simplicity):

$$x^3 + (1-\eta^2)x^2 + J^2 x + \Delta = 0. \tag{B.24}$$

where $J^2 = J_1^2 + J_2^2$ and $\Delta = J_2^2 - \eta^2 J_1^2$. We can break this into its the real and imaginary parts by defining $x = v + iw$ to get

$$v^3 - 3vw^2 + (1-\eta^2)(v^2 - w^2) + J^2 v + \Delta = 0, \tag{B.25}$$

$$-w^3 + 3v^2 w + 2(1-\eta^2)vw + J^2 w = 0. \tag{B.26}$$

There are two solutions for the imaginary part, $w = 0$ or $w^2 = 3v^2 + 2(1-\eta^2)v + J^2$. We can identify the first $w = 0$ term with the dark mode, as it has zero energy, and it is only dissipative. Plugging this back in Eq. (B.25), we find the real part then satisfies

$$v^3 + (1-\eta^2)v^2 + J^2 v + \Delta = 0, \tag{B.27}$$

which has a positive root if, and only if,

$$\Delta < 0 \iff |\eta| > \left|\frac{J_2}{J_1}\right|, \tag{B.28}$$

which is exactly the stability condition predicted from a FGR calculation, reproducing the result in Chapter 3.

We can get a very similar picture for the other branch of solution to Eq. (B.26). More concretely, if we take the imaginary part to be $w^2 = 3v^2 + 2v + J^2$, which is exactly the energy of the bright modes, plus a shift coming from the dissipation, then we get an equation

for the relaxation rates:

$$-8v^3 - 8(1-\eta^2)v^2 - 2(J^2 + (\eta^2-1)^2)v - J^2(1-\eta^2) + \Delta = 0. \tag{B.29}$$

This has a positive real root if and only if the following condition holds:

$$\Delta > J^2(1-\eta^2) \iff |\eta| > \left|\frac{J_1}{J_2}\right|. \tag{B.30}$$

This is again exactly the FGR value for the bright modes.

Finally, we consider the case when we lose the dissipative interaction. Then, creation and annihilation operators decouple, so we need only solve the spectrum of:

$$D = \begin{pmatrix} -i\frac{\kappa}{2} & -J_1 & 0 \\ -J_1 & 0 & -J_2 \\ 0 & -J_2 & i\frac{\kappa}{2}\eta^2 \end{pmatrix}, \tag{B.31}$$

where we have reintroduced the rate κ. Now, the eigenvalues correspond to solutions of the cubic equation:

$$x^3 + \frac{\kappa}{2}(1-\eta^2)x^2 + \left(J^2 - \frac{\kappa^2\eta^2}{4}\right)x + \frac{\kappa}{2}\Delta = 0. \tag{B.32}$$

In the limit of weak dissipation, $\kappa\eta \ll J$, the roots are identical to those of Eq. (B.24). (For the dark mode, they are equivalent all the way up to $|\kappa\eta| = 2|J|$, afterwards there is a sudden shift.) However, as soon as this is not the case, the instability point can move in a κ dependent manner. The interaction is perfectly balanced in Eq. (B.23) such that the instability points in that case are completely independent of κ.

B.3 Quantum Master Equation Steady State

If we start from the full lattice Hamiltonian and jump operator

$$\hat{H} = \sum_{ij} H_{ij} \hat{a}_i^\dagger \hat{a}_j + \text{H. c.}, \tag{B.33}$$

$$\hat{L}/\sqrt{\kappa} = \hat{a}_{\overline{0}} + \eta \hat{a}_{\overline{1}}^\dagger, \tag{B.34}$$

then we can diagonalize the Hamiltonian into normal modes $\hat{d}_{\pm\alpha} = \sum_i \psi_{\pm\alpha}[i]\hat{a}_i$. Here, we have defined the unitary transformation $\psi_\alpha[i]$ between real space lattice site operators $\hat{a}_i$ and eigenmode operators $\hat{d}_\alpha$. Taking advantage of the fact that there is a real space chiral sublattice symmetry, we have

$$\hat{H} = \sum_{\alpha>0} \epsilon_\alpha (\hat{d}_\alpha^\dagger \hat{d}_\alpha - \hat{d}_{-\alpha}^\dagger \hat{d}_{-\alpha}), \tag{B.35}$$

$$\psi_{-\alpha}[i] = (-1)^i \psi_\alpha[i]. \tag{B.36}$$

Next, observe that such a chiral Hamiltonian is invariant under two-mode squeezing transformations between $\hat{d}_\alpha$ and $\hat{d}_{-\alpha}$, constituting a massive $\mathrm{SU}(1,1)^{N/2}$ symmetry group. That is, we can define the new operators $\hat{\beta}_{\pm\alpha} = \cosh(r_\alpha)\hat{d}_{\pm\alpha} + e^{i\phi_\alpha}\sinh(r_\alpha)\hat{d}_{\mp\alpha}^\dagger$ with energy-dependent squeezing parameters r_α. The Hamiltonian in this basis becomes:

$$\hat{H} = \sum_{\alpha>0} \epsilon_\alpha (\hat{\beta}_\alpha^\dagger \hat{\beta}_\alpha - \hat{\beta}_{-\alpha}^\dagger \hat{\beta}_{-\alpha}), \tag{B.37}$$

which is still diagonal. Further expanding our jump operator in eigenmodes, we find

$$\hat{L}/\sqrt{\kappa} = \hat{a}_{\overline{0}} + \eta \hat{a}_{\overline{1}}^\dagger \tag{B.38}$$

$$= \sum_{\alpha>0} \left[\left(\psi_\alpha[\overline{0}]^* \hat{d}_\alpha + (-1)^{\overline{0}} \psi_\alpha[\overline{0}]^* \hat{d}_{-\alpha} \right) + \eta \left(\psi_\alpha[\overline{1}] \hat{d}_\alpha^\dagger + (-1)^{\overline{1}} \psi_\alpha[\overline{1}] \hat{d}_{-\alpha}^\dagger \right) \right]. \tag{B.39}$$

Now, we assume $\overline{0}, \overline{1}$ live on the same sublattice, and without loss of generality, we define $(-1)^{\overline{0}} = (-1)^{\overline{1}} = 1$. Thus, we can express $\hat{L}$ as

$$\begin{aligned}\hat{L}/\sqrt{\kappa} &= \sum_{\alpha>0} \left[\left(\psi_\alpha[\overline{0}]^* \hat{d}_\alpha + \eta \psi_\alpha[\overline{1}] \hat{d}^\dagger_{-\alpha} \right) + \left(\psi_\alpha[\overline{0}]^* \hat{d}_{-\alpha} + \eta \psi_\alpha[\overline{1}] \hat{d}^\dagger_\alpha \right) \right] \\ &\equiv \sum_{\alpha>0} N_\alpha (\hat{\beta}_\alpha + \hat{\beta}_{-\alpha}),\end{aligned} \tag{B.40}$$

where we define the amplified squeezing parameter and normalization:

$$\tanh r_\alpha = \eta \left| \frac{\psi_\alpha[\overline{1}]}{\psi_\alpha[\overline{0}]^*} \right|, \tag{B.41}$$

$$\phi_\alpha = \arg \left(\frac{\psi_\alpha[\overline{1}]}{\psi_\alpha[\overline{0}]^*} \right), \tag{B.42}$$

$$|N_\alpha|^2 = |\psi_\alpha[\overline{0}]|^2 - \eta^2 |\psi_\alpha[\overline{1}]|^2, \tag{B.43}$$

as desired. Thus, the placement of the dissipation sites also sets a phase reference for the lattice.

One can now straightforwardly see that, since the Hamiltonian is diagonal in the Bogoliubov modes $\hat{\beta}$, and the jump operator is purely cooling, the steady state is uniquely the joint vacuum.

As noted in Chapter 3, if $\tanh r_\alpha > 1$, we no longer have a well defined Bogoliubov transformation. This corresponds to the case that $|\psi_\alpha[0]| < |\eta \psi_\alpha[\overline{1}]|$. In such a case, to define a squeezing transformation that respects the canonical commutation relations, then we must define

$$\hat{\beta}_{\pm\alpha} \propto \eta \psi_\alpha[\overline{1}]^* \hat{d}_{-\alpha} + \psi_\alpha[\overline{0}] \hat{d}^\dagger_\alpha. \tag{B.44}$$

If we define the sets $A = \{\alpha > 0 \mid |\psi_\alpha[\overline{0}]| > |\eta \psi_\alpha[\overline{1}]|\}$ and $B = \{\alpha > 0 \mid |\psi_\alpha[\overline{0}]| < |\eta \psi_\alpha[\overline{1}]|\}$,

then Eq. (B.40) tells us

$$\hat{L}/\sqrt{\kappa} = \sum_{\alpha\in A} N_\alpha(\hat{\beta}_\alpha + \hat{\beta}_{-\alpha}) + \sum_{\alpha\in B} N_\alpha(\hat{\beta}^\dagger_\alpha + \hat{\beta}^\dagger_{-\alpha}). \tag{B.45}$$

Hence, as soon as B is non-empty, at least one eigenmode is experiencing heating, which means the dynamics are unstable.

We can finally observe that these instability points occur at

$$|\eta| > \min_\alpha \left|\frac{\psi_\alpha[\overline{0}]}{\psi_\alpha[\overline{1}]}\right|, \tag{B.46}$$

which just as before are exactly the FGR-based predictions expected from first-order perturbation theory.

B.4 Steady State with Squeezed Vacuum Noise

In this section, we will consider the steady state if, instead of the dissipative pairing interaction, we simply couple the lattice with squeezed vacuum dissipation. Specifically we will demonstrate that it is impossible to generate instability, and also that there is no useful spatial selectivity.

To see that it is impossible to generate instability, we can begin by just looking at the dynamical matrix. If we have two dissipators $\hat{L}_1 = \sqrt{\kappa}(\hat{a}_{\overline{0}} + \eta\hat{a}^\dagger_{\overline{1}})$ and $\hat{L}_2 = \sqrt{\kappa}(\hat{a}_{\overline{1}} + \eta\hat{a}^\dagger_{\overline{0}})$, then

$$\partial_t\langle\hat{a}_{\overline{0}}\rangle = \frac{1}{2}\sum_{i=1,2}\langle\hat{L}_i^\dagger[\hat{a}_{\overline{0}}, \hat{L}_i] + [\hat{L}_i^\dagger, \hat{a}_{\overline{0}}]\hat{L}_i\rangle \tag{B.47}$$

$$= -\frac{\sqrt{\kappa}}{2}\left\langle\hat{L}_1 - \eta\hat{L}_2^\dagger\right\rangle = -\frac{\kappa}{2}\left(1-\eta^2\right)\langle\hat{a}_{\overline{0}}\rangle. \tag{B.48}$$

Similarly, the dynamics is symmetric under $\hat{a}_{\overline{0}} \leftrightarrow \hat{a}_{\overline{1}}$ if we correspondingly exchange $\hat{L}_1 \leftrightarrow$

$\hat{L}_2$, so we have

$$\partial_t \langle \hat{a}_{\overline{1}} \rangle = -\frac{\kappa}{2} \left(1 - \eta^2\right) \langle \hat{a}_{\overline{1}} \rangle. \tag{B.49}$$

Taking a generic Hamiltonian $\hat{H} = \sum_{i,j} H_{i,j} \hat{a}_i^\dagger \hat{a}_j$, we get the equations of motion

$$\partial_t \langle \hat{a}_i \rangle = \sum_j \left(-iH_{i,j} - \frac{\kappa}{2}(1-\eta^2)(\delta_{j,\overline{0}} + \delta_{j,\overline{1}})\delta_{i,j} \right) \langle \hat{a}_j \rangle \tag{B.50}$$

$$\equiv -i \sum_j D_{i,j} \langle \hat{a}_j \rangle, \tag{B.51}$$

where we have defined the dynamical matrix $D_{i,j} = D^H_{i,j} + D^\kappa_{i,j}$, with

$$D^H_{i,j} = H_{i,j}, \tag{B.52}$$

$$D^\kappa_{i,j} = -i\frac{\kappa}{2}(1-\eta^2)(\delta_{j,\overline{0}} + \delta_{j,\overline{1}})\delta_{i,j}. \tag{B.53}$$

Now, if the system is unstable, then there must be an eigenvalue λ of D such that $\mathrm{Im}\lambda > 0$. Let's associate such an eigenvalue with an eigenvector $|\psi\rangle$, implying

$$\mathrm{Im}\lambda = -\frac{i}{2}\langle\psi|D - D^\dagger|\psi\rangle = -i\langle\psi|D^\kappa|\psi\rangle \tag{B.54}$$

However, $-iD^\kappa$ is negative semi-definite, a contradiction that $\mathrm{Im}\lambda$ is positive.

Next, we will prove that, if there is a pure steady state, there is uniform photon density in the lattice. To see this, note that $\hat{L}_1$ and $\hat{L}_2$ are both in the same form as the dissipator we have so far considered, so for an arbitrary Hamiltonian, we know that we can write them as a sum of Bogoliubov modes. Hence, we know that

$$\hat{L}_1/\sqrt{\kappa} = \sum_\alpha N_\alpha \left(\hat{\beta}_\alpha + \hat{\beta}_{-\alpha} \right), \tag{B.55}$$

with

$$\tanh r_\alpha = \left| \eta \frac{\psi_\alpha[\overline{1}]}{\psi_\alpha[\overline{0}]^*} \right|. \tag{B.56}$$

We can write $\hat{L}_2$ in the same form, up to exchanging $\overline{0} \leftrightarrow \overline{1}$, i.e.

$$\tanh r_\alpha = \left| \eta \frac{\psi_\alpha[\overline{0}]}{\psi_\alpha[\overline{1}]^*} \right| \tag{B.57}$$

We know that the steady state is unique and pure with just $\hat{L}_1$, hence, for it to remain pure after adding $\hat{L}_2$, the dark state must also be annihilated by $\hat{L}_2$. This is equivalent to

$$\implies |\psi_\alpha[\overline{1}]|^2 = |\psi_\alpha[\overline{0}]|^2, \tag{B.58}$$

$$\implies |\tanh r_\alpha| = \eta \tag{B.59}$$

$$\implies \langle a_i^\dagger a_i \rangle = \frac{\eta^2}{1-\eta^2} \ \forall i. \tag{B.60}$$

Thus, to get a pure steady state, it is necessary and sufficient that there exists some symmetry of the Hamiltonian that guarantees $|\psi_\alpha[\overline{1}]|^2 = |\psi_\alpha[\overline{0}]|^2$ for every eigenmode. In this case, the squeezing parameter for every pair of eigenmodes is identical to η, meaning one cannot get any topological selectivity, and in fact there is always a uniform photon density in the lattice.

If such a symmetry does not exist, the steady state is guaranteed to be in an impure state.

B.5 Topological Enhancement

B.5.1 SSH Degeneracy

In the manuscript, we considered an SSH chain with an *odd* number of lattice sites, because an even-numbered SSH chain will have two edge modes whose energies go to zero exponentially quickly in system size. When there are energy degeneracies, the steady state is no longer unique; this means that the time it would take to prepare the steady state is growing exponentially in system size, severely limiting the practical use.

First, we prove explicitly that the dissipative gap closes when the Hamiltonian is degenerate. To begin, we will assume that we have a generic Hamiltonian that satisfies the proper symmetry conditions. That is, it can be unitarily diagonalized into modes $\hat{d}_{\pm\alpha} = \sum_i \psi_\alpha[i]\hat{a}_i$ where $\psi_{-\alpha}[i] = (-1)^i\psi_\alpha[i]$ and the energy of $\hat{d}_\alpha$ is opposite that of $\hat{d}_{-\alpha}$.

As before, we assume we have a single jump operator of the form $\hat{L}/\sqrt{\kappa} = \hat{a}_{\overline{0}} + \eta\hat{a}_{\overline{1}}^\dagger$. From here, we can do the transformations:

$$\hat{H} = \sum_{\alpha>0} \epsilon_\alpha(\hat{d}_\alpha^\dagger\hat{d}_\alpha - \hat{d}_{-\alpha}^\dagger\hat{d}_{-\alpha}) \equiv \sum_{\alpha>0} \epsilon_\alpha(\hat{\beta}_\alpha^\dagger\hat{\beta}_\alpha - \hat{\beta}_{-\alpha}^\dagger\hat{\beta}_{-\alpha}), \tag{B.61}$$

$$\begin{aligned}
\hat{L} &= \sqrt{\kappa}(\hat{a}_{\overline{0}} + \eta\hat{a}_{\overline{1}}^\dagger) \\
&= \sqrt{\kappa}\sum_{\alpha>0}\left[\left(\psi_\alpha[\overline{0}]^*\hat{d}_\alpha + (-1)^{\overline{0}}\psi_\alpha[\overline{0}]^*\hat{d}_{-\alpha}\right) + \eta\left(\psi_\alpha[\overline{1}]\hat{d}_\alpha^\dagger + (-1)^{\overline{1}}\psi_\alpha[\overline{1}]\hat{d}_{-\alpha}^\dagger\right)\right] \\
&= \sqrt{\kappa}\sum_{\alpha>0}\left[\left(\psi_\alpha[\overline{0}]^*\hat{d}_\alpha + (-1)^{\overline{0}}\eta\psi_\alpha[\overline{1}]\hat{d}_{-\alpha}^\dagger\right) + (-1)^{\overline{0}}\left(\psi_\alpha[\overline{0}]^*\hat{d}_{-\alpha} + (-1)^{\overline{0}}\eta\psi_\alpha[\overline{1}]\hat{d}_\alpha^\dagger\right)\right] \\
&\equiv \sqrt{\kappa}\sum_{\alpha>0} N_\alpha(\hat{\beta}_\alpha + (-1)^{\overline{0}}\hat{\beta}_{-\alpha}),
\end{aligned} \tag{B.62}$$

where we used that $\overline{0}$ and $\overline{1}$ are on the same sublattice, so $(-1)^{\overline{0}} = (-1)^{\overline{1}}$. The system thus has a unique steady state *as long as the spectrum is non-degenerate*. If the spectrum has two degenerate modes – lets suppose $\epsilon_\gamma = \epsilon_\delta$ – then we can always rotate between them to

define the new (unnormalized) modes

$$\hat{\beta}'_\gamma = N_\gamma \hat{\beta}_\gamma + (-1)^{\overline{0}} N_\delta \hat{\beta}_\delta, \tag{B.63}$$

$$\hat{\beta}'_\delta = N_\delta \hat{\beta}_\gamma - (-1)^{\overline{0}} N_\gamma \hat{\beta}_\delta. \tag{B.64}$$

These are equally good Hamiltonian eigenmodes, but the dissipation only cools $\hat{\beta}'_\gamma$ and not $\hat{\beta}'_\delta$. Thus, the steady state cannot be unique.

In the SSH chain, the topological edge modes become degenerate zero modes exponentially quickly as $N \to \infty$, and therefore the time it takes to reach the steady state is blowing up exponentially in the system size, making one exponentially susceptible to e.g. photon loss. There is a simple solution to this problem, whereby one can always cool the slack mode Eq. (B.64) in any lattice with mirror symmetry by adding the mirrored dissipator. Here, "mirror symmetry" means the inversion symmetry about the center of the lattice, sending $\hat{a}_i \leftrightarrow \hat{a}_{N-1-i}$ (if the lattice is zero-indexed).

This symmetry means that adding a second dissipator $\hat{L}'/\sqrt{\kappa} = \hat{a}_{N-1-\overline{0}} - \eta \hat{a}^\dagger_{N-1-\overline{1}}$ will give the exact same effective squeezing parameters r_α, so it has the same dark state. However, it lives on the opposite sublattice as $\hat{L}$, and so there is a phase flip - this can be seen most clearly by simply expanding in the proper mode basis:

$$\begin{aligned}\hat{L}' &= \sqrt{\kappa}(\hat{a}_{N-1-\overline{0}} - \eta \hat{a}^\dagger_{N-1-\overline{1}}) \\ &= \sqrt{\kappa} \sum_{\alpha>0} \left[\psi_\alpha[N-1-\overline{0}]^* \left(\hat{d}_\alpha + (-1)^{N-1-\overline{0}} \hat{d}_{-\alpha} \right) - \eta \psi_\alpha[N-1-\overline{1}] \left(\hat{d}^\dagger_\alpha + (-1)^{N-1-\overline{1}} \hat{d}^\dagger_{-\alpha} \right) \right].\end{aligned} \tag{B.65}$$

Here, it is useful to observe that N is even, so $(-1)^{N-1-\overline{0}} = (-1)^{1-\overline{0}}$. Further, the mirror

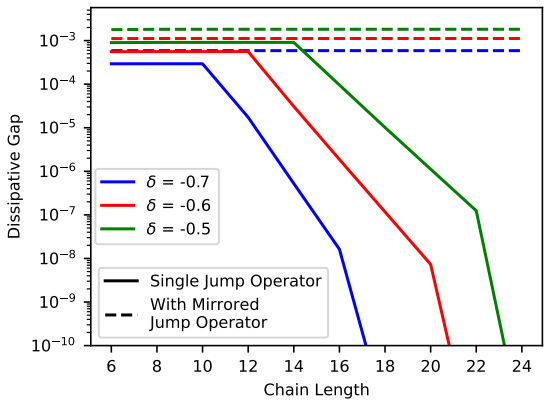

Figure B.2: This shows the dissipative gap, or the relaxation rate of the slowest mode, for an SSH chain at $\eta = 0.99\eta_c$, $\kappa = J = 1$, and $\overline{0} = 2$, $\overline{1} = 0$. Note that when we have a single jump operator, the dissipative gap decays exponentially in system size, meaning the stabilization time scale is quickly diverging. On the other hand, adding a second mirrored dissipator in the form of Eq. (B.65) removes this exponential suppression.

symmetry tells us explicitly that $\psi_\alpha[i] = \psi_\alpha[N-1-i]$, allowing us to make the simplificattion:

$$\begin{aligned}
\hat{L}' &= \sqrt{\kappa}\sum_{\alpha>0}\left[\left(\psi_\alpha[\overline{0}]^*\hat{d}_\alpha + (-1)^{1-\overline{0}}\psi_\alpha[\overline{0}]^*\hat{d}_{-\alpha}\right) - \eta\left(\psi_\alpha[\overline{1}]\hat{d}^\dagger_\alpha + (-1)^{1-\overline{0}}\psi_\alpha[\overline{1}]\hat{d}^\dagger_{-\alpha}\right)\right] \\
&= \sqrt{\kappa}\sum_{\alpha>0}\left[\left(\psi_\alpha[\overline{0}]^*\hat{d}_\alpha - (-1)^{1-\overline{0}}\eta\psi_\alpha[\overline{1}]\hat{d}^\dagger_{-\alpha}\right) + (-1)^{1-\overline{0}}\left(\psi_\alpha[\overline{0}]^*\hat{d}_{-\alpha} - (-1)^{1-\overline{0}}\eta\psi_\alpha[\overline{1}]\hat{d}^\dagger_\alpha\right)\right] \\
&\equiv \sqrt{\kappa}\sum_{\alpha>0} N_\alpha(\hat{\beta}_\alpha + (-1)^{1-\overline{0}}\hat{\beta}_{-\alpha}),
\end{aligned} \tag{B.66}$$

Since $(-1)^{1-\overline{0}}(-1)^{\overline{0}} = -1$ is negative, between $\hat{L}$ and $\hat{L}'$ they cool both the sum and difference of the two degenerate zero modes, relieving the problem of the degeneracy.

To see this in action, one can observe that even for relatively small lattice size, adding the second dissipator can increase the dissipative gap by several orders of magnitude, see Fig. B.2.

For such an even-numbered SSH chain, the steady state will still be single-mode squeezed vacuums of the edges. To see this, we can observe that the edge eigenmodes that obey the real-space chiral symmetry condition are not localized, but are superpositions of localized

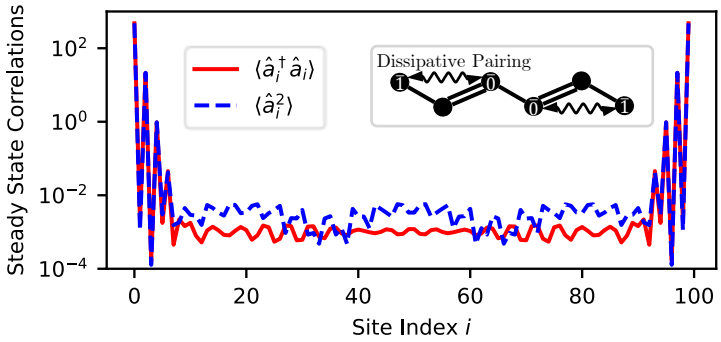

Figure B.3: This shows the steady state correlations for an even-numbered (100 site) SSH chain. We have taken $\delta = -0.7$, and two dissipators: one has $\overline{0} = 4$ and $\overline{1} = 0$, the mirrored one takes $\overline{0} = 95$, $\overline{1} = 99$. Both have $\eta = 0.999\eta_c$. The steady state solution shows single mode squeezing of each edge.

edge modes. If we let $|\psi_L\rangle$ be left-localized and $|\psi_R\rangle$ be right localized, then the edge eigenmodes are $|\psi_\pm\rangle = (|\psi_L\rangle \pm |\psi_R\rangle)/\sqrt{2}$. The steady state will therefore be a two mode squeezed vacuum of $|\psi_+\rangle$ and $|\psi_-\rangle$. However, two mode squeezing plus such a beam splitter operation is equivalent to simple having single-mode squeezing on both modes. This can be seen in Fig. B.3.

B.5.2 SSH Topological Protection

Here, we show that the SSH chain has topological protection. To do this, we will add disorder to coupling strengths of the SSH chain, whose spectrum should be robust up to disorder of $O(2|\delta|J)$. For each steady state, we will define a symmetrized edge localization factor:

$$\mathcal{S} = \frac{1}{n}\sum_i \sqrt{n_i n_{N-1-i}}\left(1 - 4\frac{i(N-i)}{N^2}\right), \tag{B.67}$$

$$n_i = \langle \hat{a}_i^\dagger \hat{a}_i \rangle, \tag{B.68}$$

$$n = \sum_i n_i. \tag{B.69}$$

It has been defined in this manner so that the edge localization value goes to unity if the particles are infinitely localized symmetrically to the edges, and goes to zero if they are

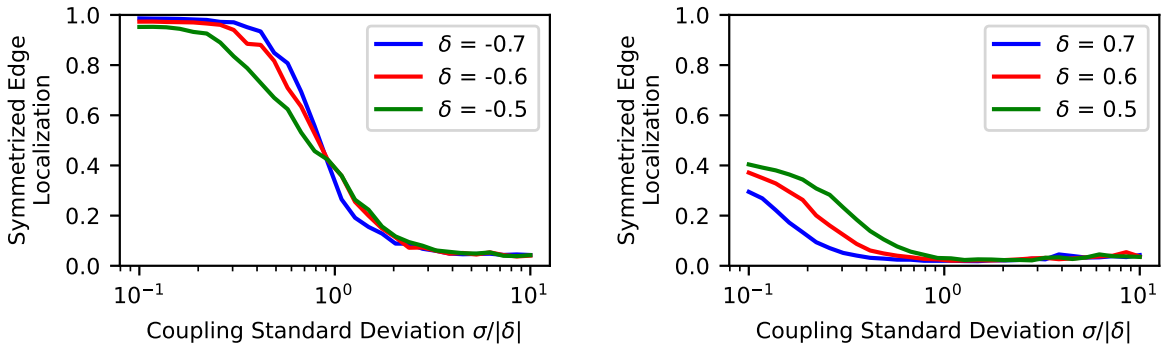

Figure B.4: Plotted on the left (right) is an $N = 20$ site SSH chain, with $\delta < 0$ ($\delta > 0$) in a topologically nontrivial (trivial) regime. In the topological regime, for all three values of $|\delta|$ shown, there is a clear crossover at $\sigma \sim |\delta|$ from topologically protected edge excitations with $\mathcal{S} \sim 1$, to Anderson localization with $\mathcal{S} \sim 0$. The topologically trivial regime has no edge modes, transitioning from extended bulk excitations when $\sigma \sim 0$ to Anderson localization when $\sigma \gg \delta$. Both plots have a single dissipator with $\kappa = 1$, $\overline{0} = 2$, $\overline{1} = 0$, and $\eta = 0.99\eta_c$. Data is averaged over 500 disorder realizations.

localized to the center of the bulk or localized to a single edge. The reason for this is that as the disorder gets large, the wavefunctions undergo Anderson localization, so if we have pumping on the edge lattice site, the steady state photon number tends to be concentrated there, but the other edge mode is not excited. On the other hand, when there is topological protection and two edge modes, there should be photon density evenly distributed to both sides of the lattice.

In Fig. B.4, we can observe that for a range of δ values, the steady state value of the symmetric edge localization is protected up to disorder $\sigma \sim |\delta|$, where the SSH Hamiltonian is

$$\hat{H} = \sum_{i=0}^{N-2} [1 - (-1)^i \delta + J_i] \hat{a}_i^\dagger \hat{a}_{i+1} + h.c., \tag{B.70}$$

and the J_i are sampled from a Gaussian distribution with zero average and width σ.

At this point, we would like to stress that the topology only protects the steady state to Hamiltonian perturbations which conserve the chiral symmetry. If one were instead inter-

ested in the effect of other perturbations, e.g. a finite lifetime of the local bosonic modes, then one would have to consider the full Liouvillian spectrum, where the Liouvillian $\mathcal{L}$ is the superoperator which governs the dynamics of the full density matrix, i.e.

$$\partial_t \hat{\rho} = \mathcal{L}\rho = -i[\hat{H}, \hat{\rho}] + \mathcal{D}[\hat{L}]\hat{\rho} \tag{B.71}$$

In this case, the Liouvillian gap is closing quickly as N gets large, which can be understood intuitively from the fact that we are using a single jump operator to stabilize the entire lattice, and so it takes time for excitations on top of the Bogoliubov vacuum to propagate to the dissipation sites and then decay away.

Hence, there is no protection to additional noise. In some sense, we have chosen the most resource-efficient scheme possible by using a single, quasi-localized jump operator. The price paid by this choice is that the single jump operator must be stronger than all of the other possible sources of relaxation in the lattice. If one considers preparing the steady state quickly more important than resource efficiency, one can imagine a continuum of possible models whereby one adds a number of other, compatible dissipators throughout the lattice, trading resources for speed.

B.5.3 SSH Output Fields

In this section, we analyze the output fields generated by weakly tapping off some light from the topological edge mode. We can imagine generating the dissipative interaction by coupling to a heavily damped ancilla mode $\hat{b}$,

$$\hat{H} = \sum_{i,j} H_{i,j} \hat{a}_i^\dagger \hat{a}_j + g(\hat{a}_{\overline{0}} + \eta \hat{a}_{\overline{1}}^\dagger)\hat{b}^\dagger + g(\hat{a}_{\overline{0}}^\dagger + \eta \hat{a}_{\overline{1}})\hat{b}. \tag{B.72}$$

If the $\hat{b}$ mode is lossy with a decay rate κ, and we also couple the edge lattice site $\hat{a}_0$ to a waveguide with a rate $\Gamma \ll \kappa$, see Fig. B.5(a), the Heisenberg-Langevin equations of motion

will be:

$$\partial_t \hat{a}_i = -i[\hat{H}, \hat{a}_i] + \delta_{i,0}\left(-\frac{\Gamma}{2}\hat{a}_0 + \sqrt{\Gamma}\hat{a}_{in}\right), \tag{B.73}$$

$$\partial_t \hat{b} = -i[\hat{H}, \hat{b}] - \frac{\kappa}{2}\hat{b} + \sqrt{\kappa}\hat{b}_{in}, \tag{B.74}$$

where $\hat{a}_{in}, \hat{b}_{in}$ are operator valued, zero-temperature white noise:

$$\langle \hat{a}_{in}(t)\hat{a}_{in}(t')^\dagger \rangle = \langle \hat{b}_{in}(t)\hat{b}_{in}(t')^\dagger \rangle = \delta(t - t'). \tag{B.75}$$

Using standard input-output theory [283], we can calculate the output field in frequency space:

$$\hat{a}_{out}(\omega) = \hat{a}_{in}(\omega) + \sqrt{\Gamma}\hat{a}_0(\omega), \tag{B.76}$$

If we define a quadrature $\hat{q}_{out}(\omega, \theta) = e^{i\theta}\hat{a}_{out}(\omega) + e^{-i\theta}\hat{a}^\dagger_{out}(-\omega)$, then we can define the squeezing spectrum as:

$$P(\omega) = \min_{\theta \in [0, 2\pi)} \langle \hat{q}_{out}(\omega, \theta)\hat{q}_{out}(-\omega, \theta) \rangle, \tag{B.77}$$

which gives us a measure of how squeezed the output field of the edge lattice site is versus frequency. This is depicted in Fig. B.5, which shows narrow-band squeezed topological output light.

B.5.4 Hofstadter Steady State Correlations

In this section, we provide all-to-all correlation plots for the Hofstadter lattices, as well as line cuts of Fig. 3.3 in Chapter 3. To show all-to-all correlations, because the lattice lies on a 2D graph, it will be necessary to pick an ordering of the lattice sites. This is done

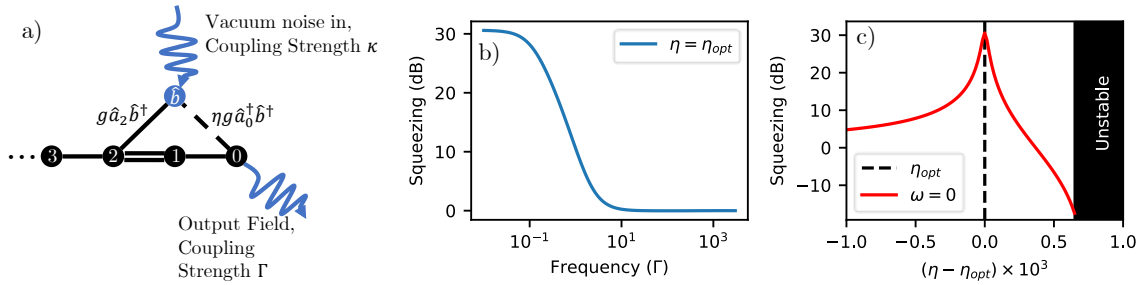

Figure B.5: a) depicts a schematic of an SSH chain, along with an auxilliary lattice site $\hat{b}$ to generate the desired dissipation. Input vacuum noise on $\hat{b}$ drives the system to the steady state, which is then allowed to leak out of the system from site 0 on the edge. b) and c) show the squeezing spectrum with $\Gamma = 10^{-3}, \kappa = 10, g = 4, J = 1, \delta = -0.65$, and $\eta_{opt} \sim 0.212$ vs (b) frequency and (c) η. η_{opt} is defined as the optimal imbalance η to maximize output squeezing at zero frequency. This is slightly less than η_c, where the system becomes unstable, with instability denoted by black shading in (c).

most easily by choosing a "spiral ordering" where we start in the upper corner, and spiral around and into the lattice, see Fig. B.6(a). By numbering the sites in this manner, the sites are grouped by their distance from the edge of the lattice, which allows one to easily discern patterns in the correlations, see Fig. B.6(b-c). The upper-left block in both plots correspond to edge-edge correlation, which are exponentially enhanced. The correlations fall off exponentially as one moves into the bulk; i.e., down and to the right in these plots.

Finally, we consider line cuts of the steady state correlations. First, we consider a horizontal line cut through the lattice, and look at local density and squeezing correlations, which shows exponential enhancement on the edges, Fig. B.7(a). Secondly, in Fig. B.7(b), we look at correlations just on the edge, with the upper-left hand corner marking site 0, and winding around in a clockwise pattern as is displayed in Fig. B.6(a). This shows nearly spatially uniform correlations and densities around the edge, once taking into account that correlations between sublattices are identically zero.

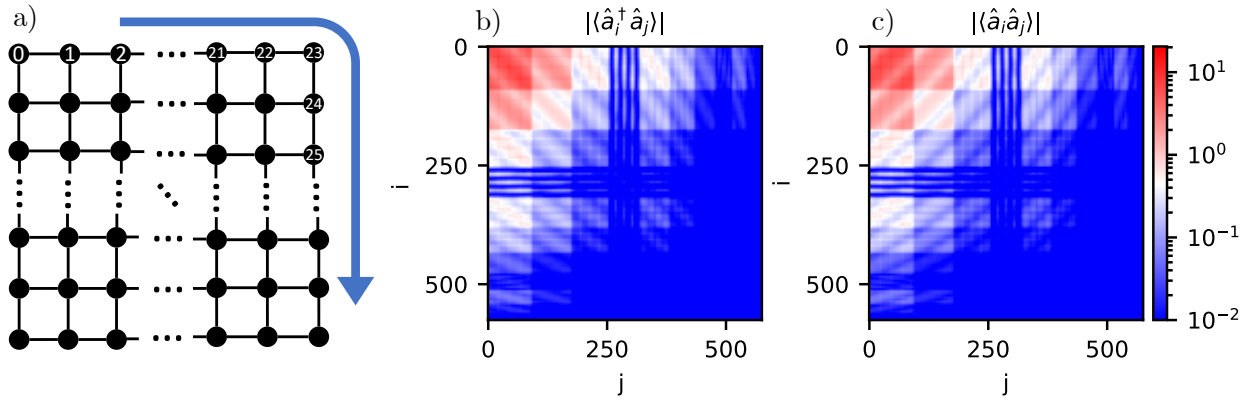

Figure B.6: (a) shows the spiral ordering direction. (b)-(c) give the correlations $\langle \hat{a}_i^\dagger \hat{a}_j \rangle$ and $\langle \hat{a}_i \hat{a}_j \rangle$, respectively for a 24×24 site quarter flux Hofstadter lattice with $\overline{1} = (11, 23)$, $\overline{0} = (12, 20)$, and $\eta = 0.999\eta_c \sim 0.0007$, which is identical to the lattice in Chapter 3.

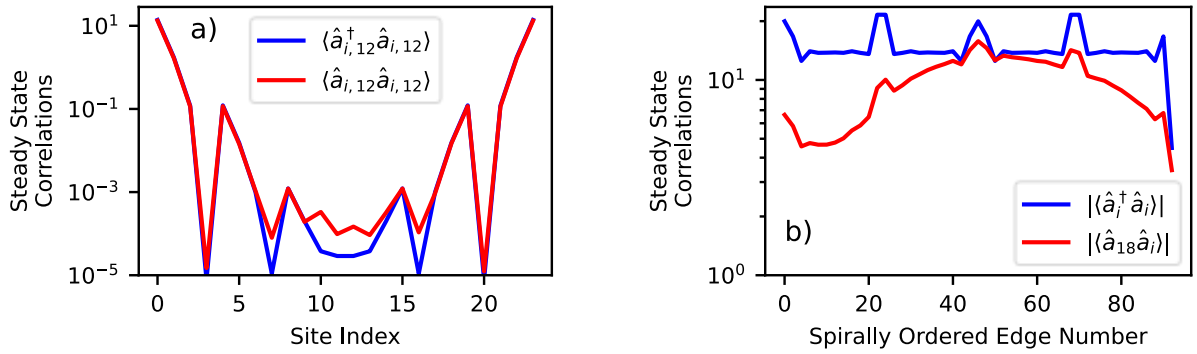

Figure B.7: The lattice parameters are the same as in Fig. B.6. a) shows a line cut through the center of the lattice, with the lattice j-coordinate fixed at 12. Note the exponential drop in correlations in the bulk compared to the edge. b) shows local photon density and correlations with the site $(18, 23)$ (or just 18 in the spiral ordering, see Fig. B.6(a)) going around just the edge. Only every other lattice site is shown, as the correlations are identically zero on different sublattices. Note that the correlations are nearly uniform around the entire edge, except at the corners.

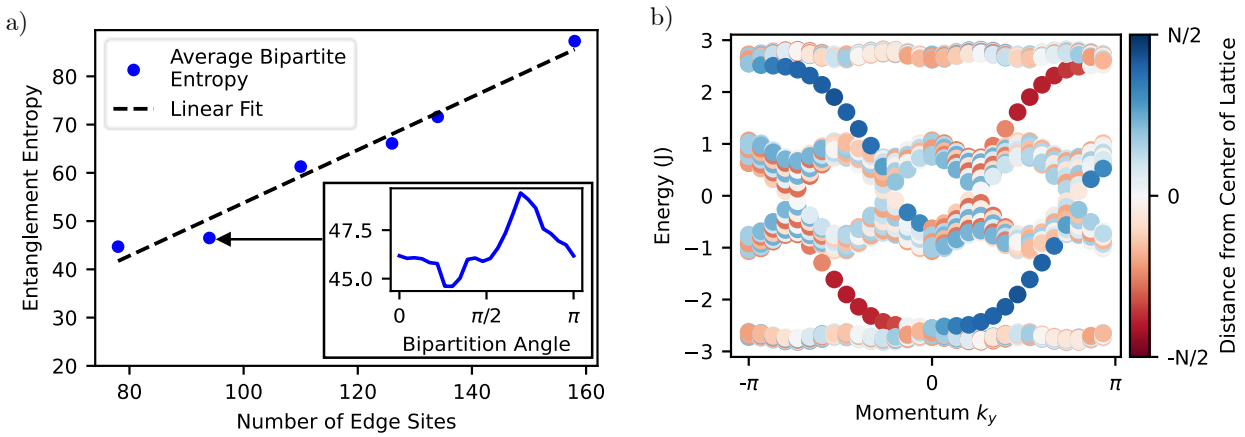

Figure B.8: a) This depicts the bipartite entanglement entropy for a 20×20 to 50×50 quarter flux Hofstadter lattice. The dissipation is placed with site $\overline{0} = (N/2 - 1, 0)$ and $\overline{1} = (N/2 + 1, 2)$, on an $N \times N$ lattice. In all plots $\eta = .087 \sim 0.97 - 0.99\ \eta_c$. Data points are shown only those for which the dimensionless pumping rate $\eta = 0.087 < \eta_c$, ensuring a steady state solution. Lattice bipartitions are made by defining a line through the center of the lattice at an angle θ to the horizontal, and data points are averaged over angles in the set $\{\theta_i = \pi i/N | 0 \leq i < N\}$, see inset. The linear fit suggests the entanglement scales with a volume-law in the number of edge sites. Inset: Entanglement entropy versus bipartition angle for a 24×24 site lattice. This is representative for all N shown, where the entropy varies by at most a few percent versus angle. b) shows the band diagram for a 30×30 quarter flux Hofstadter lattice, which is finite in x and periodic in y, making k_y a good quantum number. There are 4 distinct bands, the middle two touching at 4 Dirac points. The color shows average distance of a mode from the center of the lattice. The red (blue) band crossing edge modes are localized to the left (right) of the lattice.

B.5.5 Hofstadter Entanglement Structure

We can understand the entanglement structure of the edge modes in two ways: firstly, in real space, we observe that as $\eta \to \eta_c$, the real space entanglement approaches all-to-all correlations within each sublattice. For fixed η, the entanglement of the lattice averaged over all bipartitions scales linearly with the size of the edge. Tracing out the bulk modes to get a 1D edge picture, this constitutes a volume-law entanglement scaling, see Fig. B.8(a). The inset shows an example of the entanglement entropy versus bipartition (characterized as the angle at which we cut the lattice), which is nearly bipartition independent.

As mentioned in Chapter 3, we can also understand the entanglement structure from the band diagram, depicted in Fig. B.8(b). Again assuming we can ignore the bulk modes and looking only at the edges, we will treat this as a 1D ring. Now, the real-space chiral symmetry multiplies a mode by a phase $e^{i\pi j}$ on site j, which is equivalent to sending the momentum $k \to k + \pi$. Further, we know that it sends the mode energy $\omega \to -\omega$. Thus, if we define the group velocity $\nu_g = \partial\omega/\partial_k$, it sends

$$\nu_g = \frac{\partial\omega}{\partial k} \to \frac{\partial(-\omega)}{\partial(k+\pi)} = -\nu_g \tag{B.78}$$

Hence, the steady state pairs states with opposite group velocity, i.e. chiral edge modes propagating clockwise with ones propagating counter-clockwise. In the band structure (see Fig. B.8(b), assuming periodic boundary conditions in the y-direction), we can identify that modes localized to the left (red in the plot) pair with their partner at $k + \pi$ and negative energy. Similarly for right-localized sites in blue.

B.5.6 Topological Boundary Entanglement

Here, we prove the claim in Chapter 3 that in a topological lattice, two sites will have exponentially enhanced entanglement only if they are connected by a topological boundary.

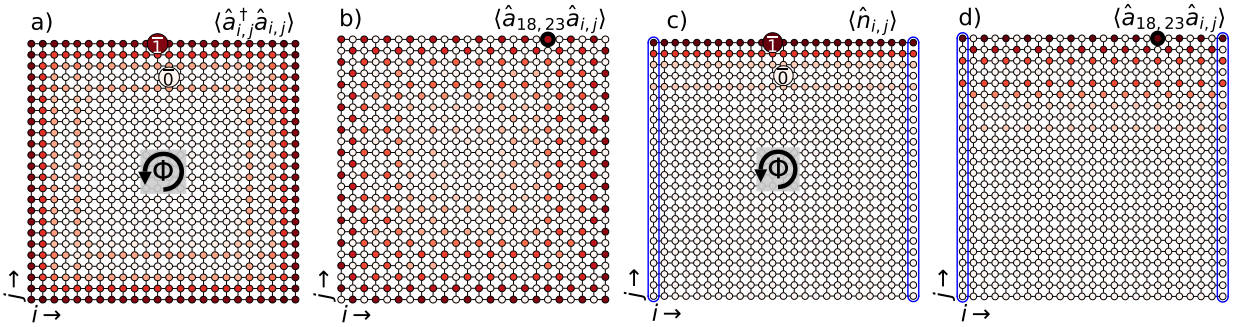

Figure B.9: All four plots show steady state correlations for a 24×24 site quarter flux Hofstadter lattice. There is a single dissipator of the form $\hat{L} = \hat{a}_{\overline{0}} + \eta \hat{a}^\dagger_{\overline{1}}$, where the sites $\overline{0} = (11, 23)$ and $\overline{1} = (12, 20)$ are shown in a) and c). $\eta = 0.999\eta_c$ in both plots. a) and c) show the local photon number density, and b) and d) show lattice correlations with the site (18,23), denoted by a dark circle. a) and b) correspond to a square lattice with open boundary conditions, giving a single extended edge. c) and d) have open boundary conditions in the j direction, and are periodic in the i direction; the lattice sites encircled in blue ellipses are identified with each other. Thus, the top-most and bottom-most rows of lattice sites are distinct edges separated by a 22-lattice site bulk. Note that the two edges are unentangled from each other completely, and the photon density is restricted to only a single edge in the steady state.

To show this, we assume that all of the bulk modes are nearly translationally invariant, and all of the edge modes have an exponentially decaying profile. We take the two lattice sites $\overline{0}, \overline{1}$ to have distances x, y from the edge. Now, we can take $\eta \sim \exp(-\zeta_L(x - y))$, so that the delocalized bulk modes have an exponentially damped squeezing parameter, but the edge modes have $\tanh r_\alpha \sim 1$, and so they are approaching criticality. Clearly, if two sites exhibit some macroscopic entanglement, it must be via an edge mode, as the bulk modes are exponentially close to the trivial vacuum.

Now, let's assume that two sites are not connected by a topological boundary; that is to say, they live on different edges. There are two ways to entangle the two sites: firstly, one can imagine that there is a mode localized to one edge, whose minus energy partner is localized to another edge, and they then form a two mode squeezed vacuum, entangling the edges. However, this would violate our real space sublattice symmetry, since flipping a sign on every other lattice site cannot change which edge a mode is localized to. Thus, the only

way to create some entanglement is if there is a mode that has a finite overlap with multiple edges. Let's define such a mode as $|\psi\rangle = (|L\rangle + |R\rangle)/\sqrt{2}$. Where $|L\rangle$ and $|R\rangle$ are localized to the left and right edges, respectively. Now, if we have a Hamiltonian $\hat{H}$, we know that

$$\hat{H}|\psi\rangle = \epsilon|\psi\rangle \tag{B.79}$$

$$\implies \hat{H}(|L\rangle + |R\rangle) = \epsilon(|L\rangle + |R\rangle) \tag{B.80}$$

Invoking the assumption that the Hamiltonian is local, we observe that $\langle L|\hat{H}|R\rangle = O(e^{-\zeta_L N})$ is exponentially suppressed, where ζ_L^{-1} is the localization length scale, and N the distance between edges. Hence, in the limit $N \gg 1$, $|L\rangle$ and $|R\rangle$ are approximately degenerate eigenmodes. From here, we can break this down into two further cases: if $\epsilon = 0$ then we could have that the proper opposite energy pairs that respect the real space sublattice symmetry are linear combinations $|\psi_\pm\rangle = (|L\rangle \pm e^{i\phi}|R\rangle)/\sqrt{2}$, which is exactly the SSH model, and leads to no long range entanglement.

The second option is that there are two other modes $|L'\rangle$ and $|R'\rangle$ with energy $-\epsilon$, and localized on the left and right, respectively. However, this just means that $|L\rangle$ is paired with $|L'\rangle$ and $|R\rangle$ is paired with $|R'\rangle$, again giving no cross-lattice entanglement.

This completes the proof that edge sites not connected by a topological boundary have exponentially suppressed correlations. A striking example of this is given in Fig. B.9, which shows the correlations in a square Hofstadter lattice identical to Fig. B.6 and Fig. 3.3, compared to the correlations where the boundary condition is made periodic along the horizontal direction, hence creating two distinct edges separated by a bulk. With open boundary conditions and a single topological edge, there is long range, volume law entanglement between all sides of the lattice (as shown in Fig. B.8(a)). However, when there are two disconnected topological boundaries, there is no long range entanglement between the upper and lower edges, see Fig. B.9(c-d).

APPENDIX C

APPENDIX TO CHAPTER 4

C.1 Bound Proof

C.1.1 Trace Relation of Maximally Entangled States

Here, we will prove the trace property of maximally entangled states mentioned in Chapter 4. Namely, if we define

$$|\psi\rangle = \frac{1}{\sqrt{N}} \sum_{i=1}^{N} |i\rangle_A \otimes |i\rangle_B, \tag{C.1}$$

then for any local operator $\hat{O}_A \otimes \hat{\mathbf{1}}$, we can see that

$$\langle\psi|\hat{O}_A \otimes \hat{\mathbf{1}}|\psi\rangle = \frac{1}{N} \sum_{i,j} \langle i|\hat{O}_A|j\rangle \otimes \langle i|j\rangle = \frac{1}{N} \sum_{i} \langle i|\hat{O}_A|i\rangle = \frac{1}{N} \ \mathrm{tr}\hat{O}_A. \tag{C.2}$$

By the symmetry of the state under $A \leftrightarrow B$, this also tells us that the expectation value of any local B operator of the form $\hat{\mathbf{1}} \otimes \hat{O}_B$ is also equivalent to its trace. Since for any jump operator $\hat{L} = \hat{A} \otimes \hat{\mathbf{1}} + \hat{\mathbf{1}} \otimes \hat{B}$ that is a sum of local operators, it's commutator with its adjoint is also a sum of local operators

$$[\hat{L}, \hat{L}^\dagger] = [\hat{A}, \hat{A}^\dagger] \otimes \hat{\mathbf{1}} + \hat{\mathbf{1}} \otimes [\hat{B}, \hat{B}^\dagger], \tag{C.3}$$

then the expectation value

$$\langle\psi|[\hat{L}, \hat{L}^\dagger]|\psi\rangle = \frac{1}{N} \Big(\ \mathrm{tr}[\hat{A}, \hat{A}^\dagger] + \ \mathrm{tr}[\hat{B}, \hat{B}^\dagger] \Big) = 0, \tag{C.4}$$

as noted in Chapter 4.

C.1.2 Proof of Main Bound

We can now move on to proving the main bound. Following a similar construction to [284], we will bound the fidelity to the steady state

$$F(t) = \left(\operatorname{tr}\sqrt{\sqrt{\hat{\rho}_{\mathrm{ss}}}\hat{\rho}_t\sqrt{\hat{\rho}_{\mathrm{ss}}}}\right)^2. \tag{C.5}$$

Because we assume the steady state is pure, this can be simplified as

$$F(t) = \operatorname{tr}(\hat{\rho}_t\hat{\rho}_{\mathrm{ss}}). \tag{C.6}$$

Now, we can bound the change in the fidelity by its maximal derivative, i.e.

$$|F(t) - F(0)| \leq \Gamma_{\max} t, \tag{C.7}$$

$$\Gamma_{\max} = \max|\partial_t F(t)|, \tag{C.8}$$

and so we will focus now on bounding $\partial_t F(t)$. Letting $\mathcal{L}$ be the Lindbladian and noting that $\hat{\rho}_{\mathrm{ss}}$ is time-independent, we can observe that

$$|\partial_t F(t)| = |\operatorname{tr}(\hat{\rho}_{\mathrm{ss}}\partial_t\hat{\rho}_t)| = |\operatorname{tr}(\hat{\rho}_{\mathrm{ss}}\mathcal{L}\hat{\rho}_t) = |\operatorname{tr}(\mathcal{L}^\dagger\hat{\rho}_{\mathrm{ss}}\hat{\rho}_t)|, \tag{C.9}$$

where we have used the definition of the adjoint Lindbladian to move it onto steady state (where the adjoint is with respect to the Hilbert-Schmidt norm). The Cauchy-Schwartz inequality gives:

$$\Gamma_{\max} \leq |\operatorname{tr}(\mathcal{L}^\dagger\hat{\rho}_{\mathrm{ss}}\hat{\rho}_t)| \leq \sqrt{\operatorname{tr}(\mathcal{L}^\dagger\hat{\rho}_{\mathrm{ss}})^2\operatorname{tr}(\hat{\rho}_t)^2} \leq \sqrt{\operatorname{tr}(\mathcal{L}^\dagger\hat{\rho}_{\mathrm{ss}})^2}. \tag{C.10}$$

Thus the rate $\Gamma_{\max}$ is bounded by the Hilbert-Schmidt norm of the adjoint Lindbladian acting on the steady state. We can further simplify this:

$$\mathcal{L}^\dagger \hat{\rho}_{\rm ss} = i[\hat{H}, \hat{\rho}_{\rm ss}] + \sum_\mu \hat{L}_\mu^\dagger \hat{\rho}_{\rm ss} \hat{L}_\mu - \frac{1}{2}\{\hat{L}_\mu^\dagger \hat{L}_\mu, \hat{\rho}_{\rm ss}\} = \sum_\mu \hat{L}_\mu^\dagger \hat{\rho}_{\rm ss} \hat{L}_\mu; \tag{C.11}$$

$$\implies \operatorname{tr}(\mathcal{L}^\dagger \hat{\rho}_{\rm ss})^2 = \operatorname{tr}\left[\sum_{\mu,\nu} \hat{L}_\mu^\dagger \hat{\rho}_{\rm ss} \hat{L}_\mu \hat{L}_\nu^\dagger \hat{\rho}_{\rm ss} \hat{L}_\nu\right] = \sum_{\mu,\nu} |\langle\psi|[\hat{L}_\mu, \hat{L}_\nu^\dagger]|\psi\rangle|^2, \tag{C.12}$$

where we have used repeatedly the fact that $[\hat{H}, \hat{\rho}_{\rm ss}] = \hat{L}_\mu \hat{\rho}_{\rm ss} = 0$. Next, we will expand out the jump operator in terms of its matrix elements in the Schmidt basis:

$$\hat{L}_\mu = \hat{A}_\mu \otimes \hat{\mathbf{1}} + \hat{\mathbf{1}} \otimes \hat{B}_\mu \equiv \sum_{ij}^{N} (A_\mu)_{ij} |i\rangle\langle j| \otimes \hat{\mathbf{1}} + \hat{\mathbf{1}} \otimes (B_\mu)_{ij} |i\rangle\langle j|. \tag{C.13}$$

To proceed, we will need to understand the relation between $(A_\mu)_{ij}$ and $(B_\mu)_{ij}$ which is implied by $\hat{L}_\mu|\psi\rangle = 0$. We find that, writing $|\psi\rangle$ in the Schmidt basis, (and removing tensor product signs for brevity)

$$0 = \sum_{ijkl}^{N} \sqrt{p_l}\left[(A_\mu)_{ij}|ik\rangle\langle jk| + (B_\mu)_{ij}|ki\rangle\langle kj|\right]|ll\rangle = \sum_{ij}^{N}\left[\sqrt{p_j}(A_\mu)_{ij} + \sqrt{p_i}(B_\mu)_{ji}\right]|ij\rangle; \tag{C.14}$$

$$\implies (A_\mu)_{ij} = -\sqrt{p_i}(B_\mu)_{ji}\frac{1}{\sqrt{p_j}}. \tag{C.15}$$

Recalling the definition of Ψ in Eq. (4.23), this is equivalent to

$$A_\mu = -\Psi B_\mu^T \Psi^{-1}, \tag{C.16}$$

as stated in Chapter 4 [Eq. (4.24)]. Coming back to the bound, we can expand Eq. (C.12) in terms of matrix elements as

$$\Gamma_{\max}^2 \leq \sum_{\mu,\nu} \left[\sum_{j,k=1}^{N} \left((A_\mu)_{j,k} (A_\nu)^*_{j,k} + (B_\mu)_{j,k} (B_\nu)^*_{j,k} \right) (p_j - p_k) \right]^2 \tag{C.17a}$$

$$= \sum_{\mu,\nu} \left[\sum_{j,k=1}^{N} (A_\mu)_{j,k} (A_\nu)^*_{j,k} \frac{(p_j - p_k)^2}{p_k} \right]^2 \leq \sum_{\mu,\nu} \left[\frac{|A_\mu||A_\nu|}{p_{\min}} \sum_{j,k=1}^{N} (p_j - p_k)^2 \right]^2 \tag{C.17b}$$

$$= \frac{1}{p_{\min}^2} \left(\sum_\mu |A_\mu|^2 \right)^2 \left[\sum_{j,k=1}^{N} (p_j - p_k)^2 \right]^2 = \frac{2N^2}{p_{\min}^2} \left(\sum_\mu |A_\mu|^2 \right)^2 \left(e^{-S^{(2)}} - N^{-1} \right)^2 . \tag{C.17c}$$

In Eq. (C.17b), we have defined $|A_\mu|$ to be the largest matrix element of A_μ in the Schmidt basis, and $\sqrt{p_{\min}}$ to be the smallest Schmidt coefficient. Taking a square root of both sides gives

$$\Gamma_{\max} \leq \frac{\sqrt{2}N}{p_{\min}} \left(\sum_\mu |A_\mu|^2 \right) \left(e^{-S^{(2)}} - N^{-1} \right), \tag{C.18}$$

recovering the result from Chapter 4.

C.1.3 Non-Full Rank Steady State

If Ψ is not full rank, then $p_{\min}^{-1}$ is ill-defined. However, a similar bound can be derived for a state that is not full rank. Beginning at Eq. (C.17), we note that

$$\Gamma_{\max}^2 \leq \sum_{\mu,\nu} \left[\sum_{j,k=1}^{N} \left(A_\mu)_{j,k} (A_\nu)^*_{j,k} + (B_\mu)_{j,k} (B_\nu)^*_{j,k} \right) \left(|\psi_j|^2 - |\psi_k|^2 \right) \right]^2$$

$$\leq \sum_{\mu,\nu} \left(|A_\mu||A_\nu| + |B_\mu||B_\nu| \right)^2 \left[\sum_{j,k=1}^{N} \left| |\psi_j|^2 - |\psi_k|^2 \right| \right]^2$$

$$\leq N^2 \sum_{\mu,\nu} \left(|A_\mu||A_\nu| + |B_\mu||B_\nu| \right)^2 \sum_{j,k=1}^{N} (|\psi_j|^2 - |\psi_k|^2)^2$$

$$= 2N^3 \sum_{\mu,\nu} \left(|A_\mu||A_\nu| + |B_\mu||B_\nu| \right)^2 \left(e^{-S^{(2)}} - N^{-1} \right), \tag{C.19}$$

$$\implies \Gamma_{\max} \leq 2N^{3/2} \sqrt{\sum_{\mu,\nu} \left(|A_\mu||A_\nu| + |B_\mu||B_\nu| \right)^2} \left(e^{-S^{(2)}} - N^{-1} \right)^{1/2}$$

$$\leq 2N^{3/2} \left[\left(\sum_{\mu=1}^{M} |A_\mu| \right)^2 + \left(\sum_{\mu=1}^{M} |B_\mu| \right)^2 \right] \delta\mathcal{E}_2^{1/2}, \tag{C.20}$$

where we see that the bound depends only on the root of $\delta\mathcal{E}_2$ as opposed to linearly for the case of a full rank system.

C.1.4 Necessity of Multiple Jump Operators

We now prove the result from Chapter 4, that the condition Eq. (4.24) implies that A and B are isospectral, necessitating multiple jump operators (or a Hamiltonian interaction) to get a unique steady state. Let's begin by assuming that the matrix A is diagonalizable. The relation $A = -\Psi B^T \Psi^{-1}$ tells us that if A is diagonalizeable via $A = P^{-1} D P$, then $B^T = -(P\Psi)^{-1} D (P\Psi)$. Hence, B is also diagonalizeable as

$$B = (P\Psi)^T (-D) ((P\Psi)^T)^{-1}. \tag{C.21}$$

Thus, we can work in the (non-orthonormal) basis of eigenvectors of A and B so that

$$\hat{L} = \hat{D}_A \otimes \hat{\mathbf{1}} - \hat{\mathbf{1}} \otimes \hat{D}_B. \tag{C.22}$$

and therefore every vector of the form $|\psi\rangle = |i\rangle_A \otimes |i\rangle_B$ is in the kernel of $\hat{L}$, where $|i\rangle_{A,B}$ are the eigenbases of A, B, respectively.

Alternatively, let's assume that A is not diagonalizeable. In this case, we can find a basis where it is in Jordan-Normal form. Let's consider just a single Jordan Block of the form

$$A = \begin{pmatrix} \lambda & 1 & 0 & 0 & \dots & 0 \\ 0 & \lambda & 1 & 0 & \dots & 0 \\ \vdots & \vdots & \vdots & \ddots & \dots & 0 \\ 0 & 0 & 0 & \dots & \lambda & 1 \\ 0 & 0 & 0 & \dots & 0 & \lambda \end{pmatrix} \tag{C.23}$$

of dimension $n \times n$. Now, we can rewrite this in the following way: A has a single eigenvector we will denote as $|0\rangle$ such that $A|0\rangle = \lambda|0\rangle$. Then, we define that $A|m\rangle = \lambda|m\rangle + |m-1\rangle$ for $m > 0$. Now, since $A, -B^T$ are similar matrices, they have an identical Jordan Normal form. Hence, we can define an identical basis for B such that $B|m\rangle = -\lambda|m\rangle - |m-1\rangle$ (for $m > 0$) and $B|0\rangle = \lambda|0\rangle$. Now, consider the set of states

$$|\phi_n\rangle = \sum_{m=0}^{n} |m\rangle \otimes |n-m\rangle. \tag{C.24}$$

Now, we can observe that $\hat{L}|\phi_n\rangle$ is

$$\begin{aligned}\hat{L}|\phi_n\rangle &= (A \otimes \hat{\mathbf{1}} + \hat{\mathbf{1}} \otimes B) \sum_{m=0}^{n} |m\rangle \otimes |n-m\rangle \\ &= \sum_{m=1}^{n} |m-1\rangle \otimes |n-m\rangle - \sum_{m=0}^{n-1} |m\rangle \otimes |n-m-1\rangle = 0. \end{aligned} \tag{C.25}$$

Repeating this construction for each Jordan block implies that the dimension of the kernel of $\hat{L}$ is always at least N. To lift this degeneracy of the Lindbladian, we need (at least) two jump operators such that $\ker \hat{L}_1 \cap \ker \hat{L}_2$ is spanned by the steady state $|\psi\rangle$, or a Hamiltonian interaction such that the intersection of the eigenvectors of the Hamiltonian and the kernel of $\hat{L}$ is spanned by the steady state $|\psi\rangle$.

In Appendix C.2 we will do this by choosing multiple random jump operators.

C.1.5 Uneven Hilbert Space Dimension

Throughout Chapter 4, we mainly limit the discussion to bipartite Hilbert spaces where each subspace has an identical Hilbert space dimension. Now, we wish to explore what happens when considering systems of uneven dimension; without loss of generality we will assume $\mathcal{H} = \mathcal{H}_A \otimes \mathcal{H}_B$ and

$$\dim(\mathcal{H}_A) \equiv N_A < N_B \equiv \dim(\mathcal{H}_B). \tag{C.26}$$

Now, we can still define a pure steady state in terms of it's Schmidt coefficients:

$$|\psi\rangle = \sum_{i=1}^{N_A} \sqrt{p_i} |i\rangle_A \otimes |i\rangle_B, \tag{C.27}$$

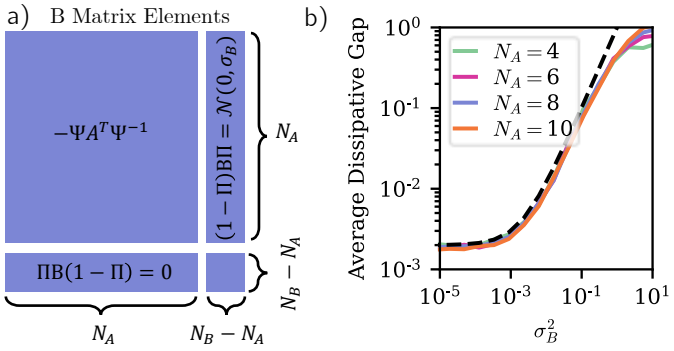

Figure C.1: a) Depiction of the matrix elements of B when there is an uneven Hilbert space dimension, breaking B into four blocks using the projector Π [c.f. Eq. (C.32)]. b) The dissipative gap for random Linbladians averaged over 100 instances, with $\delta\mathcal{E}_2$ fixed to be 10^{-3}. The A matrix is sampled from the random Ginibre ensemble with unit variance, and the elements in $(\hat{\mathbf{1}} - \Pi)B\Pi$ are sampled from a normal distribution with zero mean and variance σ_B^2. the elements of $(\hat{\mathbf{1}} - \Pi)B(\hat{\mathbf{1}} - \Pi)$ are irrelevant, and taken to be 0. The black dashed line gives the expected scaling of $\sigma_B^2 + 2\delta\mathcal{E}_2$ until the gap saturates to an $\mathcal{O}(1)$ parameter for $\sigma_B^2 \gtrsim 1$.

where p_i are real and positive. We define the remaining $(N_B - N_A)$ dimensional subspace of $\mathcal{H}_B$ as

$$\mathcal{H}'_B = \mathcal{H}_B \setminus \text{span}\{|i\rangle_B | i = 1, \ldots, N_A\}, \tag{C.28}$$

for which we will define the basis $\{|i\rangle_B | i = N_A + 1, \ldots, N_B\}$. A maximally entangled state is still defined by a flat distribution of Schmidt coefficients, where $p_i = N_A^{-1}$. Taking $\hat{L} = \hat{A} \otimes \hat{\mathbf{1}} + \hat{\mathbf{1}} \otimes \hat{B}$ as before, we now calculate $|\hat{L}^\dagger|\psi\rangle|^2$ when the $\hat{B}$ is of larger rank than $\hat{A}$ and $|\psi\rangle$ is maximally entangled. We now find that

$$\begin{aligned} |\hat{L}^\dagger|\psi\rangle|^2 &= \langle\psi|[\hat{L}, \hat{L}^\dagger]|\psi\rangle = \langle\psi|[\hat{A}, \hat{A}^\dagger] \otimes \hat{\mathbf{1}}|\psi\rangle + \langle\psi|\hat{\mathbf{1}} \otimes [\hat{B}, \hat{B}^\dagger]|\psi\rangle \\ &= \text{tr}[\hat{A}, \hat{A}^\dagger] + \frac{1}{N_A}\sum_{i=1}^{N_A}\langle i|[\hat{B}, \hat{B}^\dagger]|i\rangle = \frac{1}{N_A}\sum_{i=1}^{N_A}\sum_{j=N_A+1}^{N_B} |B_{ij}|^2 - |B_{ji}|^2. \end{aligned} \tag{C.29}$$

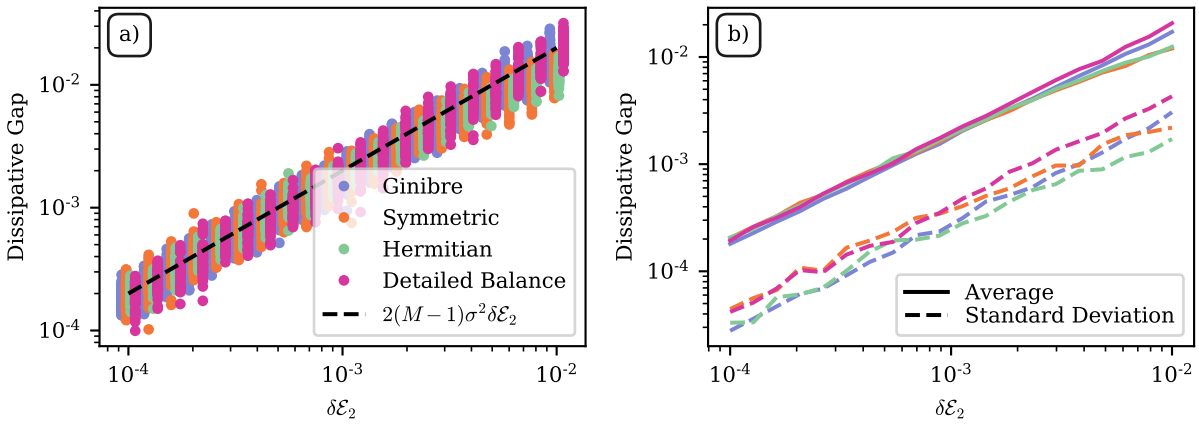

Figure C.2: (a) Dissipative gap of random Lindbladians given a fixed steady state entanglement $\mathcal{E}_2$, similar to Fig. 4.2. Different colors correspond to drawing the matrix A from different distributions, see Eq. (C.47). For each distribution and entanglement value we sample 100 Lindbladians, with local dimension $N = 10$ and $M = 2$ jump operators. The black dashed line gives the scaling as predicted in Eq. (4.27). (b) Average (solid lines) and standard deviation (dashed lines) of points in (a) for a fixed value of entanglement and distribution.

The condition $\hat{L}|\psi\rangle = 0$ implies (see Fig. C.1)

$$B_{ij} = \begin{cases} A_{ji}\frac{\psi_i}{\psi_j} & i,j \leq N_A \\ 0 & i > N_A, j \leq N_A \end{cases}, \tag{C.30}$$

which allows us to reduce Eq. (C.29) to simply

$$|\hat{L}^\dagger|\psi\rangle|^2 = \frac{1}{N_A}\sum_{i=1}^{N_A}\sum_{j=N_A+1}^{N_B}|B_{ij}|^2, \tag{C.31}$$

which can now be non-zero; i.e. it is possible to generate a maximally entangled state if $N_B > N_A$, as was noted in the case of a qubit and qutrit in [117]. Let's define the projection

operator $\hat{\Pi}$ as

$$\hat{\Pi} = \sum_{j=N_A+1}^{N_B} |j\rangle\langle j|. \tag{C.32}$$

Then Eq. (C.30) tells us that $\hat{\Pi}\hat{B}(\hat{\mathbf{1}} - \hat{\Pi}) = 0$. However, we also know that to avoid slowdown, we require that $||(\hat{\mathbf{1}} - \hat{\Pi})\hat{B}\hat{\Pi}|| \neq 0$, as otherwise we can just truncate the Hilbert space and recover the bound for $N_A = N_B$. In fact, we can rewrite the bound in this case as

$$\Gamma_{\max} \leq \frac{\sqrt{2}N}{p_{\min}} \left(\sum_{\mu} |A_\mu|^2 \right) \delta\mathcal{E}_2 + \sum_{\mu} ||(\hat{\mathbf{1}} - \hat{\Pi})\hat{B}_\mu \hat{\Pi}||_2^2, \tag{C.33}$$

where the norm $||\hat{O}||_2$ is the operator norm defined as the largest singular value of $\hat{O}$. The first term is simply the standard one from before, and the second is a measure of how much the dissipation is utilizing the extra Hilbert space available. Using an uneven Hilbert space dimension to circumvent slowdown was first considered in a qubit-qutrit system in [117]; however, it should also work perfectly well in the many body case. This can be seen in Fig. C.1, where we take $N_B = N_A + 1$, and take A from the random Ginbre ensemble. Then we take the elements of $(\hat{\mathbf{1}} - \hat{\Pi})B\hat{\Pi}$ to be normally distributed with zero mean and variance σ_B. Finally, we define the projection super-operator

$$\mathcal{P} = \sum_{i,j=1}^{N_A} |\rho_{ij}\rangle\rangle\langle\langle\rho_{ij}|, \tag{C.34}$$

$$\hat{\rho}_{ij} = |i\rangle\langle i|_A \otimes |j\rangle\langle j|_B. \tag{C.35}$$

(As before the double bracket notation $|\rho_{ij}\rangle\rangle$ signifies a vectorized density matrix.) If $\mathcal{L}$ is the Lindbladian acting on the enlarged Hilbert space ($N_B > N_A$), then we can define

$$\mathcal{L}' = \mathcal{P}\mathcal{L}\mathcal{P}, \tag{C.36}$$

which gives the effective dynamics in the subspace of dimension N_A^4. If we look at the gap as a function of σ_B^2, we can see that when $\sigma_B^2 \ll \delta\mathcal{E}_2$, then the gap is dominated by the entanglement induced slowdown. However, when $\sigma_B^2 \gtrsim \delta\mathcal{E}_2$, the gap opens up linearly in σ_B^2, before saturating at an $\mathcal{O}(1)$ value. Note the projection $\mathcal{P}$ is necessary as otherwise when $\sigma_B^2 \ll 1$ the slow time-scale would be dominated by the time to get out of the extra B system levels, and we would not see the plateau at small σ_B^2.

An alternative interpretation is that systems on uneven Hilbert space dimension can be recast as effectively being of equal dimension with non-full-rank steady state Schmidt coefficients. That is to say, again assuming $N_B > N_A$, we can always define the operator

$$\tilde{A}_\mu = A_\mu \oplus 0_{N_B - N_A}, \tag{C.37}$$

where by taking a direct sum with the 0 matrix, we essentially just pad A_μ with zeroes so it is of the same dimension as B_μ. Next, we define the steady state Schmidt coefficients

$$\tilde{\psi}_i = \left\{ \begin{array}{cc} \psi_i & i \leq N_A \\ 0 & N_A < i \leq N_B \end{array} \right\}, \tag{C.38}$$

and again choose B_μ as in Eq. (C.30). Now, we have a new master equation on an even Hilbert space dimension with identical dynamics. We have simply augmented the Hilbert space with uncoupled extra levels on the A system. This means the steady state reduced density matrix is not full rank, but still the bound Eq. (4.19) will apply. Hence, given a state on an uneven Hilbert space we can also state that

$$\Gamma_{\max} \leq 2N_B^{3/2} \left[\left(\sum_{\mu=1}^{M} |A_\mu| \right)^2 + \left(\sum_{\mu=1}^{M} |B_\mu| \right)^2 \right] \left(e^{-S_{\text{ss}}^{(2)}} - \frac{1}{N_B} \right)^{1/2}. \tag{C.39}$$

In this case, $e^{-S_{\text{ss}}^{(2)}} \geq N_A^{-1}$, and so the gap will not close even for a maximally entangled state, as shown in e.g. [117].

C.1.6 Mixing Time

Another relevant quantity in both classical or quantum Markov chains is the mixing time [132] which can be thought of as the smallest time after which any initial probability distribution (or density matrix, in the quantum case) is within ϵ distance of the steady state distribution. More formally, we can define this as

$$t_{\text{mix}}(\epsilon) = \inf\{t > 0 \mid \forall \hat{\rho}, d_{\text{tr}}(e^{\mathcal{L}t}\hat{\rho}, \hat{\rho}_{\text{ss}}) \leq \epsilon\}, \tag{C.40}$$

where d_{tr} is the trace distance and $\hat{\rho}_{\text{ss}}$ is the steady state density matrix. The bound as stated in Eq. (4.18) is in terms of the quantum fidelity; however, this is related to the trace distance by [133]:

$$d_{\text{tr}}(\hat{\rho}, \hat{\sigma}) \geq 1 - F(\hat{\rho}, \hat{\sigma}), \tag{C.41}$$

as long as at least one of $\hat{\rho}$ or $\hat{\sigma}$ is a pure state. Thus, if we now use that $F(e^{\mathcal{L}t}\hat{\rho}, \hat{\rho}_{\text{ss}}) \leq F(\hat{\rho}, \hat{\rho}_{\text{ss}}) + vt$, then we find that

$$\epsilon \geq d_{\text{tr}}(e^{\mathcal{L}t}\hat{\rho}, \hat{\rho}_{\text{ss}}) \geq 1 - F(e^{\mathcal{L}t}\hat{\rho}, \hat{\rho}_{\text{ss}}) \geq 1 - F(\hat{\rho}, \hat{\rho}_{\text{ss}}) - \Gamma_{\max} t \tag{C.42}$$

$$\implies \Gamma_{\max} t \geq 1 - \epsilon - F(\hat{\rho}, \hat{\rho}_{\text{ss}}) \tag{C.43}$$

$$\implies t_{\text{mix}}(\epsilon) \geq \frac{1-\epsilon}{\Gamma_{\max}} \tag{C.44}$$

where $\Gamma_{\max}$ is bounded from above by Eq. (4.18) as derived before. Hence, the mixing time is lower bounded by one over the distance from the maximal entropy.

C.2 Random Lindbladians

C.2.1 Random Jump Operators

It is useful to consider how well the bound is saturated on a class of random Lindbladians, as shown in Chapter 4. Let's define a distribution of Schmidt coefficients $\{p_i\}$ subject to

$$\sum_i p_i = 1, \quad -\log \sum_i p_i^2 = S^{(2)}, \tag{C.45}$$

for some fixed value of the Renyi-2 entropy $S^{(2)}$. Now, given this distribution, we define a set of random matrices A_μ sampled from the complex Ginibre ensemble where $(A_\mu)_{ij}$ are independent and identically distributed (i.i.d.) Gaussian random variables with

$$\mathbb{E}[(A_\mu)_{ij}] = 0, \quad \mathbb{E}[(A_\mu)^*_{ij}(A_\nu)_{kl}] = \delta_{ik}\delta_{jl}\delta_{\mu\nu}\sigma^2. \tag{C.46}$$

We will sample random jump operators from many ensembles, including the complex Ginibre ensemble, random Hermitian matrices, random symmetric matrices, and random matrices which obey detailed balance. For concreteness, let's define A drawn from the random Ginibre ensemble above [Eq. (C.46)]. Then we define the random Hermitian operator A_H, random symmetric operator A_S, and random detailed balance operator A_{DB} as

$$A_H = \frac{1}{\sqrt{2}}(A + A^\dagger), \tag{C.47a}$$

$$A_S = \frac{1}{\sqrt{2}}(A + A^T), \tag{C.47b}$$

$$A_{DB} = \frac{1}{\sqrt{2}}(A_S + \Psi A_S^T \Psi^{-1}). \tag{C.47c}$$

For all of these ensembles, we find that the dissipative gap scales linearly with $\delta\mathcal{E}_2$ predicted by the bound. This is shown in Fig. C.2.

C.2.2 Fidelity Rate of Change from a Haar Random State

The bound Eq. (4.18) states that no state can approach the steady state at a rate faster than $\mathcal{O}(N^2) \times \delta\mathcal{E}_2$. However, numerics seem to imply that the dissipative gap is actually $\mathcal{O}(1) \times \delta\mathcal{E}_2$. One might guess that this discrepancy is a result of the fact that dissipative gap is the slowest relaxing mode, whereas the bound applies to the fastest. To get a prefactor closer to $\mathcal{O}(1)$, we can consider bounding a Haar random state as opposed to all states. Recalling the formula from above [Eq. (C.9)], we know that

$$\partial_t F(t) = \operatorname{tr}\left(\hat{\rho}_t \mathcal{L}^\dagger \hat{\rho}_{\text{ss}}\right). \tag{C.48}$$

Let $\hat{\rho}_t = \hat{U}|0\rangle\langle 0|\hat{U}^\dagger$ with $\hat{U}$ integrated over the Haar measure. Since $\partial_t F(t)$ is linear in $\hat{\rho}_t$, we can just directly calculate that

$$\int_{\text{Haar}} \hat{U}|0\rangle\langle 0|\hat{U}^\dagger \, \mathrm{d}U = \frac{\hat{\mathbf{1}}}{N^2}; \tag{C.49}$$

$$\implies \int_{\text{Haar}} \partial_t F(t) \, \mathrm{d}U = \frac{1}{N^2} \operatorname{tr}\left(\mathcal{L}^\dagger \hat{\rho}_{\text{ss}}\right). \tag{C.50}$$

Now, we can calculate that

$$\frac{1}{N^2} \operatorname{tr}\left(\mathcal{L}^\dagger \hat{\rho}_{\text{ss}}\right) = \frac{1}{N^2} \sum_\mu \langle\psi|[\hat{L}_\mu, \hat{L}_\mu^\dagger]|\psi\rangle = \frac{1}{N^2} \sum_\mu \sum_{j,k=1}^{N} |(A_\mu)_{j,k}|^2 \frac{(p_j - p_k)^2}{p_k}. \tag{C.51}$$

Now at this point, we can see that this can be bounded in a similar way as before by

$$\int_{\text{Haar}} \partial_t F(t) \, \mathrm{d}U \leq \left(\sum_\mu |A_\mu|^2\right) \frac{2}{N p_{\min}} \delta\mathcal{E}_2. \tag{C.52}$$

We can be more precise if we know something about the distributions from which we sample A_μ and p_j. Suppose A_μ is sampled from a random distribution with variance

$$\mathbb{E}\left[|(A_\mu)_{j,k}|^2\right] = \sigma^2. \tag{C.53}$$

Further, let's rewrite the Schmidt coefficients in the following, physically motivated form:

$$p_i = \frac{e^{-\beta\lambda_i}}{\sum_{j=1}^N e^{-\beta\lambda_j}} \tag{C.54}$$

where we have defined a new set of random variables λ_i. Note that by writing it in this manner, the fact that $\sum_{i=1}^N p_i = 1$ is inherently manifest. Moreover, we have a single parameter β that can tune the steady state entanglement entropy. When $\beta = 0$, then $p_i = 1/N$ and the state is maximally entangled. As $\beta \to \infty$, the state becomes pure. Moreover, $\delta\mathcal{E}_2(\beta)$ is monotonic in β, so there is a unique value of β to fix the entanglement. Next, observe that if $\lambda_i \to \lambda_i - \overline{\lambda}$, then p_i are invariant, so without loss of generality we can take $\sum_{i=1}^N \mathbb{E}[\lambda_i] = 0$. Next, we will set a scale for β by defining

$$\frac{1}{N}\sum_{i=1}^N \mathbb{E}[\lambda_i^2] = 1 \tag{C.55}$$

We can always do this (for any distribution with a well defined second moment) by rescaling β. Finally, we will define the variable $\chi^2 = \sum_{i,j=1}^N \mathbb{E}[\lambda_i\lambda_j]$. For example, if λ_i are i.i.d. then $\chi^2 = N$. To calculate the average of the rate of change of the fidelity, it will be necessary to compute the average $\sum_{i=1}^N \mathbb{E}[p_i^{-1}]$. We can make progress by noting that, in the high entanglement limit, the variance of the p_i is highly constrained by fixing the entropy. Hence, we can compute this to leading order in $\delta\mathcal{E}_2$ (or equivalently, the small β limit). Observe

that

$$\mathbb{E}[\delta\mathcal{E}_2] = \mathbb{E}\left[\frac{\sum_{i=1}^N e^{-2\beta\lambda_i}}{\left(\sum_{j=1}^N e^{-\beta\lambda_j}\right)^2}\right] = \frac{\beta^2}{N}\left(1 - \frac{\chi^2}{N^2}\right) + \mathcal{O}(\beta^4 N^2). \tag{C.56}$$

Now, $\delta\mathcal{E}_2$ is in fact fixed, so we can invert this to be an equation instead for β:

$$\frac{\beta^2}{N}\left(1 - \frac{\chi^2}{N^2}\right) = \delta\mathcal{E}_2 + \mathcal{O}(\delta\mathcal{E}_2 N^2)^2. \tag{C.57}$$

From here, we can now calculate, to leading order in β:

$$\begin{aligned}\sum_{i=1}^N \mathbb{E}[p_i^{-1}] &= \sum_{i,j=1}^N \mathbb{E}\left[e^{-\beta(\lambda_i - \lambda_j)}\right] = N^2 + \frac{\beta^2}{2}\sum_{j,k=1} \mathbb{E}\left[(\lambda_i - \lambda_j)^2\right] + \mathcal{O}(\beta^4 N^2) \\ &= N^2\left(1 + N\delta\mathcal{E}_2\right) + \mathcal{O}(N^2\delta\mathcal{E}_2)^2.\end{aligned} \tag{C.58}$$

We can use this relation to observe that Eq. (C.51) simplifies to

$$\begin{aligned}\mathbb{E}\left[\int_{\text{Haar}} \partial_t F(t)\, \mathrm{d}U\right] &= \mathbb{E}\left[\frac{1}{N^2}\sum_{\mu=1}^M \sum_{j,k=1}^N |(A_\mu)_{j,k}|^2 \frac{\left(p_j - p_k\right)^2}{p_k}\right] \\ &= \frac{M\sigma^2}{N^2}\mathbb{E}\left[\sum_{j,k=1}^N \frac{\left(p_j - p_k\right)^2}{p_k}\right] \\ &= 2M\sigma^2\delta\mathcal{E}_2 + \mathcal{O}(\delta\mathcal{E}_2)^2,\end{aligned} \tag{C.59}$$

where we defined M to be the number of jump operators. Assuming $N\delta\mathcal{E}_2 \ll 1$, we can drop the second term as small and recover the result quoted in the text. We can also calculate the variance one would expect from such a distribution. Here, we calculate

$$\mathbb{E}\left[\int_{\text{Haar}} |\partial_t F(t)|^2\, \mathrm{d}U\right] = \mathbb{E}\left[\int_{\text{Haar}} \left|\sum_\mu |\langle\psi|L_\mu U|0\rangle|^2\right|^2 \mathrm{d}U\right]. \tag{C.60}$$

This now depends nonlinearly on $\hat{\rho}_t$, so we cannot simply replace the state with its average. However, we can still make progress. We will suppress the integral over the Haar measure for brevity, giving

$$
\begin{aligned}
&\mathbb{E}\left[|\partial_t F|^2\right] \\
&= \mathbb{E}\left[\left|\sum_\mu |\langle\psi|\hat{L}_\mu \hat{U}|0\rangle|^2\right|^2\right] \\
&= \mathbb{E}\left[\sum_{i_\alpha, j_\alpha}^{N}\sum_{\mu,\nu}^{m}(A_\mu)_{j_1k_1}(A_\nu)_{j_2k_2}(A_\mu)^*_{j_3k_3}(A_\nu)^*_{j_4k_4}U_{00}^{k_1j_1}U_{00}^{k_2j_2}(U_{00}^{k_3j_3})^*(U_{00}^{k_4j_4})^*\prod_\alpha\left(\sqrt{p_{j_\alpha}}-\frac{p_{k_\alpha}}{\sqrt{p_{j_\alpha}}}\right)\right] \\
&= \sigma^4\sum_{i_\alpha, j_\alpha}^{N}\sum_{\mu,\nu}^{m}\left(\delta_{13}\delta_{24}+\delta_{14}\delta_{23}\delta_{\mu\nu}\right)\mathbb{E}\left[U_{00}^{k_1j_1}U_{00}^{k_2j_2}(U_{00}^{k_3j_3})^*(U_{00}^{k_4j_4})^*\prod_\alpha\left(\sqrt{p_{j_\alpha}}-\frac{p_{k_\alpha}}{\sqrt{p_{j_\alpha}}}\right)\right] \\
&= \sigma^4\sum_{i_\alpha, j_\alpha}^{N}\left(M^2\delta_{13}\delta_{24}+m\delta_{14}\delta_{23}\right)\frac{(\delta_{13}\delta_{24}+\delta_{14}\delta_{23})}{N^2(N^2+1)}\mathbb{E}\left[\prod_\alpha\left(\sqrt{p_{j_\alpha}}-\frac{p_{k_\alpha}}{\sqrt{p_{j_\alpha}}}\right)\right] \\
&= \frac{\sigma^4(M^2+M)}{N^2(N^2+1)}\sum_{i_\alpha, j_\alpha}^{N}\left(\delta_{13}\delta_{24}+\delta_{1234}\right)\mathbb{E}\left[\prod_\alpha\left(\sqrt{p_{j_\alpha}}-\frac{p_{k_\alpha}}{\sqrt{p_{j_\alpha}}}\right)\right] \\
&= \frac{\sigma^4(M^2+M)}{N^2(N^2+1)}\mathbb{E}\left[\left(\sum_{jk}^{N}\frac{(p_j-p_k)^2}{p_j}\right)^2+\sum_{jk}^{N}\frac{(p_j-p_k)^4}{p_j^2}\right].
\end{aligned}
\tag{C.61}
$$

To make progress, we will again assume that $\delta\mathcal{E}_2 \ll N^{-2}$, and so we can again expand to leading order in $\delta\mathcal{E}_2 N^2$. We will also assume $N \gg 1$, and so we will only keep terms to leading order in N^{-1}, as well. This gives

$$
\mathbb{E}\left[|\partial_t F|^2\right] = \sigma^4(M^2+M+\mathcal{O}(N^{-2}))\,(\delta\mathcal{E}_2)^2+\mathcal{O}(N^2\delta\mathcal{E}_2)^3. \tag{C.62}
$$

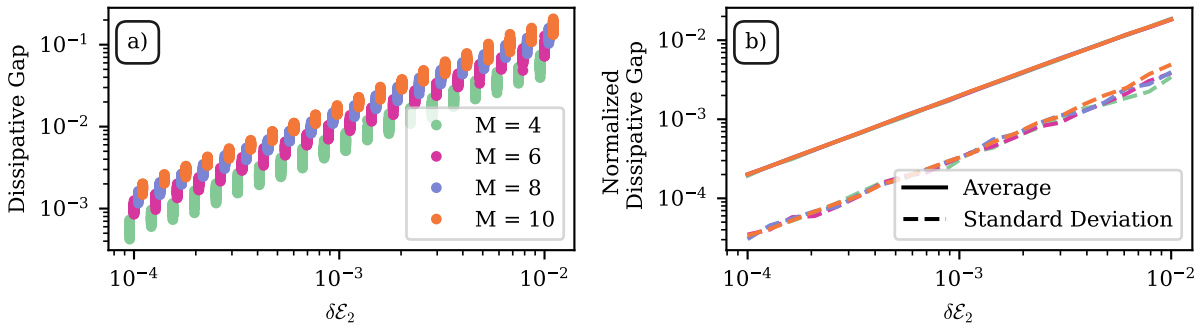

Figure C.3: (a) Dissipative gap of random Lindbladians with A_μ sampled from the complex Ginibre ensemble and local dimension $N = 10$ for varying numbers of jump operators M. There are 100 samples for each M and each value of entanglement $\delta\mathcal{E}_2$. (b) The normalized average (solid lines) and standard deviation (dashed lines) of data in (a). The average is normalized as $\mathbb{E}[\Delta]/(M-1)$ [c.f. Eq. (C.64)], and the standard deviation as $\sqrt{\frac{\mathbb{E}[\Delta^2]-\mathbb{E}[\Delta]^2}{M-1}}$ [c.f. Eq. (C.65)].

This tells us that we would expect a variance of

$$\begin{aligned}\mathbb{V}\left[|\partial_t F|\right] &= \mathbb{E}\left[|\partial_t F|^2\right] - \left|\mathbb{E}\left[|\partial_t F|\right]\right|^2 \\ &= \sigma^4 M \left(\delta\mathcal{E}_2\right)^2 + \mathcal{O}(\delta\mathcal{E}_2)^3 \\ &= \frac{1}{M}\left|\mathbb{E}\left[|\partial_t F|\right]\right|^2 + \mathcal{O}(\delta\mathcal{E}_2)^3, \end{aligned} \tag{C.63}$$

and so the distribution should get tighter as one adds more and more jump operators. This scaling can be observed in Fig. C.3. However, we note that in Fig. C.3 we are plotting the dissipative gap and not the rate of change of the fidelity. This is important because we know analytically that the gap $\Delta = 0$ if $M = 1$, given the fact that $\hat{A}$ and $\hat{B}$ are isospectral (see Appendix C.1.4). However, a single jump operator is sufficient to change the fidelity to the steady state at a non-zero rate for some states in the Hilbert space. Hence, we expect that

the average and variance of the gap should be (setting $\sigma = 1$):

$$\mathbb{E}[\Delta] \propto (M-1)\delta\mathcal{E}_2, \tag{C.64}$$

$$\mathbb{V}[\Delta] \propto (M-1)\left(\delta\mathcal{E}_2\right)^2. \tag{C.65}$$

Hence, in Fig. C.3 we normalize by these values and observe a collapse of both the average and the standard deviation (root of the variance) onto a single line.

C.3 Maximally Entangled State as a Strong Symmetry

Recall from Appendix C.1 that if $\hat{\rho}_{\text{ss}}$ is a maximally entangled state, then $\hat{\rho}_{\text{ss}}\hat{L}_\mu = 0$. However, because to be a steady state requires $\hat{L}_\mu\hat{\rho}_{\text{ss}} = 0$, this implies that the commutator of the steady state with each jump operator identically vanishes. Additionally, any pure steady state must be a Hamiltonian eigenstate as well, so all together this implies:

$$[\hat{L}_\mu, \hat{\rho}_{\text{ss}}] = [\hat{H}, \hat{\rho}_{\text{ss}}] = 0. \tag{C.66}$$

However, this is simply the statement that $\hat{\rho}_{\text{ss}}$ is a *strong symmetry* of the dynamics [131]. This means that we can interpret the steady state density matrix as a symmetry operator; i.e., it is a conserved charge. Because it is a pure state $\hat{\rho}_{\text{ss}} = |\psi\rangle\langle\psi|$, the density matrix is itself simply a projection operator onto the steady state $|\psi\rangle$, and so the conserved charge generated by such a symmetry is simply the population in the steady state. Hence, this is another way to see that if an open system has a steady state that is maximally entangled, then it is completely dynamically isolated from the rest of the system.

Now, let's suppose we perturb the Lindbladian slightly away from this point, so that the

steady state is still pure, but slightly less entangled. In this case we still have that

$$\hat{L}_\mu \hat{\rho}_{\text{ss}} = [\hat{H}, \hat{\rho}_{\text{ss}}] = 0, \tag{C.67}$$

since it is by definition a pure steady state, but if it is not maximally entangled then generically $\hat{\rho}_{\text{ss}}\hat{L}_\mu \neq 0$. We can quantify, then, how close this is to being a symmetry by defining the error Γ_{err}

$$\Gamma_{\text{err}} = \sum_\mu |[\hat{L}_\mu, \hat{\rho}_{\text{ss}}]| = \sum_\mu \langle\psi|[\hat{L}_\mu, \hat{L}_\mu^\dagger]|\psi\rangle = \text{ tr}\left(\mathcal{L}^\dagger \hat{\rho}_{\text{ss}}\right), \tag{C.68}$$

where $|\cdot|$ denotes the Hilbert-Schmidt norm. However, this is exactly the same term that shows up when calculating the rate of change of the fidelity, which we know goes to zero as [c.f. Eqs. (C.51) and (C.52)]

$$\sum_\mu \langle\psi|[\hat{L}_\mu, \hat{L}_\mu^\dagger]|\psi\rangle \lesssim N^2 \delta\mathcal{E}_2, \tag{C.69}$$

and so we can think of this entanglement term both as bounding how fast the fidelity to the steady state can change, as well as how close the Lindbladian is to having a strong symmetry.

This interpretation also explains why there is exactly one midgap state for a random Lindbladian. Let's suppose that we have a Lindbladian $\mathcal{L}_0$ with a maximally entangled steady state $\hat{\rho}_0 = |\psi_{\text{max}}\rangle\langle\psi_{\text{max}}|$. Now, we know that this implies that there is a strong symmetry in the dynamics, and therefore at least two-fold degeneracy in the steady state manifold. Moreover, in the absence of any other symmetry constraints, the degeneracy should be exactly two, and it should be split by a $\Delta_{\text{bulk}} = \mathcal{O}(1)$ bulk gap [150]. Now, let's assume that there is a very closely related Lindbladian $\mathcal{L} = \mathcal{L}_0 + \epsilon\mathcal{L}_1$ such that $\epsilon \ll \Delta_{\text{bulk}}$ the bulk gap, and so we can perform perturbation theory within the steady state manifold.

Now, we don't know exactly what the degenerate steady state actually is, but we do

know exactly what the *left eigenvectors* are, so instead we will do perturbation theory in $\mathcal{L}^\dagger$, which has the same eigenspectrum of $\mathcal{L}$. Explicitly, we know that $\mathcal{L}_0^\dagger \hat{\rho}_0 = \mathcal{L}_0^\dagger(\hat{\mathbf{1}} - \hat{\rho}_0) = 0$.

Let's suppose that $\hat{\rho}_{\text{ss}}$ is the unique steady state solution of $\mathcal{L}\hat{\rho}_{\text{ss}} = 0$. Then $\hat{\rho}_{\text{ss}} = \hat{\rho}_0 + \epsilon\hat{\rho}_1 + \mathcal{O}(\epsilon^2)$. Therefore, $\hat{\rho}_0 = \hat{\rho}_{\text{ss}} + \mathcal{O}(\epsilon)$, and specifically this means that the left eigenvector of $\mathcal{L}$, or alternatively the right eigenvector of $\mathcal{L}^\dagger$ is $\hat{\rho}_0 + \mathcal{O}(\epsilon) = \hat{\rho}_{\text{ss}} + \mathcal{O}(\epsilon)$. Hence, to first order in ϵ, we can perturbatively calculate the steady state degeneracy splitting as the eigenvalues of

$$\begin{aligned} \text{tr}\left[\begin{pmatrix} \hat{\mathbf{1}} - \hat{\rho}_{\text{ss}} \\ \hat{\rho}_{\text{ss}} \end{pmatrix} \mathcal{L}^\dagger \begin{pmatrix} \hat{\mathbf{1}} - \hat{\rho}_{\text{ss}} & \hat{\rho}_{\text{ss}} \end{pmatrix}\right] &= \text{tr}\left[\begin{pmatrix} \hat{\mathbf{1}} \\ 0 \end{pmatrix} \mathcal{L}^\dagger \begin{pmatrix} -\hat{\rho}_{\text{ss}} & \hat{\rho}_{\text{ss}} \end{pmatrix}\right] \\ &= \begin{pmatrix} -\Gamma & \Gamma \\ 0 & 0 \end{pmatrix}, \end{aligned} \tag{C.70}$$

where $\Gamma = \text{tr}(\mathcal{L}^\dagger \hat{\rho}_{\text{ss}})$. The eigenvalues of this matrix are $\{0, -\Gamma\}$, so perturbatively one would expect a dissipative gap that is equivalent to $\Gamma = \text{tr}(\mathcal{L}^\dagger \hat{\rho}_{\text{ss}})$. However, this is just exactly the error Γ_{err} defined in Eq. (C.68); that is to say, the dissipative gap is equivalent to how close the system is to having a strong symmetry.

C.4 Directional Dynamics

As mentioned in the text, the form of the jump operator Eq. (4.6) is the correct form for directional dynamics [154, 152, 153, 111]. To achieve directionality, such that the dynamics in the A system are unaffected by those in the B system, a Hamiltonian interaction is necessary. Generically, given a jump operator $\hat{L} = \hat{A} \otimes \hat{\mathbf{1}} + \hat{\mathbf{1}} \otimes \hat{B}$, one can always make this a unidirectional (chiral) process via the Hamiltonian [154, 111]

$$\hat{H}_{AB} = \frac{i}{2}\left(\hat{A}^\dagger \otimes \hat{B} - \hat{A} \otimes \hat{B}^\dagger\right). \tag{C.71}$$

More is needed, however, to ensure that the state we began with is still the steady state of this new Lindbladian.

To make this possible, firstly, we will need a local Hamiltonian $\hat{H}_A$ on the A system such that

$$\mathcal{L}_A\hat{\rho}_A = -i[\hat{H}_A, \hat{\rho}_A] + \mathcal{D}[\hat{A}]\hat{\rho}_A = 0, \tag{C.72}$$

$$\hat{\rho}_A \equiv \ \mathrm{tr}_B\hat{\rho}_{\mathrm{ss}}. \tag{C.73}$$

This is equivalent to the condition that

$$(H_A)_{nm} = \frac{i}{p_m - p_n}\langle n|\mathcal{D}[\hat{A}]\hat{\rho}_A|m\rangle, \tag{C.74}$$

which uniquely defines the matrix elements of H_A in the Schmidt basis. Note that this also gives another constraint, that

$$\langle n|\mathcal{D}[\hat{A}]\hat{\rho}_A|n\rangle = 0, \tag{C.75}$$

$$\implies \sum_k |A_{nk}|^2 p_k - |A_{kn}|^2 p_n = 0. \tag{C.76}$$

One way to satisfy this is to simply assume $A = \Psi A^T \Psi^{-1}$, which is what we have done throughout this manuscript.

With $\hat{H}_A$ now defined, we can use the general CQA construction in [111] to find the local Hamiltonian on B, which is given by

$$H_B = -\frac{1}{2}\Psi\left(H_A - \frac{i}{2}A^\dagger A\right)^T \Psi^{-1} + \mathrm{H.\,c.} \tag{C.77}$$

Then, we can define

$$\hat{H}_{\mathrm{CQA}} = \hat{H}_A \otimes \hat{\mathbf{1}} + \hat{\mathbf{1}} \otimes \hat{H}_B + \hat{H}_{AB}, \tag{C.78}$$

$$\mathcal{L}_{\mathrm{CQA}}\hat{\rho} = \mathcal{D}[\hat{A} \otimes \hat{\mathbf{1}} + \hat{\mathbf{1}} \otimes \hat{B}]\hat{\rho} - i[\hat{H}_{\mathrm{CQA}}, \hat{\rho}], \tag{C.79}$$

which generates directional dynamics with the steady state $\hat{\rho}_{\mathrm{ss}}$ as desired.

C.5 Free-Fermion Subspaces of an Interacting Hamiltonian

In Chapter 4, we consider the interacting, two-leg ladder Hamiltonian $\hat{H} = \hat{H}_{\parallel} + \hat{H}_{\perp}$, where $\hat{H}_{\parallel}$ is an XX Hamiltonian running along the legs of the ladder, and $\hat{H}_{\perp}$ is an anisotropic XXZ Hamiltonian across the rungs:

$$\hat{H}_{\parallel} = J \sum_{i=1}^{n-1} \sum_{s=A,B} \hat{\sigma}^{+}_{s,i}\hat{\sigma}^{-}_{s,i+1} + \mathrm{H.\,c.}, \tag{C.80a}$$

$$\hat{H}_{\perp} = \sum_{i=1}^{n} J\left(\hat{\sigma}^{x}_{A,i}\hat{\sigma}^{x}_{B,i} + \hat{\sigma}^{y}_{A,i}\hat{\sigma}^{y}_{B,i}\right) + J_z\hat{\sigma}^{z}_{A,i}\hat{\sigma}^{z}_{B,i}, \tag{C.80b}$$

This Hamiltonian was introduced in Ref. [156], where it was shown that (see also [119]) the Hamiltonian can be recast as particles hopping on a 1D chain, where now each lattice site has local Hilbert space dimension $d = 4$. Define the singlet and triplet states $|S/T\rangle_j$ as

$$|S/T\rangle_j = \frac{1}{\sqrt{2}}\left(|0\rangle_{A,j}|1\rangle_{B,j} \mp |1\rangle_{A,j}|0\rangle_{B,j}\right). \tag{C.81}$$

Letting $|0\rangle_j \equiv |0\rangle_{A,j}|0\rangle_{B,j}$ and similarly $|1\rangle_j \equiv |1\rangle_{A,j}|1\rangle_{B,j}$, then $\{|0\rangle, |1\rangle, |S\rangle, |T\rangle\}$ span the local Hilbert space of the single 1D chain.

Next, it is simple to observe that because the XXZ interaction conserves total angular momentum as well as total Z angular momentum on each bond, then these four states can

also be used to form an eigenbasis of $\hat{H}_\perp$. It is also of interest to note that the states

$$|\Omega_1\rangle \equiv |S\rangle_1 \otimes |T\rangle_2 \otimes \cdots \otimes |S(T)\rangle_n, \tag{C.82}$$

$$|\Omega_2\rangle \equiv |T\rangle_1 \otimes |S\rangle_2 \otimes \cdots \otimes |T(S)\rangle_n, \tag{C.83}$$

are also zero energy eigenstates of $\hat{H}_\parallel$, and so we will define these to be the "vacua" of the Hamiltonian $\hat{H}$.

From here, one can add "excitations" in the form of $|0\rangle$ or $|1\rangle$. This is because the Hamiltonian $\hat{H}_\parallel$ sends (c.f. Eq. 2 in [156])

$$|0S\rangle \leftrightarrow |S0\rangle, \quad |0T\rangle \leftrightarrow |T0\rangle, \tag{C.84a}$$

$$|1S\rangle \leftrightarrow |S1\rangle, \quad |1T\rangle \leftrightarrow |T1\rangle, \tag{C.84b}$$

where $\leftrightarrow$ represents mapping under $\hat{H}_\parallel$ modulo multiplicative constants. Furthermore, $\hat{H}_\parallel|00\rangle = \hat{H}_\parallel|11\rangle = 0$, and so any fixed number of $|0\rangle$ *or* $|1\rangle$ particles on top of the vacuum can be mapped exactly to free fermions - each individual species experiences a nearest neighbor hopping Hamiltonian without scattering. The caveat here, and the reason that the entire Hilbert space is not equivalent to free fermions, is that the $|0\rangle$ particles and $|1\rangle$ particles can scatter off of each other. I.e. $\hat{H}_\parallel$ maps (c.f. Eq. 3 in [156])

$$|01\rangle + |10\rangle \leftrightarrow |TT\rangle - |SS\rangle. \tag{C.85}$$

Hence, we can observe that for a given ground state and a given particle species, there are $\sum_{i=0}^{n} \binom{n}{i} = 2^n$ different states in the free-fermion subspace, giving overall a $2^{n+2} - 4$ dimensional Hilbert space. On the other hand, the total Hilbert space dimension is 2^{2n}, so the free-fermion sector is exponentially large in n, but still exponentially small compared to

the full space.

We now demonstrate that the state

$$|\psi\rangle_{\text{ss}} = \bigotimes_{i=1}^{n} \left[\sqrt{1-v^2}|0\rangle_{A,i}|0\rangle_{B,i} + (-1)^i v|1\rangle_{A,i}|1\rangle_{B,i}\right]. \tag{C.86}$$

is an eigenstate of $\hat{H}_{\parallel} + \hat{H}_{\perp}$, and therefore a steady state of the Liouvillian

$$\mathcal{L}\hat{\rho} = -i[\hat{H}_{\parallel} + \hat{H}_{\perp}, \hat{\rho}] + \mathcal{L}_{\text{diss}}\hat{\rho} \tag{C.87}$$

with $\mathcal{L}_{\text{diss}}$ as given in Eq. (4.34) in Chapter 4. We have already noted that $\hat{H}_{\parallel}|\psi\rangle_{\text{ss}} = 0$, so it remains only to show that $\hat{H}_{\perp}|\psi\rangle_{\text{ss}} = nJ_z|\psi\rangle_{\text{ss}}$. By direct computation, we can observe that

$$\begin{aligned}
\hat{H}_{\perp}|\psi\rangle_{\text{ss}} &= \left[\sum_{i=1}^{n} J\left(\hat{\sigma}^x_{A,i}\hat{\sigma}^x_{B,i} + \hat{\sigma}^y_{A,i}\hat{\sigma}^y_{B,i}\right) + J_z\hat{\sigma}^z_{A,i}\hat{\sigma}^z_{B,i}\right] \bigotimes_{j=1}^{n} \left[u|0\rangle_{A,j}|0\rangle_{B,j} + (-1)^j v|1\rangle_{A,j}|1\rangle_{B,j}\right] \\
&= \left[\sum_{i=1}^{n} J_z\hat{\sigma}^z_{A,i}\hat{\sigma}^z_{B,i}\right] \bigotimes_{j=1}^{n} \left[u|0\rangle_{A,j}|0\rangle_{B,j} + (-1)^j v|1\rangle_{A,j}|1\rangle_{B,j}\right] \\
&= \left[\sum_{i=1}^{n} J_z\right] \bigotimes_{j=1}^{n} \left[u|0\rangle_{A,j}|0\rangle_{B,j} + (-1)^j v|1\rangle_{A,j}|1\rangle_{B,j}\right] = nJ_z|\psi\rangle_{\text{ss}},
\end{aligned} \tag{C.88}$$

where $u = \sqrt{1-v^2}$, as desired.

C.6 Derivation of Local Lindblad Master Equations from System-Bath Coupling

Here, we will derive how one gets a Lindblad-style master equation with jump operators respecting the locality constraint [c.f. Eq. (4.6)] starting from a system-bath coupling of the form in Eq. (4.8)in Chapter 4. We will follow the general procedure of taking first the

Born-Markov and then rotating wave approximations, as laid out in, e.g., Refs. [126, 94]. We will not thoroughly justify each approximation, as this is explained in great detail already elsewhere; for these details we encourage the reader to consult Refs. [126, 94]. We begin by assuming that we have a tripartite quantum system, with a Hilbert space $\mathcal{H} = \mathcal{H}_R \otimes \mathcal{H}_A \otimes \mathcal{H}_B$. Overall, these describe a reservoir ($\mathcal{H}_R$) which will be traced out to give the open system dynamics, along with a bipartite system composed of $\mathcal{H}_{A,B}$. The full Hamiltonian can be written in the form

$$\hat{H} = \hat{H}_R + \hat{H}_S + \hat{H}_I, \tag{C.89}$$

with $\hat{H}_R$ giving local dynamics of the reservoir, $\hat{H}_S$ local dynamics of the bipartite system, and $\hat{H}_I$ giving their (weak) interaction. We will assume that the local dynamics $\hat{H}_S$ can be further decomposed $\hat{H}_S = \hat{H}_A + \hat{H}_B$, so that there is no explicit interaction between subsytems not mediated by the reservoir.

Now, let's define $\hat{\tilde{\chi}}(t)$ to be the density matrix for the entire system plus reservoir. It is governed by an equation of motion

$$\partial_t \hat{\tilde{\chi}} = -i[\hat{H}, \hat{\tilde{\chi}}]. \tag{C.90}$$

If we work in the interaction picture of the local dynamics, we can define $\hat{\mathcal{U}} = \exp\left(it\left(\hat{H}_R + \hat{H}_S\right)\right)$ so that $\hat{\chi}(t) = \hat{\mathcal{U}}\hat{\tilde{\chi}}(t)\hat{\mathcal{U}}^\dagger$ obeys simply

$$\partial_t \hat{\chi} = -i[\hat{H}_I(t), \hat{\chi}]. \tag{C.91}$$

From here, we can formally integrate the equation of motion to find that

$$\hat{\chi}(t) = \hat{\chi}(0) - i\int_0^t [\hat{H}_I(s), \hat{\chi}(s)]\ \mathrm{d}s. \tag{C.92}$$

At this point, we can define the system density matrix $\hat{\rho}$ as the partial trace over the reservoir degrees of freedom: $\hat{\rho} = \mathrm{tr}_R \hat{\chi}$. This gives an equation of motion

$$\partial_t \hat{\rho} = -\int_0^t \mathrm{tr}_B[\hat{H}_I(t), [\hat{H}_I(s), \hat{\chi}(s)]]\, \mathrm{d}s. \tag{C.93}$$

To this point, the equation is exact. However, to make progress, we will make the Born-Markov approximation that the full density matrix $\hat{\chi}(t) \approx \hat{\rho}(t) \otimes \hat{\rho}_R$ for all times: i.e. the reservoir is always approximately in the same state $\hat{\rho}_R$, which we take to be static (diagonal in the eigenvectors of $\hat{H}_R$, for example a thermal state). Next, we will assume that the local time dynamics only depend on the state at the given time, i.e. there is no memory effect. This allows us to replace $\hat{\chi}(s) \to \hat{\chi}(t)$ in the integral, giving the new equation of motion

$$\partial_t \hat{\rho} = -\int_0^t \mathrm{tr}_B[\hat{H}_I(t), [\hat{H}_I(t-s), \hat{\rho}(t) \otimes \hat{\rho}_R]]\, \mathrm{d}s. \tag{C.94}$$

The fact that we replaced $\hat{\chi}(t)$ with $\hat{\chi}(s)$ tells us that the integration kernel should be tightly peaked around $|t - s| \sim 0$, and so we can extend the upper integration bound to infinity with very little error. This gives finally the time-local Redfield equation:

$$\partial_t \hat{\rho} = -\int_0^\infty \mathrm{tr}_B[\hat{H}_I(t), [\hat{H}_I(t-s), \hat{\rho}(t) \otimes \hat{\rho}_R]]\, \mathrm{d}s. \tag{C.95}$$

To get something in Lindblad form, we must now make the rotating wave approximation. For this it will be necessary to recall the exact form of the interaction Hamiltonian:

$$\hat{H}_I = \sum_{\mu=1}^{M} \hat{R}_{A,\mu} \otimes \hat{\tilde{A}}_\mu \otimes \hat{\mathbf{1}} + \hat{R}_{B,\mu} \otimes \hat{\mathbf{1}} \otimes \hat{\tilde{B}}_\mu + \mathrm{H.\,c.} = \sum_{j=1}^{4M} \hat{R}'_j \otimes \hat{S}'_j, \tag{C.96}$$

$$\hat{R}'_j = \begin{cases} \frac{1}{\sqrt{2}}(\hat{R}_{A,j} + \hat{R}^\dagger_{A,j}) & 1 \le j \le M \\ \frac{i}{\sqrt{2}}(\hat{R}_{A,j-M} - \hat{R}^\dagger_{A,j-M}) & M < j \le 2M \\ \frac{1}{\sqrt{2}}(\hat{R}_{B,j-2M} + \hat{R}^\dagger_{B,j-2M}) & 2M < j \le 3M \\ \frac{i}{\sqrt{2}}(\hat{R}_{B,j-3M} - \hat{R}^\dagger_{B,j-3M}) & 3M < j \le 4M \end{cases} \tag{C.97}$$

$$\hat{S}'_j = \begin{cases} \frac{1}{\sqrt{2}}(\hat{\hat{A}}_j + \hat{\hat{A}}^\dagger_j) \otimes \hat{\mathbf{1}} & 1 \le j \le M \\ \frac{i}{\sqrt{2}}(\hat{\hat{A}}_{j-M} - \hat{\hat{A}}^\dagger_{j-M}) \otimes \hat{\mathbf{1}} & M < j \le 2M \\ \frac{1}{\sqrt{2}}\hat{\mathbf{1}} \otimes (\hat{\hat{B}}_{j-2M} + \hat{\hat{A}}^\dagger_{j-2M}) & 2M < j \le 3M \\ \frac{i}{\sqrt{2}}\hat{\mathbf{1}} s \otimes (\hat{\hat{B}}_{j-3M} - \hat{\hat{A}}^\dagger_{j-3M}) & 3M < j \le 4M \end{cases} \tag{C.98}$$

where we have defined $\hat{R}'_j, \hat{S}'_j$ to be Hermitian operators that act on either the reservoir or the system, respectively. It will also be extremely important to observe that each system operator is local to either the A or B subsystem. Next, we will decompose the system operators $\hat{S}'_j$ into their frequency components. If we define the operator $\hat{\Pi}_\epsilon$ as the projector onto the eigenspace of $\hat{H}_S$ with eigenvalue ϵ, then we can rewrite

$$\hat{S}'_j = \sum_\omega \hat{S}'_j(\omega), \tag{C.99}$$

$$\hat{S}'_j(\omega) = \sum_{\epsilon - \epsilon' = \omega} \hat{\Pi}_{\epsilon'} \hat{S}'_j \hat{\Pi}_\epsilon. \tag{C.100}$$

Using these operators, we can now expand the equation of motion as

$$\partial_t \hat{\rho} = \sum_{\omega,\omega',j,k} e^{i(\omega-\omega')t} C_{jk}(\omega) \left[\hat{S}'_j(\omega) \hat{\rho} \hat{S}'_j(\omega')^\dagger - \hat{S}'_j(\omega')^\dagger \hat{S}'_j(\omega) \hat{\rho} \right] + \text{H. c.}, \tag{C.101}$$

$$C_{jk}(\omega) = \int_0^\infty e^{i\omega s} \langle \hat{R}^\dagger_j(t) \hat{R}_k(s-t) \rangle \, \mathrm{d}s = \int_0^\infty e^{i\omega s} \langle \hat{R}^\dagger_j(s) \hat{R}_k(0) \rangle \, \mathrm{d}s, \tag{C.102}$$

where in the second line we used the stationarity of $\hat{\rho}_R$. Finally, we make the secular approximation and neglect rapidly rotating terms. Thus, we finally arrive at

$$\partial_t \hat{\rho} = \sum_{\omega,j,k} C_{jk}(\omega) \left[\hat{S}'_j(\omega) \hat{\rho} \hat{S}'_k(\omega)^\dagger - \hat{S}'_k(\omega)^\dagger \hat{S}'_j(\omega) \hat{\rho} \right] + \text{H. c.} \tag{C.103}$$

From here, we can define

$$\gamma_{jk}(\omega) = C_{jk}(\omega) + C_{kj}(\omega)^*, \tag{C.104}$$

$$h_{jk}(\omega) = \frac{-i}{2} \left(C_{jk}(\omega) - C_{kj}(\omega)^* \right), \tag{C.105}$$

$$\hat{H}_{LS} = \sum_{jk\omega} h_{jk}(\omega) \hat{S}'^\dagger_j(\omega) \hat{S}'_k(\omega). \tag{C.106}$$

$\hat{H}_{LS}$ is the Lamb shift Hamiltonian, and γ_{jk} describes the dissipative part of the dynamics:

$$\partial_t \hat{\rho} = -i[\hat{H}_{LS}, \hat{\rho}] + \mathcal{L}_{\text{diss}} \hat{\rho}, \tag{C.107}$$

$$\mathcal{L}_{\text{diss}} \hat{\rho} = \sum_{\omega,j,k} \gamma_{jk}(\omega) \left[\hat{S}'_j(\omega) \hat{\rho} \hat{S}'_k(\omega)^\dagger - \frac{1}{2} \left\{ \hat{S}'_k(\omega)^\dagger \hat{S}'_j(\omega), \hat{\rho} \right\} \right]. \tag{C.108}$$

The matrix $\gamma_{jk}(\omega)$ is positive, and so it can be unitarily diagonalized. Taking $U(\omega)$ to be a unitary matrix, we can rewrite

$$\gamma_{jk}(\omega) = \kappa_l(\omega) U^*_{lj}(\omega) U_{lk}(\omega). \tag{C.109}$$

The dissipation can then be rewritten as

$$\mathcal{L}_{\text{diss}} \hat{\rho} = \sum_{\omega,l} \mathcal{D}[\hat{L}_l(\omega)] \hat{\rho}, \tag{C.110}$$

$$\hat{L}_l(\omega) = \sum_n U^*_{ln}(\omega) \hat{S}'_n(\omega). \tag{C.111}$$

Recall that when we began, each operator $\hat{S}'_j$ was local to one of the two subsystems [c.f. Eq. (C.98)]. Moreover, because $\hat{H}_S = \hat{H}_A + \hat{H}_B$ contains no interactions between the subsystems, the projections into frequency space $\hat{S}'_j(\omega)$ must also remain local to a single sublattice. (I.e., the dynamics of a two non-interacting subsystems cannot mix local operators together). Thus, each jump operator in Eq. (C.111) is a sum of local operators, as we set out to prove. Moreover, we can observe that the Lamb shift Hamiltonian in Eq. (C.106) is quadratic in $\hat{S}'_j(\omega)$, and so after tracing out the reservoir there will generically be long range Hamiltonian interactions between the two systems. Such a Lamb shift Hamiltonian is generically constrained by the form of the dissipation (via Kramers-Kronig relations); however, we take it to be arbitrary since it does not affect any of the final results given in Chapter 4.

C.7 Numerical Techniques

In this section, we outline the numerical techniques used to generate the random models as presented in, e.g., Fig. 4.2. The algorithm used can be summarized into the following steps:

1. *Generate the steady state.* The first step is generating the steady state. We pick a value of the entanglement $\delta\mathcal{E}_2$ and run an optimization algorithm to find a set of Schmidt coefficients such that the normalization is fixed to unity and the Renyi-2 entropy is fixed, beginning from a set of random values.

2. *Generate Jump Operators.* Next, we generate a random $N \times N$ matrix sampled from the random complex Ginibre ensemble which becomes the A matrix. (If we wish to use a different ensemble, we follow the prescription in Eq. (C.47).) We then use this along with the Schmidt coefficients from Step 1 to generate B uniquely using Eq. (4.24). Repeat this M times to generate M jump operators.

3. *Generate Hamiltonian.* If we are simulating directional dynamics, we generate a Hamiltonian as prescribed in Eq. (C.78). Otherwise, proceed to the next step.

4. *Find Dissipative Gap.* Given the matrices A, B generated in Step 2 and Hamiltonian in Step 3 (if present), we use the QuTip [285] package to generate a Liouvillian superoperator. We extract its eigenvalues, from which we can find the dissipative gap.

These steps generate a single data point for a fixed $N, M, \delta\mathcal{E}_2$, and distribution. Each plot samples from 20 different values of $\delta\mathcal{E}_2$, and samples different random models from each value to get good convergence of the average and standard deviation, usually about 100 samples for each.

To be even more explicit, we will now go through a specific example of generating such a system for $N = 2$ and $M = 1$. First we perform Step 1. Note that because we have two constraints (normalization and entanglement), and two Schmidt coefficients, they are exactly specified. We can write the matrix Ψ as

$$\Psi = \begin{pmatrix} \frac{1}{2} - p & 0 \\ 0 & \frac{1}{2} + p \end{pmatrix}, \tag{C.112}$$

$$p = \sqrt{\frac{\delta\mathcal{E}_2}{2}}. \tag{C.113}$$

Next, we do Step 2 and generate a random matrix A, which we will leave unspecified as

$$A = \begin{pmatrix} a_{11} & a_{12} \\ a_{21} & a_{22} \end{pmatrix}. \tag{C.114}$$

This allows us to uniquely specify a matrix B as

$$B = -\Psi A^T \Psi^{-1} = \begin{pmatrix} -a_{11} & \xi a_{21} \\ \xi^{-1} a_{12} & -a_{22} \end{pmatrix}, \tag{C.115}$$

$$\xi = \frac{2p - 1}{2p + 1}. \tag{C.116}$$

Since we are not using directional dynamics, we can now proceed directly to step 4, and generate a Liouvillian superoperator. To do this, we first need to find the jump operator $L = A \otimes \hat{\mathbf{1}} + \hat{\mathbf{1}} \otimes B$, which can be written as

$$L = \begin{pmatrix} 0 & \xi a_{21} & a_{12} & 0 \\ \xi^{-1} a_{12} & a_{11} - a_{22} & 0 & a_{12} \\ a_{21} & 0 & a_{22} - a_{11} & \xi a_{21} \\ 0 & a_{21} & \xi^{-1} a_{12} & 0 \end{pmatrix}. \tag{C.117}$$

From here, it is simple to use this matrix to generate a Lindbladian and find its spectrum.

APPENDIX D

APPENDIX TO CHAPTER 5

D.1 Monotonicity of Entanglement in the Monitored Circuit

We will now show that in the monitored circuit, by flipping the phase after every jump, the entanglement grows monotonically in time. This can be understood by looking at the interplay of the coherent and dissipative dynamics. To see this, it will be useful to rewrite the dynamics as

$$\hat{H} = \sum_{i=1}^{n-1} \hat{h}_i \tag{D.1}$$

$$\hat{h}_i = J \sum_{s=A,B} \hat{\sigma}^+_{s,i}\hat{\sigma}^-_{s,i+1} + \text{H. c.} \tag{D.2}$$

$$\hat{L}_\pm = \left(\hat{\sigma}^+_{A,1} \pm \hat{\sigma}^+_{B,1}\right)/\sqrt{2}. \tag{D.3}$$

When the parity is $P = +1$, then the dynamics are given by $\partial_t\hat{\rho} = -i[\hat{H}, \hat{\rho}] + \mathcal{D}[\hat{L}_+]\hat{\rho} + \mathcal{D}[\hat{L}^\dagger_+]\hat{\rho}$. When the parity is $P = -1$, the jump operators are exchanged $\hat{L}_+ \leftrightarrow \hat{L}_-$, while the Hamiltonian is unchanged. Note that this is identical to the dynamics presented in Eqs. (5.6) and (5.7) in Chapter 5 (where we have taken maximal entanglement $u^2 = v^2 = 0.5$ and $\Delta = 0$), after performing a unitary transformation inverting every site on the B chain: $\hat{\sigma}^+_{B,i} \leftrightarrow (-1)^{i+1}\hat{\sigma}^-_{B,i}$. The phase factor $(-1)^{i+1}$ makes it so both lattices have positive hopping terms. Following this transformation, the steady state becomes

$$\hat{\rho}_{\text{ss}} = 2^{-n/2} \prod_{i=1}^{n} \left(\hat{\sigma}^+_{A,i} + (-1)^{i+1}\hat{\sigma}^+_{B,i}\right) |0\rangle^{\otimes 2n}. \tag{D.4}$$

Next, it will be useful to group the A and B lattices together into a single chain of 4-level systems. We define the following four states:

$$|00\rangle_j = |0\rangle_{A,j} \otimes |0\rangle_{B,j}, \qquad |11\rangle_j = |1\rangle_{A,j} \otimes |1\rangle_{B,j}$$
$$|T/S\rangle_j = \tfrac{1}{\sqrt{2}} \left(|0\rangle_{A,j} \otimes |1\rangle_{B,j} \pm |1\rangle_{A,j} \otimes |0\rangle_{B,j} \right), \tag{D.5}$$

In this basis, the (positive parity) steady state is simply $|T\rangle_1 |S\rangle_2 \ldots |T/S\rangle_n$. We have the following rules for local interactions under the local Hamiltonian $\hat{h}_i$:

$$|S\rangle_i |00\rangle_{i+1} \leftrightarrow |00\rangle_i |S\rangle_{i+1}, \qquad |T\rangle_i |00\rangle_{i+1} \leftrightarrow |00\rangle_i |T\rangle_{i+1}$$
$$|S\rangle_i |11\rangle_{i+1} \leftrightarrow |11\rangle_i |S\rangle_{i+1}, \qquad |T\rangle_i |11\rangle_{i+1} \leftrightarrow |11\rangle_i |T\rangle_{i+1}. \tag{D.6}$$

Taking inspiration from Refs. [119, 156], we can interpret $|00\rangle_1 |00\rangle_2 \ldots |00\rangle_n$ as a vacuum state with singlets $|S\rangle$ and triplets $|T\rangle$ hopping ballisticly under the Hamiltonian. Furthermore, the following are all zero energy eigenstates of the local Hamiltonian $\hat{h}_i$:

$$|00\rangle_i |00\rangle_{i+1}, \qquad |11\rangle_i |11\rangle_{i+1},$$
$$|S\rangle_i |T\rangle_{i+1}, \qquad |T\rangle_i |S\rangle_{i+1}.$$

Finally, $|S\rangle$ and $|T\rangle$ particles are able to scatter off of themselves under the local Hamiltonian $\hat{h}_i$:

$$|S\rangle_i |S\rangle_{i+1} \leftrightarrow -(|00\rangle_i |11\rangle_{i+1} + |11\rangle_i |00\rangle_{i+1}),$$
$$|T\rangle_i |T\rangle_{i+1} \leftrightarrow (|00\rangle_i |11\rangle_{i+1} + |11\rangle_i |00\rangle_{i+1}), \tag{D.7}$$

and so there is a second order process able to convert $|S\rangle_i |S\rangle_{i+1}$ to $|T\rangle_i |T\rangle_{i+1}$ and vice-versa.

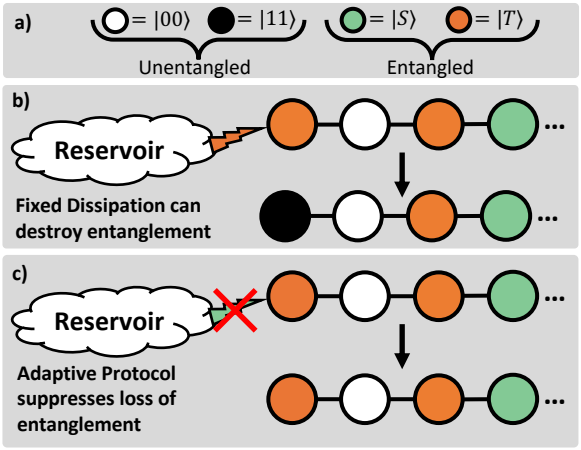

Figure D.1: a) Legend depicting different states that can exist in the doubled chain structure. The white/black states ($|00\rangle, |11\rangle$) are unentangled, while the colored Singlet/Triplet states carry maximal entanglement. b) For the non-adaptive protocol with fixed jump operators, after inserting a triplet $|T\rangle$, it can return to the dissipative site, after which trying to insert a second $|T\rangle$ converts it to $|1\rangle$, removing entanglement. c) Using the adaptive approach, because $|T\rangle, |S\rangle$ cannot cross, after inserting a $|T\rangle$, only a $|T\rangle$ can return to the dissipative site. However, inserting now an $|S\rangle$ on top of a $|T\rangle$ does nothing, and so the adaptive protocol supresses the entanglement loss. Hence, entanglement must grow monotonically in time in each stochastic unraveling.

Now the last question to ask is what the dissipation can do. We have the next set of rules:

$$\hat{L}_+|00\rangle_1 = \hat{L}_+^\dagger|11\rangle_1 = |T\rangle_1, \tag{D.8}$$

$$\hat{L}_-|00\rangle_1 = \hat{L}_-^\dagger|11\rangle_1 = |S\rangle_1, \tag{D.9}$$

$$\hat{L}_+|T\rangle_1 = -\hat{L}_-|S\rangle_1 = |11\rangle_1, \tag{D.10}$$

$$\hat{L}_+^\dagger|T\rangle_1 = -\hat{L}_-^\dagger|S\rangle_1 = |00\rangle_1, \tag{D.11}$$

with everything else annihilated. Suppose for convenience that the system begins in the vacuum of all $|00\rangle$, and we initialize to positive parity. The Hamiltonian does nothing until a quantum jump occurs, at which point a triplet $|T\rangle_1$ can be inserted in the boundary of the chain, which can then hop ballisticly under the Hamiltonian. Now we imagine two

scenarios: first, suppose that we do not update the parity, and so the jump operator is unchanged. Thus, a second jump will again try to insert a second triplet $|T\rangle_1$. Now, if the first triplet has propagated away, this will be successful, and entanglement entropy will increase. However, if the original particle is either still at the first site, or has propagated and away and then returned, a quantum jump can accidentally *destroy* the triplet as $\hat{L}_+|T\rangle_1 = |11\rangle_1$ and $\hat{L}_+^\dagger|T\rangle_1 = |00\rangle_1$, both of which are unentangled, see Fig. D.1. Note that the total amount of entanglement between the two chains can only change at the boundary, as the Hamiltonian does not contain any interactions between the A and B subsystems.

In contrast, consider the dynamics when we do update the jump operators after every jump (i.e. update the P variable). After the first jump (which injected a $|T\rangle$, the jump operator in the master equation switches to being $\hat{L}_-$. Now, a quantum jump tries inject a singlet into the chain. Again, if the original excitation has propagated away leaving vacuum at the first site, this will increase the entanglement entropy. On the other hand, if the original triplet has either not yet left or has come back, we can observe that $\hat{L}_-^{(\dagger)}|T\rangle_1 = 0$, and so a quantum jump *does nothing*. Because an alternating pattern of singlets and triplets cannot cross places or scatter off of each other, if the last type inserted was a singlet, only a singlet can come back to the first site, and so by updating the parity after every jump it is impossible to remove entanglement from the system. This process is shown in Fig. D.1. An identical argument holds if one instead considers the $|11\rangle_1 \ldots |11\rangle_n$ state to be the vacuum, where the rolls of $\hat{L}_\pm$ and $\hat{L}_\pm^\dagger$ are simply reversed.

Thus, we have shown monotonicity of the entanglement entropy - it only grows before saturating to a maximal value. This is shown at the individual trajectory level, where we compare the scheme where we keep track of jumps (variable phase) and where we do not (fixed phase). The variable phase shows monotonic entanglement growth that converges orders of magnitude more quickly, while the fixed phase dynamics take a very long time to reach the steady state and shows oscillating entanglement. See Fig. 5.2(c) in Chapter 5.

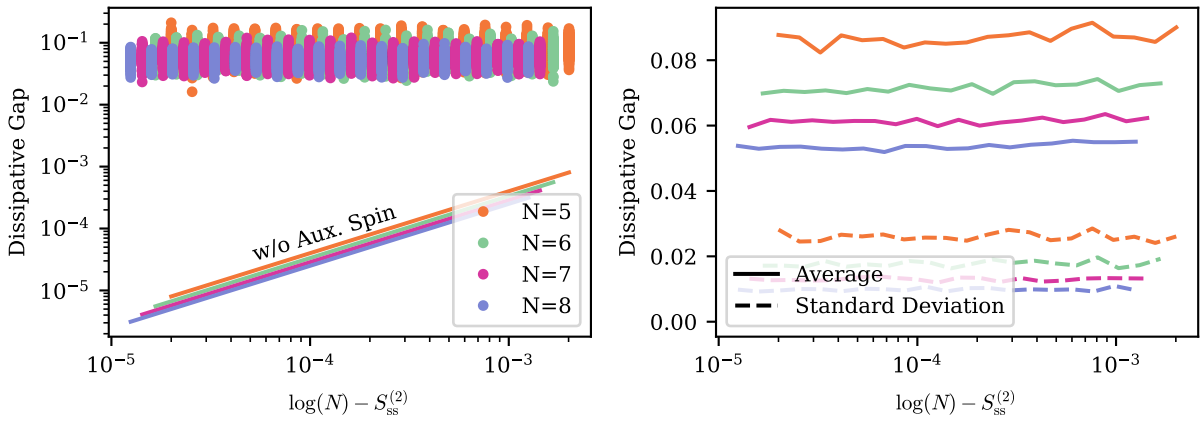

Figure D.2: Left. Random Lindbladians with fixed Renyi-2 steady state entanglement constructed using an auxiliary spin [c.f. Eqs. (D.17) and (D.18)]. 250 runs are shown for each value of the entanglement $S_{\mathrm{ss}}^{(2)}$ and system size N. Solid lines are analytical results for random Lindbladians without an auxiliary spin, see [95]. Right. Average and standard deviation of the runs.

D.2 Circumventing Slowdown in Random, Many-Body Lindbladians

The construction given in Eq. (5.12) in Chapter 5 can be straightforwardly generalized to any many-body system. In particular, recall the construction presented in Ref. [95]: given a bipartite Hilbert space $\mathcal{H} = \mathcal{H}_A \otimes \mathcal{H}_B$ of equal Hilbert space dimension $\dim \mathcal{H}_A = \dim \mathcal{H}_B = N$, then a quantum state is uniquely specified by a set of real, positive Schmidt coefficients ψ_i and basis vectors $|i\rangle$:

$$|\psi\rangle = \sum_{i=1}^{N} \psi_i |i\rangle \otimes |i\rangle. \tag{D.12}$$

Now, given any operator $\hat{A}_\mu \in \mathrm{End}\,(\mathcal{H}_A)$, we can construct a jump operator $\hat{L}_\mu$ such that $\hat{L}_\mu |\psi\rangle = 0$ by

$$\hat{L}_\mu = \hat{A}_\mu \otimes \hat{\mathbf{1}} - \hat{\mathbf{1}} \otimes \hat{\Psi} \hat{A}_\mu^T \hat{\Psi}^{-1}. \tag{D.13}$$

Here, $\hat{\Psi} = \sum_i \psi_i |i\rangle\langle i| = \sqrt{\mathrm{tr}_A |\psi\rangle\langle\psi|}$. The transposition is short hand for $\hat{A}^T = \hat{\Theta}\hat{A}^\dagger\hat{\Theta}^{-1}$ where $\hat{\Theta}$ is an anti-unitary time reversal operation (i.e., complex conjugation in the Schmidt basis).

Now, one can choose a set of N random Schmidt coefficients ψ_i (subject to normalization) to define a steady state $|\psi\rangle$, as well as N^2 random matrix elements $(A_\mu)_{ij}$ to define

$$\hat{A}_\mu = \sum_{i,j=1}^{N} (A_\mu)_{ij} |i\rangle\langle j|. \tag{D.14}$$

The construction then allows one to construct from this a Lindbladian

$$\mathcal{L} = \sum_{\mu=1}^{m} \mathcal{D}[\hat{L}_\mu] \tag{D.15}$$

where $\hat{L}_\mu |\psi\rangle = 0$ by construction. As long as $m > 1$, this state is also generically unique; however, it was shown in [95] that the dissipative gap closes as the steady state approaches maximal entanglement $S^{(2)}_{\mathrm{ss}} \to \log(N)$.

In order to still reach the state $|\psi\rangle$ in finite time, we can now use the construction in Eq. (5.12) in Chapter 5 and augment the Hilbert space to $\mathcal{H} = \mathcal{H}_{\mathrm{aux}} \otimes \mathcal{H}_A \otimes \mathcal{H}_B$ where $\dim \mathcal{H}_{\mathrm{aux}} = 2$, a single auxiliary spin degree of freedom. Now consider the new state and jump operators

$$|\psi_2\rangle = |0\rangle \otimes |\psi\rangle, \tag{D.16}$$

$$\hat{L}_{\mu,2} = \hat{\sigma}_x \otimes \hat{A}_\mu \otimes \hat{\mathbf{1}} + i\hat{\sigma}_y \otimes \hat{\mathbf{1}} \otimes \hat{\Psi}\hat{A}_\mu^T\hat{\Psi}^{-1}. \tag{D.17}$$

it is simple to check that, by construction, $\hat{L}_{\mu,2}|\psi_2\rangle = 0$, and it is once again the unique

fixed point of the Lindbladian

$$\mathcal{L}_2 = \sum_{\mu=1}^{m} \mathcal{D}[\hat{L}_{\mu,2}], \tag{D.18}$$

but $\mathcal{L}_2$ does not experience slow-down as $|\psi\rangle$ approaches maximal entanglement. Indeed, as shown in Fig. D.2, the average dissipative gap with the auxiliary spin is independent of steady state entanglement.

D.3 Spin Squeezing

D.3.1 Squeezing Induced Slowdown

Here we discuss how the adaptive protocol can be used for spin squeezing. First, it is important to understand exactly why the dynamics become slow in the large squeezing limit. This is not related to the entanglement (as it happens within a single ensemble) but instead can be related directly to the amount the variance is being squeezed.

Let's consider an extremely general scenario, such that there are dissipative dynamics

$$\partial_t \hat{\rho} = \mathcal{D}[\hat{L}]\hat{\rho}, \tag{D.19}$$

with a pure steady state $\hat{\rho}_{\text{ss}} = |\psi\rangle\langle\psi|$. Now, let's rewrite $\hat{L}$ as its Hermitian and anti-Hermitian parts:

$$\hat{L} = \hat{O}_1 + i\hat{O}_2, \tag{D.20}$$

where $\hat{O}_i = \hat{O}_i^\dagger$. Now, observe that the steady state condition tells us that $\hat{L}|\psi\rangle = 0$, so

$$\hat{O}_1|\psi\rangle = -i\hat{O}_2|\psi\rangle. \tag{D.21}$$

However, this also implies that $\mathrm{var}(\hat{O}_1) = \mathrm{var}(\hat{O}_2)$ where

$$\mathrm{var}(\hat{O}) \equiv \langle\psi|\hat{O}^2|\psi\rangle - \langle\psi|\hat{O}|\psi\rangle^2. \tag{D.22}$$

Now, we can use Heisenberg uncertainty to observe that

$$\mathrm{var}(\hat{O}_1)^2 = \mathrm{var}(\hat{O}_1)\mathrm{var}(\hat{O}_2) \geq \frac{1}{4}|\langle[\hat{O}_1, \hat{O}_2]\rangle|^2 = \frac{1}{16}|\langle[\hat{L}, \hat{L}^\dagger]\rangle|^2. \tag{D.23}$$

However, we recall from Chapter 4 that if we define $F(t) = \mathrm{tr}(\hat{\rho}_t\hat{\rho}_{\mathrm{ss}})$ the fidelity to the steady state at time t, then

$$|\partial_t F|^2 \leq |\langle[\hat{L}, \hat{L}^\dagger]\rangle|^2. \tag{D.24}$$

$$\implies \partial_t F \leq 4\mathrm{var}(\hat{O}_1). \tag{D.25}$$

At this point, it does not seem that this respects the gauge invariance of the jump operator $\hat{L} \to e^{i\phi}\hat{L}$ as such a transformation changes the definition of $\hat{O}_1 \to \cos(\phi)\hat{O}_1 - \sin(\phi)\hat{O}_2$. However, it is simple to show that if we consider

$$\begin{aligned}\left\langle \Big(\cos(\phi)\hat{O}_1 - \sin(\phi)\hat{O}_2\Big)^2 \right\rangle &= \cos^2(\phi)\langle\hat{O}_1^2\rangle + \sin^2(\phi)\langle\hat{O}_2^2\rangle - \sin(\phi)\cos(\phi)\langle\{\hat{O}_1, \hat{O}_2\}\rangle \\ &= \langle\hat{O}_1^2\rangle,\end{aligned} \tag{D.26}$$

where we use Eq. (D.21) to see that $\langle\{\hat{O}_1, \hat{O}_2\}\rangle = 0$. Eq. (D.21) also implies that $\langle\hat{O}_1\rangle = -i\langle\hat{O}_2\rangle$ and so they must both be zero (as one is purely real and the other purely imaginary). Hence, this proves the variance of the real part of the jump operator is in fact gauge invariant.

Now, if we apply this to the case of dissipative spin-squeezing, we can observe that

$$\hat{L} = \hat{S}^+ + \tanh(r)\hat{S}^- = (1+\tanh(r))\hat{S}^x + i(1-\tanh(r))\hat{S}^y, \tag{D.27}$$

which implies that, in the large r limit $e^{2r} \gtrsim N$ that

$$\partial_t F \leq 4(1-\tanh(r))^2 \mathrm{var}(\hat{S}^y) \sim 2S(S+1)e^{-4r}, \tag{D.28}$$

and hence the system slows down at large levels of squeezing. Note that because they are equal, one could also have shown the same slowdown by considering the variance $(1+\tanh(r))^2\mathrm{var}(\hat{S}^x)$. This also allows us to understand why the auxiliary qubit can speed up the dynamics. If we write the adaptive master equation

$$\partial_t \hat{\rho} = \mathcal{D}[\hat{\tilde{L}}]\hat{\rho}, \tag{D.29}$$

$$\begin{aligned}\hat{\tilde{L}} &= \hat{\sigma}^x \hat{S}^+ + i\tanh(r)\hat{\sigma}^y \hat{S}^- \\ &= \left(\hat{\sigma}^x \hat{S}^x + \tanh(r)\hat{\sigma}^y \hat{S}^y\right) + i\left(\hat{\sigma}^x \hat{S}^y + \tanh(r)\hat{\sigma}^y \hat{S}^x\right).\end{aligned} \tag{D.30}$$

The steady state solution is unchanged, but the variance now becomes

$$\mathrm{var}\left(\hat{\sigma}^x \hat{S}^x + \tanh(r)\hat{\sigma}^y \hat{S}^y\right) = \left\langle (\hat{S}^x)^2 + \tanh^2(r)(\hat{S}^y)^2 + 2\tanh(r)\hat{\sigma}^z \hat{S}^z \right\rangle \tag{D.31}$$

In the limit $r \to \infty$, the steady state is an $\hat{S}^x$ eigenstate with eigenvalue 0. Hence, we have that $\langle (S^x)^2 \rangle \to 0$ (as it is being squeezed). However, because $\hat{S}\cdot\hat{S} = S(S+1)$ where S is the total angular momentum, then by rotational invariance we must conclude that $\langle (\hat{S}^y)^2 \rangle = \langle (\hat{S}^z)^2 \rangle = S(S+1)/2$. Finally, noting that an $\hat{S}^x$ eigenstate similarly implies

$\langle \hat{S}^z \rangle = 0$, we can conclude

$$\text{var}\left(\hat{\sigma}^x \hat{S}^x + \tanh(r)\hat{\sigma}^y \hat{S}^y\right)\Big|_{r\to\infty} = \frac{S(S+1)}{2}, \tag{D.32}$$

Thus, the system no longer has to suffer from slow down, as was seen in Chapter 5.

D.3.2 Quantum Fisher Information

Throughout, we have discussed the metrological gain of the spin squeezed states in terms of their Wineland squeezing parameter, which gives the degree to which the spin squeezed state will outperform the standard quantum limit when doing a simple Ramsey measurement. Now, another manner to define the metrological use of a quantum state is via the quantum Fisher information (QFI), which gives the sensitivity to a sensing parameter optimizing over all measurement schemes.

As it turns out, for the dissipative squeezed states we have looked at, these are in one-to-one mapping, because the Ramsey measurement turns out to be optimal. There are a few ways in which one can see this. Perhaps the most straightforward is that we can directly calculate the symmetric logarithmic derivative (SLD). Let us define the squeezed state $\hat{\rho} = |\psi\rangle\langle\psi|$ as before as the kernel of the jump operator

$$(\hat{S}^+ + \tanh(r)\hat{S}^-)|\psi\rangle = 0 \tag{D.33}$$

$$\implies \hat{S}^x|\psi\rangle = ie^{4r}\hat{S}^y|\psi\rangle \tag{D.34}$$

If we are using this to sense a parameter θ encoded as a Hamiltonian $\hat{H} = \theta\hat{S}^y$, then the

SLD $\hat{L}_\theta$ is defined by

$$i[\hat{\rho}, \hat{S}^y] = \frac{1}{2}\{\hat{L}_\theta, \hat{\rho}\} \tag{D.35}$$

$$\implies \hat{L}_\theta = -2e^{-4r}\hat{S}^x \tag{D.36}$$

The QFI $\mathcal{F}_Q$ is given by the expectation value of the SLD squared, which is just

$$\mathcal{F}_Q = 4e^{-8r}\langle(\hat{S}^x)^2\rangle = 4\langle(\hat{S}^y)^2\rangle \tag{D.37}$$

Now, on the other hand, we can exactly calculate Wineland parameter using the Heisenberg uncertainty relation. The most general form of the uncertainty relation is given by

$$\sigma_A^2\sigma_B^2 \geq \frac{1}{4}\left|\langle\{\hat{A}, \hat{B}\}\rangle - \langle\hat{A}\rangle\langle\hat{B}\rangle\right|^2 + \frac{1}{4}\left|\langle[\hat{A}, \hat{B}]\rangle\right|^2 \tag{D.38}$$

The inequality is saturated when the states $|\phi_A\rangle = (\hat{A} - \langle\hat{A}\rangle)|\psi\rangle$ and $|\phi_B\rangle = (\hat{B} - \langle\hat{B}\rangle)|\psi\rangle$ are parallel. Let's consider $\hat{A} = \hat{S}^x$ and $\hat{B} = \hat{S}^y$. Now, as we know the expectation of both these operators is 0, and therefore $|\phi_{S^x}\rangle = ie^{4r}|\phi_{S^y}\rangle$, and so the inequality is saturated. Further, we can observe that

$$\langle\hat{S}^x\hat{S}^y\rangle = -ie^{-4r}\langle(\hat{S}^x)^2\rangle = -\langle\hat{S}^y\hat{S}^x\rangle \tag{D.39}$$

$$\implies \langle\{\hat{S}^x, \hat{S}^y\}\rangle = 0 \tag{D.40}$$

$$\implies \sigma_{S^x}^2\sigma_{S^y}^2 = \frac{1}{4}\left|\langle[\hat{S}^x, \hat{S}^y]\rangle\right|^2 = \frac{1}{4}\left|\langle\hat{S}^z\rangle\right|^2 \tag{D.41}$$

$$\implies \mathcal{F}_Q = 4\sigma_{S^y}^2 = \frac{\left|\langle\hat{S}^z\rangle\right|^2}{\sigma_{S^x}^2} = \frac{N}{\xi_R^2} \tag{D.42}$$

and so the QFI is simply proportional to the squeezing parameter.

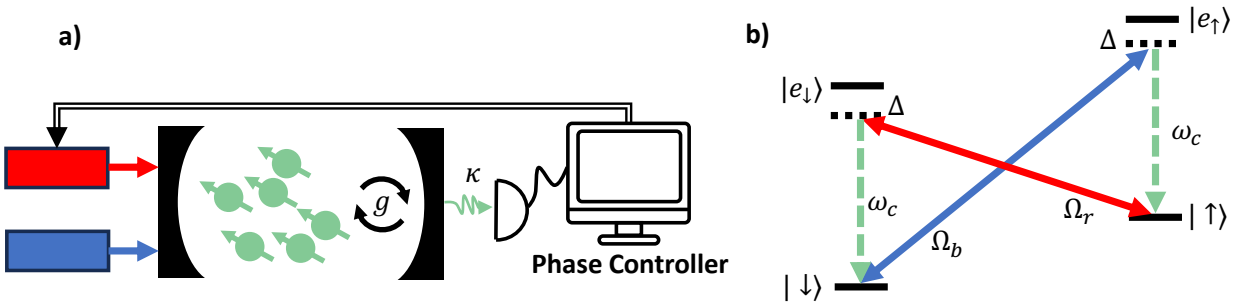

Figure D.3: a) Adaptive spin squeezing protocol. Red and Blue sideband drives on a cavity QED setup generate dissipative squeezing. The output field of the cavity is measured by a single photon detector, which is fed forward to control the relative phases of the drives. b) Level diagram of four level atoms. Sideband drives excite from the ground to excited state manifold, which can then decay back to the ground state via emission into the cavity field at frequency ω_c.

D.3.3 Experimental Implementation

While this master equation seems to be difficult to construct in the lab, one could instead consider doing the adaptive technique. To engineer dissipative spin-squeezing, we consider the protocol in Ref. [181]: we take a cavity with frequency ω_c and loss rate κ. Inside the cavity are a collection of N 4-level atoms. The spin degree of freedom will be encoded in the ground state manifold $|\uparrow\rangle, |\downarrow\rangle$, and there are also two excited states $|e_\uparrow\rangle, |e_\downarrow\rangle$. We take an atom-cavity coupling g, along with blue- and red- sideband drives with strength Ω_b, Ω_r at a detuning Δ from the $|\downarrow\rangle \leftrightarrow |e_\uparrow\rangle$ and $|\uparrow\rangle \leftrightarrow |e_\downarrow\rangle$ transitions, respectively. Assuming $\Omega_{b,r}/\Delta \ll 1$, we can trace out the excited states, and working in the proper rotating frame gives the effective Hamiltonian [181]:

$$\hat{H} = \tilde{\Omega}_b \left(\hat{a}^\dagger \hat{S}^+ + \hat{a}\hat{S}^-\right) + \tilde{\Omega}_r \left(\hat{a}^\dagger \hat{S}^- + \hat{a}\hat{S}^+\right), \tag{D.43}$$

where $\tilde{\Omega}_{b,r} = \Omega_{b,r} g/\Delta$ are effective Rabi rates [181]. If the cavity additionally is extremely lossy with a loss rate $\kappa \gg \tilde{\Omega}_b, \tilde{\Omega}_r$, then we arrive at the dissipative dynamics for just the

spins as

$$\partial_t \hat{\rho} = \frac{2}{\kappa} \mathcal{D}\left[\tilde{\Omega}_b \hat{S}^+ + \tilde{\Omega}_r \hat{S}^-\right] \hat{\rho}. \tag{D.44}$$

This gives us the dissipative dynamics necessary for spin squeezing. Finally, notice that we can keep track of the number of jumps that have occurred by doing single photon detection on the cavity output field. Every time we detect a photon, a jump occurred, and we can change the relative phase of the red and blue sideband drives to change the relative sign in the jump operator. This could be done using, e.g., electro-optic modulation of the red sideband, so that $\Omega_r \to -\Omega_r$. This process is depicted in Fig. D.3.

D.4 Scalability

In this section, we will investigate the scalability of both the proposed adaptive circuit protocol, as well as the adaptive spin-squeezing protocol. Specifically, we will be interested in understanding how the dissipative preparation time scales with the system size.

For the circuit, we can observe that the steady state has long-range entanglement between the most distant qubits in the A and B subsystems; however, the only location in which entanglement can be created between the two sub-systems is at the auxilliary lattice site. Hence, it is clear that in order to reach the fixed point, there must be at least linear-depth scaling, i.e. the number of cycles for the system to relax must scale at least as n, where n is the number of qubits in each sub-system. Numerically, we find that this is accurate, as can be seen in Fig. D.4, where it is shown that in numerically accessible system sizes, the bipartite entanglement scales as

$$S_{\text{vN}} \sim n\left(1 - e^{-d/\xi_n}\right) \tag{D.45}$$

$$\xi_n \propto n \tag{D.46}$$

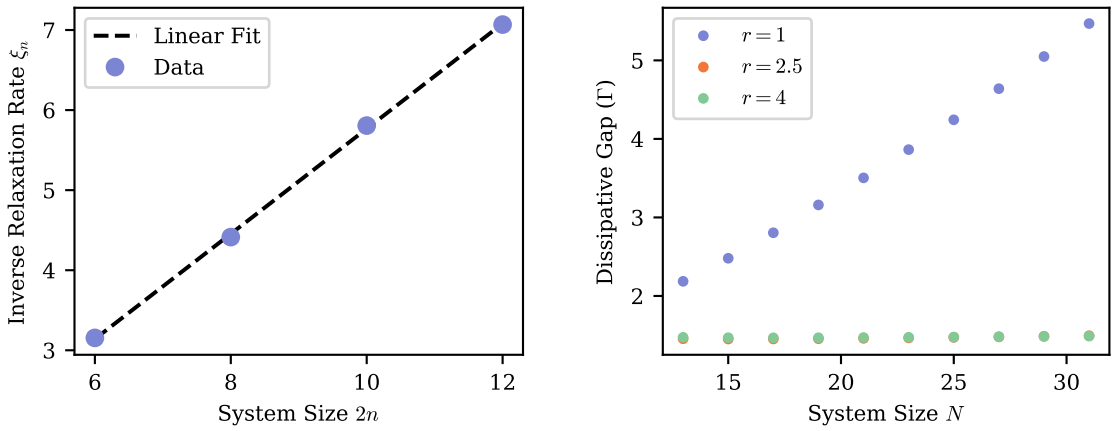

Figure D.4: On the left, we show the average preparation time for the dissipative circuit [see Eq. (D.45)] as a function of the system size $2n$, where the data points are obtained by fitting averaged bipartite entanglement to exponential decay curves. The linear fit is given by roughly $\xi_n \sim 0.66 \times (2n)$. On the right, we numerically diagonalize the Liouvillian of the spin squeezing master equation and extract the dissipative gap, or smallest non-zero eigenvalue, which sets the relaxation time.

where d is the number of circuit cycles, and ξ_n the inverse relaxation rate. This means the actual system relaxes with an optimal scaling given a 1D connectivity.

For the spin-squeezed system, we expect two different behaviors of the relaxation rate, depending on the amount of squeezing. If the squeezing is small $e^{2r} \ll N$, then there is no slow-down to alleviate, and so the system should experience super-radiant decay, with a dissipative gap scaling linearly with N, the number of qubits. On the other hand, if $e^{2r} \gtrsim N$, then the super-radiant decay has been completely eliminated by the squeezing induced slow-down, and so the adaptivity is important to speed up the dynamics. However, the adaptivity does not induce super-radiance, and so the dissipative gap should be independent of both system size and squeezing. Both of these scalings are shown numerically in Fig. D.4. Hence, the protocol is extremely scalable, as the preparation time for highly squeezed states is independent of the number of particles.

D.5 Measurement Error

In this section, we investigate the impact of measurement errors on the adaptive protocols. In both the circuit as well as the spin-squeezing, the ability to do strong, projective measurements and then feed-back on them is crucial. As it turns out, in both scenarios, measurement errors essentially become leakage out of the correct parity sector, where here parity is a joint parity of the system plus classical memory.

Let's begin by looking at the discrete circuit. The unitary operators $\hat{U}_{H,1}, \hat{U}_{H,2}$ conserve the total parity of the system. On the other hand, the unitary operators $\hat{U}_{\text{jump},1}, \hat{U}_{\text{jump},2}$ can change the parity of the system after performing a projective measurement on the auxiliary spin, which is stored in the classical memory. However, if there is a measurement error (i.e., we perform a projective measurement on the auxiliary site into $|1\rangle$ but record 0 or vice-versa), then we have accidentally switched parity subspaces. By sampling over many circuit realizations, we can define the average, impure state as a statistical mixture

$$\hat{\rho} = \lim_{m\to\infty} \frac{1}{m} \sum_{i=1}^{m} |\psi^{(i)}\rangle\langle\psi^{(i)}| \tag{D.47}$$

where m is the total number of circuit realizations, and the state $|\psi^{(i)}\rangle$ is the pure state of a single circuit realization. After many cycles, this can be written as

$$\hat{\rho} \to |\psi_{\text{ss}}\rangle\langle\psi_{\text{ss}}| + \hat{\rho}_{\text{err}} \tag{D.48}$$

where $|\psi_{\text{ss}}\rangle$ is the ideal steady state in the limit of perfect measurements, and $\hat{\rho}_{\text{err}}$ is the population that has diffused into the incorrect subspace due to measurement errors. Now, because there is random flipping between the two at a rate given by the measurement error, in the limit of many cycles, the state will be fully degraded. However, if the rate at which measurement errors is much smaller than the number of cycles required to approach the

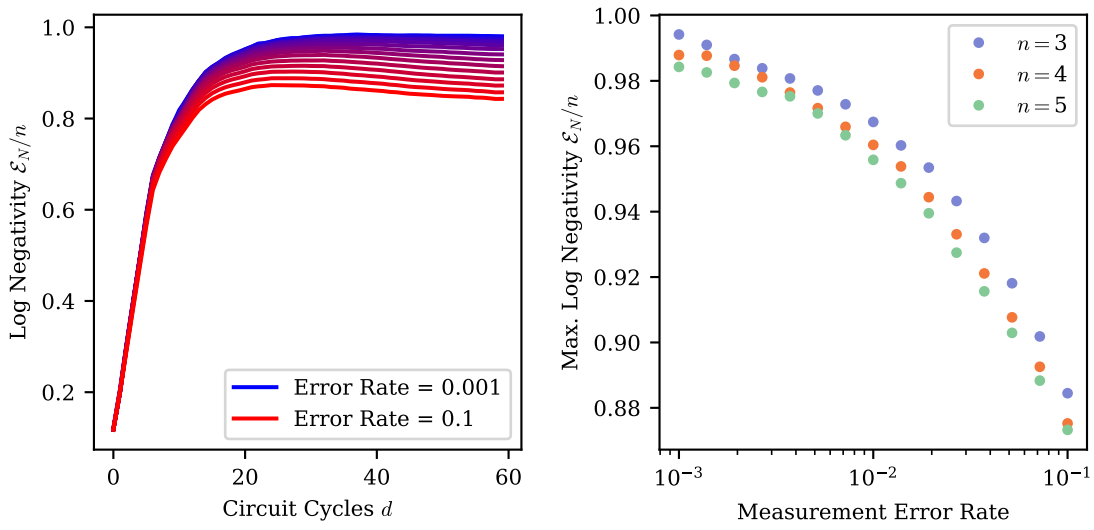

Figure D.5: On the left, we plot the normalized Logarithmic Negativity per pair of qubits as a function of the number of circuit cycles d for error rates between 0.1 and 0.001, and $n = 5$ qubit pairs. On the right is the maximal transient log negativity as a function of error rate for 3,4, and 5 pairs of qubits. Each point is averaged over 500 circuit trajectories.

ideal fixed point, there is a very long period during which the system nearly prepares the perfect state, before it is lost in the long time limit. Therefore, we can ask what the maximal amount of entanglement we prepare is after optimizing over circuit depth. We will take the logarithmic negativity as our mixed state entanglement monotone:

$$\mathcal{E}_N = \log_2 ||\hat{\rho}^{T_A}||_1 \tag{D.49}$$

where $\hat{\rho}^{T_A}$ is the partial transpose of the A system and $||\hat{O}||_1 = \text{tr}\sqrt{\hat{O}^\dagger \hat{O}}$ is the one-norm. In Fig. D.5, we can see that for a given measurement error rate, the log negativity peaks at nearly the maximal value, before slowly rolling off as measurement errors degrade the state. Moreover, we can see that even for a relatively significant error rate of 10%, we can still achieve nearly 90% of the optimal entanglement of $\mathcal{E}_N/n = 1$.

The dynamics for the spin squeezing example are very similar. Every time there is a quantum jump, the parity of the state flips, which is recorded in the classical register. If

there is a measurement error, we will accidentally flip the global parity. The steady state in the opposite parity subspace is also spin squeezed; however, it squeezes an orthogonal quadrature of the spin ensemble. This is because every time we flip the sign of the classical register, we squeeze the wrong axis - thus, if we have an odd number of measurement errors, the long time state will be spin squeezed in the wrong axis. As it turns out, this is particularly troublesome for metrology, which can be seen from looking as the Wineland parameter. Let's consider two states $|\psi_X\rangle, |\psi_Y\rangle$ which are dissipatively spin squeezed along the X and Y directions, respectively. Then, if we let α be a parameter characterized by the measurement error rate, we can write the long time steady state as a statistical mixture

$$\hat{\rho} = (1-\alpha)|\psi_X\rangle\langle\psi_X| + \alpha|\psi_Y\rangle\langle\psi_Y| \tag{D.50}$$

Now, if we are using $\hat{\rho}$ to do a Ramsey measurement, then we can characterize the sensitivity with the Wineland squeezing parameter

$$\xi_R^2 = N\frac{\mathrm{var}(\hat{S}_x^2)}{|\langle\hat{S}\rangle|^2} \tag{D.51}$$

Since both $|\psi_X\rangle$ and $|\psi_Y\rangle$ have the same expectation value of $\langle\hat{S}\rangle$, we can characterize the loss in sensitivity due to measurement error as

$$\begin{aligned}\frac{\xi_R^2(\alpha)}{\xi_R^2(\alpha=0)} &= 1-\alpha+\alpha\frac{\langle\psi_Y|\hat{S}_x^2|\psi_Y\rangle}{\langle\psi_X|\hat{S}_x^2|\psi_X\rangle} = 1-\alpha+\alpha\frac{\langle\psi_X|\hat{S}_y^2|\psi_X\rangle}{\langle\psi_X|\hat{S}_x^2|\psi_X\rangle} \\ &= 1-\alpha+\alpha\frac{(1+\tanh r)^2}{(1-\tanh r)^2} = 1+(e^{4r}-1)\alpha\end{aligned} \tag{D.52}$$

and so it appears that α must be exponentially small in order to have a state even be below the Standard Quantum Limit, let alone approach the Heisenberg limit. However, the situation is not in fact this dire. We can see that it is in fact only a few individual trajectories when we squeeze in the wrong direction that actually destroy the metrological gain of the

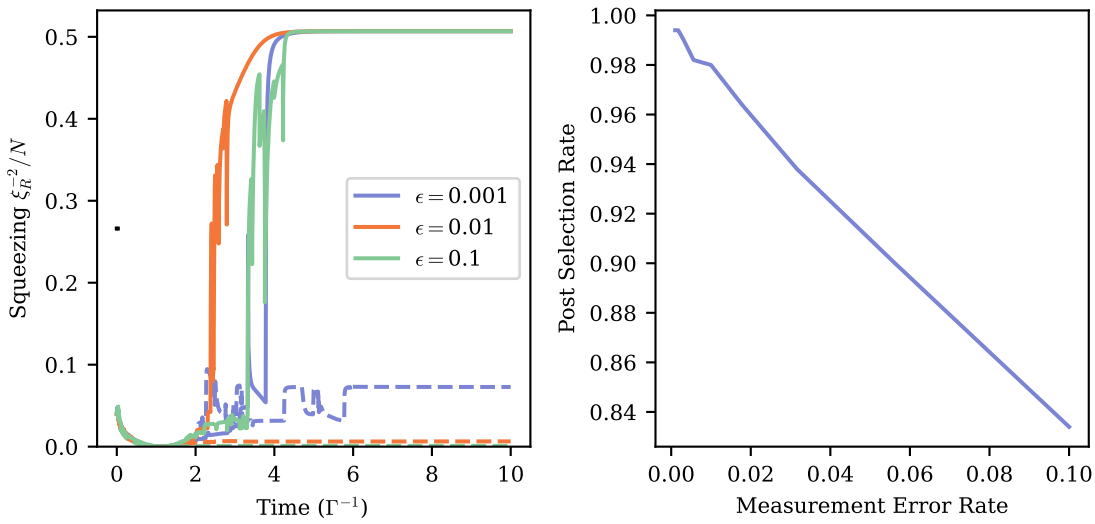

Figure D.6: Left. Average Wineland squeezing parameter for measurement error rates $\epsilon = 0.1, 0.01, 0.001$ either with (solid) or without (dashed) post-selection. We have taken $N = 24$ spin ensemble, along with a moderate squeezing $r = 2$. On the right, we plot the fraction of trajectories that survive post-selection as a function of the measurement error rate. Plots averaged over 500 individual trajectories.

entire ensemble; moreover, we always will know when they occur because we will always finish the protocol having measured an odd number of jumps. If we post-select on having performed an even number of quantum jumps at the end of the protocol, we will be able to keep the vast majority of the trajectories, and still have the ideal metrological sensitivity. This is shown in Fig. D.6. In the first plot on the left we show averaged dynamics for varying measurement error rates with either no post-selection (dashed line) or post selection (solid lines). Without post-selection, even for vanishing error rates of 0.01, there is no squeezing. However, with post-selection, we immediately recover Heisenberg scaling for all error rates. In the second figure, we see that the post-selection rate is incredibly favorable, even for a measurement that is wrong 10% of the time, we can keep more than 80% of the individual runs, and so there is extremely little overhead.

APPENDIX E

APPENDIX TO CHAPTER 6

E.1 Gaussian States Remain Gaussian

In this Appendix, we will prove that under each individual trajectory, initially Gaussian states will remain Gaussian. This requires two steps: first, we will demonstrate that time evolution under the effective Hamiltonian preserves Gaussianity, and then we will show that each quantum jump preserves Gaussianity.

We define a Gaussian operator $\hat{O}_G$ as the exponential of a quadratic fermion operator:

$$\hat{O}_G = \exp\left(\sum_{ij} O_{ij}\hat{\gamma}_i\hat{\gamma}_j\right). \tag{E.1}$$

A Gaussian state is a Gaussian operator that also is a physical density matrix: i.e., it is positive and has trace one. Gaussian operators form a group under matrix multiplication, which can be seen by observing that commutators of quadratic fermion operators are also quadratic fermion operators, along with application of the Baker-Campbell-Hausdorff formula.

For our general setup, we will take a quadratic Hamiltonian of the form

$$\hat{H} = \sum_{ij} H_{ij}\hat{\gamma}_i\hat{\gamma}_j, \tag{E.2}$$

$$\hat{L}_i = \hat{U}_i \sum_j l_{ij}\hat{\gamma}_j, \tag{E.3}$$

such that $\hat{U}_i^\dagger\hat{U}_i = \hat{\mathbf{1}}$ and $\hat{U}_i$ is a Gaussian unitary operator.

From here, we can observe that the effective Hamiltonian is

$$\hat{H}_{\text{eff}} = \hat{H} - \frac{i}{2}\sum_i \hat{L}_i^\dagger\hat{L}_i = \sum_{ij}\left(H_{ij} - \frac{i}{2}L_{ij}\right)\hat{\gamma}_i\hat{\gamma}_j, \tag{E.4}$$

where $L_{ij} = \sum_k l^*_{ki} l_{kj}$. Thus, the effective Hamiltonian is quadratic, and so the dynamics of the state (up to normalization) is given by

$$\hat{\rho}_t \propto e^{-i\hat{H}_{\text{eff}}t}\hat{\rho}_0 e^{i\hat{H}^\dagger_{\text{eff}}t}, \tag{E.5}$$

which is a product of Gaussian operators and therefore also Gaussian.

The final step is to confirm that the state remains Gaussian following each quantum jump. Since $\hat{U}_i$ is Gaussian and unitary, then the state $\hat{L}_i\hat{\rho}\hat{L}_i^\dagger$ is Gaussian if and only if $\hat{U}_i^\dagger\hat{L}_i\hat{\rho}\hat{L}_i^\dagger\hat{U}_i$ is Gaussian. To show that this is a Gaussian operation, we will demonstrate that it is equivalent to appending an auxiliary site, acting with a Gaussian operator, and then projecting the auxiliary onto a Gaussian state. Then, we will show that each of these are themselves a Gaussian operation.

First, note that adding an auxiliary site in a Gaussian state preserves Gaussianity, as one could always just imagine changing initial conditions and the auxiliary state being non-dynamical, which is equivalent to inserting it in at a later point. Acting with a Gaussian operator is tautologically Gaussian, so it remains to show that we can project onto arbitrary Gaussian states. Let's define A to be our system, B to be the auxiliary site, $\hat{\rho}_{AB}$ the joint density matrix, and $\hat{\mathbf{1}}_A \otimes \hat{\rho}_B$ to be a Gaussian state on B. Then we want to show that

$$\hat{\tilde{\rho}}_A = \text{tr}_B\left((\hat{\mathbf{1}}_A \otimes \hat{\rho}_B)\hat{\rho}_{AB}(\hat{\mathbf{1}}_A \otimes \hat{\rho}_B)\right), \tag{E.6}$$

is also Gaussian. Now, each individual operator within the trace is Gaussian, and so this reduces to showing that a partial trace preserves Gaussianity. Note that

$$\hat{\rho}_{AB} \equiv \exp\left[\begin{pmatrix}\vec{\gamma}_A \\ \vec{\gamma}_B\end{pmatrix}^T \begin{pmatrix}\Gamma_{AA} & \Gamma_{AB} \\ \Gamma_{BA} & \Gamma_{BB}\end{pmatrix}\begin{pmatrix}\vec{\gamma}_A \\ \vec{\gamma}_B\end{pmatrix}\right], \tag{E.7}$$

up to normalization. The matrices Γ_{AA}, Γ_{BB} encode local correlations and must be symmetric to satisfy hermiticity of the state, and the matrices $\Gamma_{AB} = \Gamma_{BA}^T$ encode correlations between system and auxiliary. Explicitly tracing out the state gives us that

$$\begin{aligned}\hat{\tilde{\rho}}_A =& \ \mathrm{tr}_B \hat{\rho}_{AB} \\ &= \mathrm{Pf}(\Gamma_{BB}) \exp\left[\vec{\gamma}_A^T (\Gamma_{AA} - \Gamma_{AB}\Gamma_{BB}^{-1}\Gamma_{BA})\vec{\gamma}_A\right], \end{aligned} \tag{E.8}$$

which is by definition a Gaussian state, and so projection and partial trace is a Gaussian operation.

Now finally, in order to show the action of the quantum jump preserves Gaussianity, we consider adding a Gaussian auxiliary state $\hat{\rho}_B = |0\rangle\langle 0|_B$, and then acting with the Gaussian unitary operator

$$\hat{U} = \exp\left(\alpha \hat{c}_B^\dagger \sum_j l_{ij}\hat{\gamma}_j - \mathrm{H.\,c.}\right). \tag{E.9}$$

There are now two relevant cases: if $\sum_j l_{ij}\gamma_j$ is Hermitian, then there is an orthogonal transformation such that we can assume that $\sum_j l_{ij}\hat{\gamma}_j = \beta\hat{\gamma}_0$ where β is a real normalization. If it is not Hermitian, then we can make a unitary Bogoliubov transformation such that $\sum_j l_{ij}\hat{\gamma}_j = \beta\hat{c}_0$. In either case, we can then observe in this new basis that if we take $\alpha = \pi/(2\beta)$, then we can note that

$$\begin{aligned}\hat{\tilde{\rho}}_A =& \ \mathrm{tr}_B\left[(\hat{\mathbf{1}} \otimes |1\rangle\langle 1|_B)\hat{U}(\hat{\rho}_A \otimes |0\rangle\langle 0|_B)\hat{U}^\dagger(\hat{\mathbf{1}} \otimes |1\rangle\langle 1|_B)\right] \\ &= \left(\sum_j l_{ij}\hat{\gamma}_j\right)\hat{\rho}_A\left(\sum_j l_{ij}\hat{\gamma}_j\right)^\dagger, \end{aligned} \tag{E.10}$$

as desired.

E.2 Set of Simulable 1D Systems

Here, we will outline the most general type of 1D spin chains that can be simulated using our technique. We will as before define N to be the total number of lattice sites. The Hamiltonian can be written as

$$\hat{H} = \hat{H}_\partial + \hat{H}_{\text{free}} + \hat{H}_{\text{int}}, \tag{E.11}$$

$$\hat{H}_\partial = \Omega_1 \hat{\sigma}_1^x + \Omega_2 \hat{\sigma}_1^y + \Omega_3 \hat{\sigma}_N^x + \Omega_4 \hat{\sigma}_N^y, \tag{E.12}$$

$$\hat{H}_{\text{free}} = \sum_i \Delta_i \hat{\sigma}_i^z + J_i \hat{\sigma}_i^+ \hat{\sigma}_{i+1}^- + J_i^* \hat{\sigma}_i^- \hat{\sigma}_{i+1}^+, \tag{E.13}$$

$$\hat{H}_{\text{int}} = \frac{1}{4} \sum_{ij} U_{ij} \left(\hat{\sigma}_i^z + 1\right) \left(\hat{\sigma}_j^z + 1\right), \tag{E.14}$$

where $\Omega_i, \Delta_i, U_{ij} \in \mathbb{R}$ and $J_i \in \mathbb{C}$. It is clear that $\hat{H}_{\text{free}}$ transforms to free fermions under JW. To understand how to simulate $\hat{H}_\partial$, we note that we can simply extend the size of the Hilbert space to include two additional lattice sites $i = 0, N+1$ and write a different Hamiltonian [286]

$$\hat{H}'_\partial = \sigma_0^x (\Omega_1 \hat{\sigma}_1^x + \Omega_2 \hat{\sigma}_1^y) + \hat{\sigma}_{N+1}^x (\Omega_3 \hat{\sigma}_N^x + \Omega_4 \hat{\sigma}_N^y). \tag{E.15}$$

Since $[\hat{H}'_\partial, \sigma_0^x] = [\hat{H}'_\partial, \sigma_{N+1}^x] = 0$ they are constants of motion, and if initialize these states in $|+\rangle$, then we can formally trace them out and recover $\hat{H}_\partial$. However, in the new form $\hat{H}'_\partial$ clearly also transforms to free fermions in an enlarged Hilbert space.

The Hamiltonian $\hat{H}_{\text{int}}$ is formally interacting following the JW transformation:

$$\hat{H}_{\text{int}} = \sum_{ij} U_{ij} \hat{n}_i \hat{n}_j. \tag{E.16}$$

In order to simulate $\hat{H}_{\text{int}}$ we use the result from Ref. [208] that if there is sufficient noise, the quantum channel involving a fermionic density-density interaction (which is what $\hat{H}_{\text{int}}$ is)

can be written as a map from convex sums of Gaussian states into convex sums of Gaussian states. Hence, this can be simulated in the exact same way as everything else we have simulated by simply adding more stochasticity as we sample Gaussian trajectories. We will not re-derive their result here, but simply quote that the total amount of noise must obey the inequality

$$\sum_i |U_{ij}| \leq \gamma_j \ \forall j, \tag{E.17}$$

where γ_j are the set of dephasing rates defined below in Eq. (E.19).

Next, we can consider the most general type of jump operators, which can be written as two-local operators that are linear in spin raising/lowering or as dephasing:

$$\hat{L}_i = l_{i,1}\hat{\sigma}_i^- + l_{i,2}\hat{\sigma}_i^+ + l_{i,3}\hat{\sigma}_{i+1}^- + l_{i,4}\hat{\sigma}_{i+1}^+, \tag{E.18}$$

$$\hat{D}_i = \sqrt{\gamma_i}\hat{\sigma}_i^z, \tag{E.19}$$

where $l_{ij} \in \mathbb{C}$ and $\gamma_j \in \mathbb{R}^+$. We have already discussed at length how one simulates $\hat{L}_i$. As regards $\hat{D}_i$, it is simple to note that because the jump operator is Hermitian, we can treat this a stochastic Hamiltonian, i.e. we make the transformation in $\hat{H}_{\text{free}}$

$$\Delta_i \to \Delta_i + \sqrt{\gamma_i}\xi_i, \tag{E.20}$$

where ξ_i are i.i.d. Gaussian random variables such that $\overline{\xi_i(t)\xi_j(t')} = \delta_{ij}\delta(t-t')$. Hence, $\hat{D}_i$ can be simulated since $\hat{H}_{\text{free}}$ can be simulated.

E.3 Efficiently Diagonalizable Liouvillians

Here we comment on the results contained in Ref. [205], where it is shown that for a certain class of open spin chains, one can find the entire eigensystem for the Lindbladian. Essentially,

they show that in systems with pure loss dissipation and Hamiltonians that conserve particle number, then one can block diagonalize the entire Lindbladian $\mathcal{L}$ in the particle number basis such that it is lower triangular. Specifically, let's define the Lindbladian as the sum of two different superoperators:

$$\mathcal{L} = \mathcal{H} + \mathcal{K}, \tag{E.21}$$

$$\mathcal{H}\hat{\rho} = -i\hat{H}_{\text{eff}}\hat{\rho} + i\hat{\rho}\hat{H}_{\text{eff}}^{\dagger}, \tag{E.22}$$

$$\mathcal{K}\hat{\rho} = \sum_i \hat{L}_i\hat{\rho}\hat{L}_i^{\dagger}. \tag{E.23}$$

With this definition, we can see that in the particle number basis, $\mathcal{H}$ contains diagonal blocks, and $\mathcal{K}$ strictly lowers particle number by 1, so it contains only lower triangular blocks. Hence, the entire spectrum of $\mathcal{L}$ is contained in $\mathcal{H}$, which is a quadratic operator of the fermions, and can therefore be diagonalized: the string operators do not change the spectrum of the Lindbladian. However, they can significantly alter the left/right eigenvectors of $\mathcal{L}$. Ref. [205] also shows that these eigenvectors can be solved for recursively, giving the full eigensystem of the Lindbladian.

This is an incredibly powerful result; however, as the eigenmodes no longer take a simple form, trying to calculate dynamics of observables is still an exponentially difficult task unless the recursion relations can be solved analytically. Even if one can analytically diagonalize an exponentially large matrix, taking linear combinations of an exponential number of exponentially large vectors still requires exponential resources, even if the "hard part" of performing the diagonalization is already done. Such a problem can be seen in, for example, Gaussian boson sampling: one can analytically calculate the full spectral decomposition of the unitary matrix of a Gaussian boson sampler, but using this to estimate certain observables is still an exponentially difficult task. The power of our technique is that it allows one to efficiently calculate arbitrary observables.

Additionally, the technique we have presented here is not restricted to pure loss dissipation or particle conserving Hamiltonians, as is seen in the dissipative transverse field Ising model we study in Chapter 6. Moreover, in Chapter 6, we showed that even in a system where the spectra are identical, the effect the strings have on the dynamics can still be very nontrivial.

E.4 Estimation Error and Sample Complexity

In order to estimate the sample complexity required to get convergence, it is simple to observe that if we are only interested in calculating strings of Majorana operators $\hat{O}$, then each operator has a bounded spectrum and so it expectation is bounded above and below: $-1 \leq \langle \hat{O} \rangle \leq 1$. Hence, application of the Hoeffding inequality implies that the probability

$$P(|\mathbb{E}_n[O] - O| \geq \epsilon) \leq 2 \exp\left(-\frac{n\epsilon^2}{2}\right), \tag{E.24}$$

where we have defined $O \equiv \langle \hat{O} \rangle$ the actual value, and $\mathbb{E}_n[O]$ is the arithmetic mean after running n trajectories. Hence, if we desire to estimate O with an error less than ϵ with a probability of $1 - \delta$, then we require a sample complexity

$$n \geq \frac{2 \log(2\delta^{-1})}{\epsilon^2}. \tag{E.25}$$

Crucially, this estimator does not depend on the size of the system, and therefore does not affect the computational complexity of the algorithm. Moreover, this is a worst case scenario: often we know that each individual sample has a variance significantly smaller than the maximal variance. For example, in systems with pure loss, the total number of particles in the system is tending to zero exponentially quickly. Hence, for example, the variance in the particle number is also tending to zero exponentially quickly in time, and so the number of samples to get a small additive error is also tending to zero.

E.5 Fokker-Planck Equation

In this Appendix, we will derive a closed form Fokker-Planck Equation (FPE) for the equation of motion of a real, positive, probability distribution over Gaussian states. The basis for this will be the stochastic equation of motion for the covariance matrix derived in Chapter 6. However, the exact details of the equation are irrelevant. If we define $\vec{X}$ to be a vectorized form of the covariance matrix, then we can momentarily forget the physics, and just treat the previously derived equation of motion as a nonlinear SDE driven by a point process. Specifically, it is given by the general form

$$\mathrm{d}X_i = f_i(X)\ \mathrm{d}t + g_{ij}(X)\ \mathrm{d}\xi_j, \tag{E.26}$$

$$\mathrm{d}\xi_j = \begin{cases} 1 & \text{w/prob} \quad N_j\ \mathrm{d}t \\ 0 & \text{w/prob} \quad 1 - N_j\ \mathrm{d}t \end{cases}. \tag{E.27}$$

Let's find the Ito rules for this particular kind of equation of motion. Let's suppose that $\psi(X)$ is an arbitrary function of X, and wish to find it's equation of motion. Then we can derive

$$\begin{aligned} \mathrm{d}\psi &\equiv \lim_{\Delta t \to 0} \psi(X(t+\Delta t)) - \psi(X(t)) \\ &= \lim_{\Delta t \to 0} \frac{\psi\left(\vec{X} + \vec{f}(X)\Delta t + \hat{g}(X)\Delta\vec{\xi}\right) - \psi(\vec{X})}{\Delta t}\Delta t. \end{aligned} \tag{E.28}$$

Let's first assume that in a time step Δt none of the individual point processes occur. This has probability $1 - \sum_j N_j \Delta t$. With this probability, we set all of the ξ_j to zero, giving

$$\lim_{\Delta t \to 0} \frac{\psi\left(\vec{X} + \vec{f}(X)\Delta t\right) - \psi(\vec{X})}{\Delta t}\Delta t = \frac{\partial \psi}{\partial X_i} f_i(X)\Delta t. \tag{E.29}$$

Now, suppose that instead, one of the point processes occurs (the odds of multiple are negligible to order Δt). Then, we have that this term dominates as $\Delta t \to 0$, i.e.

$$\begin{aligned}
&\lim_{\Delta t \to 0} \frac{\psi\left(\vec{X} + \vec{f}(X)\Delta t + \hat{g}(X)\Delta\vec{\xi}\right) - \psi(\vec{X})}{\Delta t}\Delta t \\
&= \lim_{\Delta t \to 0} \frac{\psi\left(X_i + f_i(X)\Delta t + g_{ij}(X)\right) - \psi(\vec{X})}{\Delta t}\Delta t \\
&= \psi\left(X_i + g_{ij}(X)\right) - \psi(\vec{X}).
\end{aligned} \tag{E.30}$$

Hence, we can rewrite the equation of motion for ψ as

$$\mathrm{d}\psi = \sum_i \frac{\partial \psi}{\partial X_i} f_i(X)\ \mathrm{d}t + \sum_j \left[\psi\left(X_i + g_{ij}(X)\right) - \psi(\vec{X})\right]\ \mathrm{d}\xi_j. \tag{E.31}$$

From here, let's define $\rho(\vec{X}, t)$ the probability distribution of $\vec{X}$ at time t. By definition, we have that

$$\mathbb{E}[O](t) \equiv \int \rho(\vec{X}, t) O(\vec{X})\ \mathrm{d}^n\vec{X}. \tag{E.32}$$

Hence, we find that taking an expectation value of the $\mathrm{d}\psi$ gives us (suppressing sums for brevity such that repeated indices are implicitly summed over)

$$\begin{aligned}
\mathbb{E}[\ \mathrm{d}\psi](t) &= \int \left[\rho(\vec{X}, t)\ \mathrm{d}\psi(\vec{X})\right]\ \mathrm{d}^n\vec{X} \\
&= \int \left[\frac{\partial \psi}{\partial X_i} f_i(X)\rho(\vec{X}, t)\ \mathrm{d}t + \left[\psi\left(X_i + g_{ij}(X)\right) - \psi(\vec{X})\right] N_j(\vec{X})\rho(\vec{X}, t)\ \mathrm{d}t\right]\ \mathrm{d}^n\vec{X},
\end{aligned} \tag{E.33}$$

We can use this to then observe that

$$\int \dot{\rho}(\vec{X},t)\psi(\vec{X})\ \mathrm{d}^n\vec{X} = \int \left[\psi(\vec{X})\left(\frac{\partial}{\partial X_i}\left[f_i(X)\rho(\vec{X},t)\right] - N_j(\vec{X})\rho(\vec{X},t)\right)\right]\ \mathrm{d}^n\vec{X} + \int \left[\psi\left(X_i + g_{ij}(\vec{X})\right)N_j(\vec{X})\rho(\vec{X},t)\right]\ \mathrm{d}^n\vec{X}. \tag{E.34}$$

At this point, let's define the vector valued family of functions $\vec{h}_j(\vec{X}) = \vec{X} + g_{ij}(\vec{X})\vec{e}_i$, where $\vec{e}_i$ is the i^{th} unit vector. Let's further assume that these functions are locally invertible. Then, consider the change of variables $\vec{Y}_j = \vec{h}_j(\vec{X})$. We can define the Jacobian M_j via the set of determinants of matrices $\check{M}_j$

$$M_j = \det \check{M}_j, \tag{E.35}$$

$$(\check{M}_j)_{mn} = \left(\frac{\partial (Y_j)_m}{\partial X_n}\right). \tag{E.36}$$

Then, we can rewrite the second integral as

$$\sum_j \int \psi\left(X_i + g_{ij}(\vec{X})\right)N_j(\vec{X})\rho(\vec{X},t)\ \mathrm{d}^n\vec{X} = \sum_j \int M_j^{-1}\psi(\vec{Y}_j)(N_j \circ h_j^{-1})(Y_j) \times \rho(h_j^{-1}(Y_j),t)\ \mathrm{d}^n Y_j. \tag{E.37}$$

Therefore, we find that (suppressing arguments for clarity)

$$0 = \int \psi\left(-\dot{\rho} + \frac{\partial}{\partial X_i}\left[f_i\rho\right] - N_j\rho + M_j^{-1}(N_j \circ h_j^{-1}) \times \rho(h_j^{-1})\right)\ \mathrm{d}^n\vec{X}. \tag{E.38}$$

Because the function ψ is arbitrary, this must hold for all possible functions, and so we get

the effective Focker-Plank equation for the distribution

$$\dot{\rho}(\vec{X},t) = \nabla \cdot [\vec{f}(\vec{X})\rho(\vec{X},t)] + \sum_j (N_j \circ h_j^{-1})(X) \times M_j^{-1}(\vec{X}) \times \rho(h_j^{-1}(X),t) - N_j(\vec{X})\rho(\vec{X},t). \tag{E.39}$$

Here, the gradient term is the standard drift term in normal FPEs. On the other hand, because we have a point process of discrete jumps instead of the standard Wiener increments, we have a much more complicated "diffusion" term, that captures the effect of these stochastic jumps. In particular, it is no longer spatially local, as jumps can cause large changes to the covariance matrix.

E.6 Second Order Cumulant Expansion

The stochastic equation of motion is convenient that it is in closed form, but because it is stochastic it requires averaging. The Fokker-Planck equation has a closed form and is also deterministic, but it is an equation of motion for a $4N^2$ dimensional distribution function, and therefore outside of limiting cases is analytically and numerically somewhat intractable. To make further simplifications, one possibility is making a second order cumulant expansion by assuming that

$$\overline{\Gamma_{ij}\Gamma_{kl}} - \overline{\Gamma_{ij}}\ \overline{\Gamma_{kl}} = 0, \tag{E.40}$$

where the overline represents a noise average. If such a simplification were to hold, then one could directly average the stochastic equation of motion for the covariance matrix and get the much simpler closed form, deterministic equation given by

$$\begin{aligned}\partial_t \Gamma_{mn} &= (\Gamma X - X^*\Gamma - \frac{1}{2}\Gamma(X - X^*)\Gamma)_{mn} \\ &\quad + \sum_{ikl} l^*_{ik} l_{il} \tau^i_m \tau^i_n (\Gamma_{km}\Gamma_{nl} + \Gamma_{kl}\Gamma_{mn} - \Gamma_{kn}\Gamma_{ml}) - l^*_{ik} l_{il} \Gamma_{kl}\Gamma_{mn} \\ &= (\Gamma X - X^*\Gamma)_{mn} + \sum_{ikl} l^*_{ik} l_{il} (\tau^i_m \tau^i_n - 1)(\Gamma_{km}\Gamma_{nl} + \Gamma_{kl}\Gamma_{mn} - \Gamma_{kn}\Gamma_{ml}). \end{aligned} \tag{E.41}$$

This has the same computational complexity of solving any given individual trajectory, with the added benefit of requiring no averaging.

Quite interestingly, we can observe that this approximation ends up being identical to assuming that Wick's theorem holds at all times t in the state. To see this, let's revert to the distribution function defined in Eq. (6.30). We can directly calculate

$$\langle \hat{\gamma}_i \hat{\gamma}_j \hat{\gamma}_k \hat{\gamma}_l \rangle = \int \operatorname{tr}(\hat{\rho}_\Gamma \hat{\gamma}_i \hat{\gamma}_j \hat{\gamma}_k \hat{\gamma}_l) p(\Gamma)\, \mathrm{d}\Gamma = \overline{\Gamma_{ij}\Gamma_{kl}} + \overline{\Gamma_{il}\Gamma_{jk}} - \overline{\Gamma_{ik}\Gamma_{jl}}, \tag{E.42}$$

and therefore, if the second cumulant in the noise vanishes, then Wick's theorem also trivially holds. Numerically, we find that this approximation often works surprisingly well to calculate local expectation values when the fixed point of the dynamics is a Gaussian state. We conjecture that in such cases, because the state must both begin and end in a Gaussian state, the trajectory-averaged state during the time dynamics never deviates too far from being actually Gaussian, and so the approximation does well to capture the dynamics.

E.7 AFM Order Melting

In this Appendix, we will give more context into the AFM order melting in both the spin system and the free fermions.

E.7.1 Free Fermions

For free fermions, we can formally make a unitary transformation into plane wave modes:

$$\hat{c}'_k = \frac{1}{\sqrt{N}} \sum_{j=1}^{N} e^{ijk} \hat{c}_j, \tag{E.43}$$

which allows us to diagonalize simultaneously the Hamiltonian and all the jump operators:

$$\hat{H} = 2J \sum_{k=1}^{N} \cos(k) (\hat{c}'_k)^\dagger \hat{c}'_k, \tag{E.44}$$

$$\hat{L}'_k = \sqrt{\kappa} \hat{c}'_k. \tag{E.45}$$

The initial Neél state has a covariance given by

$$\langle (\hat{c}'_k)^\dagger \hat{c}'_l \rangle (0) = \frac{1}{2} (\delta_{kl} + \delta_{k,l+\pi}), \tag{E.46}$$

$$\implies \langle (\hat{c}'_k)^\dagger \hat{c}'_l \rangle (t) = \frac{1}{2} (\delta_{kl} + \delta_{k,l+\pi}) e^{2i(\cos k - \cos l)t - \kappa t}. \tag{E.47}$$

Fourier transforming back into real space gives us that the AFM order parameter is now given by

$$\begin{aligned} A(t) &= \frac{1}{N} \sum_i (-1)^i \langle \hat{c}_i^\dagger \hat{c}_i \rangle (t) = e^{-\kappa t} \sum_k e^{-4iJt\cos(k)} \langle (\hat{c}'_k)^\dagger \hat{c}'_{k+\pi} \rangle (0) \\ &= \frac{1}{2} e^{-\kappa t} \sum_k e^{-4iJt\cos(k)}. \end{aligned} \tag{E.48}$$

If we then take the continuum limit $N \to \infty$, we can replace the sum with an integral to find that, as expected, we get a Bessel function $A(t) = e^{-\kappa t} J_0(|4Jt|)$.

The crucial thing to observe here is that the AFM order is completely determined by the correlations at $k - l = \pi$, and does not depend on the local density.

E.7.2 Spins

When we switch to spins, our intuition tells us that, roughly speaking, we can think of the jumps as a kind of dephasing noise: by randomly flipping signs in the Hamiltonian, we do not ever change the actual particle number, but on average we tend to dephase away correlations.

For an incredibly simple starting point, let's assume that the only difference between the spins and fermions is that the spins have disorder on the sign of the bond of each Hamiltonian. I.e., let's define the effective Hamiltonian for the spins as

$$\hat{H}_s = J \sum_{i=1}^{N-1} \xi_i \hat{c}_i^\dagger \hat{c}_{i+1} + \text{H. c.}, \tag{E.49}$$

where $\xi_i = \{-1, 1\}$ is a random variable. Now, because we have taken OBC, we can always gauge these phases away into the operators via

$$\hat{\tilde{c}}_i = \left(\prod_{j=0}^{i-1} \xi_j \right) \hat{c}_i \equiv \tau_i \hat{c}_i. \tag{E.50}$$

Using these new operators, we can rewrite the gauged Hamiltonian as

$$\hat{H}_s = J \sum_{i=1}^{N-1} \hat{\tilde{c}}_i^\dagger \hat{\tilde{c}}_{i+1} + \text{H. c.} \tag{E.51}$$

Taking infinite boundary conditions, we can diagonalize this simply into plane wave modes. Using this plane wave decomposition, we can then solve for how the underlying degrees of freedom evolve:

$$\langle \hat{\tilde{c}}_k'^\dagger \hat{\tilde{c}}_l' \rangle = e^{-\kappa t - 2iJ\cos(k)t + 2iJ\cos(l)t}. \tag{E.52}$$

Using this expression, along with Eq. (E.50), we can calculate the disorder averaged expec-

tation value of the plane waves in the ungauged basis:

$$\overline{\langle(\hat{c}'_k)^\dagger \hat{c}'_l\rangle(t)} = \frac{e^{-\kappa t}}{N^2} \sum_{m,n,q,s} e^{i(km-ln)-i(qm-sn)-2iJ\cos(q)t+2iJ\cos(s)t} \overline{\tau_m \tau_n} \langle(\hat{c}'_q)^\dagger \hat{c}'_s\rangle(0). \tag{E.53}$$

Now, if $\overline{\tau_m \tau_n} = 1$, we recover exactly the free fermion result, as desired. However, a more realistic noise model would have these phases being incredibly correlated locally: essentially, we are trying to ask about the expected number of jumps that might occur between sites m and n and then averaging over the parity of that number. In the large system size limit, this will approach zero rapidly as $m - n$ becomes large.

We will posit phenomenologically that $\overline{\tau_m \tau_n} = \exp(-\alpha(m-n)^2)$ for some constant α. We know that in order to calculate the AFM order parameter, we simply need to integrate over the correlations at π. We will again pass to the continuum limit, and observe that this can be rewritten as

$$A(t) = \frac{1}{2N} e^{-\kappa t} \int_{\mathbb{R}} \mathrm{d}x \, \mathrm{d}y \int_{-\pi}^{\pi} \frac{\mathrm{d}k}{2\pi} \frac{\mathrm{d}q}{2\pi} e^{i(x-y)(k-q)} e^{-4iJ\cos(q)t} e^{-\alpha(x-y)^2}. \tag{E.54}$$

If we rotate the angle into the new coordinates $\bar{x} = (x + y)$ and $\delta x = (x - y)$, we can observe that $\bar{x}$ does not show up in the integrand and simply cancels the factor of N in the denominator. We can similarly perform the Gaussian integral in δx to arrive at

$$A(t) = \frac{1}{2} e^{-\kappa t} \int_{-\pi}^{\pi} \frac{\mathrm{d}k}{2\pi} \frac{\mathrm{d}q}{2\pi} e^{-(k-q)^2/(4\alpha)} e^{-4iJ\cos(q)t}. \tag{E.55}$$

We can shift the integral over $k \to k - q$ to get that

$$A(t) = \frac{1}{2} e^{-\kappa t} \int_{-\pi}^{\pi} \frac{\mathrm{d}k}{2\pi} \frac{\mathrm{d}q}{2\pi} e^{-k^2/(4\alpha)} e^{-4iJ\cos(k+q)t}. \tag{E.56}$$

Now, we make the assumption that α is small enough that we can extend the bounds of integration to infinity with minimal error:

$$A(t) = \frac{1}{2} e^{-\kappa t} \int_{-\pi}^{\pi} \frac{\mathrm{d}q}{2\pi} \int_{-\infty}^{\infty} \mathrm{d}k e^{-k^2/(4\alpha)} e^{-4iJ\cos(k+q)t}. \tag{E.57}$$

This further implies we can Taylor expand around small k to find that

$$\begin{aligned} A(t) &\sim \frac{1}{2} e^{-\kappa t} \int_{-\pi}^{\pi} \frac{\mathrm{d}q}{2\pi} \int_{-\infty}^{\infty} e^{-\frac{k^2}{4\alpha}} e^{-4iJt[\cos(q) - k\sin(q)]} \, \mathrm{d}k \\ &\sim \frac{1}{2} e^{-\kappa t} \int_{-\pi}^{\pi} \frac{\mathrm{d}q}{2\pi} e^{-4iJt\cos(q) - 16\alpha J^2 \sin^2(q) t^2}. \end{aligned} \tag{E.58}$$

This tells us how we expect the off-diagonal elements to dephase:

$$|\langle (\hat{c}'_q)^\dagger \hat{c}'_{q+\pi} \rangle(t)| e^{\kappa t} \sim e^{-16\alpha J^2 \sin^2(q) t^2}. \tag{E.59}$$

Such Gaussian dephasing is common in quasi-static noise processes, and matches extremely well what we see in numerics. Intuitively, it also makes a lot of sense: we can think of the dephasing rate $\alpha J^2 \sin^2(q)$ as the group velocity multiplied by the inverse correlation length of the noise: it tells us how much of the phase randomization a given wave packet samples in time t. Wavepackets that move very slowly and have small group velocity take a very long time to notice there is any phase disorder in the lattice, and therefore are much longer lived, and vice-versa for very fast wavepackets. As can be seen in Fig. E.1, this intuitive picture matches the numerics, where the rate at which the modes are damped out depends on their group velocity. The modes at $k = 0, \pi$ which have zero group velocity are extremely long

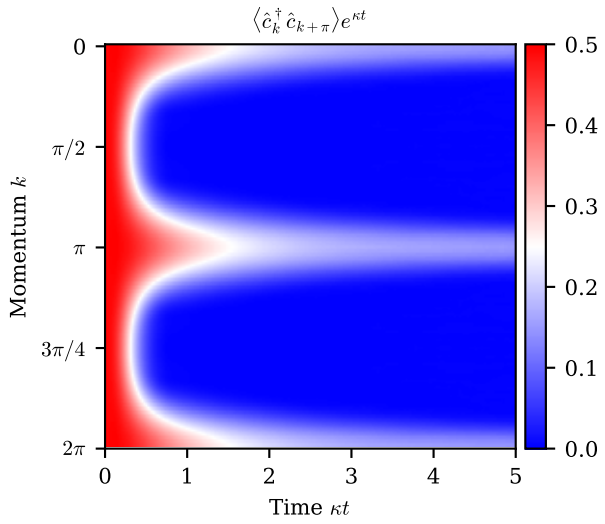

Figure E.1: Correlations in momentum space for an $N = 100$ site XX spin chain in an initial Néel state with local loss on each site. Note that the rate at which correlation decay is dependent on their group velocity.

lived, and the modes at $k = \pi/2, 3\pi/2$ with maximal group velocity decay the most rapidly.

We can finally use this expression to derive the correct power law. We wish to calculate

$$A(t) \propto \int_{-\pi}^{\pi} \frac{\mathrm{d}q}{2\pi} e^{-4iJt\cos(q) - 16\alpha J^2 \sin^2(q) t^2}. \tag{E.60}$$

At very long times, we can observe that only the values of q near $q = 0, \pi$ are relevant. Hence, we can once again approximate this as a Gaussian integral, and extend the bounds to infinity. We also Taylor expand the exponential to get

$$\begin{aligned} A(t) &\sim \int_{-\infty}^{\infty} [\cos(4Jt) + 2Jtq^2 \sin(4Jt)] e^{-16\alpha J^2 q^2 t^2} \, \mathrm{d}q \\ &= \frac{\sqrt{\pi}}{4|Jt|\sqrt{\alpha}} \left[\cos(4Jt) + \frac{\sin(4Jt)}{16Jt\alpha} + \mathcal{O}(t^{-2}) \right]. \end{aligned} \tag{E.61}$$

Hence, the leading order scaling is simply $\cos(4Jt)/|Jt|$ up to a prefactor, which agrees extremely well with numerics.

E.8 Subradiance

E.8.1 Particle Density

In this Appendix, we will formally derive the long time particle number density for the free fermions, and discuss how this is different for spins. The free fermion master equation is given by

$$\hat{H} = J \sum_i \hat{c}_i^\dagger \hat{c}_{i+1} + \text{H. c.}, \tag{E.62}$$

$$\hat{L}_i = \sqrt{\kappa}(\hat{c}_i - \hat{c}_{i+1}). \tag{E.63}$$

Using translational invariance, we can Fourier transform this as before to get the new master equation

$$\hat{H} = 2J \sum_k \cos(k)(\hat{c}'_k)^\dagger \hat{c}'_k, \tag{E.64}$$

$$\hat{L}_k = \sqrt{\kappa}(1 - e^{ik})\hat{c}'_k = -2ie^{ik/2}\sin(k/2)\hat{c}'_k. \tag{E.65}$$

If the state is initialized to be completely filled, then each momentum mode will decay independently of all the others at a rate given by

$$\langle (\hat{c}'_k)^\dagger \hat{c}'_k \rangle(t) = \exp(-4\kappa \sin^2(k/2)t). \tag{E.66}$$

From here, it is simple to integrate over all the momentum modes to find the time dynamics of the average particle density:

$$\langle \hat{n}(t) \rangle = \int_{-\pi}^{\pi} \frac{\mathrm{d}k}{2\pi} \langle (\hat{c}'_k)^\dagger \hat{c}'_k \rangle(t) = e^{-2\kappa t} I_0(2\kappa t), \tag{E.67}$$

which asymptotically tends to $(4\pi\kappa t)^{-1/2}$ in the long time limit.

We can think of the long time behavior as effectively integrating over a Gaussian in the long time limit, such that as before we can extend the bounds of the momentum integral to infinity and expand $\sin^2(k/2) \sim k^2/4$ to find the asymptotic behavior. As one might expect, after some time t the only modes that are really contributing have $|k| \lesssim (4\pi\kappa t)^{-1/2}$, which are still roughly filled.

If we were to instead try and perform the same calculation with the spins, the crucial difference here is that the different momentum modes are no longer conserved. After some time, the non-interacting master equation is trying to imprint a Gaussian distribution of k modes centered at $k = 0$ with a width $\sigma = (8\pi\kappa t)^{-1/2}$. However, the interactions allow the different k modes to scatter, which overall tries to make the distribution more uniform. The competition of these two effects - the linear term sharpening the distribution and the non-linear term trying to smoothen it - combine to allow density to leave the system more quickly, which in turn changes the power law.

We note that this simple scattering picture can be seen at the level of the second cumulant expansion as derived in Chapter 6. If we define $C'_{kk'} = \langle (\hat{c}'_k)^\dagger \hat{c}'_{k'} \rangle$ to be the covariance matrix in Fourier space, then the GGE equations of motion are given by

$$\begin{aligned}\partial_t C'_{qq'} &= -\kappa(\sin^2(q/2) + \sin^2(q'/2))C'_{qq'} \\ &\quad + \frac{\kappa}{N^3}\sum(\tau^n_m \tau^n_{m'} - 1)e^{i(m(q-l)+m'(l'-q')+n(k'-k)}(1-e^{ik})(1-e^{-ik'})(C'_{kk'}C'_{ll'} - C'_{kl'}C'_{lk'}),\end{aligned} \tag{E.68}$$

where the sum is over all repeated indices.

This is the form of a momentum-conserving 4-point scattering interaction. We can directly time-evolve the second-cumulant equation of motion, which is able to account for the scattering and qualitatively captures the correct power law for the asymptotic decay of the mean particle density, see Fig. E.2.

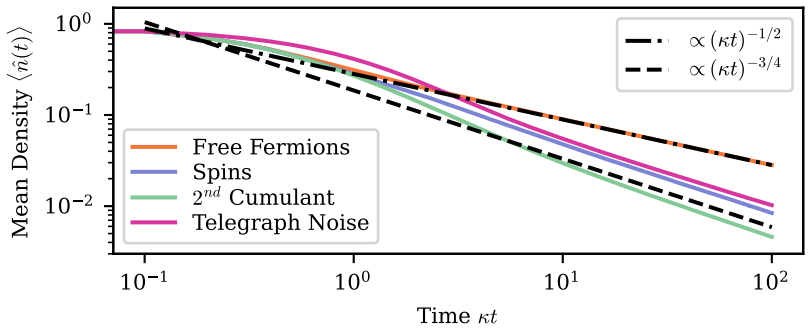

Figure E.2: Here, we compare the data in Fig. 6.3 for the full spin model (blue) and the free fermion model (orange) to the non-linear time evolution from the second order cumulant expansion method derived in Chapter 6 (green), and the telegraph noise approximation [c.f. Eq. (E.69)] (magenta). While the actual value of the density at long times is not captured quantitatively, the asymptotic power law is correctly identified to be approximately $(\kappa t)^{-3/4}$ by both the mean field and the telegraph noise.

Moreover, we can consider an even simpler heuristic model where we think of the action of the spins as causing random classical gauge field fluctuations. I.e., let's consider the following effective Hamiltonian:

$$\hat{H}_{\text{eff}} = \sum_i \xi_i \left(J + i\frac{\kappa}{2}\right)\left(\hat{c}_i^\dagger \hat{c}_{i+1} + \hat{c}_{i+1}^\dagger \hat{c}_i\right) - i\kappa \hat{c}_i^\dagger \hat{c}_i. \tag{E.69}$$

Here, $\xi_i \in \{-1, 1\}$ is a random telegraph process. Unlike in the AFM-order melting model, this time the dynamics are subradiant, and so we would expect that jumps are continuously happening for times up to $t \sim \mathcal{O}(N^2)$, and so we cannot treat ξ_i as simply static disorder. Instead, we will assume that each ξ_i is a telegraph process where the probability of flipping in a time step $\mathrm{d}t$ is given by

$$P(\xi_j \to -\xi_j) = i\frac{\kappa\ \mathrm{d}t}{N}\langle \hat{H}_{\text{eff}} - \hat{H}_{\text{eff}}^\dagger \rangle. \tag{E.70}$$

Using this model, we are also able to qualitatively capture the dynamics of the spins, as can be seen in Fig. E.2.

E.8.2 Density-Density Correlations

In addition to just studying where the average particle density in the system is, we can also study density-density correlations in the spin chain. We will be interested in the connected correlation function:

$$C_{i,j} = \langle \hat{n}_i \hat{n}_j \rangle - \langle \hat{n}_i \rangle \langle \hat{n}_j . \rangle \tag{E.71}$$

For a Gaussian state, this can be calculated using Wick's theorem to observe that $C_{i,j} = -|\langle \hat{c}_i^\dagger \hat{c}_j \rangle|^2$. Using this formula, we can first calculate how the connected correlation function should evolve for the free fermion model, which is given by (in the continuum limit, with separation $d = i - j$)

$$C_{i,j}^{\text{free}}(t) = -\left| \int \frac{\mathrm{d}k}{2\pi} e^{ikd - 4\kappa \sin^2(k/2)t} \right|^2 . \tag{E.72}$$

This can be computed by expanding the exponential, noting that

$$\begin{aligned}
\int \frac{\mathrm{d}k}{2\pi} e^{-ikd - 4\kappa \sin^2(k/2)t} &= \sum_{n=0}^{\infty} \frac{(-4\kappa t)^n}{n!} \int \frac{\mathrm{d}k}{2\pi} \sin^{2n}(k/2) e^{-ikd} \\
&= \sum_{n=0}^{\infty} \frac{(\kappa t)^n}{n!} \int \frac{\mathrm{d}k}{2\pi} \left(e^{ik/2} - e^{-ik/2} \right)^{2n} e^{-ikd} \\
&= \sum_{n=0}^{\infty} \frac{(\kappa t)^n}{n!} \sum_{j=0}^{2n} \binom{2n}{j} \int \frac{\mathrm{d}k}{2\pi} e^{ikj/2} e^{-ik(2n-j)/2} e^{-ikd} \\
&= \sum_{n=0}^{\infty} \frac{(\kappa t)^n}{n!} \binom{2n}{n+d} = e^{-2\kappa t} I_d(2\kappa t),
\end{aligned} \tag{E.73}$$

where I_d is the d^{th} modified Bessel function. This matches on cleanly to the limit $d = 0$ where we recover the value for the local density. In the long time limit $\kappa t \gg |i - j|^2$, this

can be approximated as

$$C_{i,j}^{\text{free}}(\kappa t \gg |i-j|^2) \sim -\frac{1}{4\pi\kappa t} e^{-(i-j)^2/2\kappa t}. \tag{E.74}$$

If we then normalize this by the total particle number, the result looks like pure diffusion:

$$C_{i,j}^{\text{free}}/\langle \hat{n}_i \rangle \langle \hat{n}_j \rangle \;\rightarrow\; -e^{-(i-j)^2/2\kappa t}, \tag{E.75}$$

which signifies a dynamical exponent $z = 2$. Instead, the spins appear to observe scaling collapse with a dynamical exponent of $z = 1.75$, signifying superdiffusive behavior.

E.9 Open Transverse Field Ising Model

In this Appendix, we will derive the mean field phase diagram for the open TFIM. The Hamiltonian and jump operators (as noted in the main text) ares given by

$$\hat{H} = \sum_i J\hat{\sigma}_i^x \hat{\sigma}_{i+1}^x + h\hat{\sigma}_i^z, \tag{E.76}$$

$$\hat{L}_i = \sqrt{\kappa}\hat{\sigma}_i^-. \tag{E.77}$$

This gives an equation of motion for the expectation of spin observables:

$$\partial_t \langle \hat{\sigma}_i^x \rangle = -h\langle \hat{\sigma}_i^y \rangle - \frac{\kappa}{2}\langle \hat{\sigma}_i^x \rangle, \tag{E.78}$$

$$\partial_t \langle \hat{\sigma}_i^y \rangle = -J\langle \hat{\sigma}_i^z \hat{\sigma}_{i+1}^x + \hat{\sigma}_i^z \hat{\sigma}_{i-1}^x \rangle + h\langle \hat{\sigma}_i^x \rangle - \frac{\kappa}{2}\langle \hat{\sigma}_i^y \rangle, \tag{E.79}$$

$$\partial_t \langle \hat{\sigma}_i^z \rangle = J\langle \hat{\sigma}_i^y \hat{\sigma}_{i+1}^x + \hat{\sigma}_i^y \hat{\sigma}_{i-1}^x \rangle - \kappa\left(\langle \hat{\sigma}_i^z \rangle - 1\right). \tag{E.80}$$

From here, we make the approximation that expectation values factor $\langle \hat{\sigma}_i^\alpha \hat{\sigma}_j^\beta \rangle = \langle \hat{\sigma}_i^\alpha \rangle \langle \hat{\sigma}_j^\beta \rangle$, and take the system to be translationally invariant. Then we get the new equations of motion

for $\sigma^{x,y,z}$ as

$$\partial_t \sigma^x = -h\sigma^y - \frac{\kappa}{2}\sigma^x, \tag{E.81}$$

$$\partial_t \sigma^y = h\sigma^x - 2J\sigma^x\sigma^z - \frac{\kappa}{2}\sigma^y, \tag{E.82}$$

$$\partial_t \sigma^z = 2J\sigma^x\sigma^y - \kappa(\sigma^z - 1). \tag{E.83}$$

There are two fixed points. The first is the trivial (paramagetic) phase when $\sigma^x = \sigma^y = 0, \sigma^z = 1$). We can solve for the other fixed point to find that

$$(\sigma^x)^2 = \frac{\kappa^2}{8J^2}\left(4hJ - 4h^2 - \kappa^2\right). \tag{E.84}$$

This value must be positive, which tells us the phase diagram. Define the scaled parameters $\tilde{h} = h/\kappa, \tilde{J} = J/\kappa$. Then we require that

$$\frac{\tilde{J} - \sqrt{\tilde{J}^2 - 1}}{2} \leq \tilde{h} \leq \frac{\tilde{J} + \sqrt{\tilde{J}^2 - 1}}{2}. \tag{E.85}$$

In the limit $\kappa \to 0$, then we have that $\tilde{J}^2 - 1 \sim \tilde{J}^2$, and we recover the closed system phase transition at $h = 0, J$. Note that we have assumed the sign of $h, J > 0$ here. However, local gauge transformations can move between different sectors, such that the system is ferromagnetic if h, J have the same sign, and antiferromagnetic if they have opposite sign. The phase diagram is shown in Fig. E.3.

In addition to the mean field phase diagram, we also show data for the unraveled entanglement entropy scaling with system size N in Fig. E.4.

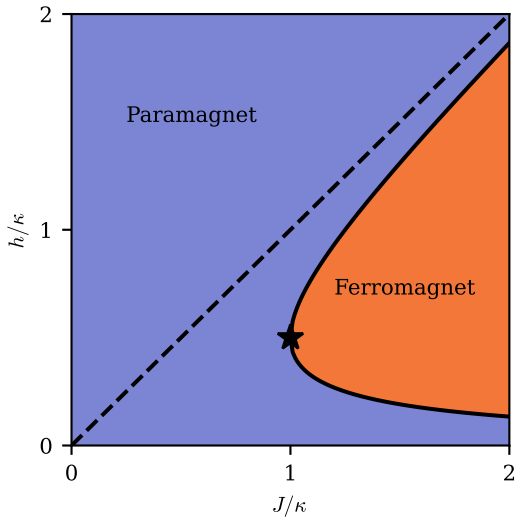

Figure E.3: Phase diagram for the mean field dissipative TFIM as defined in Eq. (E.85). The star marks the point $J = \kappa = 2h$ simulated in the main text Fig. 6.5. The solid black lines marks the phase boundary for the open system, and the dashed black line is $h = J$ the closed system phase boundary.

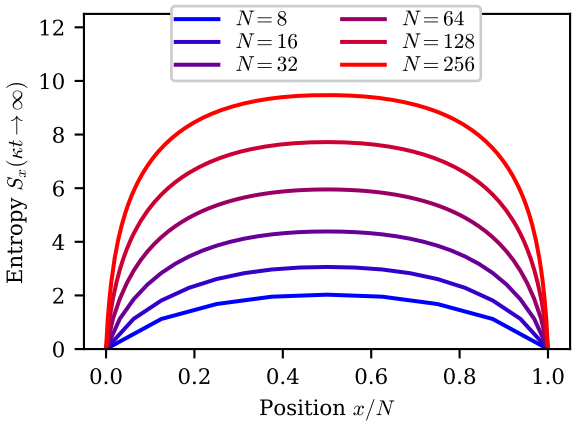

Figure E.4: Here, we plot the page curve for the parameter $h = J = \kappa$ as a function of system size from $N = 8$ to $N = 256$. We are showing the von Neumann entanglement entropy for each partition, averaged over 1000 trajectories.

E.10 Bipartite Entanglement Entropy of the Spin System

Here, we show that the bipartite entanglement entropy for certain bipartitions is independent of whether we calculate it for the spins or the fermions. To see this, let's first observe that the Jordan-Wigner transformation, when viewed as a map from density matrices to density matrices, is unitary. This can be done by picking a basis for both Hilbert spaces, and seeing that JW maps basis vectors to basis vectors. For the spins, this basis is the set of Pauli matrices:

$$\mathcal{B}_s = \{\hat{P}_1\hat{P}_2\dots\hat{P}_N|\hat{P}_i \in \{\hat{X},\hat{Y},\hat{Z},\hat{I}\}\}. \tag{E.86}$$

For fermions, we can likewise choose a basis of the set of Majorana operators:

$$\mathcal{B}_f = \{\gamma_1^{n_1}\hat{\gamma}_2^{n_2}\dots\hat{\gamma}_{2N}^{n_{2N}}|n_i \in \{0,1\}\}. \tag{E.87}$$

Now, if we ask how a generic operator in the basis $\mathcal{B}_s$ transforms under JW, we can simply note that

$$\hat{X}_i \to \left(\prod_{j=1}^{i-1} i\hat{\gamma}_{2j-1}\hat{\gamma}_{2j}\right)\hat{\gamma}_{2i-1}, \tag{E.88}$$

$$\hat{Y}_i \to \left(\prod_{j=1}^{i-1} i\hat{\gamma}_{2j-1}\hat{\gamma}_{2j}\right)\hat{\gamma}_{2i}, \tag{E.89}$$

$$\hat{Z}_i \to i\hat{\gamma}_{2i-1}\hat{\gamma}_{2i}. \tag{E.90}$$

Using the standard anticommutation relations for Majorana's, it is easy to see that any string of Pauli's can be rewritten in the canonical form of an element of $\mathcal{B}_f$ with unit norm. It thus suffices to show the map is surjective to show that this is a unitary map. However, this is also easy by noting that given an arbitrary element of $\mathcal{B}_f$ characterized by a set of

binary numbers $\{n_1, \ldots n_{2N}\}$, then we can write the Pauli string $\hat{P}$ which is it's preimage under JW as

$$\hat{P}_i = \left[\left(\prod_{j=1}^{i-1} \hat{Z}_j \right) \hat{X}_i \right]^{n_{2i-1}} \left[\left(\prod_{j=1}^{i-1} \hat{Z}_j \right) \hat{Y}_i \right]^{n_{2i}}, \tag{E.91}$$

$$\hat{P} = \hat{P}_1 \hat{P}_2 \ldots \hat{P}_N. \tag{E.92}$$

Hence, the map is a surjective map of basis vectors to basis vectors of equal dimension vector spaces, and is therefore unitary.

Specifically, this means that for any arbitrary density matrix, we can calculate any entanglement monotone from the spectrum of the density matrix, which is unchanged under unitary maps, and therefore is completely unchanged by the Jordan-Wigner transformation. This line of reasoning tells us that entanglement measures on the whole space (i.e. the full state purity) is unaffected by the Jordan-Wigner transform, but we also need to know whether it commutes with taking a partial trace.

As it turns out, for any arbitrary bi-partition of the system, there is no reason the entanglement of the fermions needs to match onto the spin system. However, let's suppose that we take a very special set of bipartitions defined by sets of lattice sites

$$A = \{i | 1 \leq i \leq m\}, \tag{E.93}$$

$$B = \{i | m < i \leq N\}, \tag{E.94}$$

such that $|A| = m, |B| = N - m$. These are perhaps the most natural bipartitions one can imagine taking, such that both subsystems are simply connected using open boundary conditions. Now, let's focus on the A subsystem. In order to understand its entropy, we

need to know about the reduced density matrix

$$\hat{\rho}_A = \text{tr}_B \hat{\rho}. \tag{E.95}$$

Now, we can construct a complete basis for this subspace

$$\mathcal{B}_{s,A} = \{\hat{P}_1 \hat{P}_2 \dots \hat{P}_m | \hat{P}_i \in \{\hat{X}, \hat{Y}, \hat{Z}, \hat{I}\}\}. \tag{E.96}$$

Since this is a basis, specifying the expectation value of these operators completely specifies the state $\hat{\rho}_A$, and thus the entanglement entropy. However, we can note that under the Jordan-Wigner transformation, we map the set

$$\mathcal{B}_{s,A} \to \mathcal{B}_{f,A}, \tag{E.97}$$

where

$$\mathcal{B}_{f,A} = \{\gamma_1^{n_1} \hat{\gamma}_2^{n_2} \dots \hat{\gamma}_{2m}^{n_{2m}} | n_i \in \{0, 1\}\}, \tag{E.98}$$

and so again on this restricted subspace, we are simply unitarily mapping basis vectors to basis vectors, and the full information of the spin reduced density matrix is completely contained in the fermionic reduced density matrix on the same sublattice. Thus, the two states have the same entanglement entropy, and we can calculate the fermionic one (which is much simpler since the state is Gaussian) in order to learn what the entanglement in the spin system is.

Note that this argument breaks down when A is not a simply connected subset, since the JW string would overlap with the complimentary subspace B, and so the total amount of information of the reduced spin system would be encoded in fermionic operators with support in both sublattices.

APPENDIX F

APPENDIX TO CHAPTER 7

F.1 Exact Dynamics for matchgate circuits with Pauli noise

We will be interested in both the continuous and discrete time evolution of a quantum state under matchgate circuits and local Pauli noise. Matchgate circuits will be defined as any unitary transformation on a set of spins that can be written as the exponential of a quadratic, fermionic Hamiltonian. For example, take a one-dimensional spin model with the following Hamiltonian:

$$\hat{H}(\vec{J},\vec{\tilde{J}},\vec{\Delta}) = \sum_j J_j \hat{\sigma}_j^+ \hat{\sigma}_{j+1}^- + \tilde{J}_j \hat{\sigma}_j^+ \hat{\sigma}_{j+1}^+ + \frac{\Delta_j}{2}\hat{\sigma}_j^z + \text{H. c.} \tag{F.1}$$

where the coefficients $J_j, \tilde{J}_j \in \mathbb{C}$ and $\Delta_j \in \mathbb{R}$ are arbitrary. Defining the set of canonical fermions

$$\hat{c}_j = \left(\prod_{i<j} \hat{\sigma}_i^z\right) \hat{\sigma}_j^-, \tag{F.2}$$

then in terms of the fermionic degrees of freedom, the Hamiltonian can be rewritten as

$$\hat{H}(\vec{J},\vec{\tilde{J}},\vec{\Delta}) = \sum_j J_j \hat{c}_j^\dagger \hat{c}_{j+1} + \tilde{J}_j \hat{c}_j^\dagger \hat{c}_{j+1}^\dagger + \Delta_j \hat{c}_j^\dagger \hat{c}_j + \text{H. c.} \tag{F.3}$$

and so any unitary

$$\hat{U}_\theta(\vec{J},\vec{\tilde{J}},\vec{\Delta}) = e^{i\theta \hat{H}(\vec{J},\vec{\tilde{J}},\vec{\Delta})}, \tag{F.4}$$

is an example of a matchgate. A matchgate circuit is one in which all unitary gates are compatible matchgates. This is in no way an exhaustive list of all possible matchgate circuits,

but it is one that is physically motivated (coming from the Hamiltonian of a 1D spin chain). Matchgate circuits can be efficiently simulated because they preserve the Gaussianity of fermionic states. That is to say, if the state begins as a Gaussian fermionic state, then it will remain a Gaussian fermionic state for all times under the circuit evolution. A Gaussian state is completely described by its covariance matrix. If one defines a set of Majorana modes

$$\hat{\gamma}_{2m} = \hat{c}_m + \hat{c}_m^\dagger, \qquad \hat{\gamma}_{2m+1} = i(\hat{c}_m - \hat{c}_m^\dagger), \tag{F.5}$$

then the covariance matrix is $\Gamma_{m,n} = \langle \hat{\gamma}_m \hat{\gamma}_n \rangle$. This is an antisymmetric matrix described by $N(2N-1)$ real coefficients if there are N spins in the problem. The dynamics of the covariance matrix can be computed in polynomial time, and so the dynamics are efficiently classically simulable. Interspersed in the matchgate circuit, we also consider Pauli noise. Pauli noise acts on the local qubit degrees of freedom via the Kraus channels:

$$\mathcal{K}[\hat{\rho}] = \sum_{s \in \{0,1\}^{2n}} p_s \hat{K}_s \hat{\rho} \hat{K}_s^\dagger, \tag{F.6}$$

$$\hat{K}_s = \sqrt{p_s} \prod_{i=0}^{n-1} (\hat{\sigma}_i^x)^{s_{2i}} (\hat{\sigma}_i^z)^{s_{2i+1}}, \tag{F.7}$$

where $\sum_s p_s = 1$.

At this point, we note that the given dynamics falls within the class of stochastically simulable dynamics given in Ref. [186]. This result implies that, while the Pauli noise does not preserve the Gaussianity of the density matrix, it maps the state to a convex sum of Gaussian states which can be efficiently sampled from to compute observables to fixed additive error. However, the special structure of the Pauli noise allows us to go one step further, and exactly re-average the stochastic equation of motion. To understand this, let's consider a single time step of first applying the matchgate circuit followed by the noise. We

have that

$$\hat{\rho} \mapsto \mathcal{M}[\hat{\rho}] \equiv \sum_s \hat{K}_s \hat{U} \hat{\rho} \hat{U}^\dagger \hat{K}_s^\dagger = \sum_s \operatorname{tr}(\hat{K}_s \hat{U} \hat{\rho} \hat{U}^\dagger \hat{K}_s^\dagger) \frac{\hat{K}_s \hat{U} \hat{\rho} \hat{U}^\dagger \hat{K}_s^\dagger}{\operatorname{tr}(\hat{K}_s \hat{U} \hat{\rho} \hat{U}^\dagger \hat{K}_s^\dagger)} = \sum_s N_s \hat{\rho}_s. \quad \text{(F.8)}$$

Here, we have defined the normalized states $\hat{\rho}_s$ and the normalization constants N_s which can depend on the state. For any fixed bitstring s, then $\hat{K}_s U$ maps Gaussian states to Gaussian states, and so it has an induced action on the set of fermionic covariance matrices. Let us define this implicit transformation by considering a Gaussian state $\hat{\rho}_\Gamma$ with covariance matix Γ:

$$\Gamma_{mn} = \operatorname{tr}(\hat{\rho}_\Gamma \hat{\gamma}_m \hat{\gamma}_n) \mapsto \sum_s N_s(\Gamma) \operatorname{tr}(\hat{\rho}_s(\Gamma) \hat{\gamma}_m \hat{\gamma}_n) \equiv \sum_s N_s(\Gamma) [\mathcal{K}_{s,\mathrm{cov}}(\Gamma)]_{mn}, \quad \text{(F.9)}$$

where the subscript "cov" denotes a transformation on the space of covariance matrices. Therefore, after a single time step, we have that

$$\Gamma \mapsto \mathcal{M}_{\mathrm{cov}}[\Gamma] = \sum_s p_s N_s \mathcal{K}_{s,\mathrm{cov}}[\Gamma] = \overline{\mathcal{K}}_{\mathrm{cov}}[\Gamma], \quad \text{(F.10)}$$

where the overline denotes averaging with respect to the probability distribution $\{N_s\}$. To understand the dynamics up to a time step t requires one to compute

$$\mathcal{M}_{\mathrm{cov}}^t = \overline{\mathcal{K}_{\mathrm{cov}}^t}. \quad \text{(F.11)}$$

Note that $\mathcal{M}_{\mathrm{cov}}$ is simple to compute, but the difficulty in computing its powers need not necessarily be simple if there are strong correlations different time steps. In general, computing powers of $\mathcal{M}$ can be done by stochastically sampling over trajectories (as is done in Ref. [186]). However, here is where Pauli noise becomes useful: because the channel is a convex sum of unitary transformations, we have that $N_s(\Gamma) = \xi_s$ is *independent of the state*. Therefore, there are no correlations between different time steps: i.e., $\overline{\mathcal{K}_{\mathrm{cov}}^t} = \left(\overline{\mathcal{K}_{\mathrm{cov}}}\right)^t$, and

so directly re-averaging the stochastic equations of motion become trivial.

Note that this is true for *arbitrary* Pauli strings, as for any Pauli string $\hat{P}$ we have that $\hat{P}^\dagger \hat{P} = 1$, and further that every Pauli string under JW maps to a Majorana string, which is a Gaussian unitary operator. Going forward, we will focus primarily on *local* Pauli channels as they are often the most physically relevant, but the results all hold for arbitrary Pauli channels.

F.1.1 Discrete time dynamics

Here, we will directly compute the evolution of the two point functions under local Pauli channels. For simplicity, we will assume the noise rates are spatially uniform, but this is not required and can be relaxed in an extremely straightforward manner.

The Kraus channel for each different type of Pauli noise are commuting, so we can calculate each of them independently. We will do this in two different methods. The first way is the one inspired by Ref. [186], where we consider the action of the strings on the fermionic two-point functions. Let's begin by defining the sign variables:

$$\eta_{i,j} = \begin{cases} 1 & i < j \\ -1 & i \geq j \end{cases}. \tag{F.12}$$

Recall the canonical Majorana modes defined in Eq. (F.5). Then we have that

$$\hat{\sigma}^x_j = \left(\prod_{i<j}(-1)^{\hat{n}_i}\right)(\hat{c}_j + \hat{c}^\dagger_j) = \left(\prod_{i<j} -i\hat{\gamma}_{2i}\hat{\gamma}_{2i+1}\right)\hat{\gamma}_{2j}, \tag{F.13}$$

$$\hat{\sigma}^y_j = \left(\prod_{i<j}(-1)^{\hat{n}_i}\right) i(\hat{c}_j - \hat{c}^\dagger_j) = \left(\prod_{i<j} -i\hat{\gamma}_{2i}\hat{\gamma}_{2i+1}\right)\hat{\gamma}_{2j+1}, \tag{F.14}$$

$$\hat{\sigma}^z_j = 2\hat{c}^\dagger_j\hat{c}_j - 1 = i\hat{\gamma}_{2j}\hat{\gamma}_{2j+1}. \tag{F.15}$$

Clearly, z-noise is the simplest, as it does not have JW strings. If we define the z-type channel $\mathcal{K}_{i,z}$ to be the induced covariance matrix transformation under $\hat{\rho} \mapsto p_z \hat{\sigma}_i^z \hat{\rho} \hat{\sigma}_i^z + (1-p_z)\hat{\rho}$ and then define $\mathcal{K}_z = \prod_i \mathcal{K}_{i,z}$ we find that

$$\begin{aligned}
&\Gamma_{mn} \mapsto (\mathcal{K}_{j,z,\mathrm{cov}}[\Gamma])_{mn} \\
&\quad = p_z \langle (i\hat{\gamma}_{2j}\hat{\gamma}_{2j+1})\hat{\gamma}_m\hat{\gamma}_n(i\hat{\gamma}_{2j}\hat{\gamma}_{2j+1})\rangle_\Gamma + (1-p_z)\Gamma_{mn} \\
&\quad = p_z \left[4\delta_{2j,m}\delta_{2j+1,n} + 4\delta_{2j,n}\delta_{2j+1,m} - 2\delta_{2j,m} - 2\delta_{2j+1,m} - 2\delta_{2j,n} - 2\delta_{2j+1,n} + 1\right]\Gamma_{mn} \\
&\qquad + (1-p_z)\Gamma_{mn}.
\end{aligned} \tag{F.16}$$

This simplifies to

$$\implies (\mathcal{K}_{z,\mathrm{cov}}[\Gamma])_{mn} = \Gamma_{mn} \times \begin{cases} 1 & \lfloor m/2 \rfloor = \lfloor n/2 \rfloor \\ (1-2p_z)^2 & \text{otherwise} \end{cases}. \tag{F.17}$$

For x- and y- type noise, we will see extremely different behavior. Consider x-noise now, given by

$$\begin{aligned}
(\mathcal{K}_{j,x,\mathrm{cov}}[\Gamma])_{mn} &= p_x \left\langle \hat{\gamma}_{2j} \left(\prod_{i<j} -i\hat{\gamma}_{2i}\hat{\gamma}_{2i+1} \right) \hat{\gamma}_m\hat{\gamma}_n \left(\prod_{i<j} -i\hat{\gamma}_{2i}\hat{\gamma}_{2i+1} \right) \hat{\gamma}_{2j} \right\rangle_\Gamma + (1-p_x)\Gamma_{mn} \\
&= p_x \eta_{j,\lfloor m/2 \rfloor}\eta_{j,\lfloor n/2 \rfloor} \langle \hat{\gamma}_{2j}\hat{\gamma}_m\hat{\gamma}_n\hat{\gamma}_{2j}\rangle_\Gamma + (1-p_x)\Gamma_{mn} \\
&= \left[p_x \eta_{j,\lfloor m/2 \rfloor}\eta_{j,\lfloor n/2 \rfloor}(1 - 2\delta_{2j,m} - \delta_{2j,n}) + (1-p_x)\right]\Gamma_{mn}.
\end{aligned} \tag{F.18}$$

If we assume that $m < n$ (the remaining covariances can be found using the skew-symmetry of the covariance matrix), and define $m_2 = m \mod 2$ and vice versa for n_2, then:

$$(\mathcal{K}_{x,\mathrm{cov}}[\Gamma])_{mn} = \Gamma_{mn} \times \begin{cases} (1-2p_x)^{|\lfloor m/2 \rfloor - \lfloor n/2 \rfloor| - m_2 + n_2} & |\lfloor m/2 \rfloor - \lfloor n/2 \rfloor| > 1 \\ (1-2p_x) & |\lfloor m/2 \rfloor - \lfloor n/2 \rfloor| = 0 \end{cases}. \tag{F.19}$$

A similar calculation gives that

$$(\mathcal{K}_{y,\mathrm{cov}}[\Gamma])_{mn} = \Gamma_{mn} \times \begin{cases} (1-2p_y)^{|\lfloor m/2\rfloor - \lfloor n/2\rfloor| + m_2 - n_2} & |\lfloor m/2\rfloor - \lfloor n/2\rfloor| > 1 \\ (1-2p_y) & |\lfloor m/2\rfloor - \lfloor n/2\rfloor| = 0 \end{cases}. \quad \text{(F.20)}$$

Putting these results together, for example if we take an infinite temperature reservoir with Kraus channels given by equal probability of exciting or de-exciting each spin (which is modeled by equal decoherence in the X and Y direction) as considered in Chapter 7, we find that

$$(\mathcal{K}_{x,\mathrm{cov}}[\mathcal{K}_{y,\mathrm{cov}}[\Gamma]])_{mn} = \Gamma_{mn} \times \begin{cases} (1-2p)^{2|\lfloor m/2\rfloor - \lfloor n/2\rfloor|} & |\lfloor m/2\rfloor - \lfloor n/2\rfloor| > 1 \\ (1-2p)^{2(1-\delta_{mn})} & |\lfloor m/2\rfloor - \lfloor n/2\rfloor| = 0 \end{cases}, \quad \text{(F.21)}$$

where $p = p_x = p_y$. For complete depolarizing noise, we have that

$$(\mathcal{K}_{z,\mathrm{cov}}[\mathcal{K}_{x,\mathrm{cov}}[\mathcal{K}_{y,\mathrm{cov}}[\Gamma]]])_{mn} = \Gamma_{mn} \times (1-2p)^{2(|\lfloor m/2\rfloor - \lfloor n/2\rfloor| + 1 - \delta_{mn})}, \quad \text{(F.22)}$$

where $p = p_x = p_y = p_z$.

A much simpler way to compute the two point functions is to, instead of working in terms of the fermion variables, note that they can be written in terms of Pauli strings. We have that (for $m < n$)

$$\Gamma_{2m,2n} = i\langle \hat{Y}_m \hat{Z}_{m+1} \dots \hat{Z}_{n-1} \hat{X}_n \rangle, \quad \text{(F.23a)}$$

$$\Gamma_{2m,2n+1} = i\langle \hat{Y}_m \hat{Z}_{m+1} \dots \hat{Z}_{n-1} \hat{Y}_n \rangle, \quad \text{(F.23b)}$$

$$\Gamma_{2m+1,2n} = i\langle \hat{X}_m \hat{Z}_{m+1} \dots \hat{Z}_{n-1} \hat{X}_n \rangle, \quad \text{(F.23c)}$$

$$\Gamma_{2m+1,2n+1} = i\langle \hat{X}_m \hat{Z}_{m+1} \dots \hat{Z}_{n-1} \hat{Y}_n \rangle. \quad \text{(F.23d)}$$

From here, it is simple to simply note that Pauli strings are mapped to themselves under

Pauli channels, and then count the number operators that anticommute to get the correct prefactors. This completely recovers the previous result, though does not immediately elucidate the convex sum of Gaussians structure.

F.1.2 Continuous time dynamics

We can similarly define the continuous time dynamics one would obtain by considering, for example, the limit $p_{x,y,z} = \gamma_{x,y,z}\ \mathrm{d}t$ as $\mathrm{d}t \to 0$. This gives Lindblad dynamics

$$\partial_t \hat{\rho} = \sum_i \sum_{\alpha \in \{x,y,z\}} \gamma_\alpha \mathcal{D}[\hat{\sigma}_i^\alpha]\hat{\rho}. \tag{F.24}$$

This induces the dynamics on the covariance matrix

$$\partial_t \Gamma_{mn} = -(\gamma_1 |\lfloor m/2 \rfloor - \lfloor n/2 \rfloor| + \gamma_2)\Gamma_{mn}, \tag{F.25}$$

$$\gamma_1 = \gamma_x + \gamma_y, \tag{F.26}$$

$$\gamma_2 = (1 - \delta_{\lfloor m/2 \rfloor, \lfloor n/2 \rfloor})(2\gamma_z + (\gamma_x - \gamma_y)(n_2 - m_2)) + \delta_{\lfloor m/2 \rfloor, \lfloor n/2 \rfloor}(1 - \delta_{mn})(\gamma_x + \gamma_y), \tag{F.27}$$

where we have re-used the variables $m_2 = m \mod 2, n_2 = n \mod 2$. Note again that if $\gamma_x = \gamma_y = \gamma_z = \gamma$, we have the simplification $\gamma_1 = 2\gamma, \gamma_2 = 2\gamma(1 - \delta_{mn})$.

F.1.3 Non-Gaussianity and violation of Wick's theorem

Here, we show that the state is able to massively violate Wick's theorem despite the fact that the dynamics of moments close on themselves. To see this, let's try and calculate the connected correlation function $\langle\langle \hat{\sigma}_m^z \hat{\sigma}_n^z \rangle\rangle \equiv \langle \hat{\sigma}_m^z \hat{\sigma}_n^z \rangle - \langle \hat{\sigma}_m^z \rangle \langle \hat{\sigma}_n^z \rangle$ in two ways, once using the full dynamics, and once using Wick's theorem, and compare the two. Under the XY noise channel, this observable (being a Pauli) evolves extremely simply and the dynamics

are described by

$$\langle\langle \hat{\sigma}_m^z \hat{\sigma}_n^z \rangle\rangle(t) = e^{-2\gamma t} \langle\langle \hat{\sigma}_m^z \hat{\sigma}_n^z \rangle\rangle(0). \tag{F.28}$$

Alternatively, if we instead were to pretend that the state was Gaussian for all times, then we could use Wick's theorem, and ask how well we do in predicting observables. This would give us

$$\begin{aligned}
\langle\langle \hat{\sigma}_m^z \hat{\sigma}_n^z \rangle\rangle_W(t) &= -\langle \hat{\gamma}_{2m} \hat{\gamma}_{2m+1} \hat{\gamma}_{2n} \hat{\gamma}_{2n+1} \rangle_W(t) + \langle \hat{\gamma}_{2m} \hat{\gamma}_{2m+1} \rangle(t) \langle \hat{\gamma}_{2n} \hat{\gamma}_{2n+1} \rangle(t) \\
&= \langle \hat{\gamma}_{2m} \hat{\gamma}_{2n} \rangle(t) \langle \hat{\gamma}_{2m+1} \hat{\gamma}_{2n+1} \rangle(t) - \langle \hat{\gamma}_{2m} \hat{\gamma}_{2n+1} \rangle(t) \langle \hat{\gamma}_{2m+1} \hat{\gamma}_{2n} \rangle(t) \\
&= e^{-4\gamma |m-n| t} \langle\langle \hat{\sigma}_m^z \hat{\sigma}_n^z \rangle\rangle(0),
\end{aligned} \tag{F.29}$$

where the subscript W denotes we use Wick's theorem to evaluate the 4 point correlation functions. Note that this differs *exponentially* from the actual result, and so Wick's theorem fails catastrophically to evaluate the dynamics for lattice sites with large spatial separation.

To understand intuitively what is going on, it is useful to consider again the exact form of the density matrix $\hat{\rho}$ as a function of time. We can write $\hat{\rho}$ as

$$\hat{\rho} = \sum_{\vec{s} \in \{0,1\}^{2N}} p_s |\Gamma_{\vec{s}}\rangle \langle \Gamma_{\vec{s}}|, \tag{F.30}$$

$$p_s = p^s (1-p)^s, \quad p = \frac{1}{2}(1 - e^{-\gamma t/2}). \tag{F.31}$$

Here, $p_{\vec{s}}$ is a classical probability distribution, $s = |\vec{s}|_1$ its 1-norm, and $|\Gamma_{\vec{s}}\rangle$ is a Gaussian

state with a covariance matrix $\Gamma_{\vec{s}}$. This covariance matrix is defined by

$$\Gamma_{\vec{s}} = \left(\prod_{i=1}^{2N} U_i^{s_i}\right) \Gamma_0 \left(\prod_{i=1}^{2N} U_i^{s_i}\right)^\dagger, \tag{F.32}$$

$$(U_{2i})_{mn} = \delta_{mn}(2\Theta(m - 2i + 0.5) - 1), \tag{F.33}$$

$$(U_{2i+1})_{mn} = \delta_{mn}(2\Theta(m - 2i - 0.5) - 2\delta_{m,2i+2} - 1), \tag{F.34}$$

where Γ_0 is the initial fermionic covariance matrix in terms of the Majorana modes. Essentially, each matrix U_{2i}/U_{2i+1} multiplies the coherences between operators on either side of the lattice site i by a sign. Now, when two lattice sites are very far away, there are many locations one can insert minus signs, giving the emergent length scale. However, note that when we look at something that depends quadratically on the covariance matrix (e.g. the 4 point functions), then all of the minus signs cancel out. We can see this in action by once more calculating the connected correlation function, but this time use the actual representation of the fermionic state. We wish to know

$$\begin{aligned}
\langle \hat{\sigma}_m^z \hat{\sigma}_n^z \rangle = &\ \mathrm{tr}(\hat{\gamma}_{2m}\hat{\gamma}_{2m+1}\hat{\gamma}_{2n}\hat{\gamma}_{2n+1}\hat{\rho}) \\
&= \sum_{\vec{s}} p_s \langle \Gamma_{\vec{s}} | \hat{\gamma}_{2m}\hat{\gamma}_{2m+1}\hat{\gamma}_{2n}\hat{\gamma}_{2n+1} | \Gamma_{\vec{s}} \rangle \\
&= \sum_{\vec{s}} p_s \left[(\Gamma_{\vec{s}})_{2m,2m+1}(\Gamma_{\vec{s}})_{2n,2n+1} + (\Gamma_{\vec{s}})_{2m,2n+1}(\Gamma_{\vec{s}})_{2m+1,2n} - (\Gamma_{\vec{s}})_{2m,2n}(\Gamma_{\vec{s}})_{2m+1,2n+1} \right],
\end{aligned} \tag{F.35}$$

where $\vec{s} \in \{0,1\}^{2N}$. From here, we note that the *product* of two covariance matrix elements only picks up a sign if exactly one of them did. The only way this occurs is if, considering only the four elements $s_{2m}, s_{2m+1}, s_{2n}, s_{2n+1}$, then an odd number of them are positive.

Since these are the only relevant terms, we can simplify the problem significantly to:

$$\begin{aligned}\langle\hat{\sigma}_m^z\hat{\sigma}_n^z\rangle &= \sum_{\vec{s}\in\{0,1\}^4} p_s\left[(\Gamma_{\vec{s}})_{2m,2m+1}(\Gamma_{\vec{s}})_{2n,2n+1}+(\Gamma_{\vec{s}})_{2m,2n+1}(\Gamma_{\vec{s}})_{2m+1,2n}\right]\\ &\quad-\sum_{\vec{s}\in\{0,1\}^4} p_s(\Gamma_{\vec{s}})_{2m,2n}(\Gamma_{\vec{s}})_{2m+1,2n+1}\\ &=\left(\sum_{\vec{s}\in\{0,1\}^4,|\vec{s}|_2=0} p_s-\sum_{\vec{s}\in\{0,1\}^4,|\vec{s}|_2=1} p_s\right)\langle\hat{\gamma}_{2m}\hat{\gamma}_{2m+1}\hat{\gamma}_{2n}\hat{\gamma}_{2n+1}\rangle_{t=0}\\ &=e^{-2\gamma t}\langle\hat{\gamma}_{2m}\hat{\gamma}_{2m+1}\hat{\gamma}_{2n}\hat{\gamma}_{2n+1}\rangle_{t=0},\end{aligned} \tag{F.36}$$

where we have defined $|\vec{s}|_2$ to be the Hamming weight of the bitstring $\vec{s}$ modulo 2. We can clearly see that the fact that the covariances matrices add incoherently means that, while there can destructive interference when calculating the average two-point functions, it can also go away when calculating higher point correlators and so Wick's theorem tends to not hold even approximately.

F.1.4 Periodic boundary conditions

There is some subtlety that comes from periodic boundary conditions, as the Hamiltonian does not map to a completely free model under the JW transformation. The problem lies in the fact that to connect the lattice sites 1 and N picks up a JW string equivalent to the total parity of the state:

$$\hat{H}_{\text{PBC}}(\vec{J},\vec{\tilde{J}},\vec{\Delta})=J_N\hat{\sigma}_N^+\hat{\sigma}_1^-+\tilde{J}_N\hat{\sigma}_N^+\hat{\sigma}_1^++\sum_{j=1}^{N-1}J_j\hat{\sigma}_j^+\hat{\sigma}_{j+1}^-+\tilde{J}_j\hat{\sigma}_j^+\hat{\sigma}_{j+1}^++\sum_{j=1}^{N}\frac{\Delta_j}{2}\hat{\sigma}_j^z+\text{H. c.} \tag{F.37}$$

Now, when doing JW, this becomes:

$$\hat{H}_{\mathrm{PBC}}(\vec{J},\vec{\tilde{J}},\vec{\Delta}) = -\left[J_N \hat{c}_N^\dagger \hat{c}_1^- + \tilde{J}_N \hat{c}_N^\dagger \hat{c}_1^\dagger\right]\hat{\Pi} + \sum_{j=1}^{N-1} J_j \hat{c}_j^\dagger \hat{c}_{j+1} + \tilde{J}_j \hat{c}_j^\dagger \hat{c}_{j+1}^\dagger + \sum_{j=1}^{N} \Delta_j \hat{c}_j^\dagger \hat{c}_j + \mathrm{H.\,c.} \tag{F.38}$$

where we have defined the total parity operator $\hat{\Pi} = \prod_{j=1}^{N}(-1)^{\hat{n}_j}$. Recall that $\hat{\Pi}$ is the generator of a weak $\mathbb{Z}_2$ symmetry (as fermions must obey superselection rules), and so we have that

$$[\hat{H}_{\mathrm{PBC}}, \hat{\Pi}] = 0. \tag{F.39}$$

This means that the Hamiltonian can be decomposed as a direct sum of $\hat{\Pi}$ eigenspaces

$$\hat{H}_{\mathrm{PBC}}^{\pm} = \mp\left[J_N \hat{c}_N^\dagger \hat{c}_1^- + \tilde{J}_N \hat{c}_N^\dagger \hat{c}_1^\dagger\right] + \sum_{j=1}^{N-1} J_j \hat{c}_j^\dagger \hat{c}_{j+1} + \tilde{J}_j \hat{c}_j^\dagger \hat{c}_{j+1}^\dagger + \sum_{j=1}^{N} \Delta_j \hat{c}_j^\dagger \hat{c}_j + \mathrm{H.\,c.}, \tag{F.40}$$

where the parity is replaced with its expectation value. Now, both $\hat{H}_{\mathrm{PBC}}^{\pm}$ are quadratic, and so their dynamics can be efficiently simulated. For a state with positive parity, one should evolve it under $\hat{H}_{\mathrm{PBC}}^{+}$ and vice-versa for odd parity states. Now, we note that the jumps always map a state with fixed parity to another state with fixed parity, as

$$\hat{\Pi}\hat{\sigma}_i^\alpha = \lambda_\alpha \hat{\sigma}_i^\alpha \hat{\Pi}, \quad \lambda_x = \lambda_y = -1, \lambda_z = 1. \tag{F.41}$$

Therefore, it tells us that under these dynamics the state will always be an incoherent mixture of different parity sectors. Thus, one can write the state as

$$\hat{\rho} = \hat{\rho}_+ + \hat{\rho}_- = \sum_{\Gamma_+} p(\Gamma_+)|\Gamma_+\rangle\langle\Gamma_+| + \sum_{\Gamma_-} p(\Gamma_-)|\Gamma_-\rangle\langle\Gamma_-|, \tag{F.42}$$

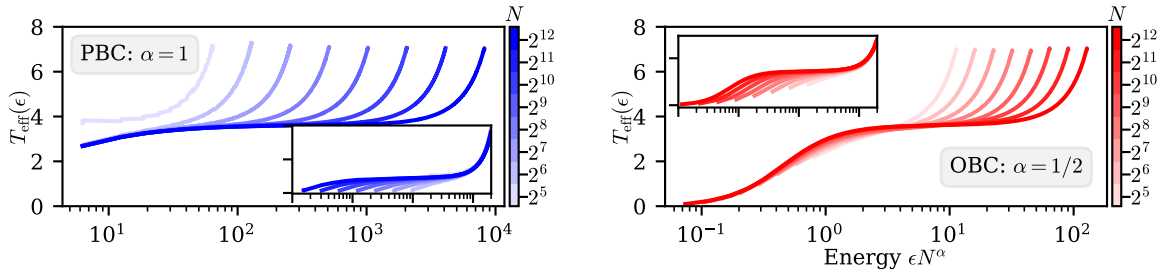

Figure F.1: Effective temperature for both periodic (upper) and open (lower) boundary conditions at the critical point with $J = g = \gamma = 1$ at time $t = 1$. We consider system sizes from $N = 32$ to $N = 4096$. The horizontal energy axis is rescaled by N^{α}, where $\alpha = 1/2$ for open boundary conditions and $\alpha = 1$ for closed boundary conditions. Inset: same data as main plot without rescaling ($\alpha = 0$).

where subscripts $+, -$ refer to even or odd states, respectively. The density matrices $\hat{\rho}_+, \hat{\rho}_-$ are each independently convex sums of either even or odd pure Gaussian states described by covariances $\Gamma_{+,-}$. The total covariance matrix of the state $\hat{\rho}$ is given by

$$\text{tr}(\hat{\rho}\hat{\gamma}_m\hat{\gamma}_n) = \sum_{\Gamma_+} p(\Gamma_+)(\Gamma_+)_{m,n} + \sum_{\Gamma_-} p(\Gamma_-)(\Gamma_-)_{m,n} \tag{F.43}$$

and similarly for higher moments. As for the dynamics, only the quantum jumps can change the parity of the state, and so the coherent dynamics are extremely simple:

$$\partial_t \hat{\rho}_\pm = -i[\hat{H}^{\pm}_{\text{PBC}}, \hat{\rho}_\pm] \tag{F.44}$$

The noise, though, will mix the sectors in an incoherent fashion:

$$\partial_t \langle \hat{\gamma}_m \hat{\gamma}_n \rangle_\pm = \sum_{\alpha=x,y} \sum_{j=1}^{N} \gamma_\alpha \left(\langle \hat{\sigma}^\alpha_j \hat{\gamma}_m \hat{\gamma}_n \hat{\sigma}^\alpha_j \rangle_\mp - \langle \hat{\gamma}_m \hat{\gamma}_n \rangle_\pm \right) + \sum_{j=1}^{N} \gamma_z \left(\langle \hat{\sigma}^z_j \hat{\gamma}_m \hat{\gamma}_n \hat{\sigma}^z_j \rangle_\pm - \langle \hat{\gamma}_m \hat{\gamma}_n \rangle_\pm \right) \tag{F.45}$$

where subscripts refer to taking expectation values with respect to either the even or odd parity sectors. What this means is that by keeping track of two different covariance matrices, one can evolve the system with periodic boundary conditions. In principle, this result is more general than just PBC. Anytime there is a model with a weak symmetry generator $\hat{G}$, and the Hamiltonian is interacting in the form $\hat{H} = \hat{H}_0 + \hat{H}_1\hat{G}$ where both $\hat{H}_0$ and $\hat{H}_1$ are free, then this would work, where one needs to keep track of as many covariance matrices as there are eigenspaces of $\hat{G}$.

In Fig. F.1, we recreate the data in Fig. 7.5 for both open and periodic boundary conditions at $\gamma t = 1$. We find that while periodic boundary conditions converge at low energies like $1/N$, for periodic boundary conditions it only converges at $1/\sqrt{N}$, and so there is value in using periodic boundary conditions as it converges significantly more quickly with large system sizes.

F.2 Ising Model Results

To set the stage, let's define the Ising model Hamiltonian as

$$\hat{H} = \sum_i -J\hat{\sigma}_i^x\hat{\sigma}_{i+1}^x + g\hat{\sigma}_i^z. \tag{F.46}$$

The Hamiltonian can be rewritten as a quadratic form of the free fermion modes:

$$\begin{aligned}\hat{H} &= \sum_i -J(\hat{\sigma}_i^+ + \hat{\sigma}_i^-)(\hat{\sigma}_{i+1}^+ + \hat{\sigma}_{i+1}^-) + g(2\hat{\sigma}_i^+\hat{\sigma}_i^- - 1) \\ &= \sum_i -J(\hat{c}_i^\dagger - \hat{c}_i)(\hat{c}_{i+1}^\dagger + \hat{c}_{i+1}) + g(2\hat{c}_i^\dagger\hat{c}_i - 1).\end{aligned} \tag{F.47}$$

If we now define the set of Fourier modes $\hat{d}_k = \sum_j e^{ijk}\hat{c}_j$, then this becomes

$$\hat{H} = \sum_k -2J\cos(k)\hat{d}_k^\dagger \hat{d}_k + iJ\sin(k)(\hat{d}_k\hat{d}_{-k} + \hat{d}_k^\dagger \hat{d}_{-k}^\dagger) + g(2\hat{d}_k^\dagger \hat{d}_k - 1). \tag{F.48}$$

This is almost diagonal, up to the fact that there is mixing between modes at $\pm k$. To solve this, we will implement a Bogoliubov transformation defined via the modes

$$\hat{\beta}_k = \cos(\theta_k/2)\hat{d}_k + i\sin(\theta_k/2)\hat{d}_{-k}^\dagger. \tag{F.49}$$

Note that this implies

$$\sum_k \epsilon_k \hat{\beta}_k^\dagger \hat{\beta}_k = \sum_k \epsilon_k \left[\cos(\theta_k)\hat{d}_k^\dagger \hat{d}_k + \sin^2(\theta_k/2) + i/2\sin(\theta_k)(\hat{d}_k^\dagger \hat{d}_{-k}^\dagger - \hat{d}_{-k}\hat{d}_k)\right]. \tag{F.50}$$

From here, we can directly read out that

$$\epsilon_k\cos(\theta_k) = -2J\cos(k) + 2g, \qquad \epsilon_k\sin(\theta_k) = 2J\sin(k). \tag{F.51}$$

$$\implies \epsilon_k = 2J\sqrt{(\cos(k) - g/J)^2 + \sin^2(k)}, \tag{F.52}$$

$$\implies \theta_k = \arctan\left(\frac{\sin(k)}{g/J - \cos(k)}\right), \tag{F.53}$$

as discussed in Chapter 7. Here and henceforth, we will work in units where $J = 1$, so the phase transition occurs at $g = 1$. We can use this form to calculate the ground state expectation value of observables by noting that, since every mode is defined as having positive

energy they are all in vacuum in the ground state. Hence

$$\begin{aligned}
\langle \hat{c}_m^\dagger \hat{c}_n \rangle_{\mathrm{GS}} &= \frac{1}{N}\sum_k e^{ik(m-n))} \langle \hat{d}_k^\dagger \hat{d}_k \rangle \\
&= \frac{1}{N}\sum_k e^{ik(m-n))} \langle (\cos(\theta_k/2)\hat{\beta}_k^\dagger + i\sin(\theta_k/2)\hat{\beta}_{-k})(\cos(\theta_k/2)\hat{\beta}_k - i\sin(\theta_k/2)\hat{\beta}_{-k}^\dagger) \rangle \\
&= \frac{1}{N}\sum_k e^{ik(m-n)} \sin^2(\theta_k/2) = \frac{1}{2}\delta_{mn} - \frac{1}{2N}\sum_k e^{ik(m-n)} \cos(\theta_k) \\
&= \frac{1}{2}\delta_{mn} - \frac{1}{2}\mathcal{F}_{\cos\theta}(m-n), \qquad \text{(F.54)}
\end{aligned}$$

where we have defined the Fourier transform of $\cos(\theta_k)$ to be $\mathcal{F}_{\cos\theta}$. A similar calculation tells us that

$$\langle \hat{c}_m \hat{c}_n \rangle_{\mathrm{GS}} = -\frac{i}{2}\mathcal{F}_{\sin\theta}(m-n). \qquad \text{(F.55)}$$

Exactly at the phase transition, these can be evaulated exactly as the form of θ_k becomes significantly simpler. When $g = J$,

$$\theta_k = \begin{cases} \frac{\pi}{2} - \frac{k}{2} & 0 < k < \pi \\ -\frac{\pi}{2} - \frac{k}{2} & -\pi < k < 0 \end{cases}. \qquad \text{(F.56)}$$

This gives us the following results

$$\begin{aligned}
\mathcal{F}_{\cos\theta}(d) &= \frac{1}{N}\sum_k e^{ikd}\cos(\theta_k) = \frac{1}{N}\sum_k e^{ikd}|\sin(k/2)| \\
&\sim \frac{1}{2\pi}\int_{-\pi}^{\pi} e^{ikd}|\sin(k/2)| = \frac{1}{\pi}\frac{2}{1-4d^2}, \qquad \text{(F.57)} \\
\mathcal{F}_{\sin\theta}(d) &= \frac{1}{N}\sum_k e^{ikd}\sin(\theta_k) = \frac{1}{N}\sum_k e^{ikd}\mathrm{sgn}(k)\cos(k/2) \\
&\sim \frac{1}{2\pi}\int_{-\pi}^{\pi} e^{ikd}\mathrm{sgn}(k)\cos(k/2) = -\frac{i}{\pi}\frac{4d}{1-4d^2}, \qquad \text{(F.58)}
\end{aligned}$$

which gives, as expected, algebraically decaying correlations at the phase transition. It is worthwhile to note that the cause of the algebraic decay is exactly due to the non-analytic behavior of θ_k at the phase transition. When it behaves smoothly (and similarly $\cos(\theta), \sin(\theta)$ are smooth), then the correlations functions are the Fourier transform of a smooth function which necessarily must decay faster than any polynomial.

F.2.1 Quasiparticle number in time

Here, we will derive the full time dynamics for the energy-resolved quasiparticle numbers in time under the noise. Using the results from the XY channel derived earlier, we have that

$$\begin{aligned}
\langle \hat{c}_m^\dagger \hat{c}_n \rangle(t) &= e^{-\gamma|m-n|t-\delta_{mn}\gamma t}\langle \hat{c}_m^\dagger \hat{c}_n \rangle(0) + \frac{1}{2}\delta_{mn}(1-e^{-\gamma t}) \\
&= e^{-\gamma|m-n|t-\delta_{mn}\gamma t}\left(\frac{1}{2}\delta_{mn} - \frac{1}{2}\mathcal{F}_{\cos\theta}(m-n)\right) + \frac{1}{2}\delta_{mn}(1-e^{-\gamma t}) \\
&= -\frac{1}{2}e^{-\gamma|m-n|t-\delta_{mn}\gamma t}\mathcal{F}_{\cos\theta}(m-n) + \frac{1}{2}\delta_{mn}. \qquad \text{(F.59)} \\
\langle \hat{c}_m \hat{c}_n \rangle(t) &= e^{-\gamma|m-n|t}\langle \hat{c}_m \hat{c}_n \rangle(0) = -\frac{i}{2}e^{-\gamma|m-n|t}\mathcal{F}_{\sin\theta}(m-n). \qquad \text{(F.60)}
\end{aligned}$$

From here, we can compute that

$$\begin{aligned}
n_k(t) &= \langle \hat{\beta}_k^\dagger \hat{\beta}_k \rangle(t) = \langle \cos(\theta_k) \hat{d}_k^\dagger \hat{d}_k + \sin^2(\theta_k/2) + i/2 \sin(\theta_k)(\hat{d}_k^\dagger \hat{d}_{-k}^\dagger - \hat{d}_{-k}\hat{d}_k)\rangle(t) \\
&= \frac{1}{N}\sum_{mn} e^{-ik(m-n)} \left\langle \cos(\theta_k)\hat{c}_m^\dagger \hat{c}_n + \sin^2(\theta_k/2) + i/2\sin(\theta_k)(\hat{c}_m^\dagger \hat{c}_n^\dagger - \hat{c}_m \hat{c}_n)\right\rangle(t) \\
&= \sin^2(\theta_k/2) + \frac{1}{N}\sum_{mn} e^{-ik(m-n)} \cos(\theta_k)\langle \hat{c}_m^\dagger \hat{c}_n\rangle(t) - ie^{-ik(m-n)}\sin(\theta_k)\langle \hat{c}_m \hat{c}_n\rangle(t) \\
&= \frac{1}{2} - \frac{1}{2N}\sum_{mn} e^{-ik(m-n)-|m-n|\gamma t - \delta_{mn}\gamma t}\cos(\theta_k)\mathcal{F}_{\cos\theta}(m-n) \\
&\quad - \frac{1}{2N}\sum_{mn} e^{-ik(m-n)-|m-n|\gamma t}\sin(\theta_k)\mathcal{F}_{\sin\theta}(m-n) \\
&= \frac{1}{2} - \frac{1}{2}e^{-\gamma t}\cos(\theta_k)\mathcal{F}_{\cos\theta}(0) - \frac{1}{2}\sum_{d\neq 0} e^{-ikd-|d|\gamma t}\cos(\theta_k)\mathcal{F}_{\cos\theta}(d) \\
&\quad - \frac{1}{2}\sum_{d\neq 0} e^{-ikd-|d|\gamma t}\sin(\theta_k)\mathcal{F}_{\sin\theta}(d) \\
&= \frac{1}{2} - \frac{1}{2}e^{-\gamma t}\cos(\theta_k)\mathcal{F}_{\cos\theta}(0) - \sum_{d=1}^{\infty} e^{-d\gamma t}\cos(kd)\cos(\theta_k)\mathcal{F}_{\cos\theta}(d) \\
&\quad + i\sum_{d=1}^{\infty} e^{-d\gamma t}\sin(kd)\sin(\theta_k)\mathcal{F}_{\sin\theta}(d).
\end{aligned} \tag{F.61}$$

This gives the general result for the quasiparticle number under the decoherence channel. If we restrict ourself to considering the quasiparticle number starting from the critical ground state, we can further simplify this expression. Using Eqs. (F.57) and (F.58), we have that

$$\begin{aligned}
n_k(t) &= \frac{1}{2} - \frac{1}{\pi}e^{-\gamma t}|\sin(k/2)| - \frac{\mathrm{sgn}(k)}{\pi}\sum_{d=1}^{\infty} e^{-d\gamma t}\cos(kd)\sin(k/2)\frac{2}{1-4d^2} \\
&\quad + \frac{\mathrm{sgn}(k)}{\pi}\sum_{d=1}^{\infty} e^{-d\gamma t}\sin(kd)\cos(k/2)\frac{4d}{1-4d^2} \\
&= \frac{1}{2} + \frac{1}{\pi}|\sin(k/2)|(1-e^{-\gamma t}) \\
&\quad - \frac{i}{\pi}\cosh(\gamma t/2)\left[\mathrm{arctanh}\left(e^{-(i|k|+\gamma t)/2}\right) - \mathrm{arctanh}\left(e^{(i|k|-\gamma t)/2}\right)\right].
\end{aligned} \tag{F.62}$$

This expression is in closed form, but we can get some more intuition by taking limiting forms. First, let's try and understand the expansion when $|k| \ll \gamma t$. Defining $x = |k|/(\gamma t)$ to be a small parameter and Taylor expanding gives us that

$$\begin{aligned} & i\left[\operatorname{arctanh}\left(e^{-(i|k|+\gamma t)/2}\right) - \operatorname{arctanh}\left(e^{(i|k|-\gamma t)/2}\right)\right] \\ &= i\left[\operatorname{arctanh}\left(e^{-\gamma t/2(-ix-1)}\right) - \operatorname{arctanh}\left(e^{-\gamma t/2(ix-1)}\right)\right] \\ &= \frac{\gamma t x}{2\sinh(\gamma t)} + \mathcal{O}(x^3) = \frac{|\sin(k/2)|}{\sinh(\gamma t)} + \mathcal{O}(x^3). \end{aligned} \tag{F.63}$$

$$\implies n_k(t) = \frac{1}{2} + \frac{1}{\pi}|\sin(k/2)|(1 - e^{-\gamma t} - \coth(t/2)) + \mathcal{O}(|k|/\gamma t)^3. \tag{F.64}$$

Asymptotically, this looks like exponential relaxation to the steady state value of $n_k = 1/2$, but starting from an initial condition $n_k(0) = 1/2 - 3|\sin(k/2)|/\pi = 1/2 - 3\epsilon_k/4\pi$. We can think of the dynamics as a quick "jump" at short times by an energy dependent amount, followed by slow exponential relaxation at a rate that is independent of energy.

We can similarly take the opposite limit, where we assume that $x = \gamma t/|k|$ is now a small parameter. In this case, we find that

$$\begin{aligned} & i\left[\operatorname{arctanh}\left(e^{-(i|k|+\gamma t)/2}\right) - \operatorname{arctanh}\left(e^{(i|k|-\gamma t)/2}\right)\right] \\ &= i\left[\operatorname{arctanh}\left(e^{|k|(-i-x)/2}\right) - \operatorname{arctanh}\left(e^{|k|(i-x)/2}\right)\right] \\ &= -\frac{\pi}{2} - \frac{|k|x}{2|\sin(k/2)|} + \mathcal{O}(x^3) \\ &= -\frac{\pi}{2} - \frac{\gamma t}{2|\sin(k/2)|} + \mathcal{O}(\gamma t/|k|)^3. \end{aligned} \tag{F.65}$$

$$\implies n_k(t) = \left(|\sin(k/2)| + \frac{1}{2|\sin(k/2)|}\right)\frac{\gamma t}{\pi} + \mathcal{O}(\gamma t/|k|)^3. \tag{F.66}$$

Given that we have taken $x = \gamma t/|k|$ to be a small fixed value, the dynamics for short times can be thought of as linear growth at a rate $\gamma/(2\pi|\sin(k/2)|)$.

F.2.2 Effective temperature

Using the quasiparticle expectations, we can define an effective non-equilibrium temperature as a function of energy and time. A temperature that is nearly independent of the energy demonstrates a near equilibrium distribution, whereas a temperature that depends strongly on the energy is a very far from equilibrium distribution. Generically, one would imagine that, because the noise process we have described is energy-agnostic (being infinite bandwidth and infinite temperature), that there is no reason that one would find an equilibrium distribution. However, we can use the limiting descriptions to try and describe an effective temperature in the model. We define the temperature using the Fermi-Dirac distribution:

$$n(\epsilon) = \frac{1}{1+e^{\epsilon/T}} \implies T_{\text{eff}}(\epsilon, t) = \frac{\epsilon}{\log(1-n) - \log(n)}. \tag{F.67}$$

At the phase transition, the energy is given by

$$\epsilon_k = 2\sqrt{(\cos k - 1)^2 + \sin^2(k)} = 2\sqrt{4\sin^2(k/2)} = 4|\sin(k/2)|. \tag{F.68}$$

We can then use this to calculate the temperature from the limiting forms of the quasiparticle number via

$$T_{\text{eff}} = \begin{cases} \pi \frac{e^{2\gamma t} - e^{\gamma t}}{3e^{\gamma t} - 1} + \mathcal{O}(|k|/\gamma t)^2 & |k| \ll \gamma t \\ -4\epsilon_k \log^{-1}\left[\left(\frac{\epsilon_k}{2J} + \frac{J}{\epsilon_k}\right)\frac{\gamma t}{\pi}\right] + \mathcal{O}(\gamma t/|k|)^2 & |k| \gg \gamma t \end{cases}, \tag{F.69}$$

where, as described in Chapter 7 we have that once the time is longer than the wavevector — or equivalently the effective length scale $\xi_F = 1/\gamma t$ is smaller than the effective wavelength $\lambda \sim 1/|k|$ — then the distribution begins to look thermal with a temperature tending to infinity as a function of time.

To understand how surprising it is that there is an emergent temperature, let's instead consider noise in the z-direction instead of the $x-y$ plane. One can again calculate the time

evolution of the quasiparticle number analytically using

$$\langle \hat{c}_m^\dagger \hat{c}_n \rangle(t) = (1-\delta_{mn}) e^{-\gamma t} \langle \hat{c}_m^\dagger \hat{c}_n \rangle(0) + \delta_{mn} \langle \hat{c}_m^\dagger \hat{c}_n \rangle(0), \tag{F.70}$$

$$\langle \hat{c}_m \hat{c}_n \rangle(t) = e^{-\gamma t} \langle \hat{c}_m \hat{c}_n \rangle(0), \tag{F.71}$$

to find that (for anywhere in the phase space) we have

$$n_k(t) = n_k(\infty)(1 - e^{-\gamma t}), \tag{F.72}$$

$$n_k(\infty) = \frac{1}{2}\left[1 - \cos(\theta_k)\mathcal{F}_{\cos\theta}(0)\right], \tag{F.73}$$

which just gives uniform relaxation to a steady state value that depends weakly and non-monotonically on k. Working at the phase transition, this can be written as

$$n_k(\infty) = \frac{1}{2}\left(1 - \frac{2|\sin(k/2)|}{\pi}\right) = \frac{1}{2}\left(1 - \frac{\epsilon_k}{2\pi}\right), \tag{F.74}$$

which to leading order gives a temperature that depends linearly on the energy is extremely non-equilibrium:

$$T_{\text{eff}}(\epsilon, t) = \frac{\epsilon}{2\text{arccoth}(e^{\gamma t})} + \mathcal{O}(\epsilon^2). \tag{F.75}$$

A third noise model one could consider is neglecting the strings in the spin dissipation. This would be modeled by the free fermion model

$$\partial_t \hat{\rho} = \gamma \sum_i \mathcal{D}[\hat{c}_i]\hat{\rho} + \mathcal{D}[\hat{c}_i^\dagger]\hat{\rho} \tag{F.76}$$

The dynamics induced by such a channel are significantly different from the XY noise, and

one can show that

$$n_k(t) = \frac{1}{2}(1 - e^{-2\gamma t}), \tag{F.77}$$

regardless of the value of g. Therefore, the temperature can be written exactly for all times as

$$T_{\text{eff}}(\epsilon, t) = \frac{\epsilon}{2\text{arccoth}(e^{2\gamma t})}, \tag{F.78}$$

with no corrections.

F.2.3 Other correlation functions

The only other two point functions allowed by translational invariance are of the form $C_k = \langle \hat{\beta}_k \hat{\beta}_{-k} \rangle$. These can also be computed exactly as a function of time:

$$\begin{aligned}
C_k &= \left\langle \cos^2(\theta_k/2)\hat{d}_k\hat{d}_{-k} + \sin^2(\theta_k/2)\hat{d}^\dagger_{-k}\hat{d}^\dagger_k + i/2\sin(\theta_k)[\hat{d}^\dagger_{-k}\hat{d}_{-k} - \hat{d}_k\hat{d}^\dagger_k] \right\rangle \\
&= \frac{1}{N}\sum_{mn} e^{-ik(m-n)} \left\langle \cos^2(\theta_k/2)\hat{c}_m\hat{c}_n + \sin^2(\theta_k/2)c^\dagger_m c^\dagger_n + i\sin(\theta_k)c^\dagger_m c_n \right\rangle - i/2\sin(\theta_k) \\
&= \frac{1}{N}\sum_{mn} e^{-ik(m-n)} \left\langle \cos(\theta_k)\hat{c}_m\hat{c}_n + i\sin(\theta_k)c^\dagger_m c_n \right\rangle - i/2\sin(\theta_k) \\
&= -\frac{i}{2}\sum_d e^{-ikd - |d|\gamma t - \delta_{d,0}\gamma t} \left(\cos(\theta_k)\mathcal{F}_{\sin\theta}(d) - \sin(\theta_k)\mathcal{F}_{\cos\theta}(d)\right).
\end{aligned} \tag{F.79}$$

Once more, we can evaluate this at the phase transition to find that

$$\begin{aligned} C_k &= -\frac{i\mathrm{sgn}(k)}{\pi}\sum_d e^{-ikd-|d|\gamma t-\delta_{d,0}\gamma t}\frac{-2id\sin(k/2)-\cos(k/2)}{1-4d^2} \\ &= \frac{i\mathrm{sgn}(k)}{\pi}\cos(k/2)e^{-\gamma t}+\frac{2i\mathrm{sgn}(k)}{\pi}\sum_{d=1}^{\infty}e^{-|d|\gamma t}\frac{2d\sin(k/2)\sin(kd)+\cos(k/2)\cos(kd)}{1-4d^2} \\ &= \frac{i\mathrm{sgn}(k)}{\pi}\cos(k/2)(e^{-\gamma t}-1) \end{aligned}$$

$$+\frac{i\mathrm{sgn}(k)}{\pi}\sinh(\gamma t/2)\left[\mathrm{arctanh}\left(e^{-(i|k|+\gamma t)/2}\right)+\mathrm{arctanh}\left(e^{(i|k|-\gamma t)/2}\right)\right]. \tag{F.80}$$

This function tends to be significantly smaller than the populations n_k. It is largest for $k=0$, where

$$C_0 \to \frac{i}{\pi}\left[e^{-\gamma t}-1+2\sinh(\gamma t/2)\mathrm{arctanh}\left(e^{-\gamma t/2}\right)\right]. \tag{F.81}$$

The maximal value of this is given by the solution of a transcendental equation $\partial_t C_0(t)|_{t=t^*}=0$. The solution found numerically is $\gamma t^* = 0.41242...$, $C_0(t^*) = 0.04285....$ Hence, the anomalous correlation functions are always at least an order of magnitude smaller than the densities. Similarly to the local density, this correlator grows superlinearly at short times:

$$C_0(t) = -\frac{i}{2\pi}\gamma t\log\gamma t+\mathcal{O}(t). \tag{F.82}$$

We can also calculate analytically the anomalous correlators for the other noise models. For the free fermion noise, we have that

$$C_k^{\mathrm{ff}}(t) = e^{-\gamma t}C_k^{\mathrm{ff}}(0) = 0. \tag{F.83}$$

Since the initial condition has no coherences, this is just identically zero for all times. For Z

noise, it is useful to calculate the time dynamics of the plane wave modes as an intermediate step.

$$\begin{aligned}\langle \hat{d}_k^\dagger \hat{d}_k \rangle(t) &= \frac{1}{N}\sum_{mn} e^{ik(m-n)} \langle \hat{c}_m^\dagger \hat{c}_n \rangle(t) \\ &= \frac{1}{N}\sum_{mn} e^{ik(m-n)} e^{-\gamma t} \langle \hat{c}_m^\dagger \hat{c}_n \rangle(0) + \frac{1}{N}\sum_{mn} e^{ik(m-n)} \delta_{mn}(1-e^{-\gamma t}) \langle \hat{c}_m^\dagger \hat{c}_n \rangle(0) \\ &= e^{-\gamma t} \langle \hat{d}_k^\dagger \hat{d}_k \rangle(0) + (1-e^{-\gamma t})\overline{n}, \end{aligned} \tag{F.84}$$

$$\langle \hat{d}_{-k} \hat{d}_k \rangle(t) = e^{-\gamma t} \langle \hat{d}_{-k} \hat{d}_k \rangle(0), \tag{F.85}$$

where $\overline{n}$ is the mean particle density (or magnetization) in the initial condition, which is unchanged by the noise. From here, it is simple to calculate that the time evolution of the coherences is given by

$$\begin{aligned} C_k^Z(t) &= \left\langle \cos^2(\theta_k/2)\hat{d}_k\hat{d}_{-k} + \sin^2(\theta_k/2)\hat{d}_{-k}^\dagger \hat{d}_k^\dagger + i/2 \sin(\theta_k)[\hat{d}_{-k}^\dagger \hat{d}_{-k} - \hat{d}_k \hat{d}_k^\dagger] \right\rangle (t) \\ &= e^{-\gamma t} C_k^Z(0) + \frac{i}{2}(1-e^{-\gamma t})\sin(\theta_k)(2\overline{n}-1). \end{aligned} \tag{F.86}$$

Working at the phase transition and taking $C_k(0) = 0$, we have $\overline{n} = \frac{1}{2} - \frac{1}{\pi}$ so

$$C_k^Z(t) = -\frac{i}{\pi}\mathrm{sgn}(k)\cos(k/2)(1-e^{-\gamma t}). \tag{F.87}$$

F.2.4 Divergent quasiparticle production rate

In addition to the energy resolved QP numbers, we can also calculate the total QP number via

$$n(t) = \int \frac{\mathrm{d}k}{2\pi} n_k(t) = \frac{1}{2} - \frac{1}{2}|\mathcal{F}_{\cos\theta}(0)|^2 e^{-\gamma t} - \sum_{d=1}^{\infty} e^{-d\gamma t}\left(|\mathcal{F}_{\cos\theta}(d)|^2 + |\mathcal{F}_{\sin\theta}(d)|^2 \right), \tag{F.88}$$

at the phase transition, this can be written as

$$n(t) = \int \frac{\mathrm{d}k}{2\pi} n_k(t) = \frac{1}{2} - \frac{2}{\pi^2} e^{-\gamma t} - \frac{4}{\pi^2} \sum_{d=1}^{\infty} e^{-d\gamma t} \frac{1+4d^2}{(1-4d^2)^2}. \tag{F.89}$$

We can note that the sum is convergent for all $t \geq 0$, as expected. This sum can be rewritten in terms of special functions, but these are not necessarily intuitive. To try and understand the short time dynamics, let's first note that when taking a derivative, the sum will be divergent, so we cannot naively perform a short time expansion. Hence, observe that

$$\begin{aligned} \sum_{d=1}^{\infty} e^{-d\gamma t} \frac{1+4d^2}{(1-4d^2)^2} &= -\sum_{d=1}^{\infty} \frac{e^{-d\gamma t}}{(1-4d^2)} + \sum_{d=1}^{\infty} \frac{2e^{-d\gamma t}}{(1-4d^2)^2} \\ &= \frac{1}{2} - \sinh(\gamma t/2)\mathrm{arccoth}(e^{\gamma t/2}) + \sum_{d=1}^{\infty} \frac{2e^{-d\gamma t}}{(1-4d^2)^2}. \end{aligned} \tag{F.90}$$

The second sum is still difficult to evaluate, but the leading order terms are now convergent, and so we can observe that

$$\sum_{d=1}^{\infty} e^{-d\gamma t} \frac{1+4d^2}{(1-4d^2)^2} = \frac{1}{2} - \sinh(\gamma t/2)\mathrm{arccoth}(e^{\gamma t/2}) + \frac{\pi^2-8}{8} - \frac{\gamma t}{8} + \mathcal{O}(\gamma t)^2, \tag{F.91}$$

$$\begin{aligned} \implies n(t) &= \frac{4}{\pi^2} \sinh(\gamma t/2)\mathrm{arccoth}(e^{\gamma t/2}) + \frac{5}{2\pi^2}\gamma t + \mathcal{O}(\gamma t)^2 \\ &= -\frac{1}{\pi^2}\gamma t \log(\gamma t) + \frac{5+4\log 2}{2\pi^2}\gamma t + \mathcal{O}(\gamma t)^2. \end{aligned} \tag{F.92}$$

From here, we can take a derivative to find that

$$\partial_t n(t) = -\frac{\gamma}{\pi^2} \log(\gamma t) + \frac{3+4\log 2}{2\pi^2}\gamma + \mathcal{O}(\gamma t). \tag{F.93}$$

which has a logarithmic divergence for small t. For completeness, we also note that we can define the long time behavior by noting that Eq. (F.89) is a power series expansion in $e^{-\gamma t}$.

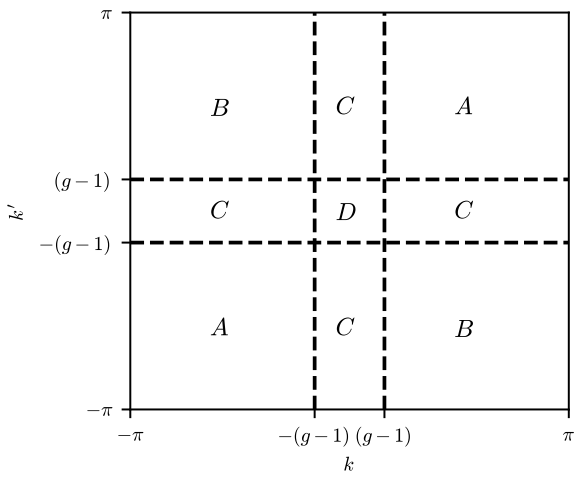

Figure F.2: Sketch depicting the four symmetry-distinct regions of the integral in Eq. (F.95).

Keeping the lowest order terms gives

$$n(t) = \frac{1}{2} - \frac{38}{9\pi^2} e^{-\gamma t} + \mathcal{O}(e^{-\gamma t})^2 \tag{F.94}$$

Going back to the short time expansion, the derivative of $n(t)$ should only be divergent when the state is critical. We can understand how this divergence appears near the phase transition by writing directly the time derivative in the number of quasiparticles at time $t = 0$:

$$\begin{aligned}
\partial_t n|_{t=0} &= \frac{\gamma}{2}|\mathcal{F}_{\cos\theta}(0)|^2 + \sum_{d=1}^{\infty} d\gamma \left(|\mathcal{F}_{\cos\theta}(d)|^2 + |\mathcal{F}_{\sin\theta}(d)|^2 \right) \\
&\sim \frac{\gamma}{2}|\mathcal{F}_{\cos\theta}(0)|^2 - 2\gamma \int_{-\pi}^{\pi} \frac{\mathrm{d}k}{2\pi} \frac{\mathrm{d}k'}{2\pi} \int_0^{\infty} \mathrm{d}x e^{ix(k-k')} x \sin^2([\theta_k - \theta_{k'}]/2) \\
&= \frac{\gamma}{2}|\mathcal{F}_{\cos\theta}(0)|^2 + 2\gamma \int_{-\pi}^{\pi} \frac{\mathrm{d}k}{2\pi} \frac{\mathrm{d}k'}{2\pi} \frac{\sin^2([\theta_k - \theta_{k'}]/2)}{(k-k')^2}.
\end{aligned} \tag{F.95}$$

We wish to evaluate this just to leading order in $g - 1$. To perform this integral, it will be useful to subdivide this into 9 relevant regions (though only four independent ones after considering symmetries), as depicted in Fig. F.2. Let's define the integrand $f_g(k, k') =$

$\frac{1}{4\pi^2}\frac{\sin^2([\theta_k-\theta_{k'}]/2)}{(k-k')^2}$:

$$\int_{[-\pi,\pi]\times[-\pi,\pi]} f_g(k,k')\ \mathrm{d}k\ \mathrm{d}k' = 2\int_A f_g(k,k')\ \mathrm{d}k\ \mathrm{d}k' + 2\int_B f_g(k,k')\ \mathrm{d}k\ \mathrm{d}k' + 4\int_C f_g(k,k')\ \mathrm{d}k\ \mathrm{d}k' + \int_D f_g(k,k')\ \mathrm{d}k\ \mathrm{d}k' \tag{F.96}$$

We will evaluate each one separately to leading order. Let's begin with C, which is defined as $g-1<k<\pi$ and $-(g-1)<k'<g-1$. Then we can note that $0\le f_g\le 1/(2\pi k)^2$. This implies that

$$\int_C f_g(k,k')\ \mathrm{d}k\ \mathrm{d}k' \le \int_C \frac{1}{(2\pi k)^2}\ \mathrm{d}k\ \mathrm{d}k' = \frac{g-1}{2\pi^2}\left(\frac{1}{g-1}-\frac{1}{\pi}\right) \le \frac{1}{2\pi^2} = \mathcal{O}(g-1)^0, \tag{F.97}$$

Next, let's evaluate D where $0<|k|,|k'|<g-1$. Here, we have that $f_g\le 1/[16\pi^2(g-1)^2]$. Therefore, $\int_D f_g(k,k')\ \mathrm{d}k\ \mathrm{d}k' \le 1/(16\pi^2)=\mathcal{O}(g-1)^0$ as well. To evaluate A and B, we first need to find the leading order behavior f_g in $g-1$. We have that

$$\begin{aligned} f_g(k,k') &= f_1(k,k') - \frac{\sin^2[(k-k')/2]}{16\pi^2(k-k')^2\sin(k/2)\sin(k'/2)}(g-1) \\ &\equiv f_1(k,k') - \tilde{f}(k,k')(g-1). \end{aligned} \tag{F.98}$$

Here, f_1 is the function f_g evaluated at $g=1$, and we have defined $\tilde{f}$ to be the leading correction. Next, we note that

$$|\tilde{f}| \le \frac{1}{64\pi^2}\frac{1}{\sin(k/2)\sin(k'/2)}, \tag{F.99}$$

$$\begin{aligned} \implies \left|\int_{g-1}^{\pi}\int_{g-1}^{\pi}\tilde{f}\right| &\le \frac{1}{64\pi^2}\left|\int_{g-1}^{\pi}\frac{1}{\sin(k/2)}\ \mathrm{d}k\right|^2 \le \frac{1}{64\pi^2}\left|\int_{g-1}^{\pi}\frac{\pi}{k}\ \mathrm{d}k\right|^2 \\ &= \frac{1}{64}\left|\log(\pi)-\log(g-1)\right|^2, \end{aligned} \tag{F.100}$$

and so the correction is of order $[\log^2(g-1)](g-1) \to 0$ as $g \to 1$, and is therefore smaller than $\mathcal{O}(g-1)^0$. Hence, we can evaluate the A and B using the values of θ_k for $g = 1$. This significantly simplifies the problem, allowing us to write that

$$\int_A \frac{\sin([k-k']/4)^2}{(k-k')^2} \frac{\mathrm{d}k\ \mathrm{d}k'}{4\pi^2} \leq \int_{g-1}^{\pi}\int_{g-1}^{\pi} \frac{1}{16}\frac{\mathrm{d}k\ \mathrm{d}k'}{4\pi^2} \leq \frac{1}{64} = \mathcal{O}(g-1)^0, \tag{F.101}$$

Finally, we come to evaluating B, which is given by

$$\int_B \frac{\cos([k-k']/4)^2}{(k-k')^2} \frac{\mathrm{d}k\ \mathrm{d}k'}{4\pi^2} = \int_{g-1}^{\pi}\int_{g-1}^{\pi} \frac{1}{(k+k')^2}\frac{\mathrm{d}k\ \mathrm{d}k'}{4\pi^2} - \int_{g-1}^{\pi}\int_{g-1}^{\pi} \frac{\sin([k+k']/4)^2}{(k+k')^2}\frac{\mathrm{d}k\ \mathrm{d}k'}{4\pi^2}. \tag{F.102}$$

We only want the divergent part, and from before we know the second term is bounded by a constant. Hence, we care about the first piece:

$$\int_{g-1}^{\pi}\int_{g-1}^{\pi} \frac{1}{(k+k')^2}\frac{\mathrm{d}k\ \mathrm{d}k'}{4\pi^2} = \frac{1}{4\pi^2}\left[2\log(g-1+\pi) - \log(4\pi) - \log(g-1)\right]. \tag{F.103}$$

Putting everything together, we have that

$$\partial_t n|_{t=0} = -\frac{\gamma}{\pi^2}\log(g-1) + \mathcal{O}(g-1)^0. \tag{F.104}$$

Another way to see the logarithmic divergence is by using Eq. (F.62). It is incredibly simple to calculate the energy resolved QP production rate:

$$\begin{aligned}\partial_t n_k = &\frac{\gamma|\sin(k/2)|}{\pi}e^{-\gamma t} + \frac{\gamma}{2\pi}\frac{\cosh(\gamma t/2)^2|\sin(k/2)|}{|\sin[(k-i\gamma t)/2]|^2} \\ &- i\frac{\gamma\sinh(\gamma t/2)}{2\pi}\left[\operatorname{arctanh}\left(e^{(ik+\gamma t)/2}\right) - \operatorname{arctanh}\left(e^{(-ik+\gamma t)/2}\right)\right]. \qquad \text{(F.105)} \\ \implies \partial_t n_k|_{t=0} = &\frac{\gamma}{\pi}|\sin(k/2)| + \frac{\gamma}{2\pi}\frac{1}{|\sin(k/2)|} = \frac{2\gamma}{\pi}\left(\frac{J}{\epsilon_k} + \frac{\epsilon_k}{J8}\right). \qquad \text{(F.106)}\end{aligned}$$

If we note that the gap is $|g-1|$ and assume the derivatives are essentially unchanged near

the critical point, then we can use the fact that the density of states near the critical point is $\rho(\epsilon) = 1/2\pi$ to calculate that

$$\partial_t n = \int_{|g-1|}^{2} \mathrm{d}\epsilon \rho(\epsilon) \partial_t n_\epsilon \sim \int_{|g-1|}^{2} \frac{\gamma}{\pi^2} \frac{1}{\epsilon} \, \mathrm{d}\epsilon \sim -\frac{\gamma}{\pi^2} \log(g-1), \tag{F.107}$$

where $\sim$ means we are only keep leading order terms.

F.3 Critical XX Model

In this section, we will show that the basic phenomena found for the critical Ising model also extends to a critical XX model. Here will consider the Hamiltonian given by

$$\hat{H} = -\frac{J}{2} \sum_{i=1}^{N-1} \hat{\sigma}_i^x \hat{\sigma}_{i+1}^x + \hat{\sigma}_i^y \hat{\sigma}_{i+1}^y = -J \sum_{i=1}^{N-1} \hat{c}_i^\dagger \hat{c}_{i+1} + \hat{c}_{i+1}^\dagger \hat{c}_i. \tag{F.108}$$

Written in terms of the plane wave momentum modes $\hat{d}_k$, this is diagonalized:

$$\hat{H} = -2J \sum_k \cos(k) \hat{d}_k^\dagger \hat{d}_k. \tag{F.109}$$

We will consider this model in the zero magnetization sector, which in its ground state is given by

$$\langle \hat{d}_k^\dagger \hat{d}_k \rangle_{\mathrm{GS}} = \begin{cases} 1 & |k| < \pi/2 \\ 0 & |k| > \pi/2 \end{cases}, \tag{F.110}$$

$$\implies \langle \hat{c}_m^\dagger \hat{c}_n \rangle_{\mathrm{GS}} = \int_{-\pi/2}^{\pi/2} e^{ik(m-n)} \frac{\mathrm{d}k}{2\pi} = \frac{\sin\left(\frac{\pi}{2}[m-n]\right)}{\pi(m-n)}. \tag{F.111}$$

From here, we can use the already known solution observe that the time evolution is given by

$$\langle \hat{c}_m^\dagger \hat{c}_n \rangle(t) = (1-\delta_{mn}) e^{-|m-n|\gamma t} \langle \hat{c}_m^\dagger \hat{c}_n \rangle_{\text{GS}} + \delta_{mn} \langle \hat{c}_m^\dagger \hat{c}_n \rangle_{\text{GS}}, \tag{F.112}$$

$$\begin{aligned}
\implies \langle \hat{d}_k^\dagger \hat{d}_k \rangle(t) &= \frac{1}{N} \sum_{m,n} e^{-ik(m-n)} \langle \hat{c}_m^\dagger \hat{c}_n \rangle(t) \\
&= \frac{1}{N} \sum_{m,n} e^{-ik(m-n)} \left[(1-\delta_{mn}) e^{-|m-n|\gamma t} \langle \hat{c}_m^\dagger \hat{c}_n \rangle_{\text{GS}} + \delta_{mn} \langle \hat{c}_m^\dagger \hat{c}_n \rangle_{\text{GS}} \right] \\
&= \frac{1}{2} + 2 \sum_{d>0} e^{-\gamma |d| t} \cos(kd) \frac{\sin(\pi d/2)}{\pi d} \\
&= \frac{1}{2} + \frac{\operatorname{arccot}(e^{-ik+\gamma t}) + \operatorname{arccot}(e^{ik+\gamma t})}{\pi}.
\end{aligned} \tag{F.113}$$

From here, we have all the quasiparticle operators defined for all times. We can calculate the long and short time expansions

$$n_k(t) = \begin{cases} n_k(0) + \frac{2J}{\pi \epsilon_k} \gamma t & \gamma t \lesssim |k| \\ \frac{1}{2} - \frac{\epsilon_k}{J\pi} e^{-\gamma t} & \gamma t \gtrsim |k| \end{cases}. \tag{F.114}$$

We can again directly define the effective temperature as

$$T_{\text{eff}}(k,t) = \frac{-2J\cos(k)}{\log(1-n_k) - \log(n_k)}. \tag{F.115}$$

To understand the emergent temperature at long times, let's define a small parameter $z = (k - \pi/2)/t$. Here, we work around the $k = \pi/2$ point as this is where the system is gapless (similarly, the $k = -\pi/2$) points but inversion symmetry implies this will behave identically. Hence, we can calculate that

$$T_{\text{eff}}(k,t) = \frac{\pi}{2} J \sinh(\gamma t) + \mathcal{O}(z^2). \tag{F.116}$$

Similarly, we can take the short time expansion to get that

$$T_{\text{eff}}(k,t) = |\epsilon_k| \log^{-1}\left(\frac{\pi|\epsilon_k|}{2J\gamma t}\right) + \mathcal{O}(z^{-2}). \tag{F.117}$$

Both of these expansions, up to constant factors, have essentially the same functional forms as was observed in the TFIM.

We can similarly calculate how the total quasiparticle number grows at short times. Now, because we start in the zero magnetization sector (which corresponds to half filling in the fermionic language), the total particle number does not change. However, we can instead calculate the imbalance between positive and negative energies. For this, we note that the density of positive energy quasiparticles is given by

$$n_{\epsilon>0} = \int_{\pi/2}^{\pi} \langle \hat{d}_k^\dagger \hat{d}_k \rangle(t) \frac{\mathrm{d}k}{\pi/2} = \frac{2}{\pi}\int_{\pi/2}^{\pi} \langle \hat{d}_k^\dagger \hat{d}_k \rangle(t)\ \mathrm{d}k = \frac{1}{2} - \frac{2}{\pi^2}\left(\mathrm{Li}_2(e^{-\gamma t}) - \mathrm{Li}_2(-e^{-\gamma t})\right), \tag{F.118}$$

$$\implies n_{\epsilon>0} = -\frac{2}{\pi^2}\gamma t \log(\gamma t) + \frac{2}{\pi^2}(1+\log(2))\gamma t + \mathcal{O}(\gamma t)^2, \tag{F.119}$$

$$\implies n_{\epsilon>0} = \frac{1}{2} - \frac{4}{\pi^2}e^{-\gamma t} + \mathcal{O}(e^{-\gamma t})^3 \tag{F.120}$$

where $\mathrm{Li}_2(z)$ is the dilogarithm function. Hence, the short time particles number grows superlinearly, and the long time relaxation looks as if it started with an initial condition of $(1/2 - 4/\pi^2)$, just as in the TFIM. We can take a derivative of this to find that

$$\partial_t n_{\epsilon>0} = \frac{2\gamma}{\pi^2}\log\left[\coth\left(\frac{\gamma t}{2}\right)\right] = -\frac{2\gamma}{\pi^2}\log(\gamma t) + \frac{2\gamma}{\pi^2}\log(2) + \mathcal{O}(t^2), \tag{F.121}$$

and so we see an almost identical logarthmic divergence as in the Ising model, up to multiplicative prefactors.

Finally, we can exactly calculate the energy resolved quasiparticle production. This is

rather simple:

$$\partial_t \langle \hat{d}_k^\dagger \hat{d}_k \rangle = -\frac{2\gamma}{\pi} \frac{\cos(k)\cosh(\gamma t)}{\cos(2k)+\cosh(2t)} = \frac{2\gamma}{\pi} \frac{J\epsilon_k \cosh(\gamma t)}{\epsilon_k^2 + 2J^2 \sinh(\gamma t)}, \tag{F.122}$$

$$\implies \partial_t \langle \hat{d}_k^\dagger \hat{d}_k \rangle \big|_{t=0} = \frac{2\gamma J}{\pi \epsilon_k}, \tag{F.123}$$

which is identical to the result for the TFIM to leading order in ϵ_k.

F.4 Experimental Protocols

F.4.1 Measuring the effective temperature

Here, we propose a possible method to measure the effective temperature of the many-body state using a single qubit probe. The proposed measurement makes use of the fact that a weakly coupled probe qubit to one end of the chain can probe the frequency-dependent density of states of the many-body state. We imagine the following sequence:

1. Prepare the many-body ground state of the Ising model.
2. Apply the noise channel for a time t.
3. Turn the noise channel off, and the Ising Hamiltonian on. The populations of eigenmodes are invariant under the Hamiltonian evolution.
4. Weakly couple a tunable qubit using an XX interaction to one end of the spin chain with an energy gap Δ beween $\hat{\sigma}^z$ eigenstates.
5. The qubit will equilibrate to a mixture of its energy eigenstates. By measuring the relative population of the spin up and spin down states, one can define a temperature as a function of Δ.

What remains to be shown is that the equilibrium distribution of the weakly coupled probe qubit will have the same effective temperature as the many-body spin state. To see this, we

can calculate the effective heating and cooling rates of the probe qubit, which we will denote via the operators $\hat{\sigma}_P^{x,y,z}$. We imagine a Hamiltonian

$$\hat{H} = \hat{H}_{\text{Ising}} + \frac{\Delta}{2}\hat{\sigma}_P^z + \lambda(\hat{\sigma}_P^+\hat{\sigma}_1^- + \hat{\sigma}_P^-\hat{\sigma}_1^+), \tag{F.124}$$

$$\hat{H}_{\text{Ising}} = -J\sum_{j=1}^{N-1}\hat{\sigma}_j^x\hat{\sigma}_{j+1}^x + g\sum_{j=1}^{N}\hat{\sigma}_j^z, \tag{F.125}$$

where the Ising model is tuned to the critical point $g = J$, the intersystem coupling $\lambda \ll g, J$ and Δ is a tunable parameter to select which frequency in the Ising chain we are sensitive to. Note that, because the probe qubit is coupled to the end of the chain, the entire system is still free-fermion. I.e., using the JW transformation we can write the dynamics as

$$\hat{H} = \hat{H}_{\text{Ising}} + \Delta\hat{c}_P^\dagger\hat{c}_P + \lambda(\hat{c}_P^\dagger\hat{c}_1 + \hat{c}_1^\dagger\hat{c}_P), \tag{F.126}$$

$$\hat{H}_{\text{Ising}} = -J\sum_{j=1}^{N-1}(\hat{c}_j^\dagger - \hat{c}_j)(\hat{c}_{j+1}^\dagger + \hat{c}_{j+1}) + 2g\sum_{j=1}^{N}\hat{c}_j^\dagger\hat{c}_j, \tag{F.127}$$

up to irrelevant constants. At this point, it will be useful to write things in terms of the energy eigenmodes of the Ising Hamiltonian:

$$\hat{H} = \Delta\hat{c}_P^\dagger\hat{c}_P + \int\frac{\mathrm{d}k}{2\pi}\epsilon_k\hat{\beta}_k^\dagger\hat{\beta}_k + \lambda\int\frac{\mathrm{d}k}{2\pi}\left[\hat{c}_P^\dagger e^{ik}(\cos(\theta_k/2)\hat{\beta}_k - i\sin(\theta_k/2)\hat{\beta}_{-k}^\dagger) + \text{H. c.}\right]. \tag{F.128}$$

If we define $\hat{n}_P = \hat{c}_P^\dagger\hat{c}_P$ and work in the interaction picture, then we can observe that

$$\hat{H}_{\text{int}} = \lambda\int\frac{\mathrm{d}k}{2\pi}\left[\cos(\theta_k/2)e^{ik+i(\Delta-\epsilon_k)t}\hat{c}_P^\dagger\hat{\beta}_k + \sin(\theta_k/2)e^{ik+i(\Delta+\epsilon_k)t}\hat{c}_P^\dagger\hat{\beta}_{-k}^\dagger + \text{H. c.}\right]. \tag{F.129}$$

Note that $\epsilon_k > 0$ and we take WLOG $\Delta > 0$, so only the term proportional to $\cos(\theta_k/2)$ can be resonant. We will make the rotating wave approximation and drop the non-resonant

terms, as in the limit $\lambda \to 0, t \to \infty$ the off-resonant terms do not cause transitions.

$$\hat{H}_{\text{int,RWA}} = \lambda \int \frac{\mathrm{d}k}{2\pi} \left[\cos(\theta_k/2) e^{ik + i(\Delta - \epsilon_k)t} \hat{c}_P^\dagger \hat{\beta}_k + \text{H. c.} \right]. \tag{F.130}$$

From this expression, it is simple to read off the Fermi's Golden rule transition rates as

$$\Gamma_\uparrow = \frac{\lambda^2}{2J} \cos^2(\theta_k/2) \langle \hat{\beta}_k^\dagger \hat{\beta}_k \rangle = \frac{\lambda^2}{2J} \cos^2(\theta_k/2) n_k, \tag{F.131}$$

$$\Gamma_\downarrow = \frac{\lambda^2}{2J} \cos^2(\theta_k/2) \langle \hat{\beta}_k \hat{\beta}_k^\dagger \rangle = \frac{\lambda^2}{2J} \cos^2(\theta_k/2) (1 - n_k), \tag{F.132}$$

where k is such that $\epsilon_k = \Delta$. We assume we are studying the low-energy spectrum of the model, and the factor of $2J$ in the denominator is the local density of states at low energy, where we use that $\epsilon_k \sim 2J|k| \implies \partial_k \epsilon = 2J$ so $\rho(\epsilon) = 1/(2J)$. In general, the density of states is given by $\rho(\Delta) = (2J\sqrt{1 - \Delta^2/4})^{-1}$. From here, we find that

$$\partial_t n_P = \Gamma_\uparrow (1 - n_P) - \Gamma_\downarrow n_P, \tag{F.133}$$

$$\implies n_P(t) = \frac{\Gamma_\uparrow}{\Gamma_\uparrow + \Gamma_\downarrow} (1 - e^{-(\Gamma_\uparrow + \Gamma_\downarrow)t}). \tag{F.134}$$

This gives a steady state value and overall relaxation rate

$$n_P(t \to \infty) = \frac{\Gamma_\uparrow}{\Gamma_\uparrow + \Gamma_\downarrow} = n_k, \tag{F.135}$$

$$\Gamma_{\text{eff}} = \Gamma_\uparrow + \Gamma_\downarrow = \frac{\lambda^2}{2J} \cos^2(\theta_k/2), \tag{F.136}$$

and so the steady state spin population will be $\langle \hat{\sigma}_P^z \rangle = 2n_P - 1 = 2n_k - 1$ where n_k is the QP density in the Ising model at energy $\epsilon_k = \Delta$. Hence, we can directly read the (non-) equilibrium temperature of the Ising model from the steady state distribution function of the probe spin. Indeed, if one were to assign a temperature to the probe spin assuming it had reached thermal equilibrium with the Ising spin bath, it would be the exact same effective

temperature as the Ising spin model, exactly as desired.

We believe that this protocol could be extremely well suited for many experimental platforms. One particular example would be long Josephson-Junction (JJ) arrays, which have recently been suggested as a simulation platform to observe Ising criticality [287, 288, 289]. These would be particularly appealing as JJ arrays are able to reach extremely large system sizes and would be able to easily observe the bulk physics. Further, it would be relatively straightforward to add a superconducting qubit coupled to the end of the chain to perform the measurement protocol.

F.4.2 Measuring the total quasiparticle number

The previously outlined protocol gives the full spectrum of quasiparticle density as a function of their energy. However, if one were instead just interested in measuring the total quasiparticle number (e.g., to observe the logarithmic divergence), then a simpler scheme can be imagined. Here, we imagine that it is possible to completely adiabatically tune the parameter g to zero. In this case, the Hamiltonian is simply given by the pure Ising model in 1D:

$$\hat{H} = -J \sum_i \hat{\sigma}_i^x \hat{\sigma}_{i+1}^x. \tag{F.137}$$

This Hamiltonian has a flat quasiparticle spectrum corresponding to domain walls, which each carry energy $2J$. Hence, by projecting each lattice site into an $\hat{X}$ eigenstate and then counting domain walls, one can count exactly the total number of quasiparticles in the system. Hence, if we assume that the sweep is truly adiabatic, then the number of QP excitations will not change and so they can be counted easily using an extremely simple projective measurement, assuming the lattice has single site readout and the ability to tune deep into the ferromagnetic regime. Alternatively, one can adiabatically sweep to the paramagnet

defined by the Hamiltonian

$$\hat{H} = -g \sum_i \hat{\sigma}_i^z, \tag{F.138}$$

which also has a flat spectrum. By measuring each spin now in the $\hat{Z}$ eigenstate basis allows one to measure the total quasiparticle number in the exact same way.

REFERENCES

[1] Andrew Pocklington, Yu-Xin Wang, Yariv Yanay, and A. A. Clerk. Stabilizing volume-law entangled states of fermions and qubits using local dissipation. *Phys. Rev. B*, 105:L140301, Apr 2022.

[2] J. F. Poyatos, J. I. Cirac, and P. Zoller. Quantum reservoir engineering with laser cooled trapped ions. *Phys. Rev. Lett.*, 77:4728–4731, Dec 1996.

[3] M. B. Plenio and S. F. Huelga. Entangled light from white noise. *Phys. Rev. Lett.*, 88:197901, Apr 2002.

[4] F. Reiter, A. S. Sørensen, P. Zoller, and C. A. Muschik. Dissipative quantum error correction and application to quantum sensing with trapped ions. *Nature Communications*, 8(1):1822, Nov 2017.

[5] José Lebreuilly, Kyungjoo Noh, Chiao-Hsuan Wang, Steven M. Girvin, and Liang Jiang. Autonomous quantum error correction and quantum computation. *arXiv:2103.05007*, 2021.

[6] Y. Lin, J. P. Gaebler, F. Reiter, T. R. Tan, R. Bowler, A. S. Sørensen, D. Leibfried, and D. J. Wineland. Dissipative production of a maximally entangled steady state of two quantum bits. *Nature*, 504(7480):415–418, Dec 2013.

[7] S. Shankar, M. Hatridge, Z. Leghtas, K. M. Sliwa, A. Narla, U. Vool, S. M. Girvin, L. Frunzio, M. Mirrahimi, and M. H. Devoret. Autonomously stabilized entanglement between two superconducting quantum bits. *Nature*, 504(7480):419–422, Dec 2013.

[8] E. E. Wollman, C. U. Lei, A. J. Weinstein, J. Suh, A. Kronwald, F. Marquardt, A. A. Clerk, and K. C. Schwab. Quantum squeezing of motion in a mechanical resonator. *Science*, 349(6251):952–955, 2015.

[9] D. Kienzler, H.-Y. Lo, B. Keitch, L. de Clercq, F. Leupold, F. Lindenfelser, M. Marinelli, V. Negnevitsky, and J. P. Home. Quantum harmonic oscillator state synthesis by reservoir engineering. *Science*, 347:53, may 2015.

[10] M. E. Kimchi-Schwartz, L. Martin, E. Flurin, C. Aron, M. Kulkarni, H. E. Tureci, and I. Siddiqi. Stabilizing entanglement via symmetry-selective bath engineering in superconducting qubits. *Phys. Rev. Lett.*, 116:240503, Jun 2016.

[11] S Diehl, A Micheli, A Kantian, B Kraus, H P Büchler, and Peter Zoller. Quantum states and phases in driven open quantum systems with cold atoms. *Nat Phys*, 4(11):878–883, September 2008.

[12] B. Kraus, H. P. Büchler, S. Diehl, A. Kantian, A. Micheli, and P. Zoller. Preparation of entangled states by quantum markov processes. *Phys. Rev. A*, 78:042307, Oct 2008.

[13] Sebastian Diehl, Enrique Rico, Mikhail A. Baranov, and Peter Zoller. Topology by dissipation in atomic quantum wires. *Nature Physics*, 7(12):971–977, Dec 2011.

[14] Stefano Zippilli, Jie Li, and David Vitali. Steady-state nested entanglement structures in harmonic chains with single-site squeezing manipulation. *Phys. Rev. A*, 92:032319, Sep 2015.

[15] Shan Ma, Matthew J. Woolley, Ian R. Petersen, and Naoki Yamamoto. Pure gaussian states from quantum harmonic oscillator chains with a single local dissipative process. *Journal of Physics A: Mathematical and Theoretical*, 50(13):135301, Feb 2017.

[16] Yariv Yanay and Aashish A. Clerk. Reservoir engineering of bosonic lattices using chiral symmetry and localized dissipation. *Phys. Rev. A*, 98:043615, Oct 2018.

[17] Stephen D. Bartlett, Barry C. Sanders, Samuel L. Braunstein, and Kae Nemoto. Efficient classical simulation of continuous variable quantum information processes. *Phys. Rev. Lett.*, 88:097904, Feb 2002.

[18] G Vitagliano, A Riera, and J I Latorre. Volume-law scaling for the entanglement entropy in spin-1/2 chains. *New Journal of Physics*, 12(11):113049, nov 2010.

[19] Zhao Zhang, Amr Ahmadain, and Israel Klich. Novel quantum phase transition from bounded to extensive entanglement. *Proceedings of the National Academy of Sciences*, 114(20):5142–5146, 2017.

[20] Shovan Dutta and Nigel R. Cooper. Long-range coherence and multiple steady states in a lossy qubit array. *Phys. Rev. Lett.*, 125:240404, Dec 2020.

[21] Shovan Dutta and Nigel R. Cooper. Out-of-equilibrium steady states of a locally driven lossy qubit array. *Phys. Rev. Research*, 3:L012016, Feb 2021.

[22] Pierre Wendenbaum, Thierry Platini, and Dragi Karevski. Entanglement replication via quantum repeated interactions. *Phys. Rev. A*, 91:040303, Apr 2015.

[23] S. Zippilli, M. Paternostro, G. Adesso, and F. Illuminati. Entanglement replication in driven dissipative many-body systems. *Phys. Rev. Lett.*, 110:040503, Jan 2013.

[24] S. Diehl, W. Yi, A. J. Daley, and P. Zoller. Dissipation-induced d-wave pairing of fermionic atoms in an optical lattice. *Phys. Rev. Lett.*, 105:227001, Nov 2010.

[25] Fernando Iemini, Davide Rossini, Rosario Fazio, Sebastian Diehl, and Leonardo Mazza. Dissipative topological superconductors in number-conserving systems. *Phys. Rev. B*, 93:115113, Mar 2016.

[26] W Yi, S Diehl, A J Daley, and P Zoller. Driven-dissipative many-body pairing states for cold fermionic atoms in an optical lattice. *New Journal of Physics*, 14(5):055002, may 2012.

[27] W. P. Su, J. R. Schrieffer, and A. J. Heeger. Solitons in polyacetylene. *Phys. Rev. Lett.*, 42:1698–1701, Jun 1979.

[28] W. P. Su, J. R. Schrieffer, and A. J. Heeger. Soliton excitations in polyacetylene. *Phys. Rev. B*, 22:2099–2111, Aug 1980.

[29] Douglas R. Hofstadter. Energy levels and wave functions of bloch electrons in rational and irrational magnetic fields. *Phys. Rev. B*, 14:2239–2249, Sep 1976.

[30] P. Jordan and E. Wigner. Über das paulische äquivalenzverbot. *Zeitschrift für Physik*, 47(9):631–651, Sep 1928.

[31] Philip Richerme, Zhe-Xuan Gong, Aaron Lee, Crystal Senko, Jacob Smith, Michael Foss-Feig, Spyridon Michalakis, Alexey V. Gorshkov, and Christopher Monroe. Non-local propagation of correlations in quantum systems with long-range interactions. *Nature*, 511(7508):198–201, 2014.

[32] Tiff Brydges, Andreas Elben, Petar Jurcevic, Benoît Vermersch, Christine Maier, Ben P. Lanyon, Peter Zoller, Rainer Blatt, and Christian F. Roos. Probing rényi entanglement entropy via randomized measurements. *Science*, 364(6437):260–263, 2019.

[33] C. Kokail, C. Maier, R. van Bijnen, T. Brydges, M. K. Joshi, P. Jurcevic, C. A. Muschik, P. Silvi, R. Blatt, C. F. Roos, and P. Zoller. Self-verifying variational quantum simulation of lattice models. *Nature*, 569(7756):355–360, 2019.

[34] P. Roushan, C. Neill, J. Tangpanitanon, V. M. Bastidas, A. Megrant, R. Barends, Y. Chen, Z. Chen, B. Chiaro, A. Dunsworth, A. Fowler, B. Foxen, M. Giustina, E. Jeffrey, J. Kelly, E. Lucero, J. Mutus, M. Neeley, C. Quintana, D. Sank, A. Vainsencher, J. Wenner, T. White, H. Neven, D. G. Angelakis, and J. Martinis. Spectroscopic signatures of localization with interacting photons in superconducting qubits. *Science*, 358(6367):1175–1179, 2017.

[35] Mattias Fitzpatrick, Neereja M. Sundaresan, Andy C. Y. Li, Jens Koch, and Andrew A. Houck. Observation of a dissipative phase transition in a one-dimensional circuit qed lattice. *Phys. Rev. X*, 7:011016, Feb 2017.

[36] Ruichao Ma, Brendan Saxberg, Clai Owens, Nelson Leung, Yao Lu, Jonathan Simon, and David I. Schuster. A dissipatively stabilized mott insulator of photons. *Nature*, 566(7742):51–57, Feb 2019.

[37] B. Kraus and J. I. Cirac. Discrete entanglement distribution with squeezed light. *Phys. Rev. Lett.*, 92:013602, Jan 2004.

[38] C. Eichler, D. Bozyigit, C. Lang, M. Baur, L. Steffen, J. M. Fink, S. Filipp, and A. Wallraff. Observation of two-mode squeezing in the microwave frequency domain. *Phys. Rev. Lett.*, 107:113601, Sep 2011.

[39] E. Flurin, N. Roch, F. Mallet, M. H. Devoret, and B. Huard. Generating entangled microwave radiation over two transmission lines. *Phys. Rev. Lett.*, 109:183901, Oct 2012.

[40] Yao Lu, S. Chakram, N. Leung, N. Earnest, R. K. Naik, Ziwen Huang, Peter Groszkowski, Eliot Kapit, Jens Koch, and David I. Schuster. Universal stabilization of a parametrically coupled qubit. *Phys. Rev. Lett.*, 119:150502, Oct 2017.

[41] R. Dassonneville, R. Assouly, T. Peronnin, A.A. Clerk, A. Bienfait, and B. Huard. Dissipative stabilization of squeezing beyond 3 db in a microwave mode. *PRX Quantum*, 2:020323, May 2021.

[42] Andrew Pocklington, Yu-Xin Wang, and A. A. Clerk. Dissipative pairing interactions: Quantum instabilities, topological light, and volume-law entanglement. *Phys. Rev. Lett.*, 130:123602, Mar 2023.

[43] Carlton M. Caves and Bonny L. Schumaker. New formalism for two-photon quantum optics. i. quadrature phases and squeezed states. *Phys. Rev. A*, 31:3068–3092, May 1985.

[44] Christopher C. Gerry. Dynamics of su(1,1) coherent states. *Phys. Rev. A*, 31:2721–2723, Apr 1985.

[45] W. H. Louisell, A. Yariv, and A. E. Siegman. Quantum fluctuations and noise in parametric processes. i. *Phys. Rev.*, 124:1646–1654, Dec 1961.

[46] Ryuichi Shindou, Ryo Matsumoto, Shuichi Murakami, and Jun-ichiro Ohe. Topological chiral magnonic edge mode in a magnonic crystal. *Phys. Rev. B*, 87:174427, May 2013.

[47] Vittorio Peano, Martin Houde, Christian Brendel, Florian Marquardt, and Aashish A. Clerk. Topological phase transitions and chiral inelastic transport induced by the squeezing of light. *Nature Communications*, 7(1):10779, Mar 2016.

[48] Emil J. Bergholtz, Jan Carl Budich, and Flore K. Kunst. Exceptional topology of non-hermitian systems. *Rev. Mod. Phys.*, 93:015005, Feb 2021.

[49] A. McDonald, R. Hanai, and A. A. Clerk. Nonequilibrium stationary states of quantum non-hermitian lattice models. *Phys. Rev. B*, 105:064302, Feb 2022.

[50] Simon Lieu. Topological phases in the non-hermitian su-schrieffer-heeger model. *Phys. Rev. B*, 97:045106, Jan 2018.

[51] Ramy El-Ganainy, Mercedeh Khajavikhan, Demetrios N. Christodoulides, and Sahin K. Ozdemir. The dawn of non-hermitian optics. *Communications Physics*, 2(1):37, Mar 2019.

[52] Weijian Chen, Sahin Kaya Özdemir, Guangming Zhao, Jan Wiersig, and Lan Yang. Exceptional points enhance sensing in an optical microcavity. *Nature*, 548(7666):192–196, Aug 2017.

[53] Hossein Hodaei, Absar U. Hassan, Steffen Wittek, Hipolito Garcia-Gracia, Ramy El-Ganainy, Demetrios N. Christodoulides, and Mercedeh Khajavikhan. Enhanced sensitivity at higher-order exceptional points. *Nature*, 548(7666):187–191, Aug 2017.

[54] Michel Fruchart, Ryo Hanai, Peter B. Littlewood, and Vincenzo Vitelli. Non-reciprocal phase transitions. *Nature*, 592(7854):363–369, Apr 2021.

[55] Colin Scheibner, Anton Souslov, Debarghya Banerjee, Piotr Surówka, William T. M. Irvine, and Vincenzo Vitelli. Odd elasticity. *Nature Physics*, 16(4):475–480, Apr 2020.

[56] Kazuki Sone, Yuto Ashida, and Takahiro Sagawa. Exceptional non-hermitian topological edge mode and its application to active matter. *Nature Communications*, 11(1):5745, Nov 2020.

[57] Xiao-Liang Qi and Shou-Cheng Zhang. Topological insulators and superconductors. *Rev. Mod. Phys.*, 83:1057–1110, Oct 2011.

[58] M. Z. Hasan and C. L. Kane. Colloquium: Topological insulators. *Rev. Mod. Phys.*, 82:3045–3067, Nov 2010.

[59] D. J. Thouless, M. Kohmoto, M. P. Nightingale, and M. den Nijs. Quantized hall conductance in a two-dimensional periodic potential. *Phys. Rev. Lett.*, 49:405–408, Aug 1982.

[60] Yasutomo Ota, Kenta Takata, Tomoki Ozawa, Alberto Amo, Zhetao Jia, Boubacar Kante, Masaya Notomi, Yasuhiko Arakawa, and Satoshi Iwamoto. Active topological photonics. *Nanophotonics*, 9(3):547–567, 2022 2020.

[61] Tomoki Ozawa, Hannah M. Price, Alberto Amo, Nathan Goldman, Mohammad Hafezi, Ling Lu, Mikael C. Rechtsman, David Schuster, Jonathan Simon, Oded Zilberberg, and Iacopo Carusotto. Topological photonics. *Rev. Mod. Phys.*, 91:015006, Mar 2019.

[62] Ling Lu, John D. Joannopoulos, and Marin Soljačić. Topological photonics. *Nature Photonics*, 8(11):821–829, Nov 2014.

[63] Sunil Mittal, Elizabeth A. Goldschmidt, and Mohammad Hafezi. A topological source of quantum light. *Nature*, 561(7724):502–506, Sep 2018.

[64] Ryan Barnett. Edge-state instabilities of bosons in a topological band. *Phys. Rev. A*, 88:063631, Dec 2013.

[65] Bolun Hu, Zhiwang Zhang, Haixiao Zhang, Liyang Zheng, Wei Xiong, Zichong Yue, Xiaoyu Wang, Jianyi Xu, Ying Cheng, Xiaojun Liu, and Johan Christensen. Non-hermitian topological whispering gallery. *Nature*, 597(7878):655–659, Sep 2021.

[66] Vittorio Peano, Martin Houde, Florian Marquardt, and Aashish A. Clerk. Topological quantum fluctuations and traveling wave amplifiers. *Phys. Rev. X*, 6:041026, Nov 2016.

[67] G. Engelhardt, M. Benito, G. Platero, and T. Brandes. Topological instabilities in ac-driven bosonic systems. *Phys. Rev. Lett.*, 117:045302, Jul 2016.

[68] Matteo Seclì, Tomoki Ozawa, Massimo Capone, and Iacopo Carusotto. Spatial and spectral mode-selection effects in topological lasers with frequency-dependent gain. *APL Photonics*, 6(5):050803, May 2021.

[69] P. St-Jean, V. Goblot, E. Galopin, A. Lemaître, T. Ozawa, L. Le Gratiet, I. Sagnes, J. Bloch, and A. Amo. Lasing in topological edge states of a one-dimensionallattice. *Nature Photonics*, 11(10):651–656, Oct 2017.

[70] Midya Parto, Steffen Wittek, Hossein Hodaei, Gal Harari, Miguel A. Bandres, Jinhan Ren, Mikael C. Rechtsman, Mordechai Segev, Demetrios N. Christodoulides, and Mercedeh Khajavikhan. Edge-mode lasing in 1d topological active arrays. *Phys. Rev. Lett.*, 120:113901, Mar 2018.

[71] Han Zhao, Pei Miao, Mohammad H. Teimourpour, Simon Malzard, Ramy El-Ganainy, Henning Schomerus, and Liang Feng. Topological hybrid silicon microlasers. *Nature Communications*, 9(1):981, Mar 2018.

[72] Diego Porras and Samuel Fernández-Lorenzo. Topological amplification in photonic lattices. *Phys. Rev. Lett.*, 122:143901, Apr 2019.

[73] Joaquin Medina Dueñas, Gabriel O'Ryan Pérez, Carla Hermann-Avigliano, and Luis E. F. Foa Torres. Quadrature protection of squeezed states in a one-dimensional photonic topological insulator. *Quantum*, 5:526, August 2021.

[74] Clara C. Wanjura, Matteo Brunelli, and Andreas Nunnenkamp. Topological framework for directional amplification in driven-dissipative cavity arrays. *Nature Communications*, 11(1):3149, Jun 2020.

[75] Hoi-Kwan Lau and Aashish A. Clerk. Fundamental limits and non-reciprocal approaches in non-hermitian quantum sensing. *Nature Communications*, 9(1):4320, Oct 2018.

[76] G. Lindblad. On the generators of quantum dynamical semigroups. *Communications in Mathematical Physics*, 48(2):119–130, Jun 1976.

[77] Vittorio Gorini, Andrzej Kossakowski, and E. C. G. Sudarshan. Completely positive dynamical semigroups of n-level systems. *Journal of Mathematical Physics*, 17(5):821–825, 1976.

[78] Yu-Xin Wang and A. A. Clerk. Non-hermitian dynamics without dissipation in quantum systems. *Phys. Rev. A*, 99:063834, Jun 2019.

[79] Morris W Hirsch, Stephen Smale, and Robert L Devaney. *Differential equations, dynamical systems, and an introduction to chaos*. Academic press, 2012.

[80] Nishant Dogra, Manuele Landini, Katrin Kroeger, Lorenz Hruby, Tobias Donner, and Tilman Esslinger. Dissipation-induced structural instability and chiral dynamics in a quantum gas. *Science*, 366(6472):1496–1499, Dec 2019.

[81] We note that an analogous master equation has been studied for spins and fermions [1]; however, because they have a finite dimensional Hilbert space, they never experience instability. This makes the physics studied here qualitatively different, as it relies heavily on the interplay between dissipative pairing, instability, and wavefunction localization. These are not present in a fermionic or spin system.

[82] Christopher Gerry and Peter Knight. *Introductory quantum optics*. Cambridge University Press, 2005.

[83] D. F. Walls and G.J. Milburn. *Quantum Optics*. Springer, 2008.

[84] Andreas P. Schnyder, Shinsei Ryu, Akira Furusaki, and Andreas W. W. Ludwig. Classification of topological insulators and superconductors in three spatial dimensions. *Phys. Rev. B*, 78:195125, Nov 2008.

[85] Eunjong Kim, Xueyue Zhang, Vinicius S. Ferreira, Jash Banker, Joseph K. Iverson, Alp Sipahigil, Miguel Bello, Alejandro González-Tudela, Mohammad Mirhosseini, and Oskar Painter. Quantum electrodynamics in a topological waveguide. *Phys. Rev. X*, 11:011015, Jan 2021.

[86] Mohammad Hafezi, Eugene A. Demler, Mikhail D. Lukin, and Jacob M. Taylor. Robust optical delay lines with topological protection. *Nature Physics*, 7(11):907–912, Nov 2011.

[87] M. Hafezi, S. Mittal, J. Fan, A. Migdall, and J. M. Taylor. Imaging topological edge states in silicon photonics. *Nature Photonics*, 7(12):1001–1005, Dec 2013.

[88] Clai Owens, Aman LaChapelle, Brendan Saxberg, Brandon M. Anderson, Ruichao Ma, Jonathan Simon, and David I. Schuster. Quarter-flux hofstadter lattice in a qubit-compatible microwave cavity array. *Phys. Rev. A*, 97:013818, Jan 2018.

[89] Zheng Wang, Yidong Chong, J. D. Joannopoulos, and Marin Soljačić. Observation of unidirectional backscattering-immune topological electromagnetic states. *Nature*, 461(7265):772–775, Oct 2009.

[90] Yongkang Gong, Liang Guo, Stephan Wong, Anthony J. Bennett, and Sang Soon Oh. Tailoring topological edge states with photonic crystal nanobeam cavities. *Scientific Reports*, 11(1):1055, Jan 2021.

[91] Daniel Leykam and Luqi Yuan. Topological phases in ring resonators: recent progress and future prospects. *Nanophotonics*, 9(15):4473–4487, 2020.

[92] Amir Youssefi, Shingo Kono, Andrea Bancora, Mahdi Chegnizadeh, Jiahe Pan, Tatiana Vovk, and Tobias J. Kippenberg. Topological lattices realized in superconducting circuit optomechanics, 2021.

[93] V. Peano, C. Brendel, M. Schmidt, and F. Marquardt. Topological phases of sound and light. *Phys. Rev. X*, 5:031011, Jul 2015.

[94] Crispin Gardiner and Peter Zoller. *Quantum noise: a handbook of Markovian and non-Markovian quantum stochastic methods with applications to quantum optics*. Springer Series in Synergetics. Springer, Berlin, 2004.

[95] Andrew Pocklington and Aashish A. Clerk. Universal time-entanglement trade-off in open quantum systems, 2024.

[96] M. B. Hastings. An area law for one-dimensional quantum systems. *Journal of Statistical Mechanics: Theory and Experiment*, 2007(08):P08024, Aug 2007.

[97] Tomotaka Kuwahara and Keiji Saito. Area law of noncritical ground states in 1d long-range interacting systems. *Nature Communications*, 11(1):4478, Sep 2020.

[98] Zhe-Xuan Gong, Michael Foss-Feig, Fernando G. S. L. Brandão, and Alexey V. Gorshkov. Entanglement area laws for long-range interacting systems. *Phys. Rev. Lett.*, 119:050501, Jul 2017.

[99] Lluís Masanes. Area law for the entropy of low-energy states. *Phys. Rev. A*, 80:052104, Nov 2009.

[100] Anurag Anshu, Itai Arad, and David Gosset. An area law for 2d frustration-free spin systems. In *Proceedings of the 54th Annual ACM SIGACT Symposium on Theory of Computing*, STOC 2022, page 12–18, New York, NY, USA, 2022. Association for Computing Machinery.

[101] Fernando G. S. L. Brandão and Marcus Cramer. Entanglement area law from specific heat capacity. *Phys. Rev. B*, 92:115134, Sep 2015.

[102] Jaeyoon Cho. Sufficient condition for entanglement area laws in thermodynamically gapped spin systems. *Phys. Rev. Lett.*, 113:197204, Nov 2014.

[103] Spyridon Michalakis and Justyna P. Zwolak. Stability of frustration-free hamiltonians. *Communications in Mathematical Physics*, 322(2):277–302, Sep 2013.

[104] Michael M. Wolf, Frank Verstraete, Matthew B. Hastings, and J. Ignacio Cirac. Area laws in quantum systems: Mutual information and correlations. *Phys. Rev. Lett.*, 100:070502, Feb 2008.

[105] N. de Beaudrap, M. Ohliger, T. J. Osborne, and J. Eisert. Solving frustration-free spin systems. *Phys. Rev. Lett.*, 105:060504, Aug 2010.

[106] J. Eisert, M. Cramer, and M. B. Plenio. Colloquium: Area laws for the entanglement entropy. *Rev. Mod. Phys.*, 82:277–306, Feb 2010.

[107] Michael J. Kastoryano and Jens Eisert. Rapid mixing implies exponential decay of correlations. *Journal of Mathematical Physics*, 54(10):102201, Oct 2013.

[108] Fernando G. S. L. Brandão, Toby S. Cubitt, Angelo Lucia, Spyridon Michalakis, and David Perez-Garcia. Area law for fixed points of rapidly mixing dissipative quantum systems. *Journal of Mathematical Physics*, 56(10):102202, Oct 2015.

[109] David Poulin. Lieb-robinson bound and locality for general markovian quantum dynamics. *Phys. Rev. Lett.*, 104:190401, May 2010.

[110] S. G. Schirmer and Xiaoting Wang. Stabilizing open quantum systems by markovian reservoir engineering. *Phys. Rev. A*, 81:062306, Jun 2010.

[111] K. Stannigel, P. Rabl, and P. Zoller. Driven-dissipative preparation of entangled states in cascaded quantum-optical networks. *New Journal of Physics*, 14(6):063014, Jun 2012.

[112] Felix Motzoi, Eli Halperin, Xiaoting Wang, K. Birgitta Whaley, and Sophie Schirmer. Backaction-driven, robust, steady-state long-distance qubit entanglement over lossy channels. *Physical Review A*, 94(3):032313, September 2016.

[113] E. Doucet, F. Reiter, L. Ranzani, and A. Kamal. High fidelity dissipation engineering using parametric interactions. *Phys. Rev. Res.*, 2:023370, Jun 2020.

[114] Stefano Zippilli and David Vitali. Dissipative engineering of gaussian entangled states in harmonic lattices with a single-site squeezed reservoir. *Phys. Rev. Lett.*, 126:020402, Jan 2021.

[115] J. Agustí, Y. Minoguchi, J. M. Fink, and P. Rabl. Long-distance distribution of qubit-qubit entanglement using Gaussian-correlated photonic beams. *Physical Review A*, 105(6):062454, June 2022.

[116] L. C. G. Govia, A. Lingenfelter, and A. A. Clerk. Stabilizing two-qubit entanglement by mimicking a squeezed environment. *Phys. Rev. Res.*, 4:023010, Apr 2022.

[117] T. Brown, E. Doucet, D. Ristè, G. Ribeill, K. Cicak, J. Aumentado, R. Simmonds, L. Govia, A. Kamal, and L. Ranzani. Trade off-free entanglement stabilization in a superconducting qutrit-qubit system. *Nature Communications*, 13(1):3994, Jul 2022.

[118] Jacopo Angeletti, Stefano Zippilli, and David Vitali. Dissipative stabilization of entangled qubit pairs in quantum arrays with a single localized dissipative channel. *Quantum Science and Technology*, 8(3):035020, May 2023.

[119] Andrew Lingenfelter, Mingxing Yao, Andrew Pocklington, Yu-Xin Wang, Abdullah Irfan, Wolfgang Pfaff, and Aashish A. Clerk. Exact results for a boundary-driven double spin chain and resource-efficient remote entanglement stabilization, 2023.

[120] Jinkang Guo, Oliver Hart, Chi-Fang Chen, Aaron J. Friedman, and Andrew Lucas. Designing open quantum systems with known steady states: Davies generators and beyond, 2024.

[121] Chi-Fang Chen, Michael J. Kastoryano, Fernando G. S. L. Brandão, and András Gilyén. Quantum thermal state preparation, 2023.

[122] Zhiyan Ding, Bowen Li, and Lin Lin. Efficient quantum gibbs samplers with kubo–martin–schwinger detailed balance condition, 2024.

[123] Shi-Kang Sun and Shu Chen. Emergence of gibbs ensemble as the unique steady state in open quantum systems, 2024.

[124] Mikhail Mamaev, Martin Koppenhöfer, Andrew Pocklington, and Aashish A. Clerk. Non-gaussian generalized two-mode squeezing: applications to two-ensemble spin squeezing and beyond, 2024.

[125] Observe that because the (e.g. Bures) metric is contractive under completely positive, trace preserving maps, then by the contraction mapping theorem the Lindblad generator acting on a finite dimensional Hilbert space must have a zero eigenvalue. Hence, we define this zero eigenvalue to be λ_0, and arrange all remaining eigenvalues according to their real parts.

[126] Heinz-Peter Breuer and Francesco Petruccione. *The theory of open quantum systems*. Oxford University Press, New York, USA, 2002.

[127] H. M. Wiseman and G. J. Milburn. Quantum theory of optical feedback via homodyne detection. *Phys. Rev. Lett.*, 70:548–551, Feb 1993.

[128] H. M. Wiseman and G. J. Milburn. Squeezing via feedback. *Phys. Rev. A*, 49:1350–1366, Feb 1994.

[129] A. Metelmann and A. A. Clerk. Nonreciprocal quantum interactions and devices via autonomous feedforward. *Phys. Rev. A*, 95:013837, Jan 2017.

[130] Howard M Wiseman and Gerard J Milburn. *Quantum measurement and control*. Cambridge university press, 2009.

[131] Berislav Buča and Tomaž Prosen. A note on symmetry reductions of the lindblad equation: transport in constrained open spin chains. *New Journal of Physics*, 14(7):073007, jul 2012.

[132] K. Temme, M. J. Kastoryano, M. B. Ruskai, M. M. Wolf, and F. Verstraete. The χ^2-divergence and mixing times of quantum markov processes. *Journal of Mathematical Physics*, 51(12):122201, Dec 2010.

[133] Michael A Nielsen and Isaac L Chuang. Quantum computation and quantum information. *Phys. Today*, 54(2):60, 2001.

[134] Franco Fagnola and Veronica Umanita. Generators of detailed balance quantum markov semigroups. *Infinite Dimensional Analysis, Quantum Probability and Related Topics*, 10(03):335–363, 2007.

[135] Franco Fagnola and Veronica Umanità. Generators of kms symmetric markov semigroups on $\mathcal{B}(h)$ symmetry and quantum detailed balance. *Communications in Mathematical Physics*, 298(2):523–547, Sep 2010.

[136] David Roberts, Andrew Lingenfelter, and A.A. Clerk. Hidden time-reversal symmetry, quantum detailed balance and exact solutions of driven-dissipative quantum systems. *PRX Quantum*, 2:020336, Jun 2021.

[137] David Roberts and Aashish A. Clerk. Driven-dissipative quantum kerr resonators: New exact solutions, photon blockade and quantum bistability. *Phys. Rev. X*, 10:021022, Apr 2020.

[138] Mankei Tsang. Quantum reversal: a general theory of coherent quantum absorbers, 2024.

[139] William Cottrell, Ben Freivogel, Diego M. Hofman, and Sagar F. Lokhande. How to build the thermofield double state. *Journal of High Energy Physics*, 2019(2):58, Feb 2019.

[140] Ja š Bensa and Marko Žnidarič. Fastest local entanglement scrambler, multistage thermalization, and a non-hermitian phantom. *Phys. Rev. X*, 11:031019, Jul 2021.

[141] Ja š Bensa and Marko Žnidarič. Two-step phantom relaxation of out-of-time-ordered correlations in random circuits. *Phys. Rev. Res.*, 4:013228, Mar 2022.

[142] Gideon Lee, Alexander McDonald, and Aashish Clerk. Anomalously large relaxation times in dissipative lattice models beyond the non-hermitian skin effect. *Phys. Rev. B*, 108:064311, Aug 2023.

[143] Shunyu Yao and Zhong Wang. Edge states and topological invariants of non-hermitian systems. *Phys. Rev. Lett.*, 121:086803, Aug 2018.

[144] Tony E. Lee. Anomalous edge state in a non-hermitian lattice. *Phys. Rev. Lett.*, 116:133903, Apr 2016.

[145] Flore K. Kunst, Elisabet Edvardsson, Jan Carl Budich, and Emil J. Bergholtz. Biorthogonal bulk-boundary correspondence in non-hermitian systems. *Phys. Rev. Lett.*, 121:026808, Jul 2018.

[146] A. McDonald, T. Pereg-Barnea, and A. A. Clerk. Phase-dependent chiral transport and effective non-hermitian dynamics in a bosonic kitaev-majorana chain. *Phys. Rev. X*, 8:041031, Nov 2018.

[147] Kohei Kawabata, Ken Shiozaki, Masahito Ueda, and Masatoshi Sato. Symmetry and topology in non-hermitian physics. *Phys. Rev. X*, 9:041015, Oct 2019.

[148] V. M. Martinez Alvarez, J. E. Barrios Vargas, and L. E. F. Foa Torres. Non-hermitian robust edge states in one dimension: Anomalous localization and eigenspace condensation at exceptional points. *Phys. Rev. B*, 97:121401(R), Mar 2018.

[149] Taiki Haga, Masaya Nakagawa, Ryusuke Hamazaki, and Masahito Ueda. Liouvillian skin effect: Slowing down of relaxation processes without gap closing. *Phys. Rev. Lett.*, 127:070402, Aug 2021.

[150] Sergey Denisov, Tetyana Laptyeva, Wojciech Tarnowski, Dariusz Chruściński, and Karol Życzkowski. Universal spectra of random lindblad operators. *Phys. Rev. Lett.*, 123:140403, Oct 2019.

[151] Florentin Reiter and Anders S. Sørensen. Effective operator formalism for open quantum systems. *Phys. Rev. A*, 85:032111, Mar 2012.

[152] H. J. Carmichael. Quantum trajectory theory for cascaded open systems. *Phys. Rev. Lett.*, 70:2273–2276, Apr 1993.

[153] C. W. Gardiner. Driving a quantum system with the output field from another driven quantum system. *Phys. Rev. Lett.*, 70:2269–2272, Apr 1993.

[154] A. Metelmann and A. A. Clerk. Nonreciprocal photon transmission and amplification via reservoir engineering. *Phys. Rev. X*, 5:021025, Jun 2015.

[155] Wojciech Tarnowski, Dariusz Chruściński, Sergey Denisov, and Karol Życzkowski. Random lindblad operators obeying detailed balance. *Open Systems & Information Dynamics*, 30(02):2350007, 2023.

[156] Marko Žnidarič. Coexistence of diffusive and ballistic transport in a simple spin ladder. *Phys. Rev. Lett.*, 110:070602, Feb 2013.

[157] Andrew Pocklington and Aashish A. Clerk. Accelerating dissipative state preparation with adaptive open quantum dynamics. *Phys. Rev. Lett.*, 134:050603, Feb 2025.

[158] Charlene Ahn, Andrew C. Doherty, and Andrew J. Landahl. Continuous quantum error correction via quantum feedback control. *Phys. Rev. A*, 65:042301, Mar 2002.

[159] D. Ristè, M. Dukalski, C. A. Watson, G. de Lange, M. J. Tiggelman, Ya. M. Blanter, K. W. Lehnert, R. N. Schouten, and L. DiCarlo. Deterministic entanglement of superconducting qubits by parity measurement and feedback. *Nature*, 502(7471):350–354, Oct 2013.

[160] J. Agustí, X. H. H. Zhang, Y. Minoguchi, and P. Rabl. Autonomous distribution of programmable multiqubit entanglement in a dual-rail quantum network. *Phys. Rev. Lett.*, 131:250801, Dec 2023.

[161] D. A. Ivanov, T. Yu. Ivanova, S. F. Caballero-Benitez, and I. B. Mekhov. Feedback-induced quantum phase transitions using weak measurements. *Phys. Rev. Lett.*, 124:010603, Jan 2020.

[162] Masaya Nakagawa and Masahito Ueda. Topology of discrete quantum feedback control, 2024.

[163] Lorenzo Piroli, Georgios Styliaris, and J. Ignacio Cirac. Quantum circuits assisted by local operations and classical communication: Transformations and phases of matter. *Phys. Rev. Lett.*, 127:220503, Nov 2021.

[164] Nathanan Tantivasadakarn, Ryan Thorngren, Ashvin Vishwanath, and Ruben Verresen. Long-range entanglement from measuring symmetry-protected topological phases, 2022.

[165] Tsung-Cheng Lu, Leonardo A. Lessa, Isaac H. Kim, and Timothy H. Hsieh. Measurement as a shortcut to long-range entangled quantum matter. *PRX Quantum*, 3:040337, Dec 2022.

[166] Katrin Kroeger, Nishant Dogra, Rodrigo Rosa-Medina, Marcin Paluch, Francesco Ferri, Tobias Donner, and Tilman Esslinger. Continuous feedback on a quantum gas coupled to an optical cavity. *New Journal of Physics*, 22(3):033020, 2020.

[167] M. Gajdacz, A. J. Hilliard, M. A. Kristensen, P. L. Pedersen, C. Klempt, J. J. Arlt, and J. F. Sherson. Preparation of ultracold atom clouds at the shot noise level. *Phys. Rev. Lett.*, 117:073604, Aug 2016.

[168] Ian D. Leroux, Monika H. Schleier-Smith, Hao Zhang, and Vladan Vuletić. Unitary cavity spin squeezing by quantum erasure. *Phys. Rev. A*, 85:013803, Jan 2012.

[169] Clément Sayrin, Igor Dotsenko, Xingxing Zhou, Bruno Peaudecerf, Théo Rybarczyk, Sébastien Gleyzes, Pierre Rouchon, Mazyar Mirrahimi, Hadis Amini, Michel Brune, Jean-Michel Raimond, and Serge Haroche. Real-time quantum feedback prepares and stabilizes photon number states. *Nature*, 477(7362):73–77, Sep 2011.

[170] R. Vijay, C. Macklin, D. H. Slichter, S. J. Weber, K. W. Murch, R. Naik, A. N. Korotkov, and I. Siddiqi. Stabilizing rabi oscillations in a superconducting qubit using quantum feedback. *Nature*, 490(7418):77–80, Oct 2012.

[171] Lorenzo Magrini, Philipp Rosenzweig, Constanze Bach, Andreas Deutschmann-Olek, Sebastian G. Hofer, Sungkun Hong, Nikolai Kiesel, Andreas Kugi, and Markus Aspelmeyer. Real-time optimal quantum control of mechanical motion at room temperature. *Nature*, 595(7867):373–377, Jul 2021.

[172] A Vourdas. Exterior calculus and fermionic quantum computation. *Journal of Physics A: Mathematical and Theoretical*, 51(44):445301, oct 2018.

[173] Oles Shtanko, Abhinav Deshpande, Paul S. Julienne, and Alexey V. Gorshkov. Complexity of fermionic dissipative interactions and applications to quantum computing. *PRX Quantum*, 2:030350, Sep 2021.

[174] Ruben Verresen, Nathanan Tantivasadakarn, and Ashvin Vishwanath. Efficiently preparing schrödinger's cat, fractons and non-abelian topological order in quantum devices, 2022.

[175] Sergey Bravyi, Isaac Kim, Alexander Kliesch, and Robert Koenig. Adaptive constant-depth circuits for manipulating non-abelian anyons, 2022.

[176] Nathanan Tantivasadakarn, Ruben Verresen, and Ashvin Vishwanath. Shortest route to non-abelian topological order on a quantum processor. *Physical Review Letters*, 131(6), August 2023.

[177] Seth Lloyd and Lorenza Viola. Engineering quantum dynamics. *Phys. Rev. A*, 65:010101, Dec 2001.

[178] Chao Shen, Kyungjoo Noh, Victor V. Albert, Stefan Krastanov, M. H. Devoret, R. J. Schoelkopf, S. M. Girvin, and Liang Jiang. Quantum channel construction with circuit quantum electrodynamics. *Phys. Rev. B*, 95:134501, Apr 2017.

[179] J. Han, W. Cai, L. Hu, X. Mu, Y. Ma, Y. Xu, W. Wang, H. Wang, Y. P. Song, C.-L. Zou, and L. Sun. Experimental simulation of open quantum system dynamics via trotterization. *Phys. Rev. Lett.*, 127:020504, Jul 2021.

[180] GS Agarwal and RR Puri. Nonequilibrium phase transitions in a squeezed cavity and the generation of spin states satisfying uncertainty equality. *Optics communications*, 69(3-4):267–270, 1989.

[181] Emanuele G. Dalla Torre, Johannes Otterbach, Eugene Demler, Vladan Vuletic, and Mikhail D. Lukin. Dissipative preparation of spin squeezed atomic ensembles in a steady state. *Phys. Rev. Lett.*, 110:120402, Mar 2013.

[182] Peter Groszkowski, Martin Koppenhöfer, Hoi-Kwan Lau, and A. A. Clerk. Reservoir-engineered spin squeezing: Macroscopic even-odd effects and hybrid-systems implementations. *Phys. Rev. X*, 12:011015, Jan 2022.

[183] E B Mpemba and D G Osborne. Cool? *Physics Education*, 4(3):172, may 1969.

[184] Federico Carollo, Antonio Lasanta, and Igor Lesanovsky. Exponentially accelerated approach to stationarity in markovian open quantum systems through the mpemba effect. *Phys. Rev. Lett.*, 127:060401, Aug 2021.

[185] Amit Kumar Chatterjee, Satoshi Takada, and Hisao Hayakawa. Quantum mpemba effect in a quantum dot with reservoirs. *Phys. Rev. Lett.*, 131:080402, Aug 2023.

[186] Andrew Pocklington and Aashish A. Clerk. Efficient simulation of nontrivial dissipative spin chains via stochastic unraveling. *PRX Quantum*, 6:030349, Sep 2025.

[187] B. Bertini, F. Heidrich-Meisner, C. Karrasch, T. Prosen, R. Steinigeweg, and M. Žnidarič. Finite-temperature transport in one-dimensional quantum lattice models. *Rev. Mod. Phys.*, 93:025003, May 2021.

[188] Gabriel T. Landi, Dario Poletti, and Gernot Schaller. Nonequilibrium boundary-driven quantum systems: Models, methods, and properties. *Rev. Mod. Phys.*, 94:045006, Dec 2022.

[189] Subir Sachdev. Quantum phase transitions. *Physics world*, 12(4):33, 1999.

[190] Thierry Giamarchi. *Quantum physics in one dimension*, volume 121. Clarendon press, 2003.

[191] Pasquale Calabrese and John Cardy. Evolution of entanglement entropy in one-dimensional systems. *Journal of Statistical Mechanics: Theory and Experiment*, 2005(04):P04010, apr 2005.

[192] Gabriele De Chiara, Simone Montangero, Pasquale Calabrese, and Rosario Fazio. Entanglement entropy dynamics of heisenberg chains. *Journal of Statistical Mechanics: Theory and Experiment*, 2006(03):P03001, mar 2006.

[193] John Preskill. Quantum Computing in the NISQ era and beyond. *Quantum*, 2:79, August 2018.

[194] Toma ž Prosen. Exact nonequilibrium steady state of a strongly driven open xxz chain. *Phys. Rev. Lett.*, 107:137201, Sep 2011.

[195] Tomaž Prosen, Enej Ilievski, and Vladislav Popkov. Exterior integrability: Yang–baxter form of non-equilibrium steady-state density operator. *New Journal of Physics*, 15(7):073051, jul 2013.

[196] Mingxing Yao, Andrew Lingenfelter, Ron Belyansky, David Roberts, and Aashish A. Clerk. Hidden time reversal in driven xxz spin chains: Exact solutions and new dissipative phase transitions. *Phys. Rev. Lett.*, 134:130404, Apr 2025.

[197] Naushad A. Kamar and Mohammad Maghrebi. Hybrid quantum-classical stochastic approach to dissipative spin-boson models. *Phys. Rev. X*, 15:021073, May 2025.

[198] Alexei Kitaev. Anyons in an exactly solved model and beyond. *Annals of Physics*, 321(1):2–111, 2006. January Special Issue.

[199] Barbara M. Terhal and David P. DiVincenzo. Classical simulation of noninteracting-fermion quantum circuits. *Phys. Rev. A*, 65:032325, Mar 2002.

[200] Leslie G. Valiant. Quantum computers that can be simulated classically in polynomial time. In *Proceedings of the Thirty-Third Annual ACM Symposium on Theory of Computing*, STOC '01, page 114–123, New York, NY, USA, 2001. Association for Computing Machinery.

[201] Birger Horstmann, J. Ignacio Cirac, and Géza Giedke. Noise-driven dynamics and phase transitions in fermionic systems. *Phys. Rev. A*, 87:012108, Jan 2013.

[202] Thomas Barthel and Yikang Zhang. Solving quasi-free and quadratic lindblad master equations for open fermionic and bosonic systems. *Journal of Statistical Mechanics: Theory and Experiment*, 2022(11):113101, nov 2022.

[203] Dorit Aharonov. Quantum to classical phase transition in noisy quantum computers. *Phys. Rev. A*, 62:062311, Nov 2000.

[204] Rahul Trivedi and J. Ignacio Cirac. Transitions in computational complexity of continuous-time local open quantum dynamics. *Phys. Rev. Lett.*, 129:260405, Dec 2022.

[205] Juan Mauricio Torres. Closed-form solution of lindblad master equations without gain. *Phys. Rev. A*, 89:052133, May 2014.

[206] A. Smith, J. Knolle, D. L. Kovrizhin, and R. Moessner. Disorder-free localization. *Phys. Rev. Lett.*, 118:266601, Jun 2017.

[207] Yu-Xin Wang, Chen Wang, and Aashish A. Clerk. Quantum nonreciprocal interactions via dissipative gauge symmetry. *PRX Quantum*, 4:010306, Jan 2023.

[208] Guillermo González-García, Alexey V. Gorshkov, J. Ignacio Cirac, and Rahul Trivedi. Dynamical complexity of non-gaussian many-body systems with dissipation, 2025.

[209] A. Asenjo-Garcia, J. D. Hood, D. E. Chang, and H. J. Kimble. Atom-light interactions in quasi-one-dimensional nanostructures: A green's-function perspective. *Phys. Rev. A*, 95:033818, Mar 2017.

[210] A. Asenjo-Garcia, M. Moreno-Cardoner, A. Albrecht, H. J. Kimble, and D. E. Chang. Exponential improvement in photon storage fidelities using subradiance and "selective radiance" in atomic arrays. *Phys. Rev. X*, 7:031024, Aug 2017.

[211] Loïc Henriet, James S. Douglas, Darrick E. Chang, and Andreas Albrecht. Critical open-system dynamics in a one-dimensional optical-lattice clock. *Phys. Rev. A*, 99:023802, Feb 2019.

[212] Andreas Albrecht, Loïc Henriet, Ana Asenjo-Garcia, Paul B Dieterle, Oskar Painter, and Darrick E Chang. Subradiant states of quantum bits coupled to a one-dimensional waveguide. *New Journal of Physics*, 21(2):025003, feb 2019.

[213] Yu-Xiang Zhang and Klaus Mølmer. Theory of subradiant states of a one-dimensional two-level atom chain. *Phys. Rev. Lett.*, 122:203605, May 2019.

[214] Yu-Xiang Zhang and Klaus Mølmer. Subradiant emission from regular atomic arrays: Universal scaling of decay rates from the generalized bloch theorem. *Phys. Rev. Lett.*, 125:253601, Dec 2020.

[215] Yu-Xiang Zhang and Klaus Mølmer. Free-fermion multiply excited eigenstates and their experimental signatures in 1d arrays of two-level atoms. *Phys. Rev. Lett.*, 128:093602, Mar 2022.

[216] Alexandra S. Sheremet, Mihail I. Petrov, Ivan V. Iorsh, Alexander V. Poshakinskiy, and Alexander N. Poddubny. Waveguide quantum electrodynamics: Collective radiance and photon-photon correlations. *Rev. Mod. Phys.*, 95:015002, Mar 2023.

[217] G. Facchinetti, S. D. Jenkins, and J. Ruostekoski. Storing light with subradiant correlations in arrays of atoms. *Phys. Rev. Lett.*, 117:243601, Dec 2016.

[218] M T Manzoni, M Moreno-Cardoner, A Asenjo-Garcia, J V Porto, A V Gorshkov, and D E Chang. Optimization of photon storage fidelity in ordered atomic arrays. *New Journal of Physics*, 20(8):083048, aug 2018.

[219] Samuel E. Begg and Ryo Hanai. Quantum criticality in open quantum spin chains with nonreciprocity. *Phys. Rev. Lett.*, 132:120401, Mar 2024.

[220] Yu-Peng Wang, Chen Fang, and Jie Ren. Superdiffusive transport in quasi-particle dephasing models. *SciPost Phys.*, 17:150, 2024.

[221] Marcos Rigol, Vanja Dunjko, Vladimir Yurovsky, and Maxim Olshanii. Relaxation in a completely integrable many-body quantum system: An ab initio study of the dynamics of the highly excited states of 1d lattice hard-core bosons. *Phys. Rev. Lett.*, 98:050405, Feb 2007.

[222] E. Ilievski, J. De Nardis, B. Wouters, J.-S. Caux, F. H. L. Essler, and T. Prosen. Complete generalized gibbs ensembles in an interacting theory. *Phys. Rev. Lett.*, 115:157201, Oct 2015.

[223] Mostafa Ali, Naushad A. Kamar, Alireza Seif, and Mohammad Maghrebi. Signatures of quantum phase transitions in driven dissipative spin chains, 2024.

[224] Isabelle Bouchoule, Benjamin Doyon, and Jerome Dubail. The effect of atom losses on the distribution of rapidities in the one-dimensional Bose gas. *SciPost Phys.*, 9:044, 2020.

[225] Chaitanya Joshi, Felix Nissen, and Jonathan Keeling. Quantum correlations in the one-dimensional driven dissipative xy model. *Phys. Rev. A*, 88:063835, Dec 2013.

[226] Charles H. Bennett, David P. DiVincenzo, John A. Smolin, and William K. Wootters. Mixed-state entanglement and quantum error correction. *Phys. Rev. A*, 54:3824–3851, Nov 1996.

[227] Kang Yang, Siddhardh C. Morampudi, and Emil J. Bergholtz. Exceptional spin liquids from couplings to the environment. *Phys. Rev. Lett.*, 126:077201, Feb 2021.

[228] Xu Feng, Shuo Liu, Shu Chen, and Wenan Guo. Absence of logarithmic and algebraic scaling entanglement phases due to the skin effect. *Phys. Rev. B*, 107:094309, Mar 2023.

[229] Yu-Peng Wang, Chen Fang, and Jie Ren. Absence of measurement-induced entanglement transition due to feedback-induced skin effect. *Phys. Rev. B*, 110:035113, Jul 2024.

[230] Ze-Chuan Liu, Kai Li, and Yong Xu. Dynamical transition due to feedback-induced skin effect. *Phys. Rev. Lett.*, 133:090401, Aug 2024.

[231] Craig S. Hamilton, Regina Kruse, Linda Sansoni, Sonja Barkhofen, Christine Silberhorn, and Igor Jex. Gaussian boson sampling. *Phys. Rev. Lett.*, 119:170501, Oct 2017.

[232] Tatiana Vovk and Hannes Pichler. Entanglement-optimal trajectories of many-body quantum markov processes. *Phys. Rev. Lett.*, 128:243601, Jun 2022.

[233] Andrew Pocklington and Aashish A. Clerk. Insights into decohered critical states using an exact solution to matchgate circuits with pauli noise, 2026.

[234] Sylvain de Léséleuc, Vincent Lienhard, Pascal Scholl, Daniel Barredo, Sebastian Weber, Nicolai Lang, Hans Peter Büchler, Thierry Lahaye, and Antoine Browaeys. Observation of a symmetry-protected topological phase of interacting bosons with rydberg atoms. *Science*, 365(6455):775–780, 2019.

[235] G. Semeghini, H. Levine, A. Keesling, S. Ebadi, T. T. Wang, D. Bluvstein, R. Verresen, H. Pichler, M. Kalinowski, R. Samajdar, A. Omran, S. Sachdev, A. Vishwanath, M. Greiner, V. Vuletić, and M. D. Lukin. Probing topological spin liquids on a programmable quantum simulator. *Science*, 374(6572):1242–1247, 2021.

[236] Pimonpan Sompet, Sarah Hirthe, Dominik Bourgund, Thomas Chalopin, Julian Bibo, Joannis Koepsell, Petar Bojović, Ruben Verresen, Frank Pollmann, Guillaume Salomon, Christian Gross, Timon A. Hilker, and Immanuel Bloch. Realizing the symmetry-protected haldane phase in fermi–hubbard ladders. *Nature*, 606(7914):484–488, Jun 2022.

[237] Fang Fang, Kenneth Wang, Vincent S. Liu, Yu Wang, Ryan Cimmino, Julia Wei, Marcus Bintz, Avery Parr, Jack Kemp, Kang-Kuen Ni, and Norman Y. Yao. Probing critical phenomena in open quantum systems using atom arrays, 2025.

[238] Lin Su, Rahul Sahay, Michal Szurek, Alexander Douglas, Ognjen Markovic, Ceren B. Dag, Ruben Verresen, and Markus Greiner. Topological phase transitions and mixed state order in a hubbard quantum simulator, 2025.

[239] Xiangkai Sun, Yuan Le, Stephen Naus, Richard Bing-Shiun Tsai, Lewis R. B. Picard, Sara Murciano, Michael Knap, Jason Alicea, and Manuel Endres. Experimental observation of conformal field theory spectra, 2026.

[240] D. Zhu, S. Johri, N. M. Linke, K. A. Landsman, C. Huerta Alderete, N. H. Nguyen, A. Y. Matsuura, T. H. Hsieh, and C. Monroe. Generation of thermofield double states and critical ground states with a quantum computer. *Proceedings of the National Academy of Sciences*, 117(41):25402–25406, 2020.

[241] K. J. Satzinger, Y.-J Liu, A. Smith, C. Knapp, M. Newman, C. Jones, Z. Chen, C. Quintana, X. Mi, A. Dunsworth, C. Gidney, I. Aleiner, F. Arute, K. Arya, J. Atalaya, R. Babbush, J. C. Bardin, R. Barends, J. Basso, A. Bengtsson, A. Bilmes, M. Broughton, B. B. Buckley, D. A. Buell, B. Burkett, N. Bushnell, B. Chiaro, R. Collins, W. Courtney, S. Demura, A. R. Derk, D. Eppens, C. Erickson, L. Faoro, E. Farhi, A. G. Fowler, B. Foxen, M. Giustina, A. Greene, J. A. Gross, M. P. Harrigan, S. D. Harrington, J. Hilton, S. Hong, T. Huang, W. J. Huggins, L. B. Ioffe, S. V. Isakov, E. Jeffrey, Z. Jiang, D. Kafri, K. Kechedzhi, T. Khattar, S. Kim, P. V. Klimov, A. N. Korotkov, F. Kostritsa, D. Landhuis, P. Laptev, A. Locharla, E. Lucero, O. Martin, J. R. McClean, M. McEwen, K. C. Miao, M. Mohseni, S. Montazeri, W. Mruczkiewicz, J. Mutus, O. Naaman, M. Neeley, C. Neill, M. Y. Niu, T. E. O'Brien, A. Opremcak, B. Pató, A. Petukhov, N. C. Rubin, D. Sank, V. Shvarts, D. Strain, M. Szalay, B. Villalonga, T. C. White, Z. Yao, P. Yeh, J. Yoo, A. Zalcman, H. Neven, S. Boixo, A. Megrant, Y. Chen, J. Kelly, V. Smelyanskiy, A. Kitaev, M. Knap, F. Pollmann, and P. Roushan. Realizing topologically ordered states on a quantum processor. *Science*, 374(6572):1237–1241, 2021.

[242] Reza Haghshenas, Eli Chertkov, Matthew DeCross, Thomas M. Gatterman, Justin A. Gerber, Kevin Gilmore, Dan Gresh, Nathan Hewitt, Chandler V. Horst, Mitchell Matheny, Tanner Mengle, Brian Neyenhuis, David Hayes, and Michael Foss-Feig. Probing critical states of matter on a digital quantum computer. *Phys. Rev. Lett.*, 133:266502, Dec 2024.

[243] X. Mi, A. A. Michailidis, S. Shabani, K. C. Miao, P. V. Klimov, J. Lloyd, E. Rosenberg, R. Acharya, I. Aleiner, T. I. Andersen, M. Ansmann, F. Arute, K. Arya, A. Asfaw, J. Atalaya, J. C. Bardin, A. Bengtsson, G. Bortoli, A. Bourassa, J. Bovaird, L. Brill, M. Broughton, B. B. Buckley, D. A. Buell, T. Burger, B. Burkett, N. Bushnell, Z. Chen, B. Chiaro, D. Chik, C. Chou, J. Cogan, R. Collins, P. Conner, W. Courtney, A. L.

Crook, B. Curtin, A. G. Dau, D. M. Debroy, A. Del Toro Barba, S. Demura, A. Di Paolo, I. K. Drozdov, A. Dunsworth, C. Erickson, L. Faoro, E. Farhi, R. Fatemi, V. S. Ferreira, L. F. Burgos, E. Forati, A. G. Fowler, B. Foxen, É. Genois, W. Giang, C. Gidney, D. Gilboa, M. Giustina, R. Gosula, J. A. Gross, S. Habegger, M. C. Hamilton, M. Hansen, M. P. Harrigan, S. D. Harrington, P. Heu, M. R. Hoffmann, S. Hong, T. Huang, A. Huff, W. J. Huggins, L. B. Ioffe, S. V. Isakov, J. Iveland, E. Jeffrey, Z. Jiang, C. Jones, P. Juhas, D. Kafri, K. Kechedzhi, T. Khattar, M. Khezri, M. Kieferová, S. Kim, A. Kitaev, A. R. Klots, A. N. Korotkov, F. Kostritsa, J. M. Kreikebaum, D. Landhuis, P. Laptev, K.-M. Lau, L. Laws, J. Lee, K. W. Lee, Y. D. Lensky, B. J. Lester, A. T. Lill, W. Liu, A. Locharla, F. D. Malone, O. Martin, J. R. McClean, M. McEwen, A. Mieszala, S. Montazeri, A. Morvan, R. Movassagh, W. Mruczkiewicz, M. Neeley, C. Neill, A. Nersisyan, M. Newman, J. H. Ng, A. Nguyen, M. Nguyen, M. Y. Niu, T. E. O'Brien, A. Opremcak, A. Petukhov, R. Potter, L. P. Pryadko, C. Quintana, C. Rocque, N. C. Rubin, N. Saei, D. Sank, K. Sankaragomathi, K. J. Satzinger, H. F. Schurkus, C. Schuster, M. J. Shearn, A. Shorter, N. Shutty, V. Shvarts, J. Skruzny, W. C. Smith, R. Somma, G. Sterling, D. Strain, M. Szalay, A. Torres, G. Vidal, B. Villalonga, C. V. Heidweiller, T. White, B. W. K. Woo, C. Xing, Z. J. Yao, P. Yeh, J. Yoo, G. Young, A. Zalcman, Y. Zhang, N. Zhu, N. Zobrist, H. Neven, R. Babbush, D. Bacon, S. Boixo, J. Hilton, E. Lucero, A. Megrant, J. Kelly, Y. Chen, P. Roushan, V. Smelyanskiy, and D. A. Abanin. Stable quantum-correlated many-body states through engineered dissipation. *Science*, 383(6689):1332–1337, 2024.

[244] Simon J. Evered, Marcin Kalinowski, Alexandra A. Geim, Tom Manovitz, Dolev Bluvstein, Sophie H. Li, Nishad Maskara, Hengyun Zhou, Sepehr Ebadi, Muqing Xu, Joseph Campo, Madelyn Cain, Stefan Ostermann, Susanne F. Yelin, Subir Sachdev, Markus Greiner, Vladan Vuletić, and Mikhail D. Lukin. Probing the kitaev honeycomb model on a neutral-atom quantum computer. *Nature*, 645(8080):341–347, Sep 2025.

[245] Shengqi Sang, Yijian Zou, and Timothy H. Hsieh. Mixed-state quantum phases: Renormalization and quantum error correction. *Phys. Rev. X*, 14:031044, Sep 2024.

[246] Tibor Rakovszky, Sarang Gopalakrishnan, and Curt von Keyserlingk. Defining stable phases of open quantum systems. *Phys. Rev. X*, 14:041031, Nov 2024.

[247] Shengqi Sang and Timothy H. Hsieh. Stability of mixed-state quantum phases via finite markov length. *Phys. Rev. Lett.*, 134:070403, Feb 2025.

[248] Zijian Wang, Zhengzhi Wu, and Zhong Wang. Intrinsic mixed-state topological order. *PRX Quantum*, 6:010314, Jan 2025.

[249] Ramanjit Sohal and Abhinav Prem. Noisy approach to intrinsically mixed-state topological order. *PRX Quantum*, 6:010313, Jan 2025.

[250] Tyler D. Ellison and Meng Cheng. Toward a classification of mixed-state topological orders in two dimensions. *PRX Quantum*, 6:010315, Jan 2025.

[251] Yimu Bao, Ruihua Fan, Ashvin Vishwanath, and Ehud Altman. Mixed-state topological order and the errorfield double formulation of decoherence-induced transitions, 2023.

[252] Ruihua Fan, Yimu Bao, Ehud Altman, and Ashvin Vishwanath. Diagnostics of mixed-state topological order and breakdown of quantum memory. *PRX Quantum*, 5:020343, May 2024.

[253] Pablo Sala and Ruben Verresen. Stability and loop models from decohering non-abelian topological order. *Phys. Rev. Lett.*, 134:250403, Jun 2025.

[254] Zijian Wang, Ruihua Fan, Tianle Wang, Samuel J. Garratt, and Ehud Altman. Fractional quantum hall states under density decoherence, 2025.

[255] Jong Yeon Lee, Chao-Ming Jian, and Cenke Xu. Quantum criticality under decoherence or weak measurement. *PRX Quantum*, 4:030317, Aug 2023.

[256] Cheng-Ju Lin, Weicheng Ye, Yijian Zou, Shengqi Sang, and Timothy H. Hsieh. Probing sign structure using measurement-induced entanglement. *Quantum*, 7:910, February 2023.

[257] Yijian Zou, Shengqi Sang, and Timothy H. Hsieh. Channeling quantum criticality. *Phys. Rev. Lett.*, 130:250403, Jun 2023.

[258] Samuel J. Garratt, Zack Weinstein, and Ehud Altman. Measurements conspire nonlocally to restructure critical quantum states. *Phys. Rev. X*, 13:021026, May 2023.

[259] Sara Murciano, Pablo Sala, Yue Liu, Roger S. K. Mong, and Jason Alicea. Measurement-altered ising quantum criticality. *Phys. Rev. X*, 13:041042, Dec 2023.

[260] Pablo Sala, Sara Murciano, Yue Liu, and Jason Alicea. Quantum criticality under imperfect teleportation. *PRX Quantum*, 5:030307, Jul 2024.

[261] Kabir Khanna and Romain Vasseur. Universal statistics of measurement-induced entanglement in tomonaga-luttinger liquids, 2025.

[262] Barbara M. Terhal and David P. DiVincenzo. Classical simulation of noninteracting-fermion quantum circuits. *Phys. Rev. A*, 65:032325, Mar 2002.

[263] Richard Jozsa and Akimasa Miyake. Matchgates and classical simulation of quantum circuits. *Proceedings of the Royal Society A: Mathematical, Physical and Engineering Sciences*, 464(2100):3089–3106, 2008.

[264] Alexander Teretenkov and Oleg Lychkovskiy. Exact dynamics of quantum dissipative xx models: Wannier-stark localization in the fragmented operator space. *Phys. Rev. B*, 109:L140302, Apr 2024.

[265] Joel J. Wallman and Joseph Emerson. Noise tailoring for scalable quantum computation via randomized compiling. *Phys. Rev. A*, 94:052325, Nov 2016.

[266] Sergey Bravyi and Alexei Kitaev. Universal quantum computation with ideal clifford gates and noisy ancillas. *Phys. Rev. A*, 71:022316, Feb 2005.

[267] M. Hebenstreit, R. Jozsa, B. Kraus, S. Strelchuk, and M. Yoganathan. All pure fermionic non-gaussian states are magic states for matchgate computations. *Phys. Rev. Lett.*, 123:080503, Aug 2019.

[268] Fernando de Melo, Piotr Ćwikliński, and Barbara M Terhal. The power of noisy fermionic quantum computation. *New Journal of Physics*, 15(1):013015, jan 2013.

[269] Guillermo González-García, Alexey V. Gorshkov, J. Ignacio Cirac, and Rahul Trivedi. Dynamical complexity of non-gaussian many-body systems with dissipation. *Phys. Rev. Lett.*, 135:190401, Nov 2025.

[270] Burkhard Kümmerer and Hans Maassen. The essentially commutative dilations of dynamical semigroups onmn. *Communications in Mathematical Physics*, 109(1):1–22, Mar 1987.

[271] Franco Fagnola, John E Gough, Hendra I Nurdin, and Lorenza Viola. Mathematical models of markovian dephasing. *Journal of Physics A: Mathematical and Theoretical*, 52(38):385301, aug 2019.

[272] Mekena Metcalf, Jonathan E. Moussa, Wibe A. de Jong, and Mohan Sarovar. Engineered thermalization and cooling of quantum many-body systems. *Phys. Rev. Res.*, 2:023214, May 2020.

[273] Stefano Polla, Yaroslav Herasymenko, and Thomas E. O'Brien. Quantum digital cooling. *Phys. Rev. A*, 104:012414, Jul 2021.

[274] Anne Matthies, Mark Rudner, Achim Rosch, and Erez Berg. Programmable adiabatic demagnetization for systems with trivial and topological excitations. *Quantum*, 8:1505, October 2024.

[275] Gilad Kishony, Mark S. Rudner, Achim Rosch, and Erez Berg. Gauged cooling of topological excitations and emergent fermions on quantum simulators. *Phys. Rev. Lett.*, 134:086503, Feb 2025.

[276] Dario Patanè, Alessandro Silva, Luigi Amico, Rosario Fazio, and Giuseppe E. Santoro. Adiabatic dynamics in open quantum critical many-body systems. *Phys. Rev. Lett.*, 101:175701, Oct 2008.

[277] P. Nalbach, Smitha Vishveshwara, and Aashish A. Clerk. Quantum kibble-zurek physics in the presence of spatially correlated dissipation. *Phys. Rev. B*, 92:014306, Jul 2015.

[278] Davide Nigro, Davide Rossini, and Ettore Vicari. Competing coherent and dissipative dynamics close to quantum criticality. *Phys. Rev. A*, 100:052108, Nov 2019.

[279] E.T. Jaynes and F.W. Cummings. Comparison of quantum and semiclassical radiation theories with application to the beam maser. *Proceedings of the IEEE*, 51(1):89–109, 1963.

[280] Bruce W. Shore and Peter L. Knight. The jaynes-cummings model. *Journal of Modern Optics*, 40(7):1195–1238, Jul 1993.

[281] Gerhard Rempe, Herbert Walther, and Norbert Klein. Observation of quantum collapse and revival in a one-atom maser. *Phys. Rev. Lett.*, 58:353–356, Jan 1987.

[282] C. W. Gardiner and M. J. Collett. Input and output in damped quantum systems: Quantum stochastic differential equations and the master equation. *Phys. Rev. A*, 31:3761–3774, Jun 1985.

[283] A. A. Clerk, M. H. Devoret, S. M. Girvin, Florian Marquardt, and R. J. Schoelkopf. Introduction to quantum noise, measurement, and amplification. *Rev. Mod. Phys.*, 82:1155–1208, Apr 2010.

[284] A. del Campo, I. L. Egusquiza, M. B. Plenio, and S. F. Huelga. Quantum speed limits in open system dynamics. *Phys. Rev. Lett.*, 110:050403, Jan 2013.

[285] J.R. Johansson, P.D. Nation, and Franco Nori. Qutip: An open-source python framework for the dynamics of open quantum systems. *Computer Physics Communications*, 183(8):1760–1772, August 2012.

[286] J. H. P. Colpa. Diagonalisation of the quadratic fermion Hamiltonian with a linear part. *Journal of Physics A: Mathematical and General*, 12(4):469–488, April 1979.

[287] Matthew T. Bell, Benoît Doucot, Michael E. Gershenson, Lev B. Ioffe, and Aleksandra Petković. Josephson ladders as a model system for 1D quantum phase transitions. *Comptes Rendus. Physique*, 19(6):484–497, 2018.

[288] Ananda Roy. Quantum electronic circuits for multicritical ising models. *Phys. Rev. B*, 108:235414, Dec 2023.

[289] Lorenzo Maffi, Niklas Tausendpfund, Matteo Rizzi, and Michele Burrello. Quantum simulation of the tricritical ising model in tunable josephson junction ladders. *Phys. Rev. Lett.*, 132:226502, May 2024.